The Complex Outgassing of Comets and the Resulting Coma, a Direct Simulation Monte-Carlo Approach

by

Nicolas Fougère

A dissertation submitted in partial fulfillment
of the requirements for the degree of
Doctor of Philosophy
(Atmospheric, Oceanic and Space Sciences)
in the University of Michigan
2014

Doctoral Committee:

Research Professor Michael R. Combi, Co-Chair
Associate Research Scientist Valeriy M. Tenishev, Co-Chair
Professor Iain D. Boyd
Professor Tamas I. Gombosi

©Nicolas Fougère 2014
All Rights Reserved

Thèse dédiée à
mes parents,
Catherine et Philippe Fougère,
mes grands-parents,
Gisèle et René Gudin, Colette et Michel Fougère,
et ma famille.

Acknowledgements

I would like to sincerely thank my dissertation committee co-chair and academic advisor Professor Michael R. Combi without who none of this work would have been possible. I would like to express my gratitude for giving me the opportunity to work on a topic of great scientific interest, and providing invaluable guidance and support toward the completion of this research work. Moreover, I am thankful to him for giving me the freedom to follow a different Masters program in the Industrial Operational Engineering (IOE) department at the same time as my research in planetary science in the department of Atmospheric Oceanic and Space Sciences (AOSS) at the College of Engineering at the University of Michigan. Also, I would like to thank him for his support when I attended the Planetary Science Summer School at the NASA Jet Propulsion Laboratory.

I would like to thank my dissertation committee Professor Michael R. Combi (co-chair), Associate Research Scientist Valeriy Tenishev (co-chair), Professor Tamas I. Gombosi, and Professor Iain for their knowledge and advice that considerably improved this thesis.

I would like to express my gratitude to Associate Research Scientist Valeriy Tenishev for his expert support with the computational part and the numerous valuable discussions about the projects. I would also like to thank him for providing the DSMC model (AMPS) that was used for this thesis.

I want to thank Dr. Martin Rubin and Dr. Boncho Bonev for their invaluable suggestions and support for this work, and continuous collaboration.

Table of Contents

List of Figures

List of Tables

List of Appendices

List of Abbreviations

AMPS	Adaptive Mesh Particle Simulator
AU	Astronomical unit
BATS-R-US	Block Adaptive Tree Solarwind Roe-type Upwind Scheme
CG	67P/Churyumov-Gerasimenko
DSMC	Direct SImulation Monte Carlo
EPOXI	Extrasolar Planet Observation and Deep Impact Extended Investigation
FOV	Field of view
FWHM	Full width at half maximum
HRI	High Resolution Instrument
HST	Hubble Space Telescope
HWHM	Half width at half maximum
ICES	Inner Coma Environment Simulator
ICT	International Critical Tables
IR	Infrared
IRCS	Infrared Camera and Spectrograph
IRTF	Infrared Telescope Facility
JFC	Jupiter-family comets
LPC	Long period comets
LTE	Local thermodynamic equilibrium
MRI	Medium Resolution Instrument
NESR	Noise equivalent spectral radiance
NTC	Non Time Counter
OPR	Ortho-para ratio
PSF	Point spread function
SNR	Signal-to-noise ratio
SOHO	Solar Heliospheric Observatory
SPC	Short period comets

SWAN	Solar Wind Anisotropy
SWMF	Space Weather Modeling Framework
SW3	73P/Schwassmann-Wachmann 3
TP	Test particles
UV	Ultraviolet
VIRTIS	Visible and Infrared Thermal Imaging Spectrometer
VLT	Very Large Telescope

Abstract

During its journey, when a comet gets within a few astronomical units of the Sun, solar heating liberates gases and dust from its icy nucleus forming a rarefied cometary atmosphere, the so-called coma. This tenuous atmosphere can expand to distances up to millions of kilometers representing orders of magnitude larger than the nucleus size. Most of the practical cases of coma studies involve the consideration of rarefied gas flows under non-LTE conditions where the hydrodynamics approach is not valid. Then, the use of kinetic methods is required to properly study the physics of the cometary coma. The Direct Simulation Monte-Carlo (DSMC) method is the method of choice to solve the Boltzmann equation, giving the opportunity to study the cometary atmosphere from the inner coma where collisions dominate and is in thermodynamic equilibrium to the outer coma where densities are lower and free flow conditions are verified.

While previous studies of the coma used direct sublimation from the nucleus for spherically symmetric 1D models, or 2D models with a day/night asymmetry, recent observations of comets showed the existence of local small source areas such as jets, and extended sources via sublimating icy grains, that must be included into cometary models for a realistic representation of the physics of the coma. In this work, we present, for the first time, 1D, 2D, and 3D models that can take into account the full effects of conditions with more complex sources of gas with jets and/or icy grains. Moreover, an innovative work in a full 3D description of the cometary coma using a kinetic method with a realistic nucleus and outgassing is demonstrated. While most of the physical models used in this study had already been developed, they are included in one self-consistent coma model for the first time.

The inclusion of complex cometary outgassing processes represents the state-of-the-art of cometary coma modeling. This provides invaluable information about the coma by refining the understanding of the material that constitutes comets. This helps us to comprehend the process of the Solar System formation, one of the top priority questions in the 2013-2022 Planetary Science Decadal survey.

Introduction

Comets are a heterogeneous class of objects that accreted in regions beyond the water frost line, where ices can condense (A'Hearn et al. 2012). While different processes such as irradiation by energetic particles, heating by passing stars, and collisions have affected the outer layer of comets during their long storage in the Oort cloud and scattered disk, cometary nuclei constitute the least modified structures from the formative epoch of the solar system and potentially in the interstellar molecular cloud from which the solar nebula condensed. Their composition and structure are critical clues to understanding the formation and evolution of the constitutive material of our planetary system, exposing processes experienced by matter prior to its inclusion into the nuclei of comets (Irvine et al. 2000, Mumma et al. 1993). The ice's higher sensitivity to thermal and radiation processes than dust particles implies that their abundances and identities are keys to answer cosmogonic questions. Then, comprehending the composition of comets and their origin helps understanding the initial stages, conditions, and processes of the Solar System formation and the nature of the interstellar matter that was incorporated, which is one of the top priority questions in the 2013-2022 Planetary Science Decadal survey.

The problem of the cometary origins is still unsolved. Several hypotheses have been advanced. The most popular theory resides in association of the formative region with the solar nebula (Lunine 1989, Fegley and Prinn 1989). However, other suggestions exist such as comets originated in fragments of the pre-solar nebula so-called satellite-nebulae (Cameron 1973), or in giant molecular clouds that would have been captured when the primordial solar system went through those clouds (Clube and Napier 1982).

Our solar system presents at least two different reservoirs of comets. The Oort cloud, which may lie at about $\sim$ 50 000 AU, is constituted of long-period comets (LPC) with period larger than 200 years that are randomly oriented on the celestial sphere. Its existence was conjectured in 1950 by Oort to explain the unique distribution of orbital energies for the observed LPC with a larger number of highly eccentric orbits and a low continuous distribution of comets with lower orbital energy. However, short period comets (SPC) are generally confined to orbits with low inclinations (<30°). These SPC would find their source in a ring of comets beyond the orbit of Neptune extending to about 50 AU, the so-called Kuiper belt.

The rapid expansion of ground-based measurements and the existence of a few in-situ measurements enabled taxonomy based on cosmogonic parameters such as composition, isotopic population, and nuclear spin temperatures (Mumma and Charnley 2011). Such taxonomy is of primary importance to extrapolate the evolution of material since the interstellar molecular cloud, which lead to the analysis of the composition of cometary material from both the nucleus and its rarefied atmosphere called coma.

Until recently, the common understanding was that the cometary tenuous atmosphere, a unique phenomenon in our planetary system due to the small influence that gravity exercises on it, was fully created by gas released directly from sublimation of the nucleus. Indeed, the fundamental idea of the physics of the comet is that as a comet approaches the Sun, the ices present on the nucleus sublimate releasing mostly water vapor with some fraction of other gases dragging out dust particles. However, volatile grains have been suggested as possible sources for observed species in comet for a long time (Festou 1999 and references therein) without any direct evidence of their existence until the recent spectacular images of EPOXI at comet Hartley 2 (A'Hearn et al. 2011). This enlarges the perspective of the possible gas sources in the cometary coma critically impacting the coma physics and measurement interpretation.

Model studies of the cometary coma are required to fully understand the phenomena leading to its formation and then comprehend the cometary physics, which provide the

basis for interpreting the different observations of comets. In his pioneering study, Eddington proposed a fountain model (Eddington 1910), which became the starting point of the approach of Haser's (1957) model, which treats the coma as a free expansion problem. The latter is still widely used today, but some physics-based model that treat dynamics, chemistry, and energy were implemented with different techniques such as hydrodynamics, kinetic, and hybrid kinetic/fluid models (Combi et al. 2004).

The first kinetic models for the coma used the test particle (TP) method, an iterative process where the calculation starts with an initial assumed description for the distribution function of the gas that serves as a background for TP of the same gas (Hodges 1990, Xie and Mumma 1996). More recently, Direct Simulation Monte Carlo (DSMC) models that follow the detailed molecular motions of a large number of molecules simultaneously became more current due to their inherent time dependent characteristic, which enables them to address a wider range of problems than TP methods (Bird 1994). The main advantage of DSMC methods compared to any hydrodynamics formulation such as Euler equations or Navier-Stokes equations is that DSMC calculations are able to treat a whole range of non-LTE processes as well as multiple species, including photochemical products that do not have Maxwellian distribution. Such regions where the hydrodynamics approach are not valid are present in the cometary coma, which makes the DSMC the method of choice to study in detail the expanding cometary atmosphere (Combi 1996).

The constant computer potential increase enabled the implementation of more physically accurate cometary models giving a better description of the coma than the classical spherically symmetric models. Tenishev et al. (2008, 2011) detailed a 2D axisymmetric approach with conditions, such as gas flux and inner boundary temperature varying with solar zenith angle computed with a thermophysical model applied to the target of the Rosetta mission comet 67P/Churyumov-Gerasimenko (CG). Models using more realistic aspherical nuclei are now possible (Crifo et al. 2003, Zakharov et al. 2009, Fougere et al. 2013). The flow and structure of a coma resulting from a relatively small active area on the nucleus as been explored by Combi et al. (2012) applied to CG after observations of Schleicher (2006) showing that only 4% of the nucleus' area would be active. Then,

jet structures as observed in several comets such as Tempel 1 and Hartley 2 (Belton et al. 2010, Farnham et al. 2007) can and must be included in modern models (Fougere et al. 2013) to reproduce measurements and analyze data.

In this thesis, I am recounting the work on the cometary coma conducted during the last four years at the University of Michigan's Department of Atmospheric, Oceanic and Space Sciences. First, some background about the existing work dealing with the coma will be presented. Then, the general cometary model and numerical method that our group uses will be detailed, followed by the physical assumptions made in the model. While most of the physical models used in this work have already been developed, it is the first time that they are included in one self-consistent cometary coma model. The model reproducing infrared (IR) spectra enabling to retrieve the local composition of the coma applied to the VIRTIS instrument on board of the Rosetta spacecraft is detailed. For the first time, sublimating icy grains contributing to the gas coma by their slow sublimation as they are dragged away from the nucleus by the gas are included in the model. Sublimating icy grains are the only way to explain the non isotropic decay of the rotational temperature and column density in the very inner coma of comet 73P/Schwassmann-Wachmann 3 (SW3) and comet ISON that were observed by high-dispersion echelle spectroscopy at IR wavelengths (Bonev et al. 2008, and Bonev - private communication). The next chapter will detail the dust and coma resulting from a small active area, showing the collimation of dust with such sources in application to the Rosetta target comet CG. Then, the ice and gas coma of comet Hartley 2, a comet with a nucleus showing areas of heterogeneous chemistries with a lobe releasing a large amount of CO_2 and ice and the waist as a source of water vapor, is detailed constraining the model with both ground-based and in-situ measurements. Finally, using a realistic nucleus, the state-of-the-art in cometary model is presented showing the different features related to the nucleus topography.

While most of the numerical and physical models were already included in the DSMC code from previous work by Dr. Valeriy Tenishev, I personally added some additional processes necessary to the completion of the work for this thesis. Moreover, while Dr. Valeriy Tenishev has maintained and updated the generic functions of the DSMC code,

I have performed further development for the sources related to the comet application and have transferred the existing physical models with respect to comets to the new 3D AMPS code. Also, I collaborated with Dr. Valeriy Tenishev in the implementation of the triangulated surface to coma outflow boundary conditions for irregular nucleus shapes in the 3D model.

Chapter 1

The Neutral Cometary Rarefied Atmosphere

This chapter will present the basis of the current understanding of the cometary atmosphere from previous work. First, the different gas sources are presented with direct sublimation of the nucleus and extended sources of sublimating icy grains. Then, an insight of the main physical processes in the coma is provided. Finally, the different models explaining the gas dynamics of the coma are detailed.

1.1 Gas Sources in the Coma

The major source of energy for the sublimation of volatiles in the coma is the solar radiation. The three major sources that produce the gas present in the coma (Figure 1.1 extracted from Huebner and Benkhoff (1999)) are:

- the surface of the nucleus mostly releasing water vapor
- the interior of the porous nucleus species more volatile than water such as CO and CO_2
- extended sources such as sublimating icy grains

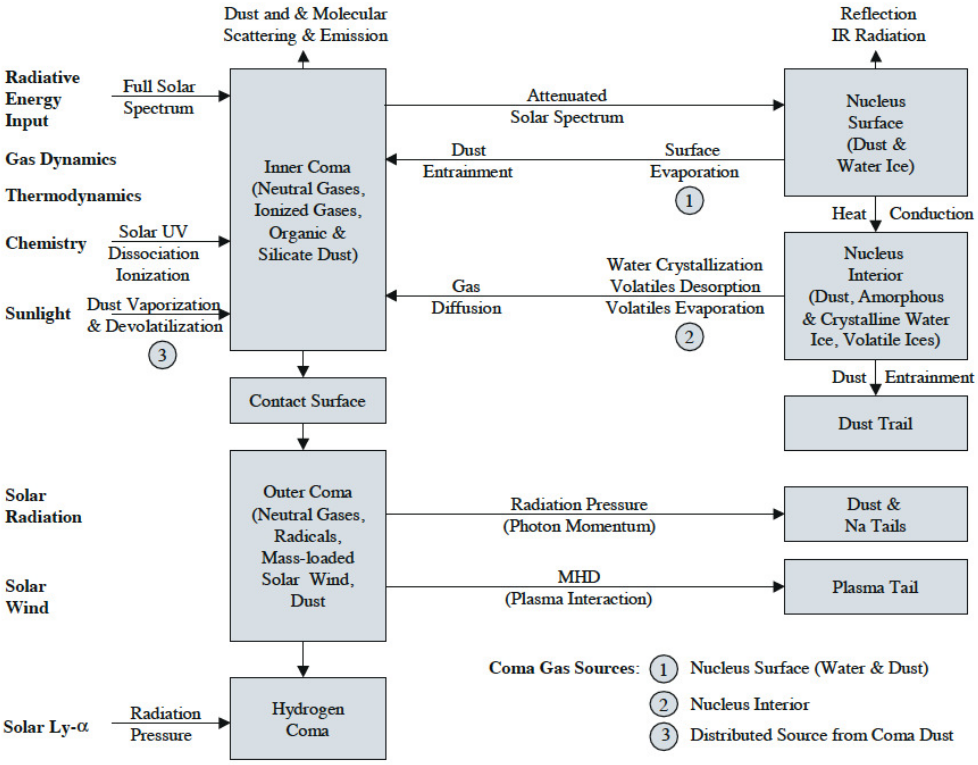

Figure 1.1: Radiative, physical, chemical, and thermodynamic processes in comets as they relate to the nucleus, coma, dust and plasma tails, and dust trails. Extracted from Huebner and Benkhoff (1999).

1.1.1 Gas Released from the Nucleus

Sublimation of the Surface of the Nucleus

Our present understanding of the cometary nuclei is based on the Whipple's (1950) "dirty snowball" picture, that is to say a mixture of frozen primary volatiles and refractory dust, whose sublimation upon warming created the visible coma and tails. This conglomerate model was able to explain cometary features such as the repeated nature of coma formation and gas loss for many revolutions, the survival of sun-grazing comets, the split-

ting of the cometary nuclei, and the occurrence of non gravitational forces (Whipple 1964). The prevailing view is that the solid components of cometary nuclei form a porous, low density, weak structure (Whipple and Huebner 1976, Donn and Rahe 1982) . When the nucleus, made up from icy conglomerates approaches the Sun, it gets directly exposed to solar radiation. Then, the nucleus absorbs an increasingly larger flux of solar radiation, and the sublimation rate of volatile molecules at the surface increases (Gombosi et al. 1986).

Models tried to estimate the production rate of outflowing gas particles. In their pioneering work, Delsemme and Swings (1952) obtain the local sublimation rate from the Hertz-Knudsen formula (Knudsen 1950, Skorov and Rickman 1998):

$$Z = P_{sat}(T_s)\sqrt{\frac{m}{2\pi k T_s}} \tag{1.1}$$

where T_s is the surface temperature, $P_{sat}(T_s)$ is the saturated vapor pressure and m is the molecular mass.

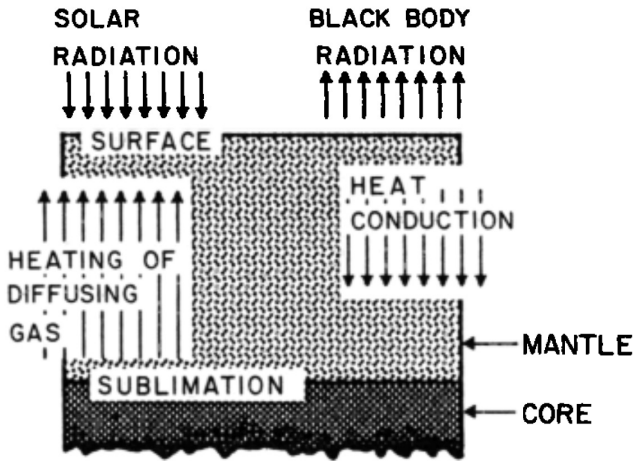

Figure 1.2: Schematic representation of energy transfer in the upper layer of a cometary nucleus (extracted from Gombosi et al. 1986)

With the hypothesis that the sublimating gas is in equilibrium with the surface of the nucleus, an approach based on energy balance can be used to derive the sublimation rate. As a first approximation, models do not take into account the differentiated layers of the nucleus assuming that it is a homogeneous mixture of dust and volatiles. This implies that the physical parameters such as albedo, emissivity or thermal conductivity are independent of time and location. Part of the solar radiation is scattered or absorbed by gas and dust in the coma. Most of the energy absorbed by the surface of the nucleus is used to sublimate water ice. Neglecting thermal radiation of the dust grains, the gas production rate can be computed from the energy balance between solar radiation input, reflection, reradiation in the IR, sublimation and heat conduction into the interior of the nucleus (Figure 1.2 extracted from Gombosi 1986), which can be written using the following energy balance equation at the cometary surface (Squires and Beard 1961):

$$\frac{F_{\odot}e^{-\tau}(1-A_{\nu})cos(\theta)}{r^2} = \epsilon\sigma_0(T_N(\theta))^4 + \frac{Z(\theta)L(T_N(\theta))}{N_A} + \kappa\frac{dT_N}{dR}|_{R_N^-} \tag{1.2}$$

where θ is the sub-solar angle, $T_N(\theta)$ is the temperature at the surface of the nucleus, $Z(\theta)$ is the gas production rate, τ is the optical depth of the coma, A_ν is the effective albedo, ϵ is the IR emissivity, σ_0 the Stefan-Boltzmann constant, $L(T_N(\theta))$ the latent heat of sublimation per mol, N_A the Avogadro number, and κ the thermal conductivity of the nucleus at the surface. Then, the vapor pressure at a given surface temperature can be found from the Clausius-Clapeyron equation of the phase transition from the ice to the gas (Huebner 1990):

$$p_N(\theta) = p_0 \exp\frac{L(T_N(\theta))}{kN_A}(\frac{1}{T_0} - \frac{1}{T_N(\theta)}) = n_N(\theta)kT_N(\theta) \tag{1.3}$$

$$Z(\theta) = \frac{1}{4}n_N(\theta)v_N(\theta) \tag{1.4}$$

where $n_N(\theta)$ and $v_N(\theta)$ are the number density and bulk velocity of the gas at the surface of the nucleus, respectively, p_0 and T_0 are the standard reference value of the gas pressure and temperature. This system of equations gives a unique solution for the gas production rate and the surface temperature of the nucleus.

Generally, the surface temperature of the nucleus is on the order of $\sim$ 200 K and the velocity of the gas at the surface is close to 300 m.s^{-1}, then a typical value of the flux of water molecules produced at the surface of a comet at heliocentric distance of 1 AU is of the order of 10^{22} m^{-2}.s^{-1} (Houpis and Mendis 1981). At heliocentric distances beyond 2.5 to 3 AU, the radiative heat input is no longer sufficient to overcome the latent heat required to sublimate water ice. The variation of the radiative heat input with heliocentric distance results in a dependence of the composition of the coma with the distance of the comet from the Sun. Indeed, the mixing ratio of volatile parent molecules relative to H_2O depends on the heliocentric distance (Biver et al. 1997). For instance, the CO and CO_2 relative population compared to water tend to increase with heliocentric distance due to their lower sublimation temperatures ($\sim$ 120 K).

Sublimation in the Interior of the Porous Nucleus

The heat conducted into the interior of the nucleus sublimates ices more volatile than water (such as CO, CO_2, CH_4 etc...). Most mantle energy balance calculations account for a solid dust mantle and a volatile component (Mendis and Brin 1977, Podolak and Hermann 1985, Fanale and Salvail 1984, Gombosi et al. 1986 and references therein). The heat is transferred into the interior of the nucleus by heat conduction in the ice-dust mixture and through the porous dust layer also called the mantle. Horizontal temperature gradients are typically much smaller than those measured in the radial direction.So, transverse heat flows are usually neglected. Then, a one-dimensional radial conduction heat flow controls the temperature distribution along the radial direction in the nucleus (Gombosi et al. 1986):

$$\rho_N C_N \frac{\partial T}{\partial t} - \frac{1}{r^2}\frac{\partial}{\partial r}(r^2 \kappa \frac{\partial T}{\partial r}) = Q_{int} \tag{1.5}$$

where C_N, ρ_N and Q_{int} are the specific heat, mass density, and internal energy source of the nucleus, respectively. Several possible sources have been considered such as decay of radioactive isotopes (Whipple and Stefanik 1966, Wallis 1980) or transition of amorphous ice to a crystalline state (Patashnick et al. 1974, Smoluchowski 1981, Klinger 1981). The mantle is very porous and therefore has poor heat conduction, which creates a strong temperature gradient through the dust layer (Weissman and Kieffer 1984, Horanyi et al.

1984).

Both heat and gas diffusion tend to chemically differentiate by layers the nucleus. Indeed, dust being the least volatile material is concentrated at the top of the nucleus. Right below it, a layer of both dust and water will be present. This will be followed by a layer containing dust, water ice, and species such as CO_2. Finally, the deepest layer includes the most volatile species (such as methane and CO). Hence, more advanced models used a three layer mantle model adding an intermediate layer with dust and clathrate (Houpis et al. 1985).

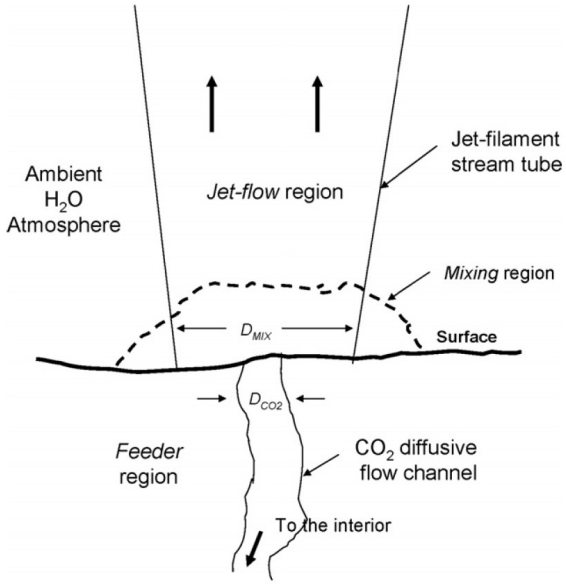

Figure 1.3: The diagram shows a jet-filament broken down into three physically distant regions: the feeder, mixing, and jet-flow regions. Extracted from Belton (2010).

Recent models attempted to explain the mechanism for creating collimated outflows such as jets as were observed in many comets now (Keller et al. 1986, Soderblom et al. 2004, Sekanina et al. 2004, Farnham et al. 2007, A'Hearn et al. 2011). Based on Deep Impact data, Feaga et al. (2007) showed a strong link between the localized CO_2 outflows

from the surface and collimated jet outflows. Belton (2010) classified these active areas in three types: Type I being dominated by the sublimation of H_2O through the porous mantle only explaining sub-solar fans, Type II being controlled by the localized and persistent effusion of super-volatiles from the interior, and Type III characterizing episodic releases of super-volatiles. Then, a jet-filament can be explained by the upward flow of super-volatiles such as CO and/or CO_2 from the interior to the surface along a diffusion channel, which then mixes locally with sublimated H_2O, the mixture being accelerated adiabatically up the stream (Belton 2010) (Figure 1.3 extracted from Belton (2010)).

1.1.2 Extended Source

Even if their existence was conjectured a few decades ago (Festou et al. 1993, Festou 1999), the first undeniable visual evidence of sublimating icy grains in the coma is due to the recent images of the EPOXI mission as the extension of the Deep Impact mission. This observation changes drastically the view of the physics of comet since direct sublimation of the nucleus is not anymore the only gas source in the coma. Indeed, as they are dragged away by the gas, icy grains slowly sublimate and release volatile particles forming an extended gas source. The nucleus may not even be the primary producer of water in the coma, which changes the thermodynamics of the cometary atmosphere since the icy grains release warmer H_2O at large distances from the nucleus (Fougere et al. 2012).

Sublimation of ice and ejection of dust particles entrained in the gas flow gradually erode the surface of the active region of the nucleus (Sekanina 1990). Grains carried away by the gas will heat up by sunlight and, as a result, organic component (hydrocarbon polycondensates) (Combi 1987, Llorca 1999) and water can be sublimated depending on the heliocentric distance and the particle size. The slow release of gas from these grains constitute the distributed source in the coma (Harris et al. 1997).

Before the EPOXI fly-by, some observations tended to confirm the hypothesis of the existence of a distributed source (Eberhardt et al. 1987, Meier et al. 1993, Biver et al. 1997, Leech et al. 1997, DiSanti et al. 2001, Combi et al. 2005). Indeed, spectroscopy

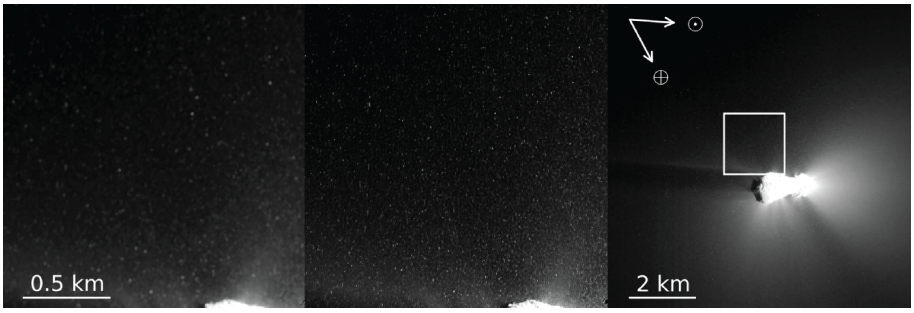

Figure 1.4: (Left) Original HRI image (left, hv5004024, E-66s, range 915 km). (Middle) Deconvolved image. (Right) MRI context image (mv5004029) showing the location of the HRI field above the large lobe of the nucleus. Arrows indicate projected directions to the Sun and Earth. (A'Hearn et al. 2011)

observations of comet show that while some components have a distribution varying in $1/r^2$, which is consistent with the simple radial expansion of the nucleus, others have a less steep distribution requiring an additional source of gas to slow down the density decrease of these molecules. In this way, the recent IR measurements of comet C/2009 Garradd showed a strong excess of water water in the projected sunward direction diverging from a classical isotropic release probably due to the release of water-rich icy grains (Villanueva et al. 2012).

The first attempt to model extended sources was done by Delsemme and Miller (1971), who have considered energy balance with temperature dependent water heat of sublimation to determine the vaporization rates of volatiles, and used an gas production release from grains analogous to the model of Haser (1957). They were able to determine grains' lifetimes depending on their initial sizes and the heliocentric distance finding that the icy halo extends to $\sim 10^4$ km at 1 AU. The application of their model to comet Burnham explained the optical depth effects on brightness measurements with grains sizes between 1 and 2 cm.

Beer et al. (2006) present a self-consistent model of the evolution of cometary icy grains in the coma. The authors provided lifetime and expansion distances for pure and dirty

(with refractories) icy grains at different heliocentric distances showing several orders of magnitude differences depending on the presence or not of refractories in the grains. Moreover, the distribution of grains of various sizes and the change of this distribution with distance from the nucleus explained variation of the power law distribution reported by the Giotto mission to comet 1P/Halley.

1.2 Physical Processes in the Coma

Intermolecular collisions in the innermost coma, photolytic reactions, and radiation cooling are the three most important processes in the coma and must be included to accurately model the cometary environment, with the addition of rotational heating by electron-neutral collisions that can play an important role in the temperature of the inner coma. Indeed, water is the primary neutral in the cometary atmosphere being up to $\sim 90\%$ of the species that outflow within heliocentric distances of 3-4 AU. After being released, neutral particles collide with each other thermalizing the inner coma. Then, at larger distances the H_2O and the other parent molecules are destroyed primarily through photodissociation, and to a lesser extent through photoionization, and dissociation and ionization interactions with solar wind ions and electrons. Eventually, the products of photodissociation themselves also undergo these photochemical processes. Moreover, water is radiatively active being the main contributor to radiative cooling via infrared radiation.

1.2.1 Intermolecular Collisions

Collisions play a fundamental role in the dynamics of the cometary coma enabling the diffusion of neutrals from high to low density regions, the conduction of heat from hot to cold regions, the exchange of energy between different particles, the acceleration of the bulk gas flow, among other processes. Collisions between particles can be either elastic or inelastic depending on the kinetic energy of the colliding particles is conserved or not, respectively. The nature of the collision process depends on both the type of particles and the relative kinetic energy in a way that generally, for low energies, elastic collisions dominate but that as the kinetic energy increases, inelastic collisions become more important

(Schunk and Nagy 2009). Collisions in the inner cometary atmosphere between neutral species are the primary mechanism of thermalization of the gas phase within the Knudsen layer with a mean free path of less than $\sim$ 1 m for typical conditions at 1 AU. Moreover, the solar intensity is weak in this region of the coma and excitation of the molecules occur through collisions (Whipple and Huebner 1976, Bockelée-Morvan 1987). Then, collisions define the vibrational and rotational distributions of the cometary species in the very inner coma, establishing local thermodynamic equilibrium. The collision rate between neutrals decreases rapidly with the distance from the nucleus so that collisions become negligible at a distance of a few times 1000 km from the nucleus (Huebner 1990), letting a fluorescence equilibrium slowly take place in the coma with a rotational temperature different than the kinetic temperature (Bockelée-Morvan 1987).

The description of the collisional relaxation in the coma is only possible using a kinetic theory. During collisions, gas molecules move through each other's potential fields of interaction. In practice, the collision time is negligible compared to the mean time between collisions implying that from a kinetic theory approach, intermolecular collisions are instantaneous.

In most cases of interest, the mean inter-molecular distance is large compared with the effective molecular diameter, so that it is much more likely that collisions only involve two particles. In order to express the different results from collision theory, we use the semantic from Schunk and Nagy (2009). In the case of elastic binary collisions, the mass, momentum, and energy of the colliding particles are conserved in the collision process. Noting $\vec{v_s}$ and $\vec{v_t}$ the particle velocities before the collision, while those after are $\vec{v_s}'$ and $\vec{v_t}'$, a binary collision can be represented in the laboratory frame of reference as in Figure 1.5 (Schunk and Nagy 2009) where θ is the scattering angle and b the so-called impact parameter, that is to say the distance of closest approach if the particles do not collide.

The use of a center-of-mass reference frame in describing binary elastic collision will become obvious with the following derivation. Then, we define the center-of-mass veloc-

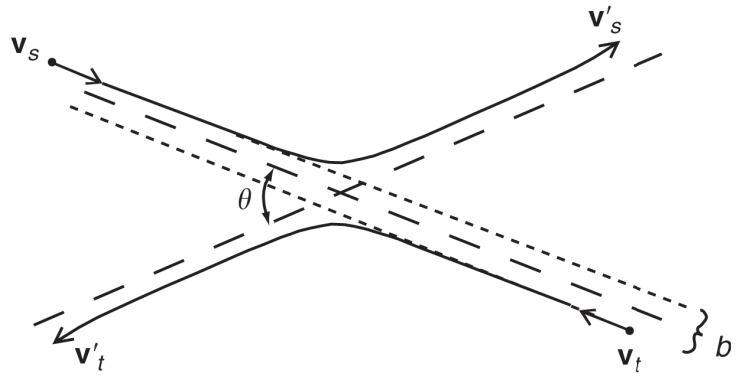

Figure 1.5: Binary elastic collision in a laboratory reference frame illustrating the velocities before and after collision, the scattering angle θ and the scattering angle b. Extracted from Schunk and Nagy (2009).

ity $\vec{V_c}$, and the relative velocity $\vec{g_{st}}$ of the colliding particles:

$$\vec{V_c} = \frac{m_s \vec{v_s} + m_t \vec{v_t}}{m_s + m_t} \tag{1.6}$$

$$\vec{g_{st}} = \vec{v_s} - \vec{v_t} \tag{1.7}$$

Similar parameters $\vec{V_c}'$ and $\vec{g_{st}}'$ can be defined using the velocities after collision. Using the fact that the particle masses do not change in a collision, in addition with conservation of momentum and kinetic energy, it can be shown that:

$$\vec{V_c} = \vec{V_c}' \tag{1.8}$$

$$g_{st}^2 = g_{st}'^2 \tag{1.9}$$

Hence, the center-of-mass velocity does not change in a collision while only the magnitude of the relative velocity is conserved (Schunk and Nagy 2009). Therefore, if the initial

velocities and the scattering angle are known, the velocities of the particles after collision can be calculated (Schunk and Nagy 2009).

In the center-of-mass reference frame, the two body problem of the particle motion of a particle of mass m_s with respect to another particle of mass m_t is equivalent to a one body problem of the motion of a molecule of mass m_r relative to a fixed center of force, where m_r is the reduced mass defined by:

$$m_r = \frac{m_s m_t}{m_s + m_t} \tag{1.10}$$

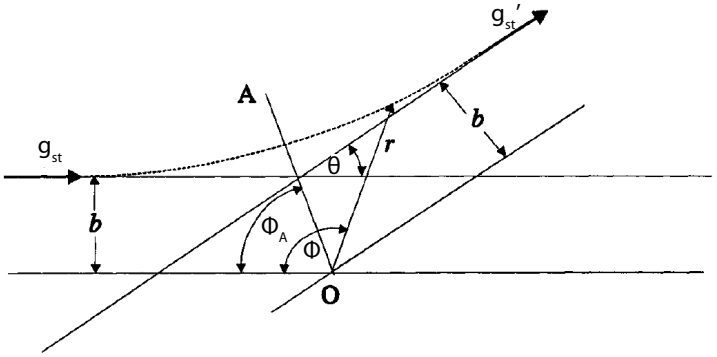

Figure 1.6: Frame of reference for the analysis of binary collisions using the interaction of the reduced mass particle with a fixed scattering center. Extracted from (Bird 1994).

This trajectory remains symmetrical about the transformed apse line which passes through the scattering center O (Bird 1994). With reference to the polar coordinates (r,Φ) represented in Figure 1.6 (adapted from Bird 1994), the angular momentum and energy of the particle of reduced mass may be equated to the limiting values of these quantities as $r \to \infty$, and using the fact that at the apse line OA $d\left(b/r\right)/d\theta = 0$, we find that:

$$\theta = \pi - 2\Phi_A \tag{1.11}$$

where Φ_A is the angle between $-\vec{g_{st}}$ and $\vec{OA}$ as indicated in Figure 1.6. Finally, defining

ϵ the angle between the collision plan and the frame of reference, we can express the coordinates (u'_r,v'_r,w'_r) of $\vec{g_{st}}'$ from the coordinates (u_r,v_r,w_r) of $\vec{g_{st}}$ with the following formulas (Bird 1994):

$$u'_r = cos(\theta)u_r + sin(\theta)sin(\epsilon)\left(v_r^2 + w_r^2\right)^{1/2} \tag{1.12}$$

$$v'_r = cos(\theta)v_r + sin(\theta)\frac{g_{st}w_r cos(\epsilon) - u_r v_r sin(\epsilon)}{\left(v_r^2 + w_r^2\right)^{1/2}} \tag{1.13}$$

$$w'_r = cos(\theta)w_r - sin(\theta)\frac{g_{st}v_r cos(\epsilon) + u_r w_r sin(\epsilon)}{\left(v_r^2 + w_r^2\right)^{1/2}} \tag{1.14}$$

From another part, it is necessary to know how often collisions between two molecules occur. This is usually defined by one of two parameters that are the collision frequency ν, which is the reciprocal of the mean time between two successive collisions suffered by a particular molecule, and the mean free path λ, defined as the average distance travelled by a molecule between collisions (Bird 1994). They are given by the following expressions (Bird 1994):

$$\nu = n\overline{V_c \sigma_T} \tag{1.15}$$

$$\lambda = \frac{V_{th}}{\nu} \tag{1.16}$$

where σ_T is the total cross section, n the gas density, V_{th} the mean thermal speed, and the bar notation relates to the average value over all molecules.

1.2.2 Photochemistry

Photochemistry plays a critical role in the coma notably via photodissociation and photoionization, where solar electromagnetic radiation gives the necessary energy resulting in the destruction of parent molecules released from the nucleus into daughter species, present in the coma but not directly created by the nucleus. While strong uncertainties are still present in the photochemistry of minor species such as organic, sulfur or nitrogen

species, the photochemical processes especially with respect to water in comets have been the object of numerous studies in the past refining the photodestruction rates and exothermic velocities thanks to the more accurate determination of cross sections and the solar flux spectrum (Huebner and Carpenter 1979, Openheimer and Downey 1980, Schleicher and A'Hearn 1982, Huebner et al. 1985, Allen et al. 1988, Huebner et al. 1992).

The destruction of H_2O creates OH, H_2, O, H, and various ion species in the inner and outer coma. The relevant photodestruction reactions of water are divided into four wavelength rages (Combi et al. 2004): 1357-1860 Å bounded by the effective onset wavelength for a non zero photoabsorption cross section (1860 Å) and the wavelength for which OH can be produced in excited electronic states (1357 Å), the Lyman-α peek 1216 Å, 984-1357 Å excluding 1216 Å, and below the ionization threshold 984 Å. The photodestruction rates depend upon the specification of the wavelength-dependent cross sections and the variable solar flux. Combi et al. (2004) reported updated calculations from Budzien et al. (1994) summarizing the relevant photodissociation reactions of water (Table 1.1).

The dominant photolytic process in the cometary comae takes place creating OH in an excited electronic state that occurs with a rate of β=1.2$\times 10^{-5}$ s^{-1} (Xie and Mumma 1996) and a mean excess energy ΔE=1.78 eV which corresponds to a mean ejection velocity of 18.5 km.s^{-1} for H atoms and 1.09 km.s^{-1} for OH in the rest frame of reference of the parent molecule. A photolytic heating process is efficient in the region where the dissociation products can be thermalized through collisions. This photolytic heating rate can be expressed as:

$$\Gamma = n_{H_2O} \beta \Delta E \tag{1.17}$$

where n_{H_2O} is the local water density.

Subsequent daughter species also undergo photochemical processes. For example, OH is photodissociated into O and H by photons with wavelength ranging between 958 Å and 2450 Å (Van Dishoeck and Dalgarno 1984, Schleicher and A'Hearn 1988) and at smaller

Wavelength Range (Å)	Reaction		Product Exothermic Velocities ($km.s^{-1}$)		Branching Ratio
1357-1860	$H_2O + h\nu$	$\rightarrow H + OH(X^2\Pi)$	18.5 (H)	1.09 (OH)	0.465
		$\rightarrow H_2 + O(^1D)$	13.7 (H_2)	1.71 (O)	0.005
1216	$H_2O + h\nu$	$\rightarrow H + OH(X^2\Pi)$	17.2 (H)	1.01 (OH)	0.291
		$\rightarrow H + OH(A^2\Sigma^+)$	5 (H)	0.3 (OH)	0.033
		$\rightarrow H_2 + O(^1D)$	15 (H_2)	1.8(O)	0.042
		$\rightarrow H + O + H$	7.4 (2H)	0.87(O)	0.050
984-1357 (no 1216)	$H_2O + h\nu$	$\rightarrow H + OH(X^2\Pi)$	<37 (H)	<2.2 (OH)	0.028
		$\rightarrow H + OH(A^2\Sigma^+)$	<25 (H)	<1.5 (OH)	0.003
		$\rightarrow H_2 + O(^1D)$	<22 (H_2)	<2.7(O)	0.004
		$\rightarrow H + O + H$	<17 (2H)	<2.0(O)	0.005
<984	$H_2O + h\nu$	$\rightarrow$ neutrals	X	X	0.024
	$H_2O + h\nu$	$\rightarrow$ ions	X	X	0.050

Table 1.1: Photochemical branching ratios for quiet Sun and exothermic velocities for H_2O vapor (Combi et al. 2004).

wavelength, OH is photoionized. In the high end of this UV wavelength range, the dissociation rates do not vary between quiet and active solar conditions due to the high stability of the solar flux at these wavelengths. However, a variation of about a factor of 2 in the rate at which these reactions occur appears with heliocentric radial velocity due to its influence on the solar radiation-pumping rates due to the Swings effect (Jackson 1980). The photodissociation rates and branching ratios for major cometary components are presented in the literature (Huebner et al. 1992) and have to be introduced in a cometary model.

1.2.3 Water Radiative Cooling

The temperature distribution in the coma has been extensively studied in the past. Water plays an important role in the thermal balance of the inner coma (Shimizu 1976, Marconi and Mendis 1982, Ip 1983, Huebner and Keady 1983, Crovisier 1984, Xie and Mumma 1996). Indeed, an accurate computation of the temperature is critical for cometary models

since most of the chemical processes occurring in the coma are temperature dependent.

Shimizu (1976) conjectured that the coma was efficiently cooled down by the emission of rotational lines by H_2O particles and came up with an empirical formula for the cooling rate L expressed as follow in units of erg.cm^{-3}.s^{-1}:

$$L = \frac{8.5 \times 10^{-19} T^2 n_{H_2O}^2}{n_{H_2O} + 2.7 \times 10^7 T} \tag{1.18}$$

with n_{H_2O} the local water density in cm^{-3} and T the water temperature. However, while the formalism by Shimizu (1976) was a successful first attempt to estimate the water radiative cooling in the coma, Crovisier (1984) performed an analytical analysis based on the GEISA spectroscopic data that suggested that the empirical cooling rate of Shimizu (1976) overestimated this effect, especially as low temperatures by as much as a factor of 10, because it does not take into account the optical thickness of the different lines. Indeed, radiative cooling is effective only when the emitted photon escapes the coma and for typical coma conditions all rotational lines are optically thick up to at least r=10^4 km (Bockelée-Morvan 1987). The curve presented by Crovisier (1984) can be analytically approximated providing a better estimate of the cooling rate (Gombosi et al 1986):

$$L = \begin{cases} -4.4 \times 10^{-22} T^{3.35} n_{H_2O} exp(-\tau_{IR}), & if \quad T < 52K \\ -2.0 \times 10^{-20} T^{2.47} n_{H_2O} exp(-\tau_{IR}), & if \quad T \geq 52K \end{cases} \tag{1.19}$$

where τ_{IR} is the infrared optical depth estimated by Huebner (1985) at a distance r from the nucleus by:

$$\tau_{IR} = \frac{0.4 n \sigma R_n^2}{r} \tag{1.20}$$

where n is the number density of absorbing gas at the nucleus, R_n the nucleus radius, and σ the mean infrared absorption cross section approximated by a typical value of 4×10^{-15} cm^2 (Huebner 1985).

1.2.4 Rotational Heating by Electron-Neutral Collisions

Xie and Mumma (1992) showed that the e-H_2O collisional rate exceeds that for excitation by neutral-neutral collisions at distances exceeding 3000 km from the cometary nucleus showing that the rotational temperature of the water molecules in the intermediate coma may be controlled by collisions with electrons rather than with neutral molecules. Indeed, theory showed that cross sections for rotational transitions are large for molecules with large permanent dipole moments such as water with 1.85 debye (Takayanagi and Itikawa 1970, Itikawa 1972). Similarly, experimental results from Sokolov and Sokolova (1982) reporting total cross section measurements from electron scattering experiments at low impact energy show reasonable agreement with theoretical calculations with rotational cross section for e-H_2O collisions of the order of 10^{-13} cm^2 at impact energy of 0.02 eV (Xie and Mumma 1992).

Assuming that the electron density and temperature are equal to the total ion density and temperature measured by the Giotto spacecraft at comet Halley, Xie and Mumma (1992) deduced that for a comet with a gas production rate of 5×10^{29} s^{-1}, the e-H_2O collisional excitation rate will dominate over the neutral-neutral collisions at a distance of about 3000 km as an upper limit. Moreover, most of the coma of interest are optically thick in the rotational lines, which enhances the significant role of collisions in both exciting and de-exciting rotational transitions showing that in the intermediate region of the coma, the rotational temperature is controlled by the electrons.

Since little experimental data is available for the rotational excitation of water by electrons (Jung et al. 1982), Cravens and Körösmezey (1986) used a theoretical calculation, via the energy transfer function for rotational excitation and de-excitation of water by electron impact, to derive analytical formula for the e-H_2O temperature exchange rates R:

$$R = \left(a + b \ln\left(\frac{T_e}{T_n}\right)\right) \frac{T_e - T_n}{T_e^{5/4}} \tag{1.21}$$

with T_e and T_n the electron and water temperature respectively, and the coefficients a and b defined by:

$$a = 1.052 \times 10^{-8} + 6.043 \times 10^{-10} \ln T_n \tag{1.22}$$

$$b = 4.18 \times 10^{-9} + 2.026 \times 10^{-10} \ln T_n \tag{1.23}$$

We point out that the temperature exchange rate is zero when $T_e = T_n$ as expected. Equation (1.21) is accurate within 12% for the typical temperatures encountered in the coma (Cravens and Körösmezey 1986).

1.3 Gas Dynamics of the Coma

In this section, we concentrate on the aspects of photochemistry and dynamics that are of primary importance for understanding the overall physical state of the coma. Quantitative model of the coma from Eddington's original fountain model, continued by Haser's model that treated the coma as a free expansion problem, to physically based models, provide the basis for interpreting the multiple diagnostic observations of comets. A full review of the gas dynamics of the cometary coma can be found in Combi et al. (2004).

1.3.1 Free-Expansion Models

Eddington's fountain model (1910) assumes that the comet is an isotropic and uniform point source releasing gas or dust with no particle decay such that their density would follow a $1/r^2$ decrease with the distance from the nucleus, except that the particles are also subject to a uniform acceleration a that pushes them to the opposite direction from the Sun. The latter model defines a paraboloid of revolution along a line parallel to the additional uniform acceleration and passing through the point source:

$$x^2 + y^2 = 2z\frac{v^2}{a} + \frac{v^4}{a^2} \tag{1.24}$$

where the acceleration a is aligned with the positive values of the z-axis, x and y complete the Cartesian coordinates, and v is the initial uniform outflow speed of the emitting particles.

The fountain model has been utilized by Mocknatsche (1938) and Wallace and Miller (1958) to show that the column density N, the parameter that would be observed by a remote observer neglecting optical depth effects and the heliocentric velocity dependence of the g-factor, is the same as for a point source without the acceleration (Combi et al. 2004):

$$N = \frac{Q}{4v\rho} \tag{1.25}$$

where Q is the particle production rate, ρ the projected distance on the sky plane from the nucleus, and v the radial flow speed.

Haser (1957) developed a still widely used model that takes into account production and destruction processes of daughter species in the cometary coma. The density of a parent species n_p and a daughter species n_d at some distance from the point source r are respectively given by the following formulas:

$$n_p(r) = \frac{Q}{4\pi r^2 v} e^{\frac{-r}{\gamma_p}} \tag{1.26}$$

$$n_d(r) = \frac{Q}{4\pi r^2 v} \frac{\gamma_d}{\gamma_p - \gamma_d} (e^{\frac{-r}{\gamma_p}} - e^{\frac{-r}{\gamma_d}}) \tag{1.27}$$

where γ_p and γ_d are the parent and daughter scale lengths derived from the product of the radial outflow speed and lifetimes of the parent and daughter of the considered species, and r the distance from the nucleus.

1.3.2 Hydrodynamics

Continuity, momentum, and energy conservation laws combined with the ideal gas law, which constitute the hydrodynamics equations, can describe the transport and energy of

the gas in the coma. At typical conditions, the mean free path in the coma close to the surface of the nucleus is less than a meter, which legitimizes the use of the hydrodynamics approach in the vicinity of the nucleus. Neglecting the Coriolis force, viscous stress, and internal energy, the conservation equations for the density, momentum and energy for a species s can be expressed in the form (Gombosi et al. 1986):

$$\frac{\partial n_s}{\partial t} + \nabla.(n_s \vec{u}_s) = \frac{\delta n_s}{\delta t} \tag{1.28}$$

$$m_s n_s \frac{D\vec{u}_s}{Dt} + \nabla p_s - m_s n_s \vec{G} = \frac{\delta \vec{M}_s}{\delta t} \tag{1.29}$$

$$\frac{3}{2}\frac{Dp_s}{Dt} + \frac{5}{2} p_s (\nabla.\vec{u}_s) + \nabla.\vec{q}_s = \frac{\delta E_s}{\delta t} \tag{1.30}$$

where D/Dt is the convective derivative, m_s, $\vec{u}_s$, n_s, p_s, and T_s are the mass, velocity, number density, kinetic pressure, and temperature of the gas species s, respectively, $\vec{q}_s$ is the heat flux and $\vec{G}$ is the external gravity. Finally, $\delta n_s/\delta t$, $\delta \vec{M}_s/\delta t$, and $\delta E_s/\delta t$ are the source terms of the number density, momentum, and energy terms due to collisions.

The density source term is difference between the chemical production (p_s) and the loss rate (l_s) of the neutral species s:

$$\frac{\delta n_s}{\delta t} = p_s - l_s \tag{1.31}$$

Momentum and energy sources have been rigorously derived considering the simplistic model of elastic collisions, inelastic processes being introduced in a heuristic manner. With this assumption, the momentum source term taking into account thermal diffusion and thermoelectric effects is given by (Schunk 1975):

$$\frac{\delta \vec{M}_s}{\delta t} = -\sum_t n_s m_s \nu_{st} (\vec{u}_s - \vec{u}_t) - \frac{1}{5}\sum_t \nu_{st} \frac{\mu_{st}}{kT_{st}} (\vec{q}_s - \frac{p_s}{p_t}\vec{q}_t) \tag{1.32}$$

where ν_{st} is the momentum transfer collision frequency between the neutral species s and t, μ_{st} and T_{st} the reduce mass and temperature, respectively, which can be expressed as follows:

$$\mu_{st} = \frac{m_s m_t}{m_s + m_t} \tag{1.33}$$

$$T_{st} = \frac{m_s T_s + m_t Tt}{m_s + m_t} \tag{1.34}$$

$$\nu_{st} = \frac{8\sqrt{\pi}}{3} \frac{n_t m_t}{m_s + m_t} r_{st}^2 \sqrt{\frac{2kT_{st}}{\mu_{st}}} \tag{1.35}$$

with r_{st} the sum of the radii of the colliding particles.

Finally, the energy source term for neutral gas taking into account energy transfer between neutral gas species via collisions (assumed elastic), radiative energy absorption, scattering, and emission processes (Q_{rad}) by the radiatively active molecules in the coma, and heating due to chemical processes (Q_{ch}) is given by (Schunk 1975):

$$\frac{\delta E_s}{\delta t} = -\sum_t \frac{n_s m_s \nu_{st}}{m_s + m_t} 3k(T_s - T_t) + Q_{rad} + Q_{ch} \tag{1.36}$$

The hydrodynamic approach is valid only within a collisional-dominated region. A typical definition of the collision zone of a spherical coma is bounded by the distance (R_{coll}) where the local value of the mean free path is equal to the distance to the center of the nucleus (Whipple and Huebner 1976, Combi et al. 1997):

$$R_{coll} = \frac{Q_{gas}\sigma}{4\pi v} \tag{1.37}$$

where σ is the collision cross section and v the outflow speed. Generally, the size of the collision sphere is about 10^4 km at an heliocentric distance of 1 AU for typically active comets (Tenishev et al. 2008).

The general three-dimensional time-dependant equations of hydrodynamics presented above can be reduced to a steady-state version. The main difficulty in implementing hydrodynamic equations is the definition of the boundary conditions. Indeed, when the boundary conditions are defined at the surface of the nucleus where the gas is subsonic, the gas will accelerate to eventually become supersonic going through a transonic transition which is an undefined point with a singularity. Different techniques have been used to address this issue. Marconi and Mendis (1983) used a shooting method to traverse the sonic point smoothly while Gombosi et al. (1985) solved the equations explicitly right above the sonic point (typically a few meters above the surface of the nucleus). However, the fluid region is unavoidably separated from the nucleus by a thin Knudsen layer region, where the boundary condition may not be compatible with the gas distribution from the equilibrium state (Gallis et al. 2006, Lilley and Sader 2008) and then cannot be treated as a fluid. Thus, recent work using the hydrodynamic approach formulates the boundary condition on top of the Knudsen layer (Crifo and Rodionov 1997, Crifo et al. 2002).

To study the entire coma including the regions where collisions do not drive the flow, kinetic methods are required. The kinetic technique was used to perform the work describe in this thesis. Then, it will be explained in details in the next chapter.

Chapter 2

Model and Numerical Method

In this chapter, the coma model from our approach, the kinetic method, will be detailed. The main assumptions in the kinetic approach used to model the coma and the numerical method (Fougere et al. 2012, 2013, Tenishev et al. 2008, 2011) are described.

2.1 Physics-Based Coma Model: the Kinetic Approach

2.1.1 Necessity of the Kinetic Approach

Most of the practical cases of coma studies involve the consideration of rarefied gas flows under non-LTE conditions where the classical hydrodynamics approach is not valid. This inaccuracy resides in the assumption that the system of the moment equations can be closed, which implies inherent limitations of the functional form of the velocity distribution function. The fluid approximation, which enables the use of an hydrodynamic approach, fails when the characteristic length of the flow gradient (L) becomes comparable with the mean free path (λ). The practical non-dimensional quantity to indicate the degree of flow rarefaction is called the Knudsen number and is defined as $Kn = \lambda/L$. Navier-Stokes and Euler equations do not take into account rarefaction effects so that they are strictly valid only at $Kn = 0$. Four different domains are usually considered (Bird 1994):

- $Kn < 0.01$: the flow can be considered as a continuum
- $0.01 < Kn < 0.1$: the so-called slip-flow regime
- $0.1 < Kn < 3$: the transition-flow regime where the assumption of the hydrodynamics approach are violated
- $3 < Kn$: the flow can be considered as free molecular and collisions between molecules may be neglected

It is important to insist on the fact that kinetic methods are valid for all values of Knudsen number even where hydrodynamics techniques can be used. This does not mean that all other modeling methods should be ignored and always substituted by kinetic approaches, which require long computation. Indeed, models such as Haser, Euler equations, or Navier-Stokes equations are highly useful and can give some critical insight of the physics of the phenomenon considered and the criterion of validity tends to be pushed to an upper limit of Kn=0.05 (Chen et al. 2003). However, assuming that the computation time is not too important, kinetic methods have a wider range of applications.

2.1.2 The Boltzmann Equation

Phase-Space Distribution Function

Kinetic theory uses a statistical description of the gas in terms of probability distributions defined in the phase space defined by ($\vec{r}$,$\vec{v}$) where $\vec{r}$ is the position vector and $\vec{v}$ the velocity vector. Indeed, the number of molecules in a real gas is so large that a description listing the position, velocity, and internal state of every molecule at a particular instant is unthinkable (Bird 1994). The phase space distribution $F(\vec{r}, \vec{v}, t)$ characterizes the number of particles in an infinitesimal volume element d^3rd^3v at time t (Gombosi 1998). Hence, noting d^6N the number of molecule at a particular phase-space location ($\vec{r}$,$\vec{v}$) at time t to be found in the space volume element d^3rd^3v is given by (Gombosi 1998):

$$d^6N = F(\vec{r}, \vec{v}, t)d^3rd^3v \tag{2.1}$$

Then, the local particle number density $n(\vec{r},t)$ describing the number of particles in a small volume element d^3r at time t can be found by integrating the phase-space distribution function over all possible velocity values (Gombosi 1998):

$$n(\vec{r},t) = \iiint F(\vec{r},\vec{v},t)d^3v \tag{2.2}$$

The normalized phase-space distribution function $f(\vec{r},\vec{v},t)$ is then usually introduced such that its integration over all velocity space yields to unity:

$$f(\vec{r},\vec{v},t) = \frac{F(\vec{r},\vec{v},t)}{n(\vec{r},t)} \tag{2.3}$$

The normalized phase-space distribution function can be physically interpreted such that $f(\vec{r},\vec{v},t)$ is the probability density of finding a particle at the velocity space point $\vec{v}$ at the space location $\vec{r}$ at time t (Gombosi 1998).

All average macroscopic properties can be derived from the normalized phase-space distribution function (Bird 1994, Gombosi 1998):

$$\overline{Q}(\vec{r},t) = \int Q(\vec{r},t)f(\vec{r},\vec{v},t)d^3v \tag{2.4}$$

where Q is any molecular quantity and $\overline{Q}$ its average.

Derivation of the Boltzmann Equation

After defining the statistical description of a gas at the molecular level, one needs to establish the relationships between the distribution function and the variables it depends on. The evolution of the phase-space distribution function of species s, F_s, is determined by the flow of particles under the influence of external forces and by the net effect of collisions (Schunk and Nagy 2009). The rate of change of F_s due to a time variation is given by:

$$\frac{dF_s(\vec{r},\vec{v_s},t)}{dt} = \lim_{dt\to 0} \frac{F_s(\vec{r}+d\vec{r},\vec{v_s}+d\vec{v_s},t+dt) + F_s(\vec{r},\vec{v_s},t)}{dt} \tag{2.5}$$

Since dt is a small quantity, the term $F_s(\vec{r}+d\vec{r},\vec{v_s}+d\vec{v_s},t+dt)$ can be expanded in a Taylor series such that:

$$F_s(\vec{r}+d\vec{r},\vec{v_s}+d\vec{v_s},t+dt) = F_s(\vec{r},\vec{v_s},t)+\frac{\partial F_s(\vec{r},\vec{v_s},t)}{\partial t}dt+\nabla_{\vec{r}}F_s.d\vec{r}+\nabla_{\vec{v_s}}F_s.d\vec{v_s}+... \quad (2.6)$$

Neglecting all the higher terms in the Taylor series expansion, and taking the limit when $dt \to 0$ with $v_s = d\vec{r}/dt$ and the acceleration $a_s = d\vec{v_s}/dt$, equation (2.5) becomes:

$$\frac{dF_s(\vec{r},\vec{v_s},t)}{dt} = \frac{\partial F_s(\vec{r},\vec{v_s},t)}{\partial t} + (\vec{v_s}.\nabla_{\vec{r}})F_s(\vec{r},\vec{v_s},t) + (\vec{a_s}.\nabla_{\vec{v_s}})F_s(\vec{r},\vec{v_s},t) \quad (2.7)$$

When collisions are not important, the left hand side is equal to zero and the equation is the so-called Vlasov equation. On the other hand, if collisions are important, then instantaneous change of particle velocities occur and the left hand side cannot be taken to be zero. This leads to the Boltzmann equation (1872), which is the appropriate description for the physical state of a rarefied gas (Bird 1994, Gombosi 1998, Schunk and Nagy 2009):

$$\frac{\delta F_s(\vec{r},\vec{v_s},t)}{\delta t} = \frac{\partial F_s(\vec{r},\vec{v_s},t)}{\partial t} + (\vec{v_s}.\nabla_{\vec{r}})F_s(\vec{r},\vec{v_s},t) + (\vec{a_s}.\nabla_{\vec{v_s}})F_s(\vec{r},\vec{v_s},t) \quad (2.8)$$

where $\delta F_s/\delta t$ is the integral of collisions that account for interparticle interaction.

The Boltzmann equation only assumes that the distribution function is a one-particle distribution, so that there is no correlation between particles in the phase space and then does not assume a particular form of the distribution function. From the Boltzmann equation, the assumption of LTE and the resulting Maxwell-Boltzmann distribution functions leads to the Euler equations while the Chapman-Enskog theory allows to find the Navier-Stokes equations. In order to study rarefied atmospheres and problems that span different domains of Knudsen numbers with transitions from LTE fluid with a high number of collisions to free-flow, the latter assumptions are violated and the use of an arbitrary form for the distribution function must be considered.

The velocity moments of the Boltzmann equation yield to the continuity, momentum, and energy equations. Thus, macroscopic physical quantities that characterize the gas

at a given location can be computed with this approach. It is possible to link kinetic approaches to hydrodynamics via the Boltzmann equation. Indeed, Schunk and Nagy (2009) presented a general system of transport equations for flowing neutral gases derived using Grad's (1958) formulation and Burger's (1969) collision terms referred as the 13 moment equations, which include continuity, momentum, internal energy, pressure tensor, and heat flow equations for each species. However, for cometary studies, only the five moment approximation is considered to characterize the neutral gas behavior within the collision-dominated region, which leads to the equations of hydrodynamics.

While using simplifying assumptions, the collision term can be simplified (short range interactions, Fokker-Planck approximation), the Boltzmann equation cannot be solved analytically for flows that involve complex geometries (Bird 1994). This justifies the use of required complex numerical methods to find a solution to this equation.

2.2 DSMC as Numerical Method

2.2.1 Description of the Method

Today, no general analytical solution to the Boltzmann equation exists and its numerical solution is still challenging. In fact, numerical solutions that require a computational mesh in phase space give problems because of the resulting number of dimensions and the difficulty to set boundary conditions (Bird 1994). The DSMC method is one of the most used numerical method to find a numerical solution to the Boltzmann equation. Indeed, one of the most important characteristics of the DSMC technique is that it does not require the formulation of integro-differential equations, so that it can be used to solve the kinetic equations with a collision integral accounting for elastic and inelastic collisions (Tenishev et al. 2008). Moreover, the DSMC method can be adopted to treat multispecies gas flows including their responses to imposed fields, collisions, and chemistry. Conservation of mass, momentum, and energy to machine accuracy are enforced since the post-collision velocities are determined using these conservation laws.

The fundamental work that resulted in the DSMC is described in Bird (1976, 1994), following by some review papers Bird (1978), Muntz (1989), Cheng (1992), Cheng and Emmanuel (1995), and Oran et al. (1998). A convergence proof of the DSMC method to the Boltzmann equation was proposed by Wagner (1992). The DSMC technique determines the state of a gas flow by following the collisional dynamics of a large number of statistically representative particles, which enables this approach to provide information about the gas where the collisions are too rare to maintain LTE conditions. The simulated particles' motion and interactions are used to modify their positions, velocities, or chemical reactions (Oran et al. 1998). The fundamental attribute of the method is the separation of the translational motion from the intermolecular interaction over small time intervals. Then, the general scheme of Monte Carlo models can be described by Markov chains with a finite set of states. Indeed the probability of transition depends only on the current state and is not affected in any way by the previous history. The evolution of the distribution function within a Markov process can be expressed as follows (Hochstim 1970, Ichimaru 1973):

$$f(\vec{v}, t + \Delta t) = \int f(\vec{v} - \Delta\vec{v}, t) P_{\Delta t}(\vec{v} - \Delta\vec{v}, \Delta\vec{v}) d(\Delta\vec{v}) \tag{2.9}$$

where $P_{\Delta t}(\vec{v}, \Delta\vec{v})$ is the probability for a particle having the velocity $\vec{v}$ at time t to have the velocity $\vec{v} + \Delta\vec{v}$ at time $t + \Delta t$.

To apply the previous equation to a real gas, a model for the transition probabilities needs to be implemented, most of which are available for practical cases. Since no simultaneous change of velocity coordinates for both partners during a collision is required by this formulation, the latter enables the description of a wider class of relaxation processes than the Boltzmann collision integral. Then, the result of a DSMC is an averaged value of a function that gives measurable quantities over a region of the phase space. To improve the computation time, the relatively complicated Markov chain needs to be approximated by a means of a simpler one so that the mean value of the function of interest remains the same in both cases. The development of collision relaxation schemes is based on the total collision frequency ν, which can be defined using a probability density ω of transition from $(\vec{v_i}, \vec{v_j})$ before collision to $(\vec{v_i}', \vec{v_j}')$ after collision, or with the total collision cross

section $\sigma_t(g_{ij})$ where g_{ij} is the relative speed between the particles i and j (Tenishev et al. 2008):

$$\nu = \frac{n}{N} \sum_{i<j} \int \omega(\vec{v_i}\vec{v_j} \rightarrow \vec{v_i}'\vec{v_j}')d\vec{v_i}d\vec{v_j} = \frac{n}{N} \sum_{i<j} \sigma_t(g_{ij})g_{ij} \tag{2.10}$$

In order to get the correct relaxation dynamics in a gas flow, the characteristic size of computational cells must be smaller than the value of the local mean free path.

The physical assumptions on which the numerical schemes of the DSMC method are founded (Bird 1994) are equivalent to solving the Boltzmann equation for gas undergoing binary collisions (Nanbu 1980, Babovsky and Illner 1989), which is a relatively good assumption for a dilute gas (Bird 1994). Indeed, the molecular chaos assumption is strictly valid only for an infinite number of particles. A correlation factor is inevitable when a finite number of modeled particles is used which, if significant, could cause the DSMC to converge to a different solution than the Boltzmann equation. Thus, there is a time interval of validity (Ivanov et al 1998) for which the correlation is negligible that needs to be respected for the DSMC to provide the right solution to the problem.

A DSMC modeling begins by setting the initial state of a certain number of molecules for all species in question throughout the simulation volume. Different boundary conditions from which particles are introduced into the simulation must be defined and characterized. The time steps that divide the simulation must be small enough so that only a small fraction of particles in any volume of space will collide over that time, and so that the accelerations lead to small enough velocity changes to allow finite-difference formulation to follow the particle trajectories. Each spatial cell can have its own collision time step so that useless collision testing do not need to be performed when the densities are relatively low. After a free-molecular motion, particles change their location and a set of representative collisions is computed. The final steady state is reached by running the simulation for a sufficiently long time, and the final state is independent of the initial state when an adequate "time to relax" is provided. The macroscopic flow properties are sampled using coordinates, velocity components and internal energy (when internal degrees of freedom are considered) of molecules in a particular cell every few time steps. The typical main

procedures involved in applying DSMC to a flow problem are summarized in Figure 2.1 extracted from (Oran et al. 1998).

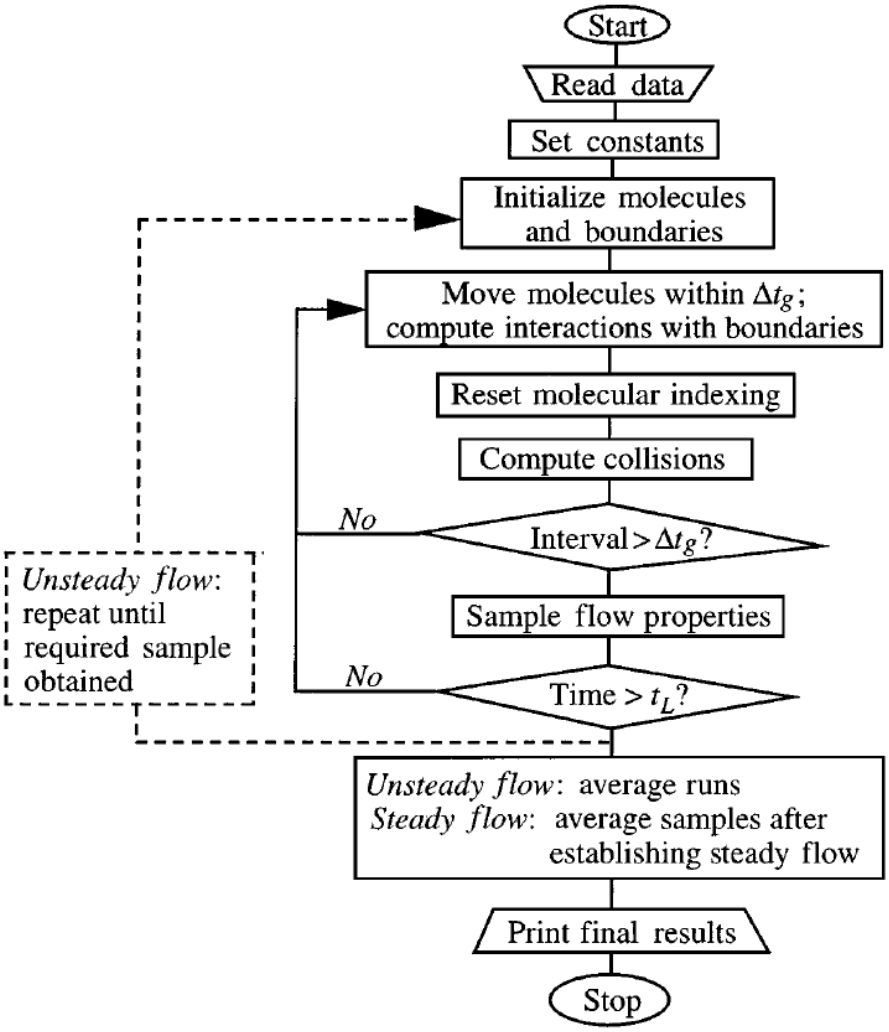

Figure 2.1: Flowchart presenting the DSMC method (Oran et al. 1998).

The DSMC code used in this thesis, called Adaptive Mesh Particle Simulator (AMPS), was adapted from the gas kinetic DSMC comet model by Tenishev et al. (2008, 2011), which includes a very general DSMC core of routines modules that can be applied to

a wide range of applications such as Mars' exosphere (Valeille et al. 2010), the lunar exosphere (Tenishev et al. 2013), Mercury's exosphere (Tenishev et al. 2012). It can adapt to the dimension of the coma inputs, and therefore can either be 1D, 2D, or 3D. The one-dimensional case is used mostly for validation purposes and models with lots of free parameters such as theoretical studies with icy grains as will be detailed in chapter 6. The calculations are made along the radial direction at the sub-solar point so are only functions of the distance from the nucleus. When more data about the comet is available providing more constraints on the model, a 2D model can be applied showing day/night asymmetries and active areas (Tenishev et al. 2008, 2011, Combi et al. 2012). Finally, three dimensional models give the most detailed description of the cometary coma with the use of a realistic nucleus (Fougere et al. (2013b), and chapter 8 in this thesis).

2.2.2 Particle Collisions

Hard Sphere Approximation

The simplest model to derive collision between molecules is the so-called hard sphere model, where two particles can collide if the distance between their two centers does not exceed the sum of the particles radii (Figure 2.2 adapted from Bird 1994). Indeed, the force between the two particles becomes effective when (Bird 1994):

$$r = \frac{d_1 + d_2}{2} = d_{12} \tag{2.11}$$

In such a case, the apse line goes through the centers of the two spheres approximating the molecules. Therefore, the impact parameter b and the total collision cross section σ_T can be found by:

$$b = d_{12} cos\left(\frac{\theta}{2}\right) \tag{2.12}$$

$$\sigma_T = \pi d_{12}^2 \tag{2.13}$$

It appears clearly that the scattering from hard sphere molecules is isotropic in the center-of-mass frame of reference (Bird 1994). Thus, the scattering angle θ can be generated

randomly with a uniform distribution.

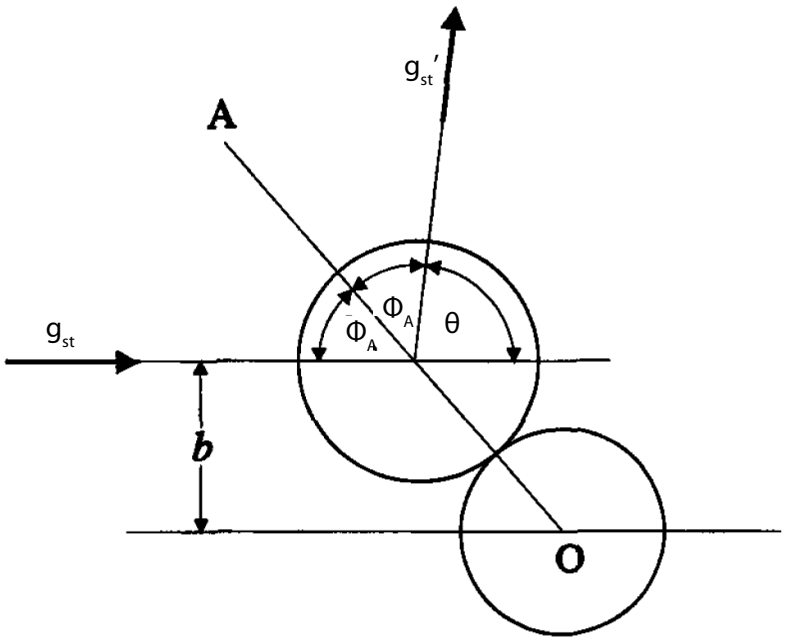

Figure 2.2: Collision geometry of hard sphere molecules. Extracted from Bird (1994).

With the Hard Sphere approximation, the collision frequency ν and mean free path λ defined in equations (1.15) and (1.16), respectively, become in the case of a simple gas:

$$\nu = n\sigma_T \overline{g} \tag{2.14}$$

$$\lambda = \frac{1}{\sqrt{2} n \sigma_T} \tag{2.15}$$

with n is the number density of the gas and $\overline{g}$ the average relative velocity in the center-of-mass frame of reference.

The advantage of the Hard Sphere model is obviously its simplicity. There exists more complicated model with more realistic scattering laws such as the Variable Soft Sphere model. However, it was shown that the variations in cross-section produce effects on the DSMC results that are far more important than those due to the scattering laws (Bird 1994). Moreover, by the use of phenomenological models, it is possible to incorporate in the cross sections used in the model different quantum information (Bird 1994). Hence, adding complexity to the scattering model does not appear to provide any significant improvement to the model.

Viscosity equivalent hard sphere cross sections were used for H_2O-H_2O while the other cross sections are estimated from combined atomic cross sections (Table 2.1).

H_2O-H_2O	$1.66 \times 10^{-15}(T/300)^{-0.6}$	OH-H_2	3.0×10^{-15}	H_2-CO	3.0×10^{-15}
H_2O-OH	3.2×10^{-15}	OH-H	1.5×10^{-15}	H-H	1.2×10^{-15}
H_2O-H_2	3.2×10^{-15}	OH-O	1.5×10^{-15}	H-O	1.2×10^{-15}
H_2O-H	1.8×10^{-15}	OH-CO	3.0×10^{-15}	H-CO	1.5×10^{-15}
H_2O-O	1.8×10^{-15}	H_2-H_2	3.0×10^{-15}	O-O	1.2×10^{-15}
H_2O-CO	3.2×10^{-15}	H_2-H	1.5×10^{-15}	O-CO	1.5×10^{-15}
OH-OH	3.0×10^{-15}	H_2-O	1.5×10^{-15}	CO-CO	3.2×10^{-15}

Table 2.1: Hard Sphere collision cross sections from Combi (1996) in cm^2

Numerical Model of Collisions

Diffferent models of numerical collisions exist such as the Time Counter scheme (Bird 1994), the Collision Frequency scheme (Koura 1986), the Null-Collision technique (Koura 1986, 1990), the Non Time Counter (NTC) scheme (Bird 1989, 1994), or the Majorant Frequency scheme (Ivanov and Rogasinsky 1988). Lutisan (1995) compared these different methods and found out that the NTC and the Null-Collision technique are the most reliable and fastest techniques. Tenishev et al. (2008, 2011) decided to use the NTC approach

for its clear representation of kinetic theory and its simplicity, enabling to add adaptivity techniques to the general simulation.

In the NTC method, the number of collisions undergone by a real particle $\mathfrak{N}$ during the time interval Δt is derived by the ratio of the volume spanned by average of the product between the total cross section σ_T and the particles relative speed g, to the cell volume $\mathcal{V}$ (Nanbu 1983, Abe 1993, Bird 1994):

$$\mathfrak{N} = w\overline{g\sigma_T}\frac{\Delta t}{\mathcal{V}} \tag{2.16}$$

where w is the particle weight. It is possible to check in turn the all $N(N-1)/2$ possible pairs where N is the number of simulated molecules in the given cell. However, it is very inefficient to proceed this way. The efficiency of this all procedure can be increased if only a fraction of the possible collision pairs is included and the resultant collision probability is then divided by this fraction. Then, the number of pairs selected to collide in the NTC approach is (Nanbu 1983, Abe 1993, Bird 1994):

$$\frac{N\left(N-1\right)}{2}w\frac{\left[\sigma_T g\right]_{max}}{\mathcal{V}}\Delta t \tag{2.17}$$

The collisions between two particles with relative speed g are then computed with the following probability:

$$P_{NTC} = \frac{\sigma_T g}{\left[\sigma_T g\right]_{max}} \tag{2.18}$$

It is important to point out that the rate of collisions is not affected by $\left[\sigma_T g\right]_{max}$ value. Initially, this parameter is set to a large but reasonable value for the species combination considered. Then, it is stored for each cell with the provision for it to be automatically updated in case a larger value is encountered.

2.2.3 Internal Energy Transfers

In a collision, the relative velocity at the point of contact is reversed leading to an interchange of energy between the rotational and translational modes, as well as between

the collision partners, the total energy being conserved (Bird 1994). The typical way to deal with these internal energy transfers is to use phenomenological models such as that of Borgnakke and Larsen (1975).

Borgnakke-Larsen model

The widely used Borgnakke-Larsen model ensures a detail balance by the selection of the post-collision values directly from the Maxwellian distributions, and the relaxation rate is controlled by considering a fraction of the collisions as elastic (Bird 1994). While it uses unphysical assumptions, it gives great results for the energy transfer during collisions. Indeed, in the Borgnakke-Larsen approach, the post-collision internal energy is a fraction of the total collision energy, which is directly sampled from a known equilibrium distribution associated with a temperature determined from the total energy of collision (Tenishev et al. 2008).

The distribution function for the translational kinetic energy of the relative motion of the collision partners E_t for a gas with coefficient of viscosity proportional to the temperature to the power ω is given by (Bird 1994):

$$f_{E_t} \propto E_t^{3/2-\omega} \exp\left(-\frac{E_t}{kT}\right) \tag{2.19}$$

where T is the gas temperature and k the Boltzmann constant. While the internal energy of the collision pair E_i is the sum of the internal energies of each of the collision partner, Hinshelwood (1940) showed that the distribution function for the internal energy of a molecule ϵ_i with ζ internal degrees of freedom, which represent the mean energy normalized by $kT/2$, can be expressed as:

$$f_{\epsilon_i} \propto \epsilon_i^{\zeta/2-1} \exp\left(-\frac{\epsilon_i}{kT}\right) \tag{2.20}$$

Then, using the previous equation and by simple integration, it is possible to show that (Bird 1994):

$$f_{E_i} \propto E_i^{\zeta-1} \exp\left(-\frac{E_i}{kT}\right) \tag{2.21}$$

Finally, using the fact that the collision energy is the sum of the translational energy and the internal energy, the probability density function for the collision energy E_c is proportional to the product of f_{E_t} and f_{E_i} (Bird 1994):

$$f_{E_c} \propto E_t^{3/2-\omega} \left(E_c - E_t\right)^{\zeta-1} \exp\left(-\frac{E_c}{kT}\right) \tag{2.22}$$

The term in the exponential can be seen as a constant since the temperature is defined by the total energy, so that the probability P of a particular value of the translational energy is proportional to the term in front of the exponential $E_t^{3/2-\omega} \left(E_c - E_t\right)^{\zeta-1}$ (Bird 1994). This probability reaches a maximum so that (Bird 1994):

$$\frac{P}{P_{max}} = \left(\frac{\zeta + 1/2 - \omega}{3/2 - \omega} \frac{E_t}{E_c}\right)^{3/2-\omega} \left(\frac{\zeta + 1/2 - \omega}{\zeta - 1} \left(1 - \frac{E_t}{E_c}\right)\right)^{\zeta-1} \tag{2.23}$$

The ratio P/P_{max} is compared to a uniformly distributed random variable between 0 and 1 to accept or not a post-collision value of translational energy E_t^* (Bird 1994). The post-collision internal energy is then derived using the conservation of the collision energy.

These computed energies must be divided between the two colliding molecules. In order to do so, one needs to derive the probability P that molecule number 1 has a post-collision energy $\epsilon_{i,1}^*$ given by the following formula (Bird 1994), assuming that the particles have the same number of degrees of freedom:

$$P \propto \left[\epsilon_{i,1}^* \left(E_i^* - \epsilon_{i,1}^*\right)\right]^{\zeta/2-1} \tag{2.24}$$

The previous expression has an extremum when the internal energy is equally split between the two molecules, giving a similar test for a comparison between P/P_{max} and a uniformly distributed random variable between 0 and 1 as an acceptance-rejection method to derive the repartition of energy (Bird 1994). Similar expressions can be found in the case of a gas mixture where the two molecules in the collision differ (Bird 1994).

The Borgnakke-Larsen model can be applied to both vibrational-translational and rotational-translational energy exchanges. This method explicitly assumes that the rotational and vibrational energies can be treated independently (Fujita and Abe 2002), which is important due to the fact that vibrational levels are widely spaced and vibration can, in general, not be seen as fully excited (Bird 1994).

Vibrational-Translational Energy Transfers

Two separate classes of vibrational relaxation within the DSMC frame exist: phenomenological approaches (Borgnakke and Larsen 1975) and state-to-state analysis of vibrational transitions (Fujita and Abe 2002, Josyula and Bailey 2001). The latter method is not practical due to the current lack of knowledge of energy-dependant level-to-level cross sections, and has only been developed for simple molecules. The phenomenological methods can themselves be subdivided into continuum (Borgnakke and Larsen 1975) and discrete (Haas and Boyd. 1993, Bergemann and Boyd 1994) representation of the energy spectra of vibrations. AMPS uses a continuum approach so we will limit to the description of this method. Indeed, while the assumption of continuity in the vibrational energy spectrum can become a significant approximation at very low temperatures, it is sufficient for our application.

In the classical approach, the degree of excitation and the effective number of vibrational degrees of freedom is variable (Bird 1994). The model assumes that the vibrational energy levels follow a simple harmonic oscillator model, so that the energy e_v associated with a mode with a characteristic vibrational temperature Θ_v is (Bird 1994):

$$e_v = \frac{kT}{\exp\left(\Theta_v/T\right) - 1} \tag{2.25}$$

Also, the number of effective vibrational degrees of freedom is determined by the following formula (Bird 1994):

$$\zeta_v = \frac{2\Theta_v/T}{\exp\left(\Theta_v/T\right) - 1} \tag{2.26}$$

The total vibrational energy for a given molecule is then obtained in summing over all modes relative to that molecule since each vibrational mode contributes to the energy exchange independently.

The temperature dependance of the vibrational relaxation process was first established by Landau and Teller (1936). The probability of a vibrational-translational energy exchange during a collision is usually defined by the relaxation collision number Z_v, which is equal to the ratio between the mean time of vibrational energy redistribution events and the mean collision time, such that (Landau and Teller 1936, Millican and White 1963, Boyd 1991):

$$Z_v \propto \frac{1}{T^{\omega}} \exp\left(\frac{A}{T^{1/3}}\right) \tag{2.27}$$

where A and ω are constants that depends on the properties of the considered molecules. Within the DSMC approach, the energy exchange between different internal degrees of freedom is considered during the relaxation stage of computations with a probability $1/Z_v$.

Rotational-Translational Energy Transfers

A similar approach can be used to model the exchanges between rotational and translational energies during collisions. Indeed, the process of rotational relaxation can be described in terms of the rotational collision number (Z_{rot}) defined as:

$$Z_{rot} = \frac{\tau_{rot}}{\tau_c} \tag{2.28}$$

Where τ_{rot} is the inverse of the frequency of energy redistribution evens and τ_c is the inverse of the collision frequency. For most cases of practical interest, Z_{rot} can be taken equal to a value of the order of 5 for water (Zeleznik 1969, Bird 1994). Within the DSMC method, the energy exchange between internal degrees of freedom is considered during the relaxation stage of computations. After collision partners are selected, the energy redistribution between rotational and translational degrees of freedom are considered using the ratio between inelastic to elastic collisions Z_{rot}. The number of rotational degrees of freedom depends on the geometry of the considered molecules. Linear molecules have 2

rotational degrees of freedom while more complex molecules such as H_2O have 3 rotational degrees of freedom.

2.2.4 Adaptivity of the Code

A significant difficulty in modeling the cometary coma is the large difference in scales from one region to another. Indeed, the mean free path varies by orders of magnitude from close to the surface where $\lambda \sim 1$m to the outer coma. We also face the challenge to simulate regions with orders of magnitude differences in density and also the inclusions of chemistry including trace species. In order to solve these problems without knowing in advance the structure of the flow, the code uses different techniques such as varying particle weights, varying time steps, and an adaptive grid structure.

Varying Particle Weight

Usually, each particle in a simulated cell represents a fixed number of real particles. Yet, this leads to issues in the case of an underrepresented species since a large number of samples is then necessary to get reasonable statistics for this species. The most straightforward method to adjust the number of simulated particles in a cell is to artificially adjust the particle weight across the computational domain (Serikov 1991, Miller and Combi 1994, Kannenberg and Boyd 2000) to allow for more modeled particles while keeping the total number of particles computationally reasonable.

AMPS (Tenishev et al. 2008, 2011) uses a weighting scheme consistent with the NTC approach, which allows for trace species while conserving momentum and energy on average. Indeed, when a particle crosses the boundary between two cells with different defined particle weights, a mass flow discontinuity appears across the interface. Then, particles with higher weights are cloned, while those with lower weights are deleted with a probability set by the ratio between the particle weight and the new cell weight.

Varying Time Step

In order to decouple particle motion from collisions, a finite time step is used in the DSMC method (Bird 1994). The time step has to be a small fraction of the mean collision time, which is inversely proportional to the density (Kannenberg and Boyd 2000). Then, when a single time step is used for the entire computational domain, it is limited to the minimum value corresponding to the highest density region, which in the case of the cometary coma corresponds to the region close to the nucleus, creating computational inefficiencies in low density locations where a single larger step would be sufficient (Kannenberg and Boyd 2000). The use of a varying time step prevents this issue and enables an optimal run of the simulation. Moreover, the use of a larger time step enables a better resolution since the sampling is then done over a larger number of different particles for a given sample length.

Adaptive Mesh

The different cometary coma calculations were done using a 1D spherically symmetric mesh, a 2D axisymmetric mesh extending from the surface of the nucleus to 10^6 km, or a 3D mesh up to a few tens of kilometers. Different mesh types are used for these different dimensional cases.

The 1D mesh is an exponentially distributed set of cells that spans from the surface of the nucleus to 10^6 km. The typical size of a cell, which is determined by the local mean free path, varies from a minimum of 0.1 m close to the nucleus where collisions are frequent to a maximum of $\sim$ 1000 km in the rarefied area of the coma, for a total about 2000 cells. Such a 1D DSMC simulation typically takes a couple of hours to reach steady state using 64 processors. Most runs are performed using the NAS computer resources at NASA Ames.

The 2D mesh is an unstructured mesh of triangular cells (Figure 2.3) that allows a pertinent description of the domain around complex 2D bodies such as projected aspherical nuclei. The mesh presents exponentially distributed cells allowing a rather constant num-

ber of particles per cell. Once again, the small cells ($\sim$ 0.5 m) are found close to the nucleus where the mean free path is low and the largest ones ($\sim$ 1000 km) are located at the largest distances from the nucleus to avoid useless collision testing for a total of more than 150000 cells. Typically, 2D DSMC simulations with AMPS reach steady state in a day or two using 128 processors.

The 3D mesh uses blocks of cubical cells (Figure 2.3) with increasing resolving power as the blocks get closer to the nucleus for similar reasons as in the other cases listed above. The DSMC requirement of the cell size to be smaller than the local mean free path implies that for typical comets, the number of cells becomes a strong limitation in the computation. Indeed, when a relatively active comet is relatively close to the Sun, the mean free path is a fraction of a meter so that the number of cells to map a spherical nucleus of 2 km radius can reach more than 50 million cells. Using a reduced cometocentric distance range to a few tens of kilometers, the minimum number of cells for a case with a gas production rate of 10^{24} s^{-1} is about 300000, so that AMPS runs with 256 processors for more than a day to reach steady state. However, it is necessary to understand that this is a lower limit and that the required number of cells increases strongly increasing with the gas production rate due to the decreasing mean free path.

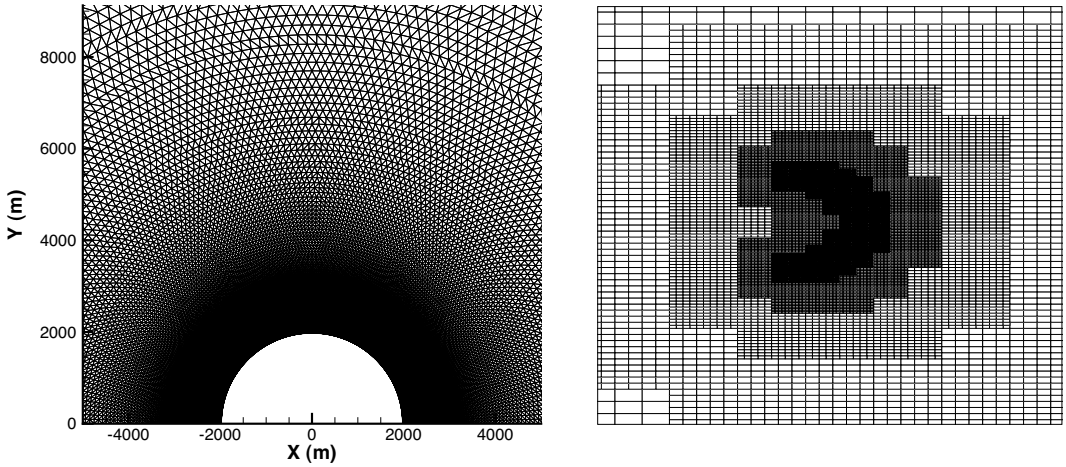

Figure 2.3: 2D adaptive mesh with exponentially distributed triangular cells (left panel) and a section of a 3D adaptive mesh with blocks of parallelepipedon cells (right panel).

Chapter 3

Physical Model and Assumptions

This chapter will detail the physical assumptions and models used in this work. The gas production from the nucleus is presented, together with the grain model used for both dust and ice. Then, the two grain sublimation models adopted for the gas extended source are described, followed by the electron model, which will be used for the study of the rotational temperature of the inner coma. Finally, a non-LTE line-by-line fluorescence model computed with the escape probability method used to simulate IR spectra is detailed. The reproduction of IR spectra is a valuable tool to derive the composition of the gas present and then, the different gas production rates.

While most of the physical models presented in this chapter were already included in AMPS from previous work by Dr. Valeriy Tenishev, I added some additional processes such as the electron-neutral collision heating model or the grain sublimation in particular for dirty icy grains for the purpose of this thesis. Also, AMPS is based on a core which contains the DSMC solver and generic functions for rarefied atmospheres that can be applied to different physical problems, themselves detailed within user source folders where the corresponding applied functions are defined. While Dr. Valeriy Tenishev maintains and updates the core of the AMPS code, I am in charge of further development for the sources related to the comet application and transferring the existing physical models with respect to comets to the new 3D AMPS code.

3.1 Gas Production from the Nucleus

3.1.1 Day/night Asymmetrical Gas Production.

While spherically symmetrical coma are assumed in 1D model and still broadly used to analyze data, the porous layer of ice and solid grains that covers the surface of a cometary nucleus is subjected to a periodic solar illumination that implies sublimation of volatiles and serves as a source of gas in the coma. The determination of the production rate from the surface of the nucleus requires accounting for a large number of processes such as the gradual absorption of the solar energy in a surface layer due to a finite optical opacity of the ice/dust mixture, thermal radiation, recondensation of the gas on the surface of the nucleus, the solid-state heat conduction, the subsurface ice sublimation and recondensation, and the subsurface transport of mass and energy due to gas diffusion (Tenishev et al. 2008). The thermophysical model from Davidsson and Gutiérrez (2004, 2005, 2006) is based on these processes and enables us to define the inner boundary conditions.

The source distribution from Tenishev et al. (2008) is extensively used in the current work. Tenishev et al. (2008) set the dayside condition using a rotating body with the spin axis assumed to be pointed at the Sun producing an axisymmetric distribution on the dayside hemisphere. While the night side condition was deduced from the average state of a fast rotating nucleus with a spin axis oriented normal to the orbit plane. Then, the two hemispheres were smoothly connected near the terminator. Ice and dust were assumed to be well mixed in volumetric proportion 0.7:0.3 with the bulk porosity of 70% on the surface of the nucleus. The heat conductivity is a volume-weighted average of the temperature-dependent conductivities of ice and dust reduced by a factor of 10 to account for porosity. Both the effective radius and length of pores were set to be 1 cm. The surface albedo was set to be 0.032, and finally, the opacity of the medium had a scale length of 2 cm (Tenishev et al. 2008).

In order to apply the previous thermophysical model to the outgassing of different comets, the modeled gas flux were scaled to the corresponding total production rate. The

temperature and gas flux distribution on the surface of the nucleus to formulate the inner boundary conditions used for comet CG as an example from Tenishev et al. (2008) are illustrated in Figure 3.1.

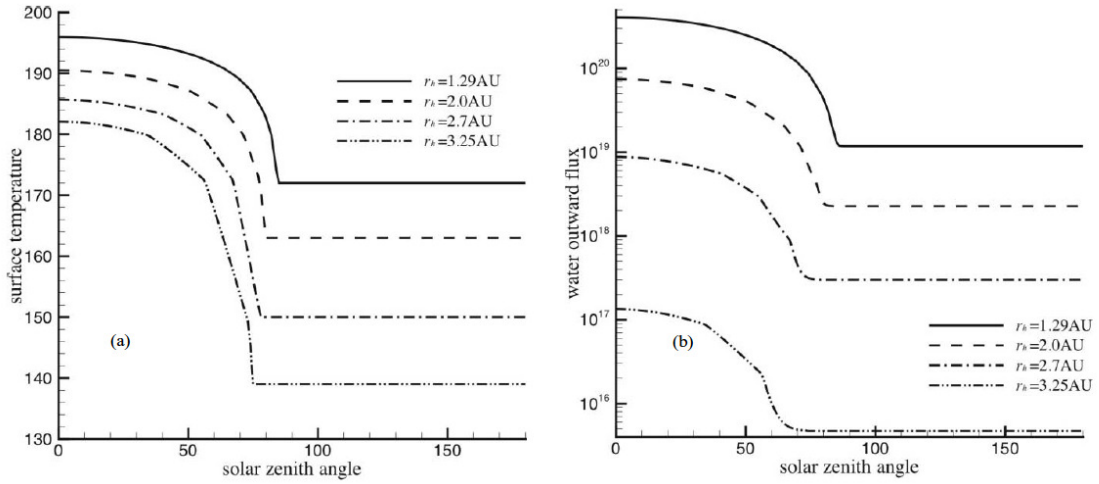

Figure 3.1: (a) The surface temperature (K) (b) water flux ($m^{-2}.s^{-1}$) distributions at heliocentric distances of 1.29, 2.0, 2.7, and 3.25 AU used to formulate boundary conditions for the gas flow on the surface of the nucleus (Tenishev et al. 2008).

The resulting general structure of the water flow in the coma is given in Figure 3.2 for the 1.29 AU case from Tenishev et al. (2008) applied to comet CG. The gas flux from the surface is produced from the results of the thermophysical model. The flux on the day side concentrated around the sub-solar point strongly dominates creating higher particle densities on the day side. Similarly, particles are created at higher temperatures on the day-side so that the coma is warmer on the day hemisphere than on the anti-sunward area. Momentum exchange with energetic daughter species such as H_2 and H heats the water coma and leads to a perturbation of the tail of the H_2O velocity distribution in the region of collisional transition of the coma (Tenishev et al. 2008). This effect decreases as the heliocentric distance increase due to the less important gas flux sublimated from the nucleus and the longer lifetimes of the particles with respect to photochemistry, reducing the momentum exchange between energetic particles and water (Tenishev et al. 2008).

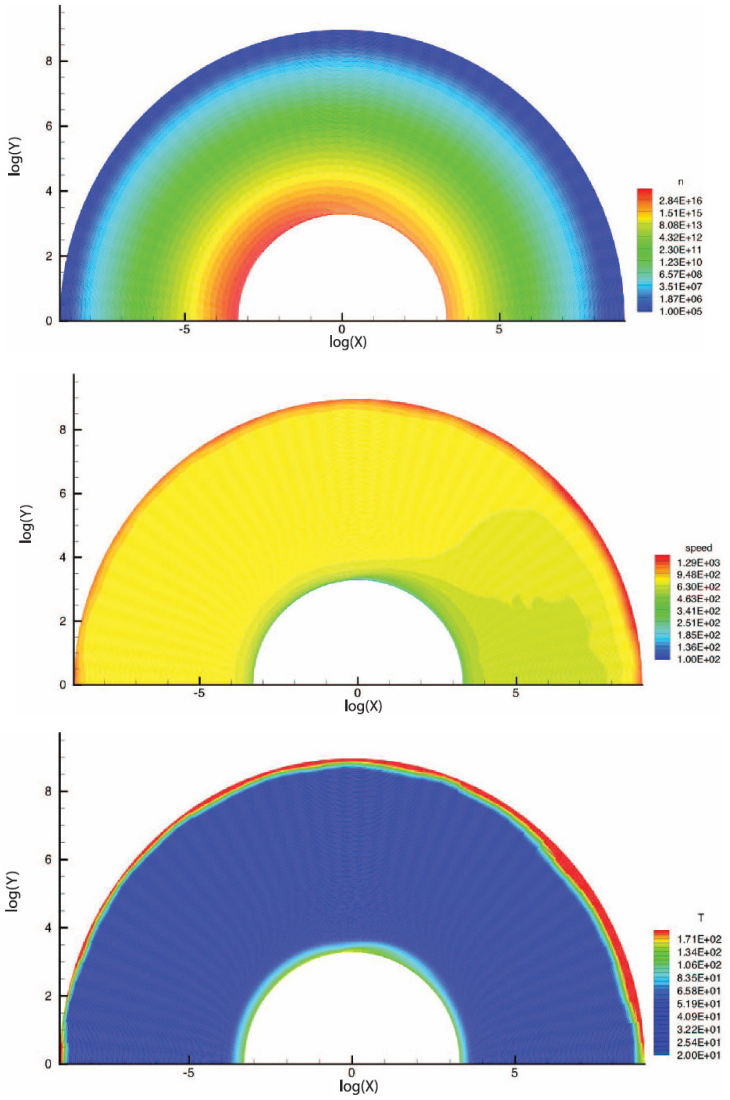

Figure 3.2: Number density (m^{-3}) (top), mean flow velocity ($m.s^{-1}$) (middle), and kinetic temperature (K) (bottom) of water at a heliocentric distance of 1.29 AU in logarithmic scale. The internal boundary on the plot represents the surface of the nucleus, and the outer boundary represents a distance of 10^6 km from the nucleus. (Tenishev et al. 2008)

3.1.2 Constant Flux over Active Areas.

The previously introduced day/night asymmetrical models cannot reproduce all cometary outgassing. Indeed, discrete active areas need to be included to provide a complete description of the cometary coma. Due to their small size with respect to the nucleus' surface and concerning the uncertainties with respect to their exact position, we decided to use a simple constant flux of gas released by these active areas.

An active area is then defined by the intersection of a cone whose apex is at the center of the nucleus with the nucleus' surface. Hence, the active patch is fully described by its position, its semi-angle, and the total gas production rate which will be equally divided over the active area.

3.2 Grain Model

A relatively simple power-law expression for the distribution of grain size has been proposed (Hanner 1982, Divine et al. 1986, Grun et al. 1989) based on the observations of the spectral energy distribution from Sekanina and Farrell (1982):

$$f(a) \propto a^n \tag{3.1}$$

where a is the radius of the grain and n the power-law index typically varying between -2.7 and -4.5 (Jockers, 1997).

Assuming spherical grains and neglecting the influence of the Lorentz force, and using an accelerated coordinate system where solar gravity is already taken into account, the only remaining three forces acting on the grains are the gas drag, the gravity attraction from the nucleus, and the solar radiation pressure (commonly given by its value with respect to the solar gravity). Assuming that the position of the grain with respect to the nucleus r is much smaller than its position with respect to the sun r_h which is the case in typical applications, the grains' motion is governed by the following expression (Gombosi et al.

1986, Tenishev et al. 2011):

$$\frac{4}{3}\pi a^3 \rho_d \frac{d\vec{v_d}}{dt} = \pi a^2 \frac{C_d}{2} \rho_g (\vec{v_g} - \vec{v_d}) \|\vec{v_g} - \vec{v_d}\| - \frac{4}{3}\pi a^3 \rho_d \frac{GM_n}{r^2}\frac{\vec{r}}{r} + \beta \frac{4}{3}\pi a^3 \rho_d \frac{GM_s}{r_h^2}\frac{\vec{r_h}}{r_h} \quad (3.2)$$

where G is the gravitational constant, M_n and M_s the masses of the comet's nucleus and the Sun respectively, $\vec{v_g}$ and $\vec{v_d}$ are the velocity of the surrounding gas and the velocity of a spherical grain with radius a, respectively, ρ_g is the mass density of gas molecules, and ρ_g is the mass density of an individual grain. The factor β is the ratio of the radiation force to the solar gravitational force following the notation from Burns et al. (1979). β has been calculated for different materials, notably for pure and dirty icy grains where it is always less than 1 (Burns et al. 1979, Mukai et al 1989). An analytical formula for β was derived by Agarwal et al. (2007):

$$\beta = \frac{3L_\odot Q_{pr}}{16\pi c G M_\odot \rho_g a} \quad (3.3)$$

Where $L_\odot$ and $M_\odot$ are the luminosity and mass of the Sun, respectively, and Q_{pr} is a material-dependant radiation pressure efficiency (Ishiguro 2008, Burns et al. 1979). While, radiation pressure was ignored for most of the applications presented in this work, it is of critical importance to explain the OH asymmetry in comet Hartley 2 that will be presented in chapter 7. For typical conditions in the coma, the drag coefficient C_d is approximated by the constant value of 2 (Gombosi et al. 1986) which is a good approximation for typical conditions in the coma.

The above expression implies that there is a maximum liftable grain size a_{max} determined by the balance of the gas drag applied to the grains, the radiation pressure, and the nucleus' gravity (Gombosi et al. 1986, Tenishev et al. 2011, Combi et al. 2012), which in the case of a spherical nucleus and neglecting the radiation pressure can be written as:

$$a_{max} = \frac{3R_c^2 C_d n_g m g v_g^2}{8\rho_d G M_c} \quad (3.4)$$

where R_c is the radius of the nucleus, ρ_c is the nucleus' mass density, $M_c = \frac{4}{3}\pi R_c^3$ is the total mass of the nucleus, m_g is the gas molecular mass, $v_g = \sqrt{\frac{2kT_{Knudsen}}{\pi m_g}}$ is the mean

upward expansion velocity (Bird 1994), and n_g the gas number density.

Finson and Probstein (1968) showed that the dust effectively decouples from the gas within a few nucleus radii and reaches a terminal velocity varying by a few orders of magnitude over the grain size range. At large distances from the coma, the trajectory of the grain is determined by the combination of solar radiation pressure and solar gravity.

Figure 3.3 shows the distribution of the dust in the inner coma for comet CG at 1.29 AU with a dust size distribution exponent of -4 and a dust to gas ratio of 0.8 from Tenishev et al. (2011). A dust density spike clearly appears above the terminator resulting from the sharp variation of the water production rate. Indeed, the gas in the coma expands into the region with the lower density and forms a tangential component to the gas flow, which sweeps dust grains toward the night side of the coma where they accumulate (Tenishev et al. 2011).

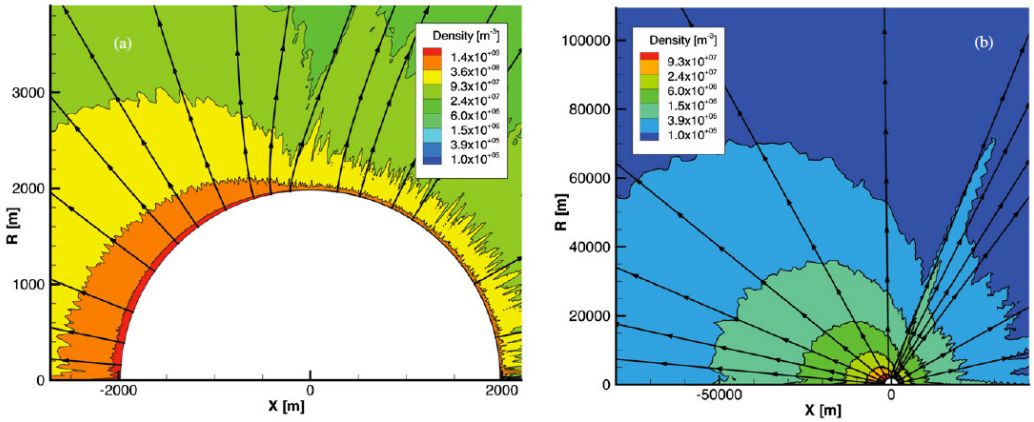

Figure 3.3: Number density of dust in the immediate vicinity of the nucleus (a) and at a cometocentric distance up to ∼80 km (b) at a heliocentric distance of 1.29 AU. Extracted from Tenishev et al. (2011).

The dust grains start their motion with a negligibly small velocity at the surface of the nucleus set at 0.001 m.s^{-1} and are accelerated by the gas drag as they move into the coma.

Then, the dust decouples from the gas within a distance of about 10 nucleus radii after which it will expand with a constant velocity and a density varying with r^{-2}. Figure 3.4 illustrates this property of the grains using the 1.29, 2.0, 2.7, and 3.25 AU cases from Tenishev et al. (2011).

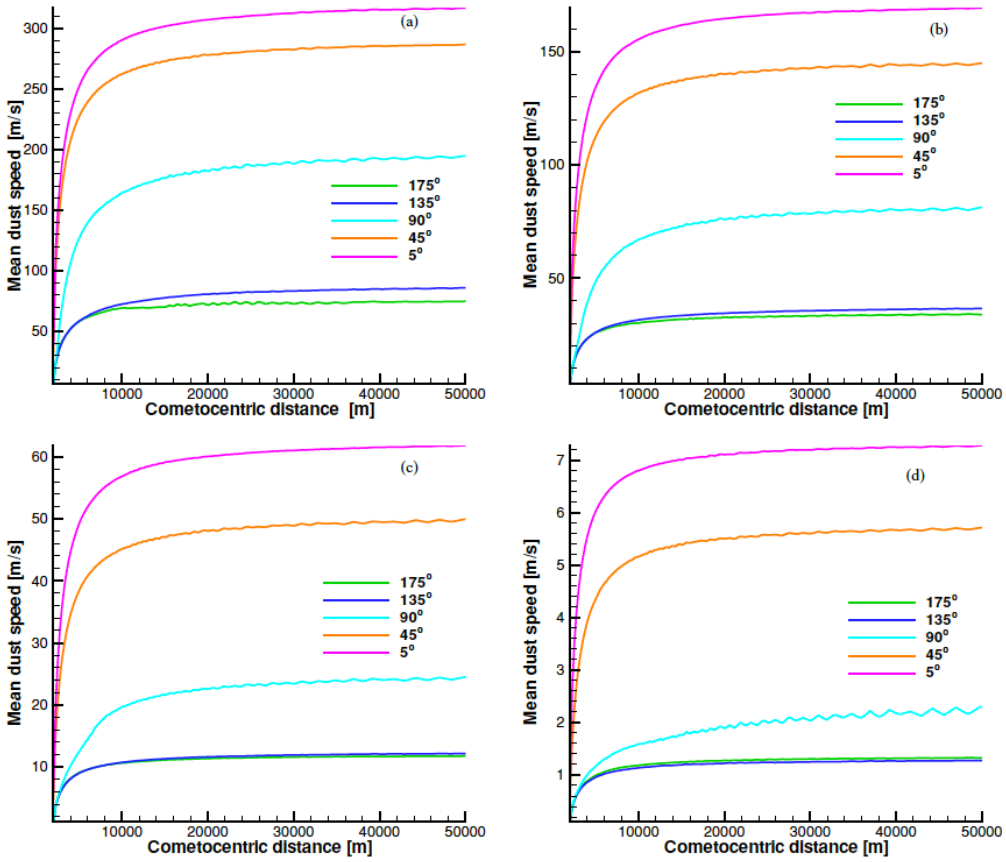

Figure 3.4: Mean dust velocity at heliocentric distances of 1.29 AU (a), 2.0 AU (b), 2.7 AU (c), and 3.25 AU (d) as a function of cometocentric distances for different sub-solar angles. Extracted from Tenishev et al. (2011).

3.3 Sublimating Icy Grains

Two different models of sublimating grains were used: pure icy grains and "dirty" icy grains. While pure ice grains absorb in the UV and in the IR, dirty icy grains absorb well in the visible. Hence, the equilibrium temperature and a fortiori the sublimation rate of dirty icy grains is considerably higher than that of pure icy grains. Grain analysis shows that the grain equilibrium temperature is not sensitive to the exact amount of dirt (Beer et al., 2006) so, we arbitrarily decided to use grains with 90% of ice and 10% of dirt. In the process of our study, we noticed that the nature of the dirt had a negligible influence on the results, which leads to the choice of magnetite as the dirt component.

The pure icy grain model follows the results from Patashnick et al. (1975) who derived grains' equilibrium temperatures and sublimation rates as a function of the grain size and heliocentric distance through conservation of energy. Four components control the energy of the grains: the power dissipated by sublimation or released by condensation P_s, the power absorbed P_a, the power emitted by the ice particle P_τ, and the energy stored by the particle which can be ignored in a quasi-steady state situation. Conservation of energy requires that:

$$P_s + P_a + P_\tau = 0 \tag{3.5}$$

When sublimation occurs, P_s can be expressed as follows: that:

$$P_s = -HA\Phi \tag{3.6}$$

where H is the heat of sublimation for ice with a typical value of 2.78×10^6 J.kg^{-1}, A is the surface area of the ice particle, and Φ the sublimation rate takes the form (Delsemme and Miller 1971, Patashnick et al 1975, Gombosi 1986, Lien 1990):

$$\Phi = \alpha(T_s)P(T_s)\left(\frac{m}{2\pi kT_s}\right)^{1/2} \tag{3.7}$$

where $P(T_s)$ is the equilibrium vapor pressure at the surface temperature obtained from the Clausius-Clapeyron equation, m is the mass of the water molecule, and $\alpha(T_s)$ is the

accommodation coefficient which for the range of temperatures considered here is close to unity.

Then, the absorbed power for a spherical particle can be written (Patashnick et al. 1975):

$$P_a = A \int_0^\infty \left[\frac{S(\lambda)}{4R^2} + F(\lambda, T_w) \right] Q(\lambda, r, n^*) d\lambda \tag{3.8}$$

with $S(\lambda)$ the solar energy spectrum at wavelength λ that was approximated by a 5900 K blackbody radiation, $F(\lambda, T)$ the blackbody radiation of temperature T (here used with $T = T_w$ the background temperature set to the usually accepted 4 K), R is the heliocentric distance in AU, and Q the absorption coefficient for a complex index of refraction n^*. The values of n^* were obtained from previous work from Irvine and Pollack (1968), and Bertie, Labbe, and Whalley (1969). Then, Q was derived using Mie theory for particles with radius smaller than 100 μm when $|n^*| \frac{2\pi r}{\lambda} > 0.3$, Rayleigh approximation was used when the previous inequality does not hold, and for particles greater than 100 μm the so-called van de Hulst approximation (1957) was used.

Using similar notations, the last term P_τ can be expressed (Patashnick et al. 1975):

$$P_\tau = -A \int_0^\infty F(\lambda, T_s) Q(\lambda, r, n*) d\lambda \tag{3.9}$$

The energy conservation equation can be solved for the equilibrium temperature T_s and the sublimation rate Φ, which are both functions of heliocentric distance and grain size (Figure 3.5). A sublimation rate minimum develops for particles with radii of a few tens of microns which can be explained by the ability of the grain to absorb and reradiate energy (Lien 1990). This can be measured by the ratio $\frac{Q(V)}{Q(IR)}$ noting $Q(V)$ and $Q(IR)$ the average absorption efficiency in the visible and IR region, respectively. When $\frac{Q(V)}{Q(IR)}$ increases, the temperature increases as well. For very small grains ($x = \frac{2\pi r}{\lambda} << 1$, with r the grain radius), the absorption efficiencies are proportional to x (Bohren and Huffman 1983) so that the ratio $\frac{Q(V)}{Q(IR)}$ is constant and independent of the grain radius. The increase in temperature for these small grains is explained by the cooling due to sublimation. Then, $Q(V)$ starts increasing more rapidly than $Q(IR)$ increasing the equilibrium temperature of the grains until $x_v = \frac{2\pi r}{\lambda_v} \sim 2$. As the grain size continues increasing, $Q(V)$ begins to

decrease eventually reaching a constant while $Q(IR)$ continues increasing, which results in a drop in equilibrium temperature reaching a minimum at $x_{IR} = \frac{2\pi r}{\lambda_{IR}} \sim 2$ where $Q(IR)$ will start decreasing. This last increase of temperature will eventually reach the blackbody temperature when $\frac{Q(V)}{Q(IR)} \sim 1$.

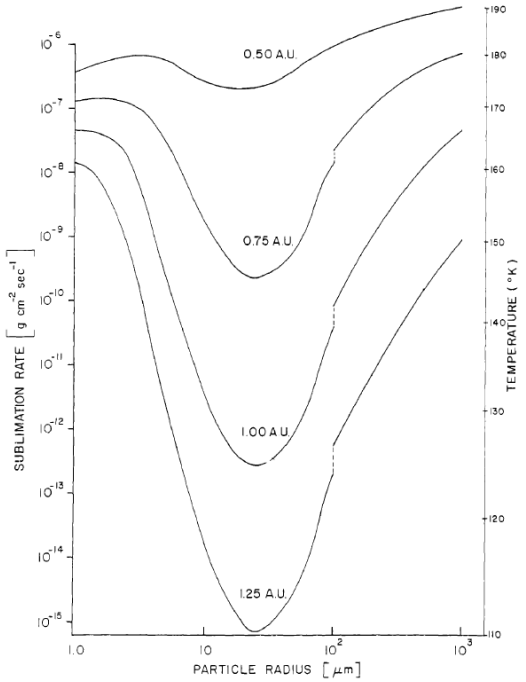

Figure 3.5: Sublimation rates and equilibrium temperatures for pure icy grains at four heliocentric distances. Extracted from Patashnick et al. (1975).

The models adopted for dirty icy grains follows the results from Lien (1990) where the author found the equilibrium grain temperatures for heterogeneous grains calculated using the Maxwell Garnett (1904) method for grains with small inclusions embedded in a homogeneous matrix and Bruggerman (1935) theory for aggregate-type grains for mixtures of magnetite, water ice, and silicate. A similar but more detailed technique than Patashnick et al. (1975) using energy conservation led to the equilibrium grain temperature profiles for different nature and amount of dirt in the grains, which are higher than for pure ice due to the energy absorption of dirt in the visible (Figure 3.6).

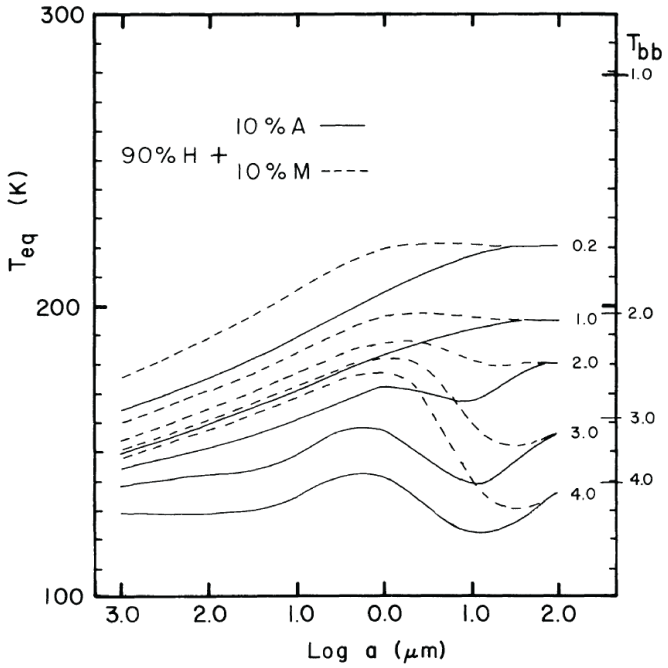

Figure 3.6: Equilibrium temperatures for dirty icy grains with 90% of water and 10% of either magnetite (M; dashed line) or astronomical silicate (A;solid line) at five heliocentric distances. Extracted from Lien (1990).

Several sublimation rate models exist and give some different values for a given equilibrium temperature. They usually differ in the way to compute the equilibrium vapor pressure. Leger et al. (1982) gave a complete physical explanation of the way to find this equilibrium vapor pressure. Mukai et al. 1986 compared these different methods to some laboratory measurements and found that the formula given by the International Critical Tables (1929) gives a better fit to the experimental results than the data from Kelley (1935). Moreover, their analysis showed a relatively good agreement between the values found with the study of Leger et al. and the ICT data. Therefore, we decided to use the ICT formula in order to compute the equilibrium water vapor when dirty icy grains were used in agreement to Lien (1990). However, some final tests showed that the difference in the sublimation rates does not significantly impact the values of the two macroscopic value of interest.

The difference in sublimation rate between pure and dirty grains will drastically affect their lifetime and then, their contribution to the coma. While dirty icy grains will sublimate relatively fast and release water molecules in the coma close to the nucleus, pure icy grains will extend at very large distances from the nucleus creating a halo of about 10^4 km (Delsemme and Miller, 1971). Beer et al. (2006) computed grain lifetimes for several heliocentric distances and grain sizes (Figure 3.7) where a sharp increase can be observed where the minimum sublimation rate occurs.

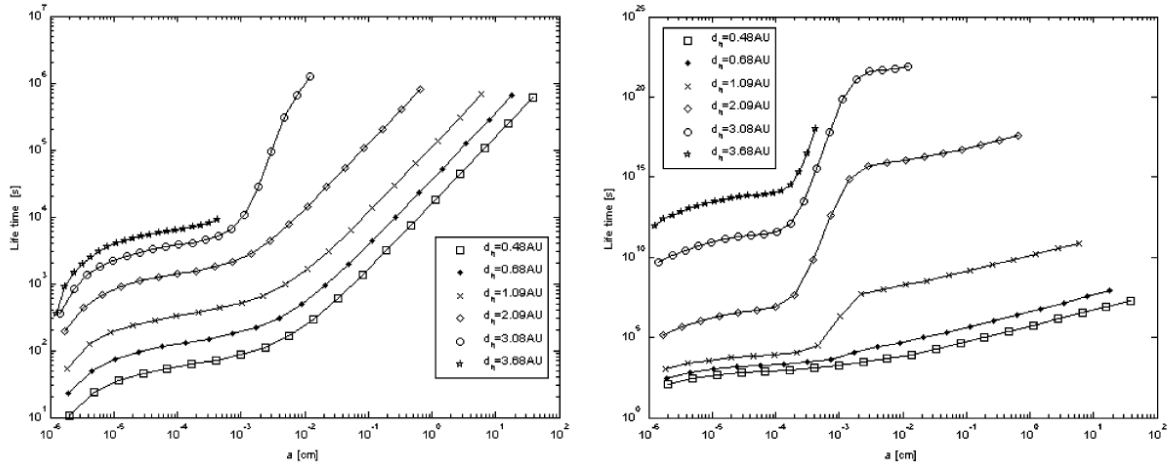

Figure 3.7: Lifetime of dirty ice with 10% of impurity (left) and pure ice (right) grains for different heliocentric distances. Extracted from Beer et al. (2006).

While pure ice grains absorb in the UV and in the IR, dirty icy grains absorb well in the visible. Hence, the equilibrium temperatures and a fortiori the sublimation rates of "dirty" icy grains are considerably higher than those made of pure ice. Grain analysis shows that the grain equilibrium temperature is not sensitive to the exact amount of dirt (Beer et al., 2006), so we arbitrarily decided to use grains with 90% ice and 10% dirt. In the process of our study, we noticed that the nature of the dirt had a negligible influence on the results, which led to the choice of magnetite as the dirt component as explained in section 3.3.

3.4 The Electron Model

In order to properly model the rotational heating due to collisions between water molecules and electrons, it is necessary to properly model the electron densities and temperatures in the coma. The only in-situ measurements of electron density and temperature profile were deduced from ion densities and temperatures given by the Giotto and Vega data (Balsiger et al. 1986, and Lammerzahl et al. 1987). Then, large uncertainties still exist for the electron density and temperature profiles in the cometary comae. The electron population has been modeled in Gan and Cravens (1990), in which they constructed a model of the spatial and energy distributions of electrons in the vicinity of comet Halley using a two-stream transport technique. A steep increase in the electron density takes place outside the diamagnetic cavity, which is explained by the increase of the electron temperature that implies a decrease in electron-ion recombination efficiency. This can be explained by taking into account an additional energy source for the electrons more important than photoionization, which may be produced by an increase of the high energetic solar wind electrons in this region of the compressed interplanetary magnetic field (Häberli et al. 1995 and 1996).

We used the same method as Biver (1997), which was also used in more recent studies (Bensch and Bergin 2004, Zakharov et al. 2007, Hartogh et al. 2010, Paganini et al. 2010, and Lee et al. 2011). The positions of the contact surface where the electron-gas collision rate becomes too small to maintain thermal equilibrium between electrons and gas, and the recombination surface outside of which the recombination rate of electrons with ions is negligible are determined by two scaling factors respectively referred to as R_{cs} and R_{rec} hereafter.

$$R_{cs} = 1.125 \times 10^6 Q_{29}^{3/4} \tag{3.10}$$

$$R_{rec} = 3.2 \times 10^6 Q_{29}^{1/2} \tag{3.11}$$

where $Q_{29} = 10^{-29} Q$ and Q is the gas production rate at the surface of the nucleus. This approach matches the location of the contact surface for 1P/Halley during the Giotto

encounter measured by the ion mass spectrometer (Balsiger et al. 1986, Häberli et al. 1995) with Rcs$\sim$ 3750 km and Rrec$\sim$ 7150 km.

The electron temperature profile T_e in function of the distance from the nucleus r is separated into three domains where the electron temperature increases from the gas temperature to a maximum set temperature of 10000 K:

$$T_e(r) = \begin{cases} T_{gas}, & if \quad r < R_{cs} \\ T_{gas} + (10000 - T_{gas}) \left(\frac{r}{R_{cs}} - 1 \right), & if \quad R_{cs} < r < 2R_{cs} \\ 10000, & if \quad 2R_{cs} < r \end{cases} \tag{3.12}$$

The electron density profile n_e is defined by:

$$n_e(r) = \left(\frac{Qk_{ion}}{r^2 v_{exp} k_{rec}} \right)^{1/2} \left(\frac{T_e}{300} \right)^{0.15} \left(1 - exp\left(-\frac{r}{R_{rec}} \right) \right) + \frac{5 \times 10^6}{r_h^2} \tag{3.13}$$

where k_{ion} is the water photoionization rate in unit of s^{-1}, k_{rec} the recombination rate of electrons with ions in $s^{-1}.m^{-3}$, r_h the heliocentric distance of the comet nucleus in AU, and v_{exp} the gas expansion velocity. k_{ion} and k_{rec} were computed as follows:

$$k_{ion} = \frac{4.1 \times 10^{-7}}{r_h^2} \tag{3.14}$$

$$k_{rec} = 7 \times 10^{-13} \left(\frac{300}{T_e} \right)^{1/2} \tag{3.15}$$

This approach shows a recombination zone in the inner coma inside the contact surface, where the electrons are thermalized to the temperature of the gas, a pileup region beginning at the contact surface where the electron density increases at the result of an increasing electron temperature and decreasing electronic recombination (Eberhardt and Krankowsky 1995), and an external region free of recombinations with a $1/r^2$ density profile (Biver et al. 1999).

3.5 Line-by-Line Radiative Transfer Model

Different processes control the distribution of the level population in the coma: spontaneous emission, stimulated emission, absorption, molecular collisions, electron-molecule collisions, and infrared pumping by solar radiation (Zakharov et al. 2007, and references therein). Then, the statistical equilibrium equations yield the relative population of the rotational level i at the vibrational level ν that is given by:

$$n_i^\nu = \frac{\sum_{j>i} n_j^{\nu'} A_{ji}^{\nu'\nu} + \sum_{j\neq i} n_j^{\nu'} (B_{ji}^{\nu'\nu} J_{ji}^{\nu'\nu} + C_{ji}^{\nu'\nu} + N_{ji}^{\nu'\nu})}{\sum_{j<i} A_{ij}^{\nu\nu'} + \sum_{j\neq i} (B_{ij}^{\nu\nu'} J_{ij}^{\nu\nu'} + C_{ij}^{\nu\nu'} + N_{ij}^{\nu\nu'})} \tag{3.16}$$

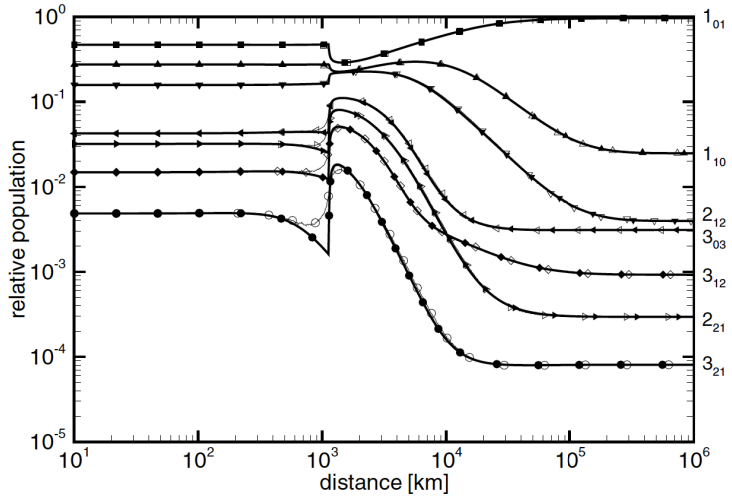

Figure 3.8: Level populations of seven para levels of H_2O by the Monte Carlo (thin lines and open symbols) and the escape probability (thick lines and plain symbols) methods for a water production rate of 10^{29} (Zakharov et al. 2007).

Where superscripts and subscripts refer to vibrational and rotational states, respectively. When two indices are used at the same level, the first refers to the initial state of the transition while the second one to the final state. The Einstein coefficients coupling the levels (ν', j) and (ν, i) are $A_{ij}^{\nu\nu'}$ in s^{-1} for spontaneous emission and $B_{ij}^{\nu\nu'}$ in $J^{-1}.m^2.s^{-1}$ for induced emission or absorption found in the spectral database GEISA (Jacquinet-Husson

2011), the molecular and electronic collision rates are $C_{ij}^{\nu\nu'}$ and $N_{ij}^{\nu\nu'}$ in s^{-1}, and $J_{ij}^{\nu\nu'}$ in $J.m^{-2}$ is the radiation average intensity over all directions. With numerical integration of the radiative transfer equation it is possible to compute $J_{ij}^{\nu\nu'}$. However, it requires a significant computational effort. Two methods exist to avoid this long computation: a Monte-Carlo method (Bensch and Bergin 2004, Zakharov et al. 2007, Lee et al. 2011) and the escape probability method (Bockelée-Morvan 1987, Zakharov et al. 2007). Although it is physically less exact, the escape probability method is faster than the Monte-Carlo one, and it has been shown to lead to similar results except in the regions of high gradients of electron densities and temperatures (Zakharov et al. 2007) (Figure 3.8), which is why we picked the escape probability method for our study. Indeed, the escape probability method reduces the global problem to a local one by assuming that each point of the gas is essentially coupled radiatively to the near surrounding region. Then, the model follows the steps presented by Bockelée-Morvan (1987). The radiation mean intensity is computed according to the escape probability method (Rybicki 1984):

$$J_{ij}^{\nu\nu'} = (1 - \beta_{ij}^{\nu\nu'})S_{ij}^{\nu\nu'} + \overline{\beta}_{ij}^{\nu\nu'} I_{ij}^{\nu\nu'} \tag{3.17}$$

where $\beta_{ij}^{\nu\nu'}$ is the average over a 4π solid angle of $\beta_{ij}^{\nu\nu'}(\vec{n})$ the probability that an emitted photon escapes the line trapping region in a given direction $\vec{n}$ without suffering any absorption, $\overline{\beta}_{ij}^{\nu\nu'}$ describes $\beta_{ij}^{\nu\nu'}$ averaged over the solar zenith angle, $I_{ij}^{\nu\nu'}$ the solar radiation at frequency $\nu_{ij}^{\nu\nu'}$ deduced from the molecular database GEISA. The line source function $S_{ij}^{\nu\nu'}$ is computed using the ratio between the optical absorption $\alpha_{ij}^{\nu\nu'}$ and the emission coefficient $æ_{ij}^{\nu\nu'}$ given by the following expressions:

$$\alpha_{ij}^{\nu\nu'} = \sum_{i>j} \frac{h\nu_{ij}^{\nu\nu'}}{4\pi}(n_i^{\nu} B_{ji}^{\nu'\nu} - n_j^{\nu'} B_{ij}^{\nu\nu'}) \tag{3.18}$$

$$j_{ij}^{\nu\nu'} = \sum_{i>j} \frac{h\nu_{ij}^{\nu\nu'}}{4\pi} n_i^{\nu} A_{ij}^{\nu\nu'} \tag{3.19}$$

where $\nu_{ij}^{\nu\nu'}$ is the Doppler shifted frequency for the transition between the level of energy E_i and E_j. The computation of $\beta_{ij}^{\nu\nu'}$ requires the calculation of the Sobolev optical depth

given by:

$$\tau_{ij}^{\nu\nu'} = \frac{A_{ij}^{\nu\nu'} c^3 g_j}{8\pi\nu_{ij}^{\nu\nu}} \left(\frac{n_i^\nu}{g_i} - \frac{n_j^\nu}{g_j} \right) \frac{n(r) r}{v_{th}(r)} \tag{3.20}$$

where g_i and g_j are the degeneracies of the lower and upper transitions, and $n(r)$ and $v_{th}(r)$ are the density and thermal velocity of the particles at distance r from the nucleus, respectively. $\beta_{ij}^{\nu\nu'}$ has different expressions depending on the sign of the optical depth. In fact, when the optical depth is positive, $\beta_{ij}^{\nu\nu'}$ is given by the formula from Litvak and Kuiper (1982):

$$\beta_{ij}^{\nu\nu'} = \frac{2}{3\tau_{ij}^{\nu\nu'}} - e^{-\frac{\tau_{ij}^{\nu\nu'}}{2}} \left[\frac{\tau_{ij}^{\nu\nu'}}{3} \left(K_2 \left(\frac{\tau_{ij}^{\nu\nu'}}{2} \right) - K_1 \left(\frac{\tau_{ij}^{\nu\nu'}}{2} \right) \right) - K_1 \left(\frac{\tau_{ij}^{\nu\nu'}}{2} \right) \right] \tag{3.21}$$

where K_1 and K_2 are the modified Bessel functions of second kind.

On the other hand, for negative optical depth, $\beta_{ij}^{\nu\nu'}$ does not represent a probability but a maser amplification factor which occurs with population inversions, we assume that in that case $\beta_{ij}^{\nu\nu'}$ increases using the expression of the photon escape probability (Bockelée-Morvan 1987):

$$\beta_{ij}^{\nu\nu'} = \frac{1 - e^{\tau_{ij}^{\nu\nu'}}}{\tau_{ij}^{\nu\nu'}} \tag{3.22}$$

$\overline{\beta}_{ij}^{\nu\nu'}$ is deduced from the value of $\beta_{ij}^{\nu\nu'}$ divided by the dilution factor $\Omega/4\pi$ with Ω the solar zenith angle, which is strictly valid only for a velocity field proportional to r.

The neutral-neutral collision rate is given by $C_{ij}^{\nu\nu'} = nv\sigma_{ij}^{\nu\nu'}(T/100)^{-0.6}$, where the collisional cross sections $\sigma_{ij}^{\nu\nu'}$ were computed using the values from Buffa et al. (2000) for the vibrational ground state of water, and constant values for the other vibrational levels. $\sigma_{ji}^{\nu'\nu}$ is deduced from $\sigma_{ij}^{\nu\nu'}$ using the balance equation, similarly as Zakharov et al. (2007) and Lee et al. (2011).

Finally, the electron-neutral collision rate is calculated using the electron density model from Biver (1997) described in the previous section. This approach matches the location of the contact surface for 1P/Halley during the Giotto encounter and enables us to derive the electron parameters such as their density and temperature. Then, for de-excitation,

from the level (ν, i) to (ν', j):

$$N_{ij}^{\nu\nu'} = n_e v_e \sigma_{ij}^{e\nu\nu'} 2a_{ij}^{\nu\nu'} e^{a_{ij}^{\nu\nu'}} K_0(a_{ij}^{\nu\nu'}) \tag{3.23}$$

where n_e and v_e are the electron density and averaged thermal velocity, respectively, K_0 the modified Bessel function of second kind, and $a_{ij}^{\nu\nu'} = h\nu_{ij}^{\nu\nu'}/2kT_e$, with T_e the electron temperature. While for excitation:

$$N_{ji}^{\nu'\nu} = n_e v_e \frac{g_i}{g_j} \sigma_{ij}^{e\nu\nu'} 2a_{ij}^{\nu\nu'} e^{-a_{ij}^{\nu\nu'}} K_0(a_{ij}^{\nu\nu'}) \tag{3.24}$$

The cross-sections $\sigma_{ij}^{e\nu\nu'}$ are given by the expression from Itikawa (1972):

$$\sigma_{ij}^{e\nu\nu'} = \frac{m_e e^2 c^3 A i j^{\nu\nu'}}{16\pi^2 \epsilon_0 h^2 (\nu_{ij}^{e\nu\nu'})^4} \tag{3.25}$$

where m_e is the electron mass. Finally, in order to provide the modeled spectra, we need to calculate the radiance at each frequency, which is given by adapting the formula to compute the monochromatic flux from Bockelée-Morvan (1987) to the monochromatic radiance:

$$I(\nu) = \int \beta_{ij}^{\nu\nu'}(r) j_{ij}^{\nu\nu'}(r) dr \tag{3.26}$$

The different physical models that were detailed in this chapter have been developed in the past and are now, for the first time, included in a self-consistent coma model. The next chapter will present an application of the escape probability method using the DSMC outputs from the cometary model to the VIRTIS instrument on board the Rosetta spacecraft.

Chapter 4

The VIRTIS Observation of the Coma of Comet 67P/Churyumov-Gerasimenko

The Rosetta spacecraft will rendezvous with comet CG in 2014 with a landing and extensive orbital phase. Model studies are required for planning of the mission and interpretation of the spacecraft data. After the cancellation of the original launch, the original target of the Rosetta mission comet 46P/Wirtanen was replaced by comet CG, a short-period Jupiter comet discovered in 1969. After a close approach to Jupiter in 1959, the orbital period of the comet changed from 8.97 years to 6.6 years (Hanner et al. 1985) with a shift of the orbit of the comet around the Sun. Rosetta will encounter comet CG at an heliocentric distance of 3.25 AU and will orbit and accompany the comet through its perihelion located at 1.29 AU.

The Rosetta orbiter's scientific payload includes eleven experiments in addition to the lander, including a Visible and Infrared Thermal Imaging Spectrometer (VIRTIS) that will identify comet gases and characterize the physical conditions of the coma, in addition to the determination of nucleus' properties such as shape, albedo, or topography. Indeed, the identification of spectral features is a primary goal of the Rosetta mission and will allow identification of the nature of the main constituents of the comet (Coradini et al. 2007). VIRTIS' extensive wavelength coverage from the near UV (0.25 μm) to the near-

IR (5.0 μm) enables the detection of many different types of molecules including the most abundant ones in the cometary coma such as water, CO_2, CO and organic species.

	VIRTIS-M Visible	VIRTIS-M InfraRed	VIRTIS-H
Spectral Range (nm)	220.1-1046.0	952.8-5059.2	1880-5030
Spectral Resolution ($\lambda/\Delta\lambda$)	100-380	70-360	1300-3000
Spectral Sampling (nm)	1.89	9.44	0.6
Field of View (mrad x mrad)	63.6 x 64.2	63.6 x 64.2	0.49 x 1.47
Max Spatial Resolution (μrad)	248.6 x 250.8	248.6 x 250.8	

Table 4.1: VIRTIS characteristics and performances overview. Extracted from Coradini et al. (2007)

The VIRTIS instrument is a combination of three different data channels: two are devoted to spectral mapping and are housed in the mapper (-M) and a third channel is devoted only to spectroscopy and is located in the high resolution optical system (-H). While the -M subsystem has a high spatial resolution, the -H part has a high spectral resolution. Such a combination of high spatial and high spectral resolution should give invaluable information about the coma and its composition. An overview of the characteristics of the VIRTIS instrument is provided in Table 4.1 adapted from (Coradini et al. 2007).

In order to identify the complex release of gas from a comet, it is necessary to be able to derive accurately the composition of the coma. This chapter will present a set of IR spectra applied to the VIRTIS instrument on board of Rosetta using a cometary coma model simulated using the DSMC approach.

4.1 The Coma Model

This chapter is mainly focused on the IR spectra modeling more than on the cometary coma model itself. Hence, although the coma of comet CG has extensively been studied with 2D models (Tenishev et al. 2008 and 2011, Combi et al. 2012), we will use a 1D

model for this application for the sake of simplicity. However, it is necessary to keep in mind that a similar approach could be applied using a 2D or even 3D cometary model. Then, we used a 1D DSMC approach to model the cometary coma of comet CG at a heliocentric distance of 2.0 AU assuming a nucleus of 2 km radius (Lamy et al. 2006) with H_2O, CO, and CO_2 production rates corresponding to the 2.0 AU case from Tenishev et al. (2008), with addition of other parent species such as CH_3OH, H_2CO, NH_3, CH_4, C_2H_6, C_2H_2, and HCN. The distance of 2.0 AU corresponds to a typical heliocentric distance where the Rosetta spacecraft will be orbiting comet CG. The different gas production rates used in this simulation were deduced from Mumma et al. (2005), Schleicher (2006) and Ootsubo et al. (2012) and are summarized in Table 4.2. The inner boundary temperature at the surface of the nucleus was chosen to be 190 K corresponding to the Knudsen layer temperature, enabling correct gas outflow speeds. Parent and daughter species were sampled over a range of distances from the nucleus surface at 2.0 km to the external boundary at 10^6 km. Direct DSMC outputs for the three main species are illustrated on Figure 4.1. The number density decreases with distance with a slope close to $1/r^2$ until photodissociation starts to be important around 10^5 km for water while CO and CO_2 have larger lifetimes with respect to photochemistry and are only slightly affected by it within the range of the simulations at a heliocentric distance of 2.0 AU. In the DSMC, the rotational temperature is computed using the phenomenological model from Borgnakke and Larsen (1975) described in detail in section 2.2.3 of this thesis. The rotational temperature of all the species are similar up to about 4 km from the center of the nucleus where they start differing. The water rotational temperature eventually decreases to a value relatively close to zero while the CO_2 and CO rotational temperatures stay close to 100 K until approximately 1000 km where the CO rotational temperature starts to decrease to reach about 70 K at 10^6 km. These high rotational temperatures at large distances from the nucleus in the DSMC output are common to the different species other than water due to the fact that radiative cooling is not included for these species in the model. Some work presenting results of radiative cooling for other species than water exist in the literature such as in Chin and Weaver (1984) for CO and can be included in the model. However, since this work focuses on the inner coma, the outer regions do not significantly affect the results presented in this section.

Species	Production Rate (s^{-1})	Ro-vibrational transitions modeled
H_2O	7.62×10^{26}	ν_3-ground state, ν_1-ground state, $\nu_2\nu_3$-ν_2
CO	3.81×10^{25}	ν_1-ground state
CO_2	1.91×10^{25}	00011-00001, 02211-02201, 10011-10001, 01111- 01101
CH_3OH	1.30×10^{25}	X
H_2CO	1.14×10^{25}	ν_1-ground state, ν_5-ground state
NH_3	1.14×10^{25}	ν_1-ground state, ν_3-ground state, $2\nu_4$-ground state
CH_4	6.10×10^{24}	ν_3-ground state
C_2H_6	3.05×10^{24}	ν_7-ground state
C_2H_2	3.05×10^{24}	ν_3-ground state, $\nu_2\nu_4\nu_5$-ground state
HCN	1.52×10^{24}	ν_3-ground state

Table 4.2: Gas production rates for a CG case at 2.0 AU with the corresponding ro-vibrational transitions included in the model to compute the VIRTIS spectra computation

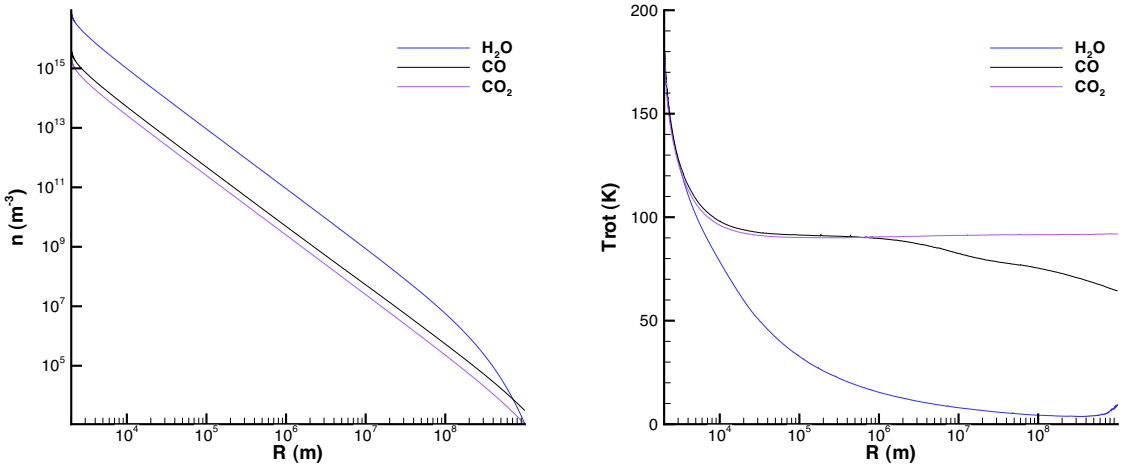

Figure 4.1: DSMC output for H_2O, CO, and CO_2 for the presented 2.0 AU case.

One of the limitations of the Bornakke-Larsen model approach in the case of the cometary coma is that at sufficiently large distances from the nucleus (typically 100-1000 km according to Bockelée-Morvan 1987), the coma is in fluorescence equilibrium and the rotational

populations are controlled by radiative effects, which are not included in the Bornakke-Larsen model. Actually, the relative importance of radiative effects is different for each transition impacting mostly levels with lower radiative lifetimes, especially for those located near the ground rotational state (Bockelée-Morvan 1987). Indeed, where low densities preclude excitation by collision, the population of the different vibrational and rotational levels is only determined by the balance between solar infrared excitation and spontaneous decay (Bockelée-Morvan 1987). This influences only the outer coma and does not strongly impact the results presented in this section where we focus within a few kilometers from the nucleus where neutral-neutral collisions dominate.

4.2 Line-by-Line Model Using a Rotational Temperature

4.2.1 The Ro-Vibrational Transitions Considered in the Model

This section mostly focuses on the IR spectra that will be observed by the VIRTIS instrument on board of the Rosetta spacecraft such as the 2.7 μm emission of H_2O, the 4.3 μm emission of CO_2, CO's 4.5 μm emission, and the organics' emission at $\sim$ 3.2-3.6 μm. Our approach is based on that introduced by Bockelée-Morvan (1987) and Bockelée-Morvan and Crovisier (1989) generalized to treat the variable rotational temperature along the line-of-sight integration enabled by the AMPS code (Tenishev et al. 2008). Only a few vibrational bands contribute to the emission at those wavelengths and are then relevant for the current purpose (Table 4.2), and for each of them the model includes all the transitions available in the HITRAN database.

For water we only consider the contribution from the following vibrational transitions: ν_3-ground state, ν_1-ground state, and $\nu_2\nu_3$-ν_2. Indeed, 84% of the total infrared excitation is represented by the excitation of ν_1 and ν_3 (Crovisier 1984), but the hot-bands $\nu_2\nu_3$-ν_2, $\nu_1\nu_3$-ν_1, and $\nu_1\nu_3$-ν_3 contribute (by decreasing importance) to the water emission (Bockelée-Morvan and Crovisier 1989).

In the same way, the vibrational transitions considered for CO_2, given with the notation from McClatchey et al. (1973), are: the fundamental 00011-00001, 02211-02201 (SH_a

according to the notation from Lopez-Valverde et al. 2007), 10011-10001 (SH_c), and 01111- 01101 (FH) (Lopez-Valverde et al. 2007). These levels enable us to simulate the absorption of solar radiation by CO_2 at 2.7 μm, which results in fluorescent emission at 4.3 μm (James and Kumer 1973, and Nebel et al. 1994). The inclusion of the different hot bands is of primary importance for CO_2 since the relative intensity of some of these hot bands may not be negligible compared to the emission from the fundamental band (Lopez-Valverde et al. 2005). Only the transitions that contribute significantly to the total emission of CO_2 at 4.3 μm were included following the results from Lopez-Valverde et al. (2005).

For CO, only the fundamental transition ν_1-ground state was considered due to its much stronger emission than any other bands in the wavelength range of interest (Crovisier and Encrenaz 1983).

The organics emission at 3.2-3.6 μm is mostly created by the stretching vibrations of CH bonds in organic molecules such as: CH_4, H_2CO, CH_3OH, and to a lesser extent by HCN, NH_3, C_2H_2, and C_2H_6 (Crovisier and Encrenaz 1983). For methane, the only excited vibrational state that was modeled is the fundamental band ν_3. Such emission lines from this band were detected with CSHELL at IRTF and NIRSPEC at the Keck Observatory on eight different comets, from which Gibb et al. (2003) reported g-factors for the R0 and R1 transitions. Then, in the same way as in the model from Reuter et al. (1989) validated by IR observations of comet C/2002 T7 (LINEAR) (DiSanti et al. 2006), formaldehyde's ground state, ν_1, and ν_5 bands were modeled. Three vibrational transitions were modeled for NH_3, the two fundamentals ν_1-ground state and ν_3-ground state, and $2\nu_4$-ground state (Crovisier and Encrenaz 1983). HCN's emission mainly results from the fundamental ν_3 band (Crovisier and Encrenaz 1983). C_2H_2 presents two majors transitions: ν_3-ground state and $\nu_2\nu_4\nu_5$-ground state, while only C_2H_6's ν_7-ground state transition is currently available in HITRAN.

Finally, methanol's strongest emissions results from its ν_2 and ν_9 excited states, and to a lesser extent from its ν_3 band. In their recent work, Villanueva et al. (2012) constructed a line-by-line model for the ν_3 excited state of CH_3OH and created a database of line lists and fluorescence efficiencies for the latter band. However, similar individual line models are not yet available in the literature for the stronger bands ν_2 and ν_9, which made it

impossible to model the methanol emission at the moment using the presented technique. Methanol having an important contribution to the organic emission between 3.2 and 3.6 μm (Bockelée-Morvan et al. 1995), this is an important caveat to model the full spectra measured by VIRTIS. However, it does not prevent the model to give critical information for the other species.

4.2.2 Computation of the Line Fluxes

Most of the IR observations that we will be modeling are within a few kilometers from the nucleus well within the region where collisions dominate and the coma is in local thermodynamic equilibrium. Indeed, Bockelée-Morvan (1987) defined the disequilibrium distance where LTE breakdowns and the rotational temperature differs from the kinetic temperature by more than 10%. This LTE violation occurs at different distances from the nucleus for each transition depending on the relative magnitude of the radiative rates related to a given transition with respect to the collision rate (Bockelée-Morvan 1987). Table 4.3 presents disequilibrium distances for a few water rotational lines in the vibrational ground state for an assumed water production rate of 2×10^{29} s^{-1} extracted from Bockelée-Morvan (1987). Then, it can be assumed that the rotational distribution follows a Boltzmann distribution where a line population n_i within each band can be found using the rotational temperature T_{rot}:

$$n_i = \frac{g_i e^{-\frac{E_i}{kT_{rot}}}}{\sum_i g_i e^{-\frac{E_i}{kT_{rot}}}} \tag{4.1}$$

where g_i and E_i are the degenerescency and the energy of the i^{th} level. This assumption enables us to compute the different line populations without iterative process, which makes possible the use of a larger number of lines per vibrational level. All the subsequent processes to derive the flux and opacity are similar to the description in section 3.5 from this thesis.

Line i-j	D (km)	R (km)
1_{10}-1_{01}	1.66×10^3	7.24×10^4
2_{12}-1_{01}	1.74×10^3	2.19×10^4
2_{21}-1_{10}	1.45×10^3	2.29×10^4
2_{21}-2_{12}	1.20×10^3	1.05×10^4
3_{30}-3_{03}	3.31×10^1	2.75×10^1
4_{14}-3_{21}	3.98×10^1	< 10

Table 4.3: Examples of disequilibrium distances (D) and critical radii (R) inside of which the rotational lines are thick for the water vibrational ground state, extracted from Bockelée-Morvan (1987).

While most techniques assumed a constant rotational temperature over the line of sight, our model uses the local parameters from the results of the DSMC calculations to derive the local level populations which contributes to the brightness of each line so that the monochromatic radiance is given by:

$$I_{ij}^{\nu\nu'} = \frac{h\nu_{ij}^{\nu\nu'}}{4\pi}\beta_{ij}A_{ij}^{\nu\nu'}\int n_i^{\nu}(r)n(r)dr \tag{4.2}$$

where h is the Planck constant, $\nu_{ij}^{\nu\nu'}$ and $A_{ij}^{\nu\nu'}$ are the transition wavelength and Einstein coefficient of the transition of higher level i from the ν band to the lower level j from the ν' band, $n(r)$ the local number density, $n_i^{\nu}(r)$ the local population of the i (upper) level, and $\beta_{ij}^{\nu\nu'}$ the escape probability for the transition $i \rightarrow j$. Also, the opacity plays a critical role in the shape of the spectra by altering lines' brightnesses with an impact depending on the line considered. The inner coma being optically thick in typical conditions, a careful computation of the opacity is necessary to obtain meaningful results. Some examples of critical radii inside of which the rotational lines are thick are presented in Table 4.3. The opacity at a given point r along the line of sight can be computed for the real path of the photon and not some average properties as was done with previous models:

$$\tau_{ij}^{\nu\nu'} = \frac{A_{ij}^{\nu\nu'}c^3}{8\pi\nu_{ij}^{\nu\nu'}}\frac{g_i}{g_j}\int_0^r n_j^{\nu'}(r')\frac{n(r')}{v_{th}(r')}dr' \tag{4.3}$$

where g_i and g_j are the degenerescencies of the levels i and j respectively, and $v_{th}(r')$ the local thermal velocity. The model returns the line-by-line flux for the bands considered for each species for a particular geometry. This approach gives a better representation of the actual physics of the coma by using local gas conditions from the model at each step of the integration. However, some recent techniques of opacity calculations take into account the effect of the Doppler shift leading to some asymmetries in the flux even for a spherically symmetric coma (Debout et al. 2013). The present model should have a small impact on the results and may cause Swings effect, that is to say that the excitation could depend on the comet heliocentric velocity, affecting individual line brightnesses by less than 20% (Bockelée-Morvan 1987). Figure 4.2 shows the relative flux for the ν_3 band of water for a case of a limb 2 km above the surface of the nucleus when the spacecraft is located at a distance of 50.1 km from the center of the nucleus using the local gas parameters during both integrations of the flux and opacity (green), and a case with a constant rotational temperature along the line of sight as would be seen from the observer (red), that is to say an averaged rotational temperature weighted by the density:

$$\overline{T_{rot}} = \frac{\int T_{rot}(r')n(r')dr'}{\int n(r)dr'} \tag{4.4}$$

where $T_{rot}(r)$ and $n(r)$ are the modeled rotational temperature and density at distance r from the center of the nucleus. This approach enables a direct comparison between the assumption of constant rotational temperature along the line of sight and a more realistic model that uses the local rotational temperature and density during the integrations. The difference between the two methods in the resulting flux depends on the line considered and can reach up to 40% for the major lines. This shows that models that use a constant coma temperature over the line of sight impose an inherent distortion to the resulting spectrum, which can lead to a less good agreement with observations.

4.2.3 Validation of the IR Model

Since this IR model has been created from scratch, it is necessary to test it with respect to verified models. Unfortunately, published model spectra with all the necessary parameters

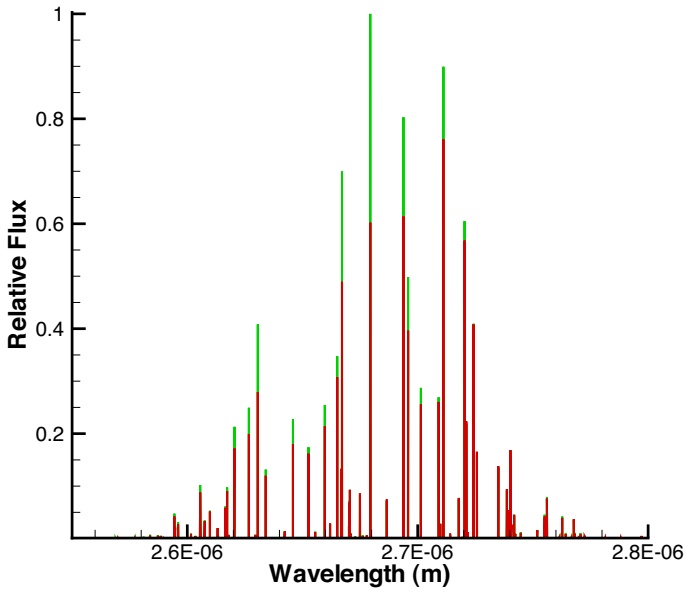

Figure 4.2: Relative flux of the ν_3 band of water for a case using the local gas parameters during the integration (green), and a case with a constant rotational temperature along the line of sight (red). The geometry considered is a limb measurement at 2 km above the surface of the nucleus when the spacecraft is located at 50.1 km from the center of the nucleus.

to reproduce them are relatively scarce. Then, in order to test our model, we used one of the CO_2 ν_3 band cases generated by Dr. Bockelée-Morvan at 1.3 AU with a CO_2 production rate of 8.0 $\times$ 10^{26} s^{-1} with a nucleus surface temperature of 353 K where the Rosetta spacecraft is located at a distance of 100 km and the limb distance is 5 km (Bockelée-Morvan - private communication). A column density over the line of sight of 2.71 $\times$ 10^{19} m^{-2} and a coma temperature of 101.53 K (Bockelée-Morvan - private communication). To compare accurately the two models, we decided to use the reported line of sight and coma temperature as a constant in our model. We used spectral resolutions corresponding to the average of VIRTIS -M and -H ranges, that is to say $\lambda/\Delta\lambda$ of 240 and 2200, respectively.

The two models show similar output spectra at both medium and high resolutions (Figure 4.3). The medium resolution shows two "bumps" that peaks at more than 0.0005

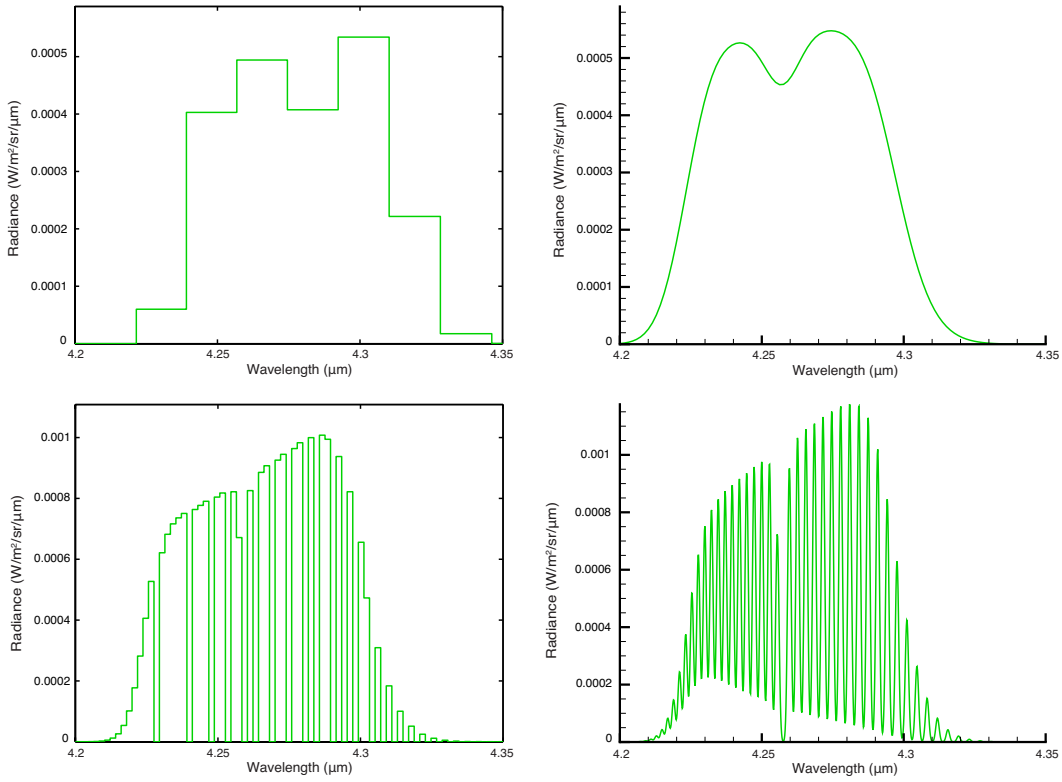

Figure 4.3: IR spectra of the ν_3 band of CO_2 using a line of sight of 2.71 $\times$ 10^{19} m^{-2} and a coma temperature of 101.53 K for a $\lambda/\Delta\lambda$ of 240 (top) and 2200 (bottom) comparing the present model (left panels) and results from Dr. Bockelée-Morvan (right panels) (Bockelée-Morvan - private communication)

W/m^2/sr/μm in both methods. However, the whole spectrum seems to be shifted by about one wavelength bin toward higher values in the case of our model. This shift in wavelength is due to the different approaches used to compute the resolution. Indeed, while Dr. Bockelée-Morvan used a convolution with a gaussian leading to a smooth spectrum, we decided to use wavelength bins that would reflect the actual spectra returned by VIRTIS. The drawback of this method is that a line that would be close to the boundary between two bins can arbitrarily be in either of them depending on where the overall beginning of the range is. To prevent these effect, the best way would be to use the actual ranges of wavelength used by the instrument, but for the purpose of this study, we will neglect this

effect. This issue is less obvious on the high resolution spectrum since the bins are smaller, and the spectra show very similar trends with both methods for computed radiances within 10% of each other.

4.3 Modeled VIRTIS IR Spectra

As mentioned in section 2.3.4, the existing spectral databases such as HITRAN and GEISA do not provide any individual line model for the CH_3OH's strongest bands preventing us to take into account the methanol contribution around 3.3 microns, where it should be the dominant emission (Bockelée-Morvan 1995). However, we can model a full spectra from 2.5 to 5.0 μm for the other major species providing an insight to the future VIRTIS measurements. The direct flux output for each considered band of each modeled species before degradation due to the spectral resolution of the instrument for a typical limb measurement with the Rosetta spacecraft at a distance of 50.1 km from the nucleus observing at a projected distance of 2 km above the nucleus surface are presented in Appendix A. The structure of the spectra appears clearly different depending on the molecule type. Indeed, Herzberg (1957) classified polyatomic molecules in different groups with: linear molecules, symmetric top molecules, spherical top molecules, asymmetric top molecules, and other molecules. Each group of molecules needs to be described separately and presents different characteristics and even different nomenclatures (Herzberg 1957). Linear molecules such as CO_2, CO, and HCN have very structured spectra clearly showing the P, Q, and R branch where the change of rotation ΔJ=-1, 0, and 1, respectively. While other polyatomic molecules from other groups have at least one vibrational bond coupled to another, which leads to complicated motion and then more complicated spectra.

The VIRTIS instrument has a finite spectral resolution $\lambda/\Delta\lambda$ ranging from 70 to 380 for VIRTIS-M and 1300 to 3000 for VIRTIS-H. The resolution degradation was applied using bins of wavelength width corresponding to some rather average spectral resolutions for each channel with $\lambda/\Delta\lambda$ of 200 and 1900 for VIRTIS-M and -H, respectively. This technique reflects better the spectrum that would be returned by the instrument than a

convolution with a gaussian that tends to give a smooth solution.

The modeled spectra for the considered limb measurement with the Rosetta spacecraft at a distance of 50.1 km from the nucleus observing at a projected distance of 2 km above the nucleus surface are illustrated in Figure 4.4 and with the detailed contribution from each species in Figure 4.5. The brightnesses of the emissions resulting from different species vary by several orders of magnitude with the water having the strongest emission with a few times 10^{-3} W.m^{-2}.sr^{-1}.μm^{-1}. CO_2 and CO emissions follow with brightnesses of a few time 10^{-4} and 10^{-5} W.m^{-2}.sr^{-1}.μm^{-1} respectively. Of course, the absence of the emission resulting from CH_3OH is a major flaw in this representation of the VIRTIS spectra. However, the resolution of the instrument is sufficient in order to determine the organics components between 3 and 3.7 microns. Then, this tool enables us to identify the amount of organics present in a particular location using individual lines.

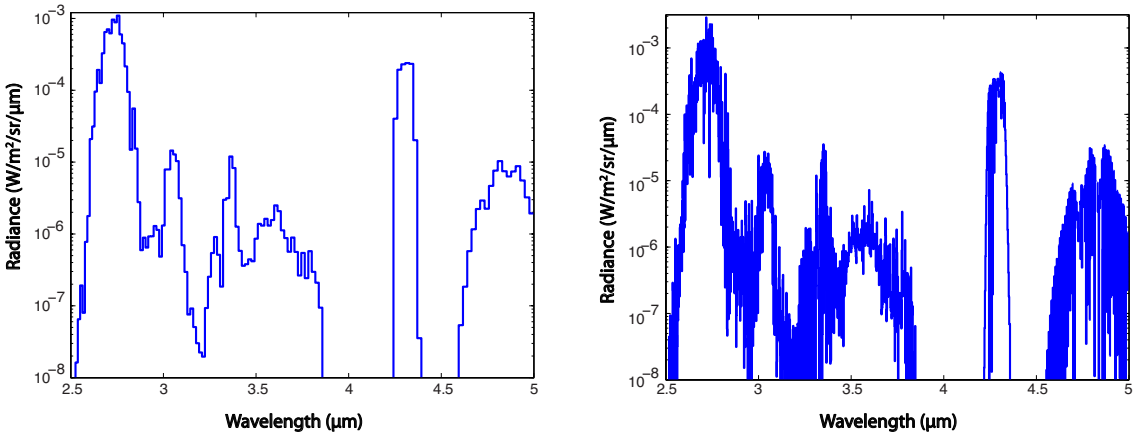

Figure 4.4: Total modeled radiance spectra for a limb measurements from the spacecraft located at 50 km from the nucleus observing at a projected distance of 2 km above the nucleus surface for VIRTIS -M (left) and -H (right) without CH_3OH's contribution.

Also, modeling such spectra can be of critical importance for mission planning. Indeed, the signal-to-noise ratio (SNR) constitutes an intrinsic difficulty for coma observations and is an important constraint in the measurements. The noise equivalent spectral radiance (NESR), which is defined as the root mean squared noise of a given measurement

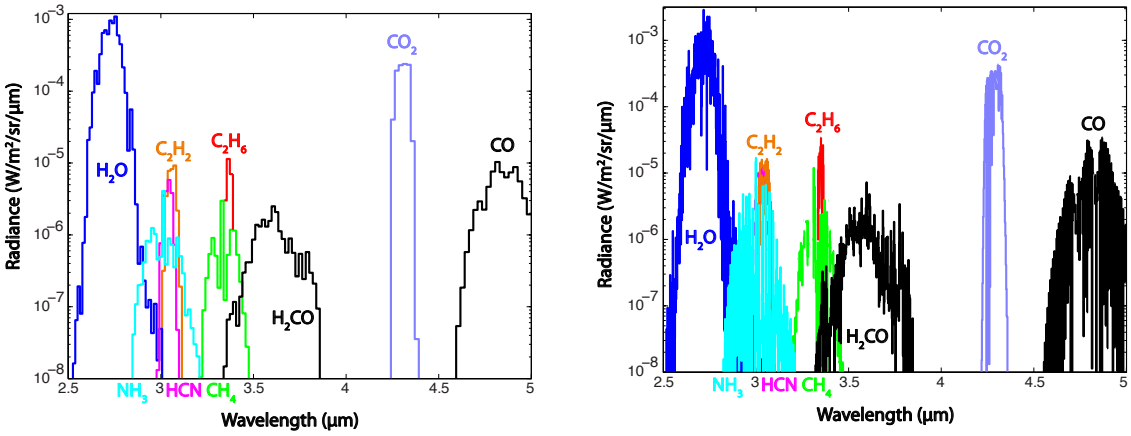

Figure 4.5: Total modeled radiance spectra for a similar case as Figure 4.4 illustrating the emission contribution from each species.

in units of radiance, corresponds to the instrument signal if it was measuring an empty medium. The NESR can help figure out the amount of individual spectra that need to be added together in order to achieve a desired SNR. The NESR depends on the internal temperature of the spectrometer, which itself depends on the exposure of the radiator to different regions warmer than deep sky. Figure 4.6 represents a NESR case for a 1 second integration relative to VIRTIS-M (Capaccioni - private communication). It appears that the NESR peaks at about 9×10^{-3} W.m^{-2}.sr^{-1}.μm^{-1} for a 1 second integration time, which is less than an order of magnitude above the radiances that we obtained with our model, showing that several spectra will have to be added in order to reach a decent SNR for the overall wavelength range at 2.0 AU for the case of a 1 second integration assuming that the gas production rates are similar to the ones used here.

This approach can be extended to other coma cases and observation geometries, enabling us to make the link between the physics and the measurements in order to get the best description of the gas release from comet CG. Once VIRTIS will start sending data, we will be able to construct modeled spectra to reproduce the measurements in a similar way as with the HRI measurements from EPOXI at comet Hartley 2, giving the composition of the coma at a particular location and then, constraining the gas production rates of the different areas of the nucleus as will be presented in chapter 7.

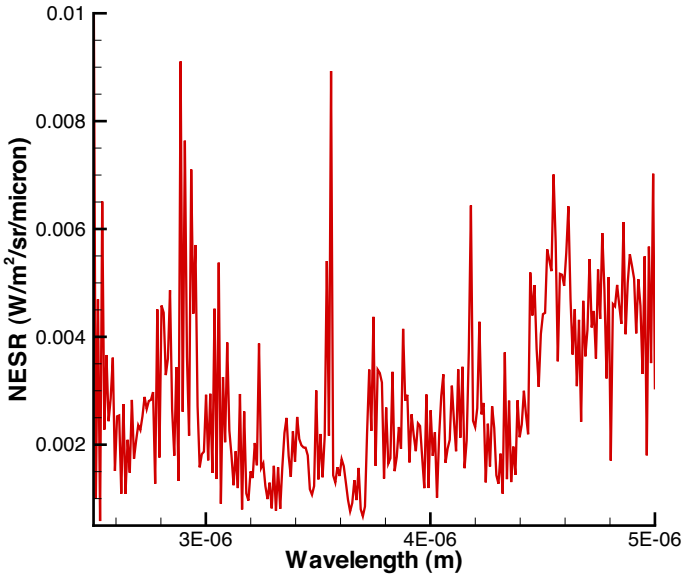

Figure 4.6: NESR of VIRTIS-M for a 1 second integration, representing the response of the instrument measuring an empty medium (Capaccioni - private communication).

The next chapter will present the cometary coma resulting from a nucleus with a small active area and compare it with a simple day/night asymmetrical gas release.

Chapter 5

The Dust and Gas Coma Resulting from a Nucleus with a Small Active Area

While gas production from the surface of the nucleus with dominant day/night asymmetries seems intuitive, observations show that cometary nuclei present isolated source regions of activity. Indeed, jet features have been observed on several comets such as at the scarp of Comet Tempel 1 (Farnham et al. 2007, Belton 2010) or at the large lobe of Comet Hartley 2 (A'Hearn et al. 2011). Also, small active areas as patches of activity seem to be common on comet nuclei such as the water vapor outflow at the waist of Comet Hartley 2 (A'Hearn et al. 2011). In the same way, Schleicher (2006) presented and analyzed a set of photometric observations of CG from its 1982/1983 and 1995/1996 apparitions showing that the main source of activity corresponds to only 3%-4% of the total surface of the nucleus (Figure 5.1). These observations were corroborated by a model from Groussin et al. (2007) that accounted for polar orientation, rotation period, and size and location of active regions to reproduce water vapor production rate, showing that observations of rotationally driven and strong seasonal effect in both gas and dust could be matched by a spot located in the north at a latitude of about 65°, while two active regions could be possible but less likely. There is a strong seasonal effect so that the active region comes mostly into the day side around perihelion after staying in the night hemisphere during the comet's journey toward the Sun.

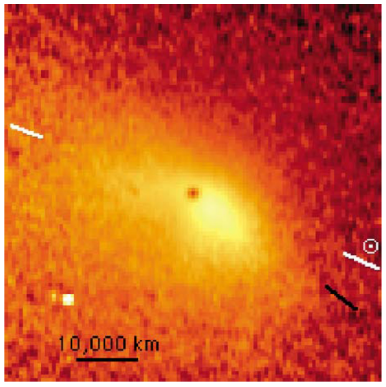

Figure 5.1: R band composite image enhanced by dividing by a canonical ρ^{-1} profile of CG from January 25, 1996, one week after perihelion showing the jet resulting from the small area (Schleicher et al. 2006).

These small regions of activity seem to dominate the gas and grain release for some comets and then play a critical role in the physics of the coma. A rigorous study of the gas and dust particles released from jets and patches of activity is necessary to fully understand the behavior of these discrete sources. While numerous models have been presented with broadly distributed day/night asymmetries (Combi 1996, Crifo and Rodionov 1997, Tenishev et al. 2008), the coma resulting from such a small outgassing area on a nucleus has not yet been explored. Most of the results presented in this section have already been published in a paper by Combi et al. (2012), though the detailed quantitative work was done as part of this thesis.

5.1 The DSMC Model of the Coma Resulting from a Small Active Area

A coma mostly produced by a small fraction of the nucleus surface will inherently have large gradients of gas densities at the boundary of the active area with some very rarefied gas outside of the outgassing patch. A kinetic approach using DSMC is the method of choice to study such a flow with large ranges of Knudsen numbers.

The dust and gas coma resulting from such an active area is studied in the present section using a 2D axisymmetric DSMC approach applied to comet CG for conditions ranging from the Rosetta spacecraft rendez-vous with comet CG at 3.25 AU to CG's perihelion at 1.29 AU corresponding to the four cases from Tenishev et al. (2008, 2011) (Table 5.1), where a small active area representing 4% of the total surface of the nucleus emitting 95% of the gas and dust, while the remaining 5% were distributed on the remaining surface of the nucleus proportionally to the distribution from Tenishev et al. (2008). The small active area gas production is assumed to be constantly distributed over the active region as explained in section 3.1.2.

Composition	95% H_2O and 5% CO	
Nucleus density	300 $\mathrm{kg.m^{-3}}$	
Dust/gas production ratio	0.8	
Dust particle size distribution	$Z(a) \sim a^{-4}$	
Dust particle size range	10^{-7} to 10^{-2} m	
Production distribution	95% from a 4% active area spot	
	5% distributed as Tenishev et al. (2008)	
Four cases	r (AU)	Q ($\mathrm{s^{-1}}$)
	1.29	5×10^{27}
	2.0	8×10^{26}
	2.7	8×10^{25}
	3.25	8×10^{24}

Table 5.1: DSMC model parameters for the CG simulations. Extracted from Combi et al. (2012)

To ensure the cylindrical symmetry, the active area was centered on the symmetry axis which corresponds to the solar direction. The active area spans 4% of the total surface of the nucleus, which represents the intersection of the assumed spherical nucleus of 2 km radius (Lamy et al. 2006) with a cone of origin (0, 0, 0) and semi-angle θ given by the

formula of the area A of the patch:

$$A = \int_0^{2\pi} \int_0^{\theta} r^2 \sin(\theta) d\theta d\phi = 2\pi r^2 \left(1 - \cos(\theta)\right) \tag{5.1}$$

where θ is the inclination angle, which corresponds to the cone semi-angle, and ϕ the azimuth angle. Then, taking the ratio of the previous equation over the total area of the sphere $A_{sphere} = 4\pi r^2$ so that $A/A_{sphere} = 4\%$ and solving for θ, leads to an expression for θ:

$$\theta = \arccos\left(1 - 2 \times 4\%\right) = 23^{\circ} \tag{5.2}$$

These results are compared to previous models with a broadly distributed dayside dominated source from Tenishev et al. (2008, 2011) enabling a clear comparison between the coma produced by broadly distributed sources and discrete outgassing patches.

5.2 The Gas Coma Generated by a Small Active Area

5.2.1 Parent Species Model Outputs and Macroscopic Parameters

The general structure of the water flow in the coma from the small active area simulation is given in Figure 5.2 for the case at a heliocentric distance of 1.29 AU using a logarithmic scale where the distance from the center of the nucleus to a particular point in the space is given by $10^{\sqrt{(logX)^2+(logY)^2}}$ and the tangent of the angle between the radius vector of the point and the direction is the Sun is log Y/log X such as in Tenishev et al. (2008), while the other cases can be found in Appendix B. Here, the 1.29 AU case is compared with a broadly distributed source with day/night asymmetry corresponding to the case from Tenishev et al. (2008). In both cases, the flux dominates on the day side due to the boundary conditions. However, an even stronger asymmetry is created in the small area case so that the water density is enhanced on the day-side in the range considered. The overall velocity and temperature profiles are rather similar in both cases with the only major difference a higher temperature along with smaller molecular velocities beyond 10^5 km on the night side in the small area case.

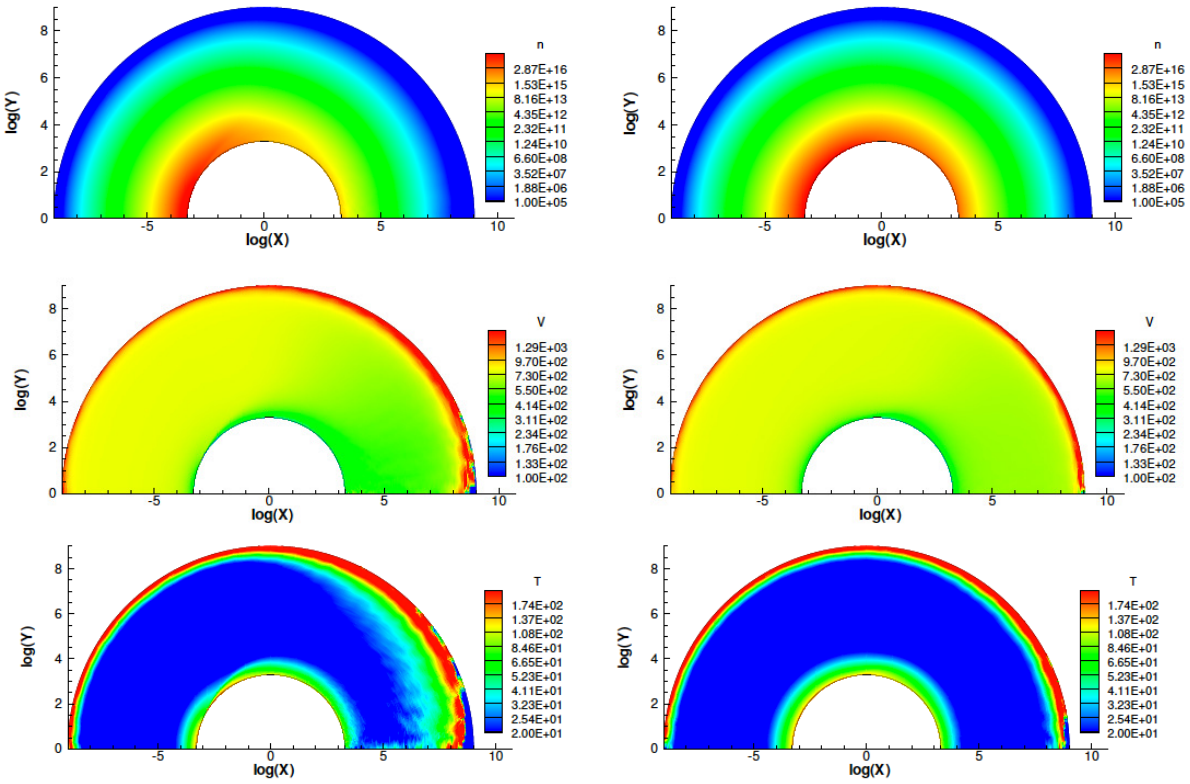

Figure 5.2: Number density (m^{-3}), velocity ($m.s^{-1}$), and temperature (K) of water at a heliocentric distance of 1.29 AU for a 4% active area case (left) and a broad day/night asymmetrical source from Tenishev et al. (2008) (right). A logarithmic scale is used on the plots, where the distance from the center of the nucleus to a particular point in the space is given by $10^{\sqrt{(logX)^2+(logY)^2}}$ and the tangent of the angle between the radius vector of the point and the direction is the Sun is log Y/log X such as in Tenishev et al. (2008).

This general view of the coma gives a clear idea of the overall structure of the coma but prevents a more quantitative analysis. Then, Figure 5.3 (which appeared in Combi et al. 2012) shows false color contour plots of the water density distribution within 100-200 km from the center of the nucleus comparing the 4% active area with a mostly dayside-distributed source from Tenishev et al. (2008). Once again, the active area releases most of the gas emitted from the nucleus so that the gas flux is very high in that area resulting in a strong asymmetry between the day and night hemispheres of the coma. This results in higher gas densities in the small area region than in the broad source case. The determinative effects of a dominant small active area occur within the first 50 km of the nucleus (Combi et al. 2012). It is noticeable that even if the gas emission is strongly dominated by the small surface area within a cap extending only 23°from the center of the active area, the gas coma fills nearly the entire hemisphere centered on the active area by 10-20 times the nucleus radius in all four cases (Combi et al. 2012).

In the 1.29 AU case, the day-side densities are such that collisions are important enough for the flow to be in a fluid regime, where particles have relatively large tangential velocity so that the gas released from the surface expands not only radially but tangentially also (Combi et al. 2012). As the heliocentric distance increases, the gas densities drop and collisions become more scarce resulting in a coma that flows more and more radially to essentially reach a free molecular flow at 3.25 AU (Combi et al. 2012). Indeed, the rarefaction of the flow can be determined by the computation of the Knudsen number (Kn) and then compare its value with respect to 0.05 as the upper limit for validity of hydrodynamic methods as explained in section 2.1. The characteristic length necessary to compute Kn can be defined in a few different ways for this application. We decided to use the variation of density to do so since it is our main macroscopic parameter directly related to the mean free path:

$$Kn = \frac{\lambda}{n}\|\nabla n\| \tag{5.3}$$

where λ is the local mean free path and n the local number density. Contour plots of the Knudsen number for the different cases are reported on Figure 5.4. In the 1.29 AU case, one can observe Knudsen numbers as small as 10^{-3} showing the fluid character of

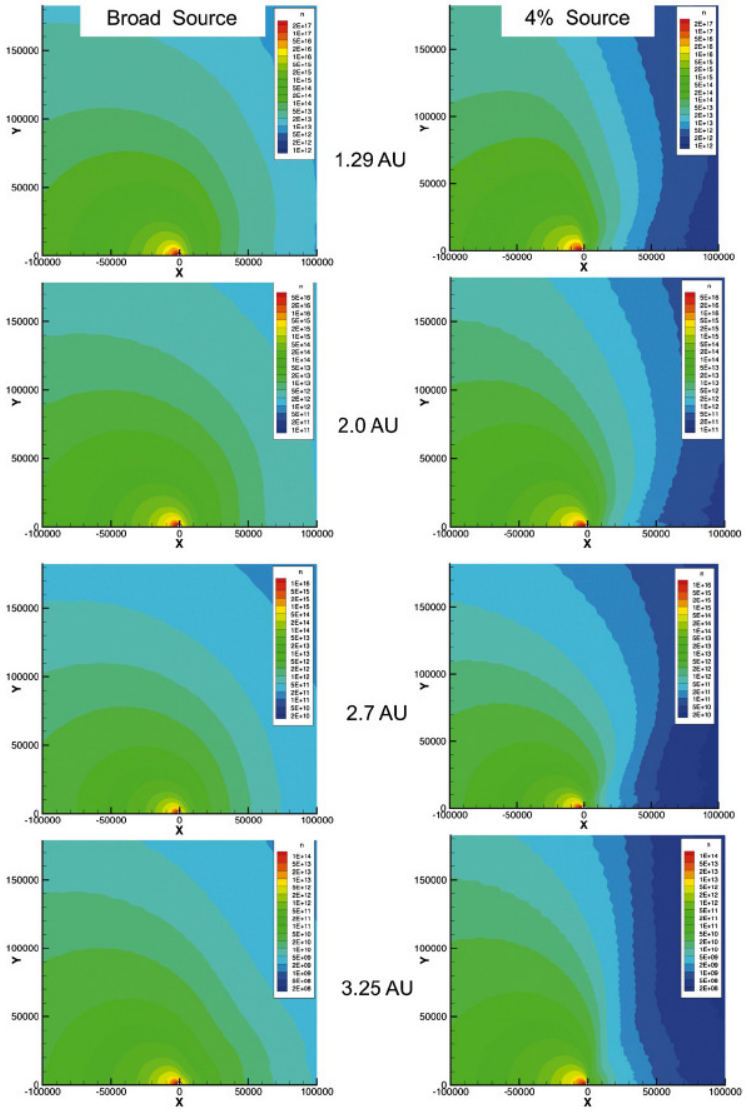

Figure 5.3: Distribution of H_2O vapor in the inner 100 km of the coma, comparing the broad hemispherical source (left) with the small 4% active area (right). Distances are in meters and densities are in m^{-3}. Panels from top down are for heliocentric distances of 1.29, 2.0, 2.7, and 3.25 AU, respectively. Appeared in Combi et al. (2012).

this flow in the active region area. However, the night side coma presents relatively large Knudsen numbers already larger than 2 fully justifying the use of the DSMC method to study the full coma of such a comet with a patch of activity where different flow regimes are observed. At a distance of 3.25 AU, it appears clearly that the hydrodynamic conditions are not respected even in the active area where the Knudsen number is always above 5 due to the lower mean free path generated by the lower gas densities, so that the coma can only be studied on the basis of a kinetic model.

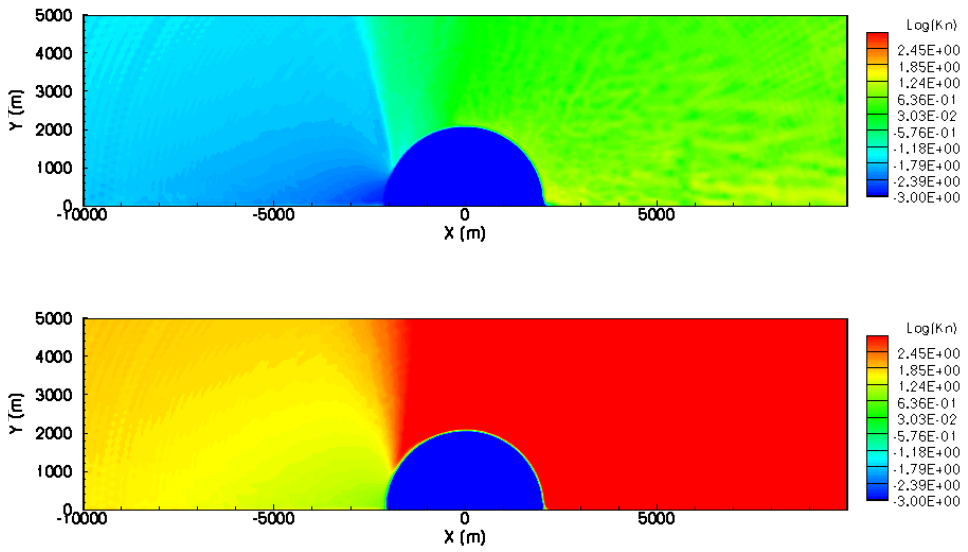

Figure 5.4: Knudsen number plot for the 1.29 and 3.25 AU cases for a 4% active area.

Figure 5.5 illustrates the expansion phenomenon resulting from the tangential velocity generated by collisions showing the water day-side coma within 20 km from the nucleus with streamlines compared to similar cases with a broad source. It appears that the streamlines in the region right next to the active area are strongly bent toward regions of lower densities at low heliocentric distances where the densities are high enough for collisions to be important. Hence, at low heliocentric distances, the gas released by the small area

tends to expand and populate parts of the coma at larger sub-solar angles.

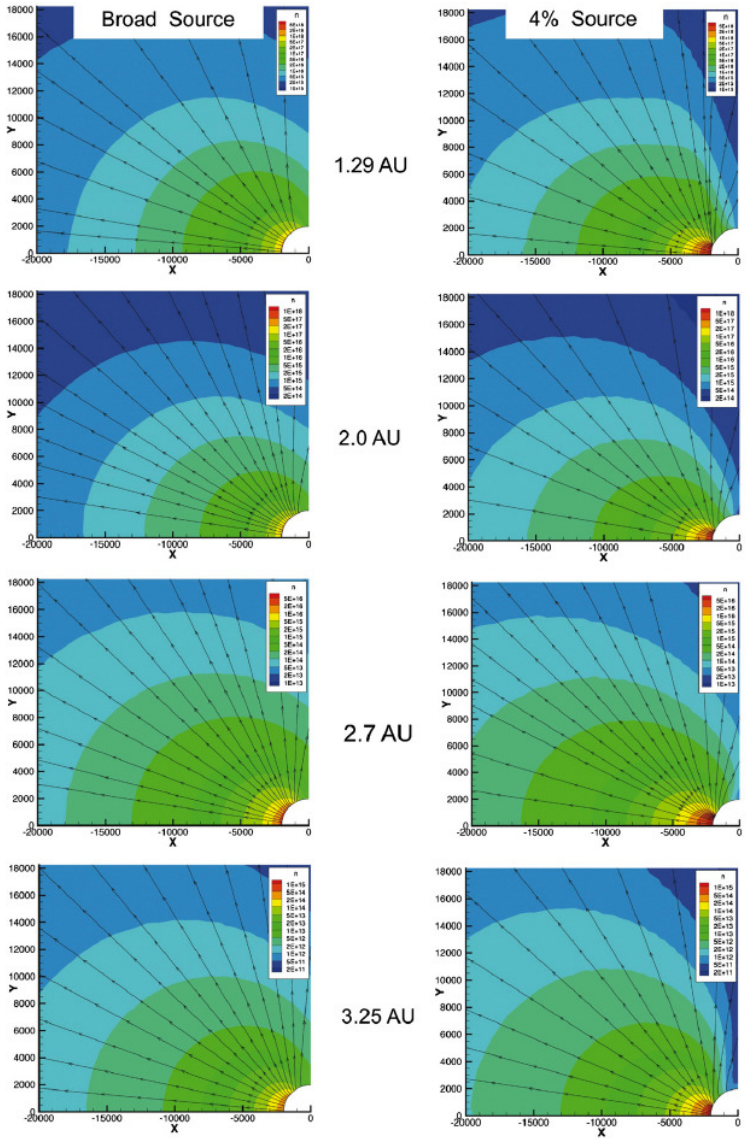

Figure 5.5: Water vapor density distribution in the very inner coma with flow streamlines, comparing the broad hemispherical source (left) with the small 4% active area (right). Distances are in meters and densities are in m^{-3}. Panels from top down are for heliocentric distances of 1.29, 2.0, 2.7, and 3.25 AU, respectively. Appeared in Combi et al. (2012).

For a more quantitative view of the phenomenon of expansion of the flow presented above, Figure 5.6 (which appeared in Combi et al. 2012) shows the water density as a function of the angle from the center of the active area and comparison with broad source cases at distances ranging from just above the surface of the nucleus to 50 km from its center. As expected, the variation in density with angle is clearly less strong in the case of a broad source than with a small active area where the densities are mostly concentrated above the active region especially at small distances from the nucleus. The angular asymmetry tends to smear out with distance as the gas expands so that at 50 km, even if the gas is still more collimated in the 4% active area case, the gas originating from the small area populates almost all the coma at all heliocentric distances.

5.2.2 Daughter Species Coma and its Appearance from Ground Based Measurements

Similarly as done in Tenishev et al. (2008), the water photodissociation products can be dividing according to their mass into two groups: the light species (H and H_2) and the heavier products (OH and O). Because of the difference in molecular masses, the members of light products group have a bulk velocity and kinetic temperature that exceed those of the heavier species. Yet, within each group, the different species have a similar flow pattern (Tenishev et al. 2008). OH and H are chosen as a representative heavy and light daughter species result from water photodissociation, respectively. The overall H and OH coma density for the 1.29 AU case is represented in Figure 5.7 from the inner boundary at the surface of the nucleus up to the outer boundary at 10^6 km. It appears clearly that density profiles are almost identical for broadly distributed sources and small active area cases for a given daughter species of the photodissociation of water. Indeed, both cases present a relatively strong day/night asymmetry with a somehow larger angular extension in the broadly distributed source case within 100 km. At larger distances, both cases seem to present relatively spherical distributions.

In the case of a broadly distributed asymmetrical gas source, the daughter species tend to appear relatively circular from ground-based measurements (Tenishev et al. 2008). It

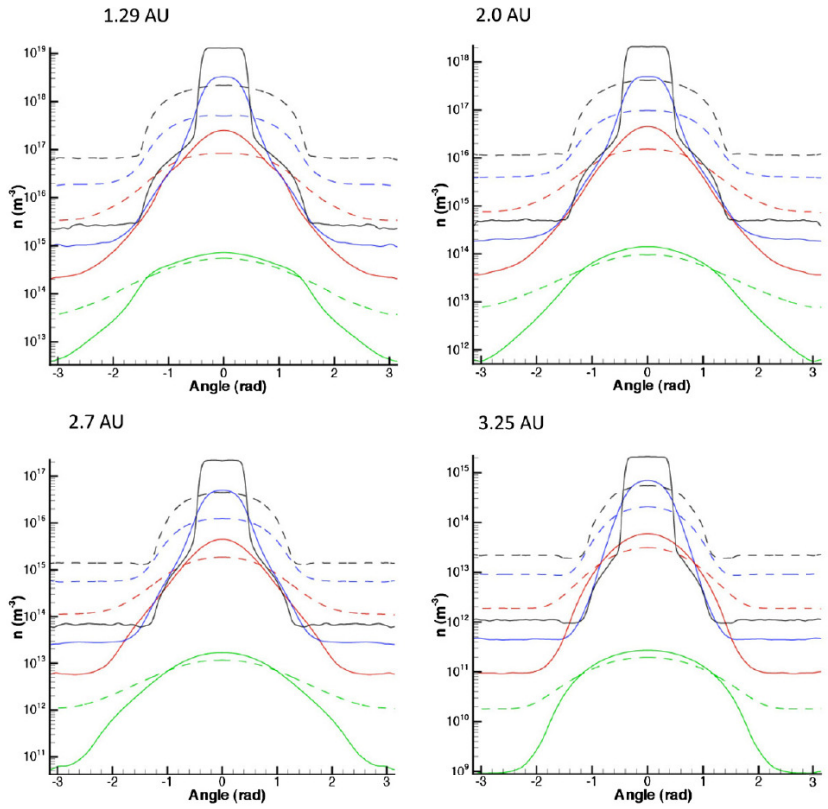

Figure 5.6: Water vapor density as a function of angle from the center of the active area for a broad and small (4%) active area models. The black, blue, red, and green lines are values at 2 km, 2.5 km, 5 km, and 50 km from the center of the nucleus, respectively. Appeared in Combi et al (2012).

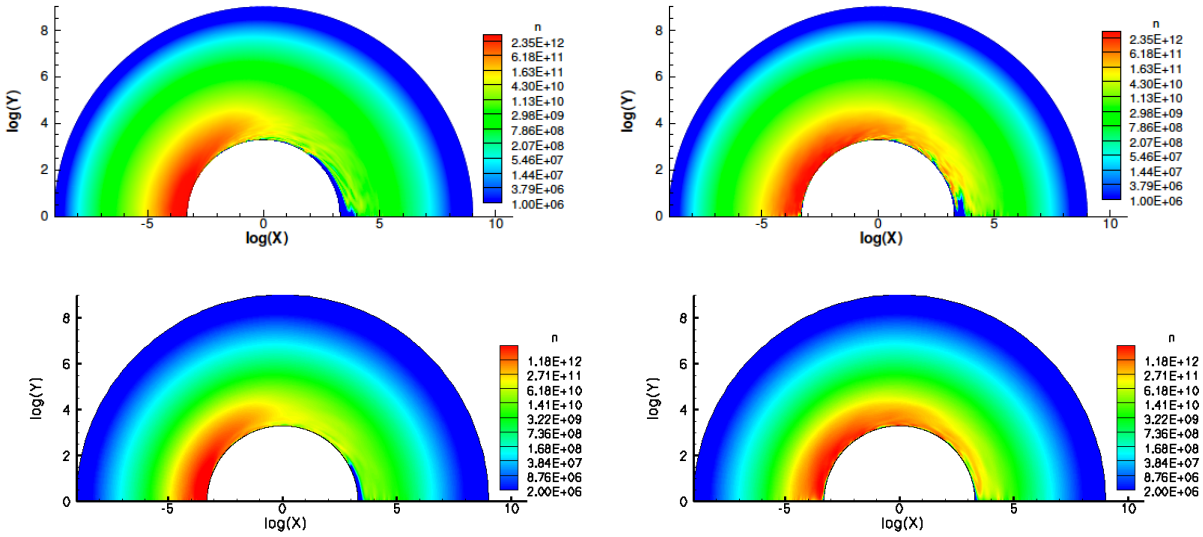

Figure 5.7: Number density (m^{-3}) of OH (top) and H (bottom) at a heliocentric distance of 1.29 AU for a 4% active area case (left) and a broad day/night asymmetrical source from Tenishev et al. (2008) (right). A logarithmic scale is used on the plots.

is then legitimate to wonder if when most of the gas is released from a small active area, the daughter species' coma keeps this circular shape. Tenishev et al. (2008) showed the modeled appearance of the OH coma for a broad source for a geometry corresponding to the 2009 apparition of CG assuming a Sun-comet-observer angle of 35°. Then, using a similar geometry, the OH coma resulting from a small source area was computed and illustrated Figure 5.8 (which appeared in Combi et al. 2012). The respective halves of the coma containing most of the activity are similar for both broadly distributed and small active area cases, which results directly from the fact that the determinative effects of a small active area occur within the first 50 km of the nucleus (Combi et al. 2012), which is consistent with what was observed with the density plots.

As detailed in Combi et al. (2012), this comparison is not meant to be literally predictive of an actual observation due to the fact that the small active area would not be aligned with the nucleus' spin axis so that its activity would vary with its illumination by sunlight.

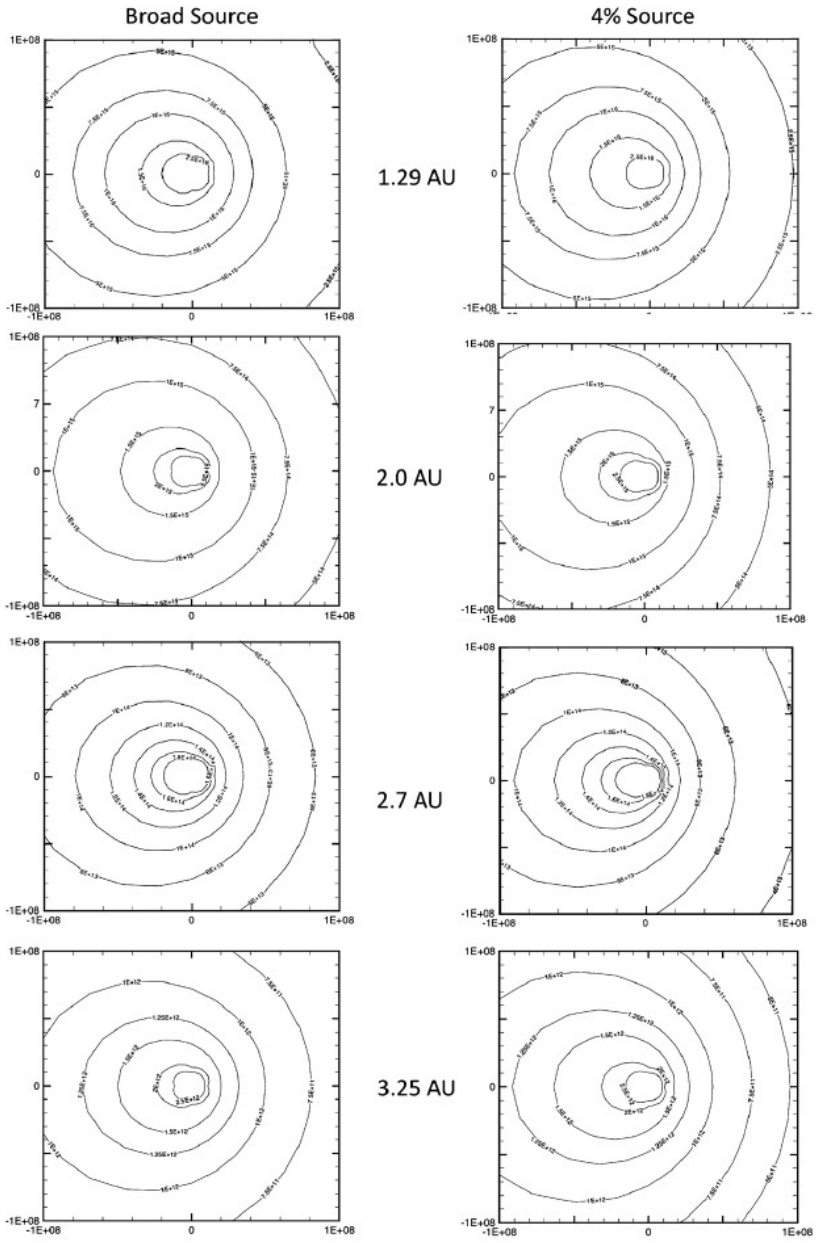

Figure 5.8: OH coma produced by broad day/side asymmetry distribution (left) and small active sources (right) from top to bottom at heliocentric distances of 1.3, 2.0, 2.7, and 3.25 AU. Appeared in Combi et al. (2012).

Moreover, since the rotation period is significant compared to the transport time of parent and daughter molecules and that the position of the active region with respect to the line of sight will vary, the nucleus rotation will contribute to a resulting OH coma even more circular than in the presented model outputs. The main result from this comparison is that the daughter species' comas resulting from a small active area and a broadly source observed at a large distance from the nucleus are not distinguishable from one another and will both appear rather circular (Combi et al. 2012).

5.3 The Dust Coma Generated by a Small Active Area

The dust dynamics being driven by the nucleus gravity and the gas drag is directly affected by the presence of a small active area. Because local gas densities are much larger in the case of a small active area than in the case of a broadly distributed source close to the nucleus' surface, larger particles are lifted. Indeed, the dynamics of the dust grains is driven by the local drag force and the gravity force so that using equation (3-2), we derived the maximum liftable sizes for the different cases (Figure 5.9). It occurs that particles about 3 to 6 times larger are lifted in the case of a 4% active area than in the broad source case. Indeed, for the heliocentric distances considered, the maximum liftable sizes range from about 5 μm to less than a centimeter in the case of a broad source, and between about 20 μm to a few centimeters in the case of an active area. This is a critical result since most of the total dust mass is located in the larger particles. Moreover, the gas fluxes being much lower outside of the small active area, the variation in the maximum liftable size with solar zenith angle shows a strong decrease at the edge of the active patch where only small grains are lifted. Hence, most of the dust mass injected in the coma results from the active area production.

A comparison between the acceleration region of the dust by gas in the coma for small active area and broad day-side activity (Figure 5.10 which appeared in Combi et al. 2012) shows that the gas velocity can be as much as twice as large in the presence of a small active area due to the stronger gas drag on the dust grains (Combi et al. 2012). In a direction aligned with the center of the maximum of activity, micron-sized particles are

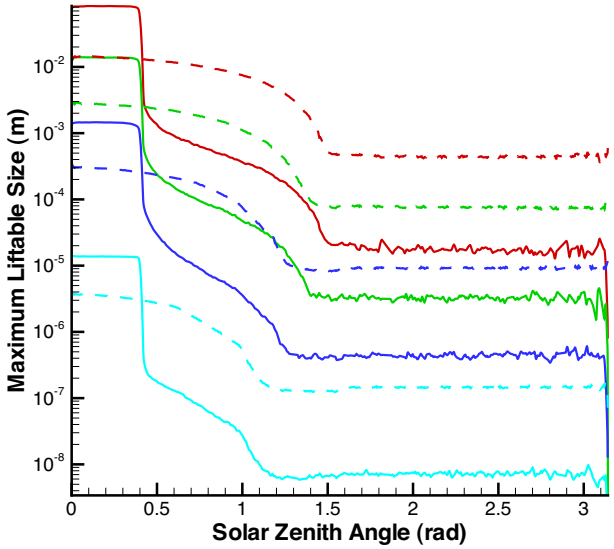

Figure 5.9: Dust maximum liftable size in function of the solar zenith angle for the different considered cases: 1.29 AU (red), 2.0 AU (green), 2.7 AU (blue), and 3.25 AU (teal) for the 4% small active area (solid line) and the broadly distributed source (dashed line).

accelerated up to a velocity of approximatively 180 m.s^{-1} and 100 m.s^{-1} for the perihelion case compared to about 3 m.s^{-1} and 1.5 m.s^{-1} at 3.25 AU, for a 4% active area case and a broad source respectively. In all cases, dust particles reach their terminal velocities by about 20 km from the center of the nucleus independently of the heliocentric distance in agreement with the classical result that dust grains decouple from the gas within a 10 to 20 nucleus radii.

The dust density profiles in the inner coma from direct DSMC output are illustrated in Figure 5.11 (which appeared in Combi et al. 2012) showing that the density values are very similar in the case of a broad source and a 4% active area at all heliocentric distances. While the gas tangential expansion was important, the dust particle density distributions in the inner coma show that the dust emission right above the active area is more concentrated than in the case of a broad source even out to 50 km (Combi et al. 2012). Then, while the gas were filling the all day-side hemisphere by 20 km, the dust stays collimated above the active area because the dust acceleration occurs just above the surface of the nucleus

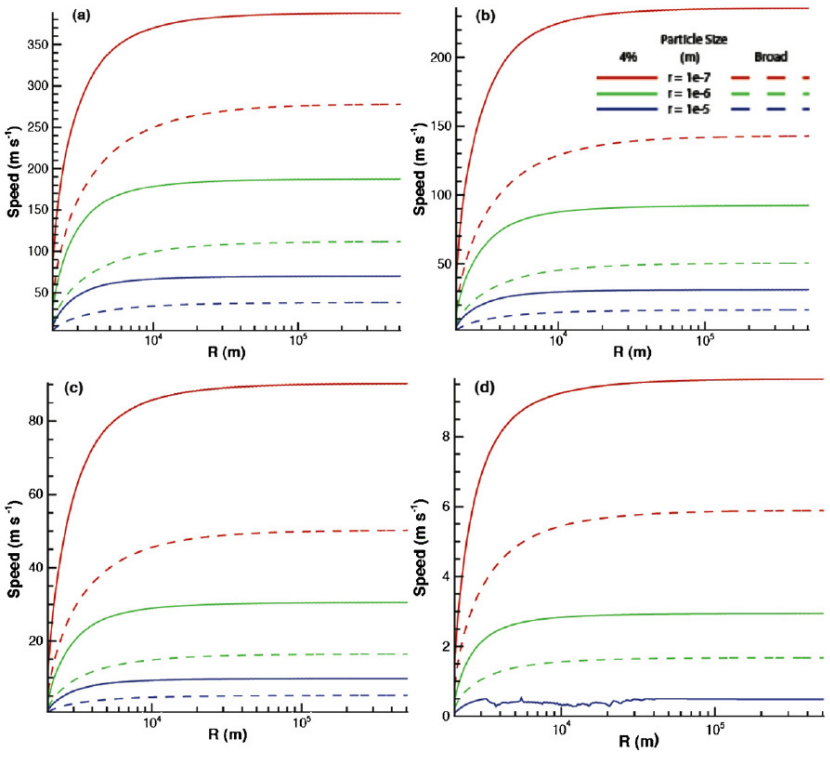

Figure 5.10: Dust velocities as a function of distance from the center of the nucleus for heliocentric distances of (a) 1.29, (b) 2.0, (c) 2.7, and (d) 3.25 AU for the broad (dashed) day/night asymmetrical source and the small 4% active area (solid). Appeared in Combi et al. (2012).

where the gas densities are much higher than with the corresponding broad source cases, then eventually the dust particles decouple from the gas and travel radially with ballistic trajectories at their terminal velocities (Combi et al. 2012). In contrast, the gas continues expanding tangentially at larger distance from the nucleus due to gas pressure in the high production rate cases and from free expansion of the initial non-collimated gas velocity distribution function (Combi et al. 2012). This result is fundamental in order to interpret the observation of dust jets in comets. Hence, it is more likely to find active area traces observing density of dust grains than the gas particles since the dust collimation is more important than for the gas.

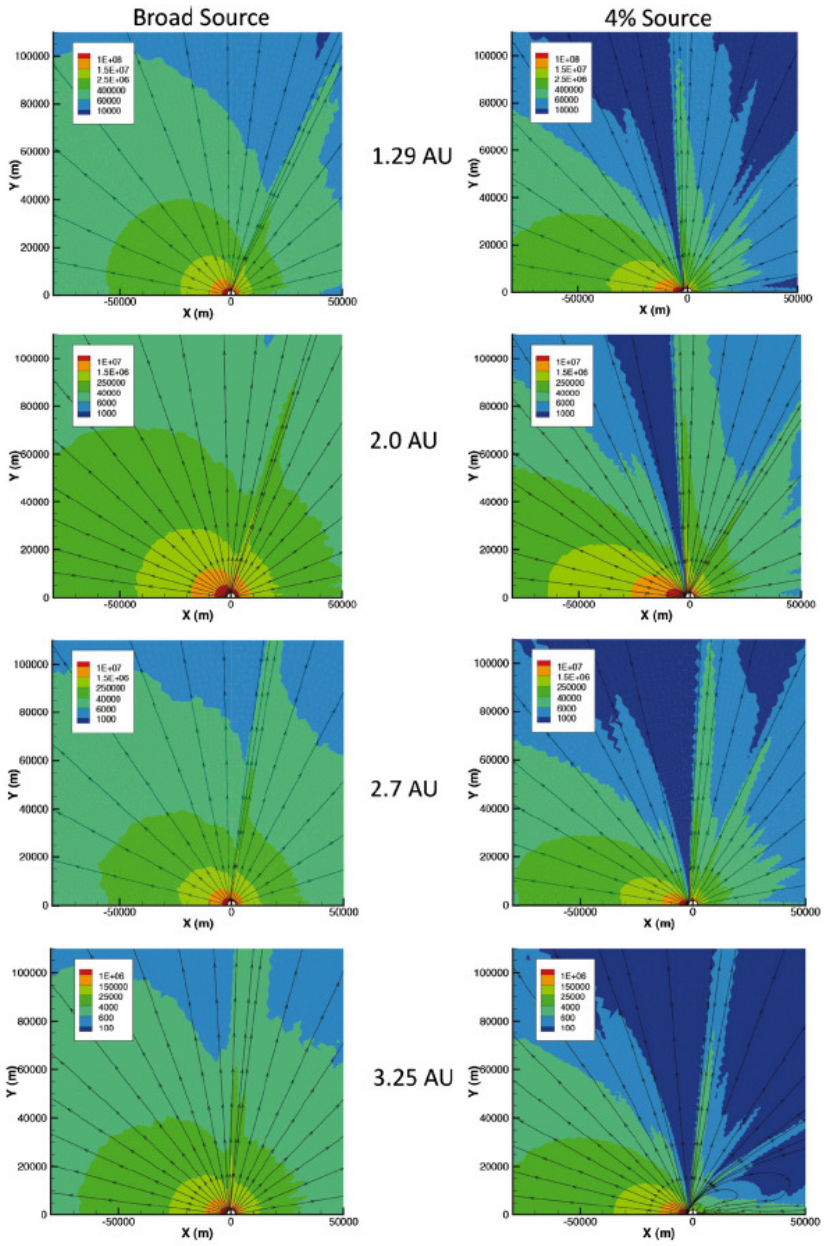

Figure 5.11: Dust distribution in the very inner coma for the broadly distributed source (left) and the 4% area source (right). Appeared in Combi et al. 2012.

Nonetheless, when looking at the bigger picture, the discontinuity of the flux between the small source area and the rest of the nucleus creates a feature that extends up to the upper boundary (Figure 5.12). This feature starts almost tangentially to the surface before being slowly tilted away from the nucleus surface until it becomes radial. It is necessary to mention that at large distances from the nucleus, this feature is located at a completely different position than the active area boundary where it originated. Hence, it can be misleading to over interpret the position of a jet by observing the dust features at large distances from the nucleus. A less prominent similar structure appears in the broad day/night asymmetrical source at the terminator also displaced from its original source location at large distances from the nucleus.

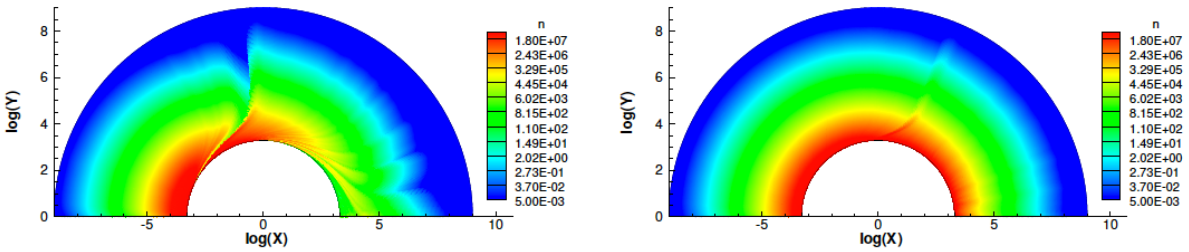

Figure 5.12: Number density (m^{-3}) of dust particles at a heliocentric distance of 1.29 AU for a 4% active area case (left) and a broad day/night asymmetrical source from Tenishev et al. (2008) (right). A logarithmic scale is used on the plots.

Coma resulting from small active areas have a relatively different structure than the prediction that would be made by a spherical assumption such as in a Haser model. The difference is even more important for dust grains than it is for gas due to their stronger collimation. What if these grains possess some ice that will sublimate as they are carried away from the nucleus by the gas? The next chapter will focus on the coma resulting from extended sources with sublimating icy grains.

Chapter 6

The Impact of Sublimating Icy Grains on the Coma

Direct sublimation of a comet nucleus surface is usually considered to be the main source of gas in the coma of a comet. However, evidence from a number of comets including the recent spectacular images of comet 103P/Hartley 2 by the EPOXI mission indicates that the nucleus alone may not be responsible for all, or possibly at times even most, of the total amount of gas seen in the coma. Indeed, the sublimation of icy grains, which have been injected into the coma, appears to constitute an important source of gas in the cometary atmosphere. The presence of such sublimating icy grains modifies the cometary environment, this chapter focuses on describing such a coma. This is the first coma model including a consistent interaction and mutual feedback of accelerating and sublimating grains by the outflowing gas and the newly sublimated gas released by the grains back on the gas in the coma.

6.1 The Ice and Gas Dynamics when Gases are Released from both the Nucleus and Sublimating Icy Grains

While the gas dynamics in the coma has been extensively studied in the past for cases where the nucleus is the sole source of gas release (Combi et al. 2004 and references

therein), the complex coma resulting from the interaction of particles released from the nucleus with an extended source of warmer particles still needs to be assessed. We use the DSMC model to describe the ice and water molecules' dynamics for cases with gas particles released from both the nucleus and sublimating icy grains. We address a large number of 1D cases, including water's daughter species, varying parameters such as the total production rate, the heliocentric distance, the grain size distribution, the grain to gas mass ratio, and grain nature from a reference case with a water production rate of 5×10^{27}s^{-1} with a grain to water mass release ratio of 1:1 with a grain size distribution of -3.5 at 1 AU. All the runs have been performed using a nucleus of 1500 m of radius with a mass density of 300 kg.m^{-3}, and a grain size range of 10^{-7} to 10^{-2} m assuming a grain mass density of 1000 kg.m^{-3}. The gas to grain mass ratios given are the inputs in the DSMC code over the computed radius range (10^{-7} to 10^{-2} m) and not the actual lifted grain mass, enabling an easy reproduction of these results. This theoretical study gives a better insight of the impact of the water release from sublimating icy grains into the cometary coma.

6.1.1 Production Rate and Heliocentric Distance Effects on the Coma

It is intuitive that the extended release of warmer water molecules impacts on the dynamics of the water molecules in the coma. The production rate and heliocentric distance have an important influence on the gas dynamics. The coma temperature and gas expansion velocity are affected notably due to photochemical heating efficiency that increases with larger gas production rates and smaller heliocentric distances because of increased gas densities (Tenishev et al. 2008). The icy grains are directly impacted by these changes in macroscopic parameters in addition to the variation in grains' lifetimes and sublimation rates with heliocentric distance, influencing the release of gas particles (Patashnick et al. 1975, Lien 1990, Beer et al. 2006). Figure 6.1 shows a comparison between the temperature, velocity, number density, and flux integrated over a sphere for cases with water production rates of 5×10^{26} s^{-1}, 5×10^{27} s^{-1}, and 5×10^{28} s^{-1} with a "dirty" grain to water mass release ratio of 1:1 with a grain size distribution of -3.5 at 1 AU, compared with cases at the same heliocentric distance with water solely released from the nucleus with

production rates of 10^{27} s^{-1}, 10^{28} s^{-1}, and 10^{29} s^{-1}. Since, if all icy grains are lifted, the total water production rate (ice + gas) should equal the gas production rate of its paired case with the nucleus as the sole source of water, the direct effect of the sublimation of icy grains on the coma can be examined.

The flux integrated over a sphere represents the gas production rate that stays constant with distance from the nucleus for cases where the gas is solely released from the nucleus according to the continuity equation up to about 10 million km at 1 AU where photodissociation becomes important. When sublimating icy grains are present, the water flux increases with distance until the grains are fully sublimated where it reaches a maximum equal to the sum of the contribution from the nucleus and the grains. In the case of large gas production rate from the nucleus (here 5×10^{28} s^{-1}), all the grains from the range considered are lifted which implies that the maximum gas flux is equal to the sum of the water mass flux released from the nucleus and the water mass released from the grains both with a contribution of 5×10^{28} s^{-1} in this case, for a total of 10^{29} s^{-1} and eventually follows the same trend as the case of gas solely created at the nucleus' surface. The other cases do not reach the maximum that would have been expected with the input parameters due to the fact that the larger grains are not lifted, so that the actual amount of grains injected in the coma is lower than the value included in the input of the code.

An increase in production rate from the nucleus increases the drag force that the gas exert on the icy grains leading to higher expansion velocities for each grain size with 10 microns particles almost reaching speeds 50 $m.s^{-1}$ when the gas production rate from the nucleus is 5×10^{28} s^{-1} (Figure 6.1). Higher velocities result in larger maximum distances reached by the grains for a given size (which fully defines the lifetime as long as the heliocentric distance is fixed) with values of a few kilometers when the nucleus gas production rate is 5×10^{26} s^{-1} to a few hundred of kilometers for a nucleus production rate 100 times larger (5×10^{28} s^{-1}). The grain number densities clearly depend on the mass that is injected at the surface of the nucleus.

In all cases, the coma is warmer and the water molecules are slower when water is released through sublimation icy grains than the corresponding cases with water only produced by the nucleus. Finally, the number density profile is somehow less steep than in the

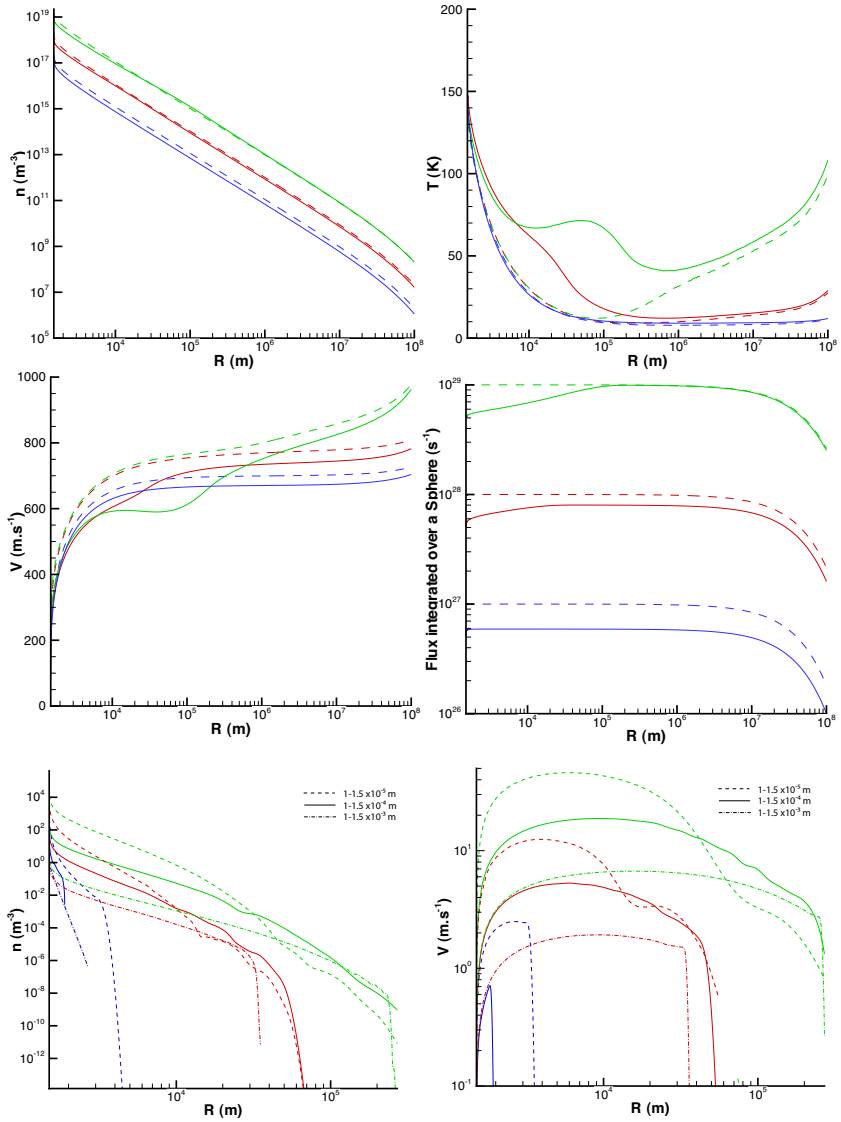

Figure 6.1: The four top panels represent temperature, velocity, number density, and flux integrated over a sphere of water molecules for cases with water production rates from the nucleus of 5×10^{26} s^{-1} (blue), 5×10^{27} s^{-1} (red), and 5×10^{28} s^{-1} (green) with a "dirty" grain to water mass ratio of 1:1 with a size distribution of -3.5 at 1 AU in solid lines, compared with cases at the same heliocentric distance with water solely released from the nucleus with production rates of 10^{27} s^{-1} (dashed blue), 10^{28} s^{-1} (dashed red), and 10^{29} s^{-1} (dashed green). The two bottom plots are the grain number density and velocity with radii between 1-1.5$\times10^{-5}$ (dashed line), 1-1.5$\times10^{-4}$ (solid line), and 1-1.5$\times10^{-3}$ (dot-dashed line) for the cases with icy grains.

case of water produced only by the nucleus. The icy grains constitute an extended source of warm gas that heats up the coma up to large distances from the nucleus.

Similarly, Figure 6.2 illustrates direct DSMC outputs for cases with a water production rate of 5×10^{27} s^{-1} with a "dirty" grain to water mass release ratio of 1:1 with a grain size distribution of -3.5 compared with cases with water only released from the nucleus with a production rate of 10^{28} s^{-1} at heliocentric distances of 1.0 AU, 1.5 AU and 2.0 AU. By fixing the production rate from the nucleus, we ensure that the same amount of icy grains is released in the coma and will eventually sublimate to contribute to the water coma. The variation in heliocentric distance changes the lifetime of water with respect to photodissociation and the sublimation rate due to the amount of radiation that reaches each grain (Patashnick et al. 1975, Lien 1990, Beer et al. 2006) following the model from Lien 1990.

The grain lifetime for a given size is increased by about a factor 5 between 1 and 2 AU (Beer et al. 2006) so that the ice particles reach a distance of about 400 km at 2 AU for only approximately 70 km at 1 AU. The water flux integrated over a sphere clearly shows that it reaches a plateau at larger distances from the nucleus with increasing heliocentric distance (approximately 30 km at 1 AU compared to about 300 km at 2 AU), which is due to the lower sublimation rate of the icy grains at larger heliocentric distances. Eventually, photodissociation plays a critical role in the water flux imposing a fast decay that starts closer to the nucleus when closer to the Sun.

Water particles released by icy grains clearly take longer to impact the water coma at larger heliocentric distances than close to the Sun due to lower sublimation rates, with the 2 AU case starting by following the trend of a case with water only released from the nucleus before slowly diverging from it at a few kilometers from the nucleus. Then, for the first time, the water molecules are faster at 2 AU than at 1.5 and 1 AU, but then the particles' velocity starts to decrease at about 10 km reaching a minimum at approximately 100 km while the particles at lower heliocentric distances are still accelerating (with a small inflection at 1.5 AU). In the same time, the gas temperature follows the opposite trend by starting to increase at 10 km to reach a maximum at about 100 km where it

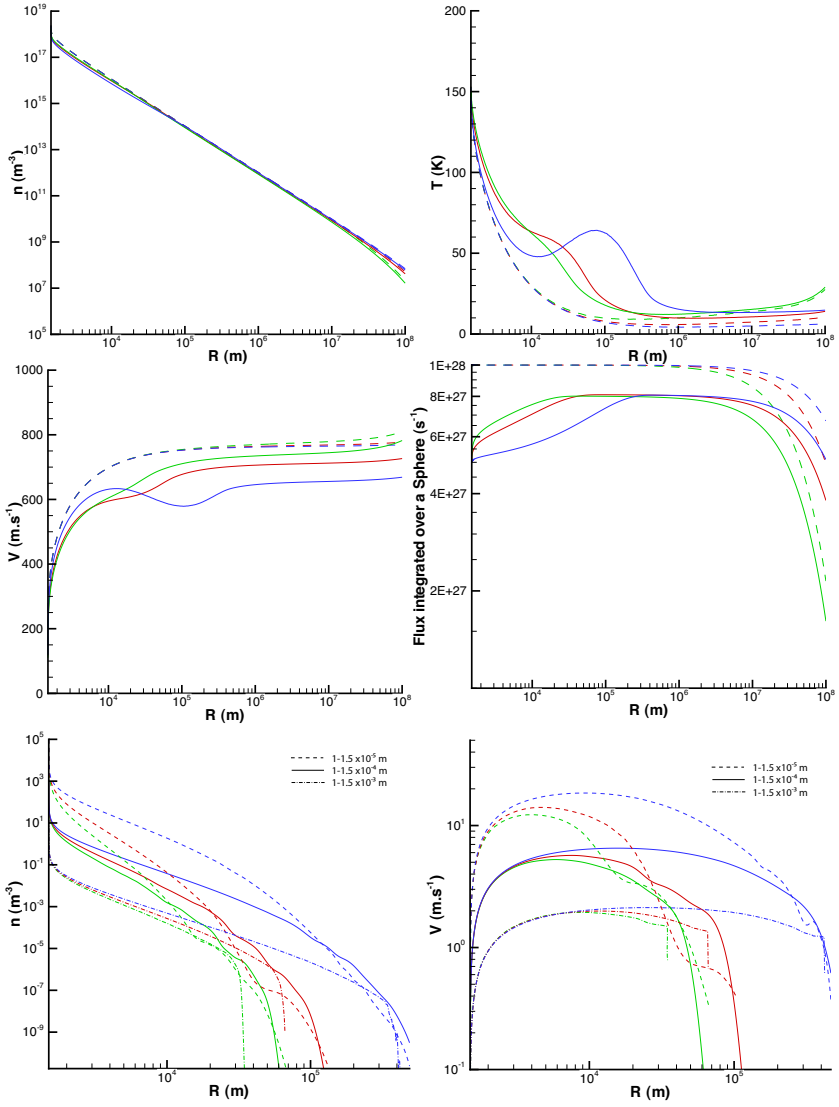

Figure 6.2: The four top panels represent temperature, velocity, number density, and flux integrated of water molecules over a sphere for cases with a water production rate from the nucleus of 5×10^{27} s^{-1} (solid lines) with a "dirty" grain to water mass release ratio of 1:1 with a grain size distribution of -3.5 compared with cases with water only released from the nucleus with with a production rate of 10^{28} s^{-1} (dashed lines) at heliocentric distances of 1.0 AU (green), 1.5 AU (red) and 2.0 AU (blue). The two bottom plots are the grain number density and velocity with radii between 1-1.5$\times10^{-5}$ (dashed line), 1-1.5$\times10^{-4}$ (solid line), and 1-1.5$\times10^{-3}$ (dot-dashed line) for the cases with icy grains.

becomes warmer than at small heliocentric distances suggesting that the contribution of the icy grain to the water coma is maximum at 100 km at 2 AU. Then, the gas particles cool down until collisions with daughter species become important enough to increase the temperature similarly to cases with water only produced by the nucleus.

6.1.2 The Grain Parameters' Impacts on the Coma

The water coma is directly impacted by the grain gas source. Then, the grain parameters such as the size distribution, the grain amount with respect to water, and the nature of the grains drives the way the grain source behaves in the coma.

The size distribution describes the relative amount of large and small grains that are injected in the coma. Since the sublimation rate and the grain dynamics depend on the particle size, the amount of water molecules released at a given location by the grain source varies with grain size distribution. To illustrate this impact, Figure 6.3 shows two runs with a nucleus water production rate of 5×10^{27} s^{-1} with a "dirty" grain to water mass release ratio of 1:1 with grain size distributions of -2.7 and -3.5 at 1 AU, and a reference case without grain sublimation with a water production rate of 10^{28} s^{-1} at the same heliocentric distance. The flux integrated over a sphere clearly shows that less mass is included in the system in the -2.7 case than in the -3.5 case due to the fact that the distribution puts more weight on the large particles that are actually not lifted. With a less steep distribution, the particle velocity and temperature respectively increase and decrease faster with distance from the nucleus showing the delayed impact of the grain source on the water coma due to the less numerous small particles that fully sublimate almost immediately, then eventually reach the same values as in the steeper distribution case at about 30 km.

Similarly, the relative amount of icy grains in the coma with respect to the outgassing from the nucleus drives the grain contribution to the total coma. This is illustrated by Figure 6.4 where the relative amount of ice with respect to the gas produced by the nucleus is 1:1 and 0.5:1 where the sum of the input parameters leads to a total gas production rate of 10^{28} s^{-1}.

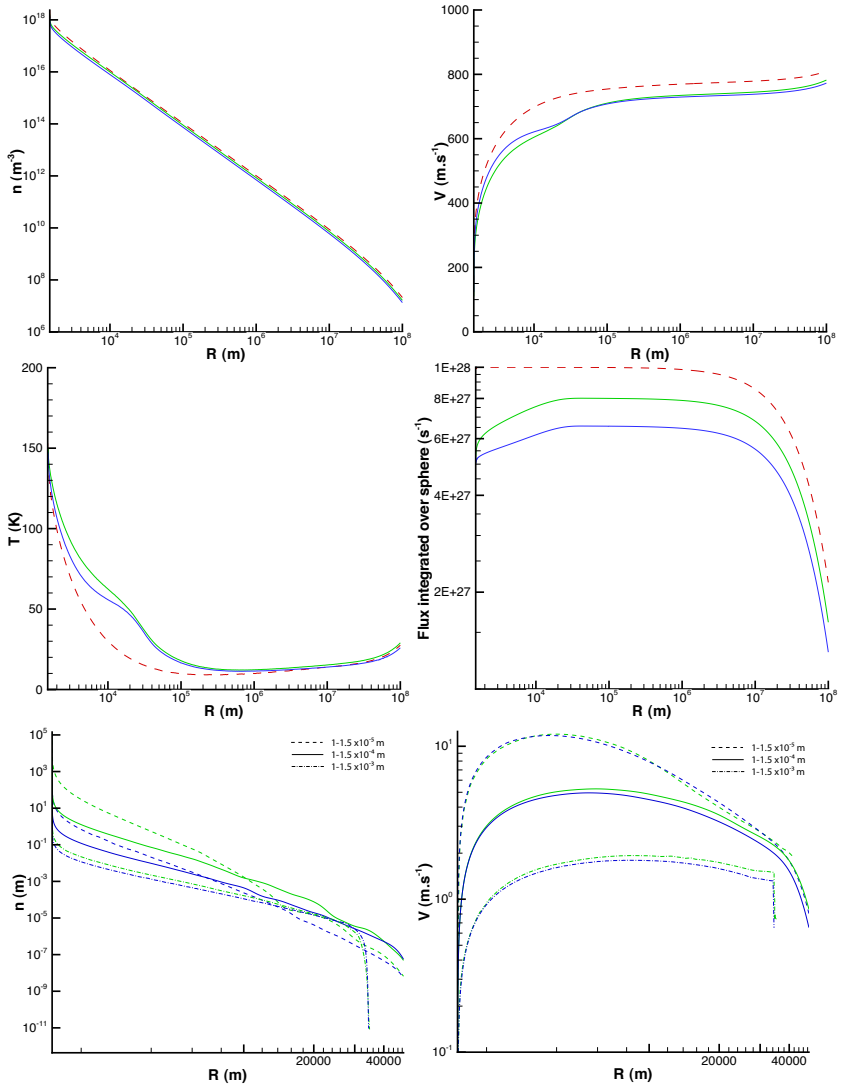

Figure 6.3: Temperature, velocity, number density, and flux integrated of water molecules over a sphere for cases with a nucleus water production rate of 5×10^{27} s^{-1} (solid lines) with a "dirty" grain to water mass release ratio of 1:1 with a grain size distributions of -2.7 (blue) and -3.5 (green) at 1 AU compared with a case with water only released from the nucleus with with a production rate of 10^{28} s^{-1} (red dashed line) at a heliocentric distance of 1 AU. The two bottom plots are the grain number density and velocity with radii between 1-1.5$\times10^{-5}$ (dashed line), 1-1.5$\times10^{-4}$ (solid line), and 1-1.5$\times10^{-3}$ (dot-dashed line) for the cases with icy grains.

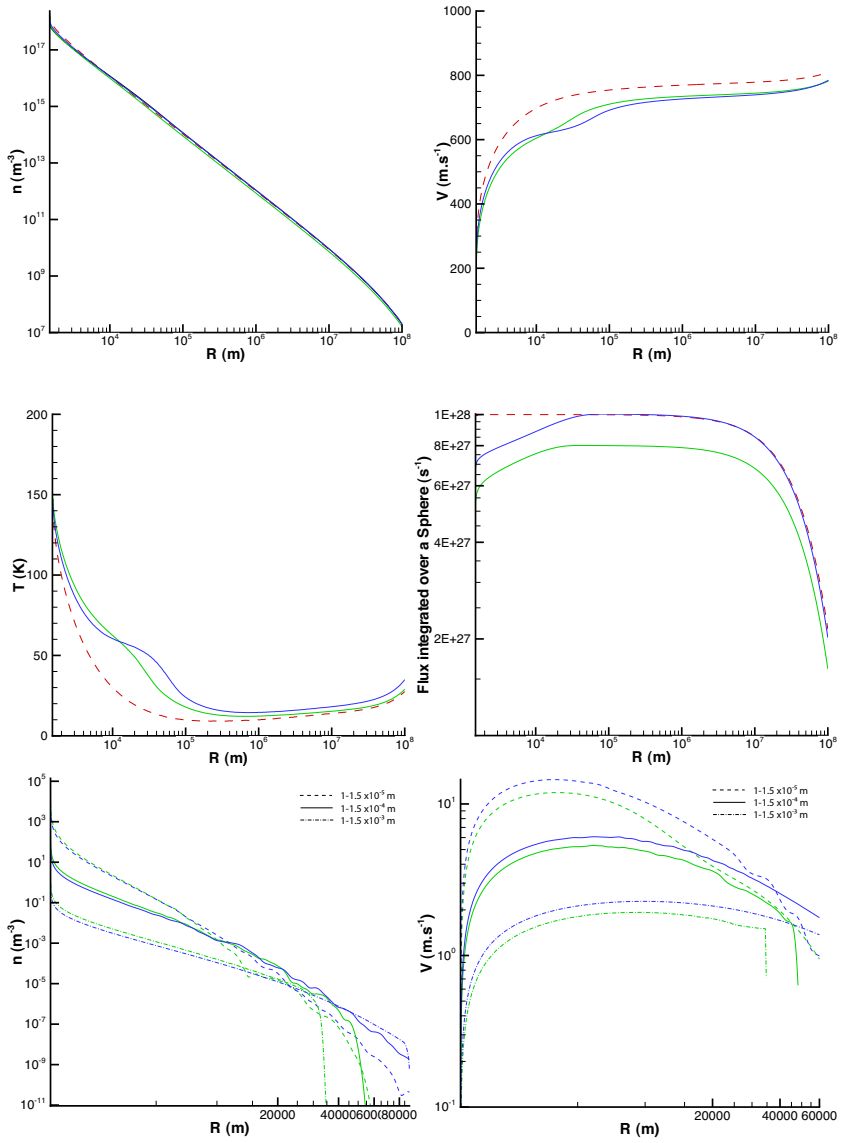

Figure 6.4: The four top panels represent temperature, velocity, number density, and flux integrated of water molecules over a sphere for cases with a nucleus water production rate of 5×10^{27} s^{-1} with a "dirty" grain to water mass release ratio of 1:1(green solid) and a case with a nucleus production rate of 6.67×10^{27} s^{-1} with a "dirty" grain to water mass release ratio of 0.5:1(blue solid) with a grain size distributions -3.5 at 1 AU, compared with a case with water only released from the nucleus with with a production rate of 10^{28} s^{-1} (red dashed line) at a heliocentric distance of 1 AU. The two bottom plots are the grain number density and velocity with radii between 1-1.5$\times10^{-5}$ (dashed line), 1-1.5$\times10^{-4}$ (solid line), and 1-1.5$\times10^{-3}$ (dot-dashed line) for the cases with icy grains.

Finally, as explained in section 3.3, the nature of the grains, that is to say if the grains are pure or dirty (with refractories), is of critical importance in order to derive the lifetime of the grain due to the absorption of solar radiation in the visible by the refractory components (Figure 6.4). Pure icy grains live much longer than dirty icy grains and then expand to larger cometocentric distances (up to about 4000 km in the present case) where they release water molecules. The resulting ice and gas coma are then completely different depending on the nature of the grains chosen in the model. Dirty icy grains start to release an important amount of water relatively close to the nucleus so that the temperature and velocity of the gas clearly differ from the case with gas solely produced by the nucleus even in the very inner coma. While pure icy grains have a relatively small effect close to the nucleus, they strongly warm up and slow down the water molecules by 40 km from the nucleus to reach a local temperature maximum (respectively velocity minimum) at a distance close to 800 km from the nucleus. Eventually, the macroscopic parameters converge for the different cases with and without sublimating grains.

6.2 The Very Inner Coma of Comet 73P-B/Schwassmann-Wachmann 3

In this section, we use the fully-kinetic DSMC model to reproduce the measurements of column density and rotational temperature of water in fragment B of comet 73P/Schwassmann-Wachmann 3 (hereafter, SW3) obtained with a very high spatial resolution of $\sim$ 30 km using IRCS/Subaru in May 2006 (Bonev et al. 2008). This will show the importance of the inclusion of icy grains in cometary models in order to reproduce observations. The results presented in this section have previously been published in a paper by Fougere et al. (2012).

6.2.1 Introduction of the Observations

The ecliptic comet 73P/Schwassmann-Wachmann 3 was discovered by astronomers Arnold Schwassmann and Arno Arthur Wachmann in 1930, and is now classified as a member of Jupiter's dynamical Family of short-period Comets (JFC). It has a period of

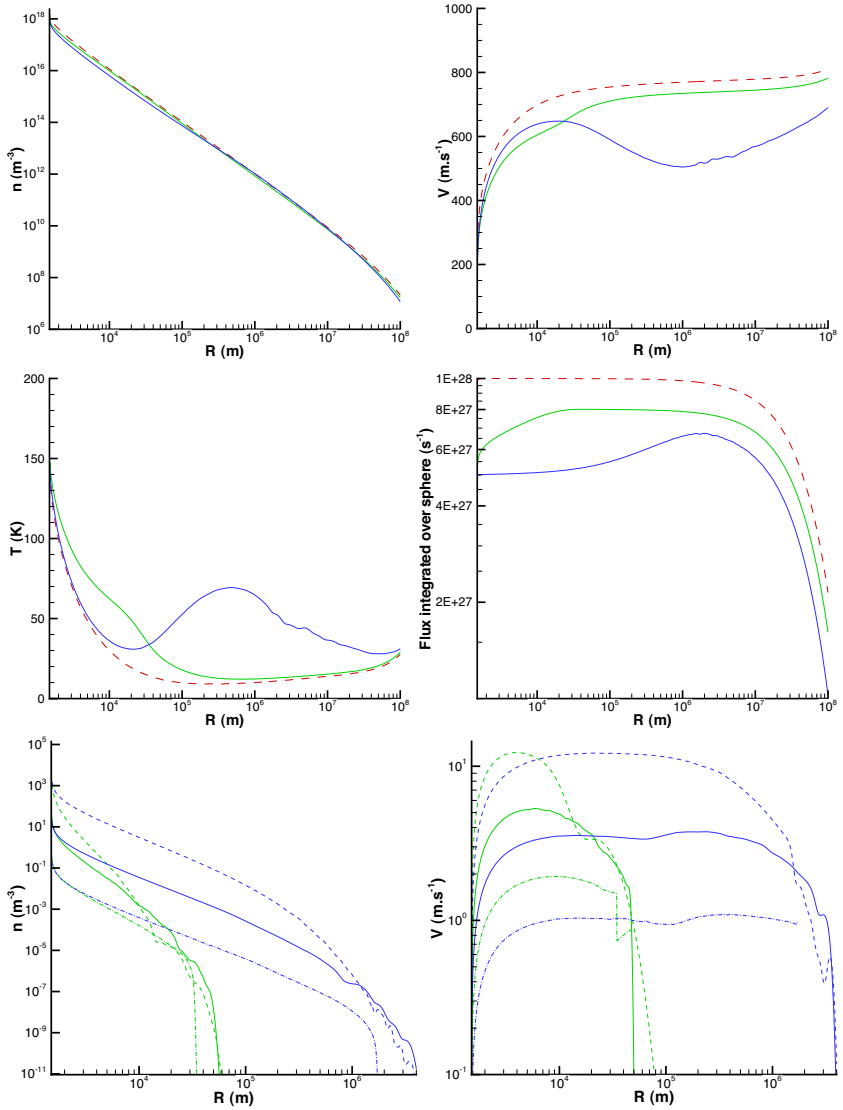

Figure 6.5: The four top panels represent temperature, velocity, number density, and flux integrated of water molecules over a sphere for cases with a nucleus water production rate of 5×10^{27} s^{-1} with a "dirty" grain to water mass release ratio of 1:1(green solid) and a case with pure icy grains (blue solid) with a grain size distributions -3.5 at 1 AU, compared with a case with water only released from the nucleus with with a production rate of 10^{28} s^{-1} (red dashed line) at a heliocentric distance of 1 AU. The two bottom plots are the grain number density and velocity with radii between 1-1.5$\times10^{-5}$ (dashed line), 1-1.5$\times10^{-4}$ (solid line), and 1-1.5$\times10^{-3}$ (dot-dashed line) for the cases with icy grains.

5.4 years, and the perihelion distance during the 2006 apparition was 0.94 AU. In 1995, SW3's nucleus fragmented into three large pieces labeled -A, -B and -C (Sekanina, 2005) more fragmentation occurred in 2001 and 2006. While the pre-breakup radius of the original nucleus was 1.3 km (Boehnhardt et al., 2002), images of fragment B in November 2001 showed that its radius was only about 0.6 km (Planetary Camera 2, Hubble Space Telescope Toth et al. 2003) and it disintegrated completely in 2006 (Weaver et al. 2006 2008). During this process of disintegration, it is most likely that grains of ice were ejected from the nucleus, and constituted an extended source of water.

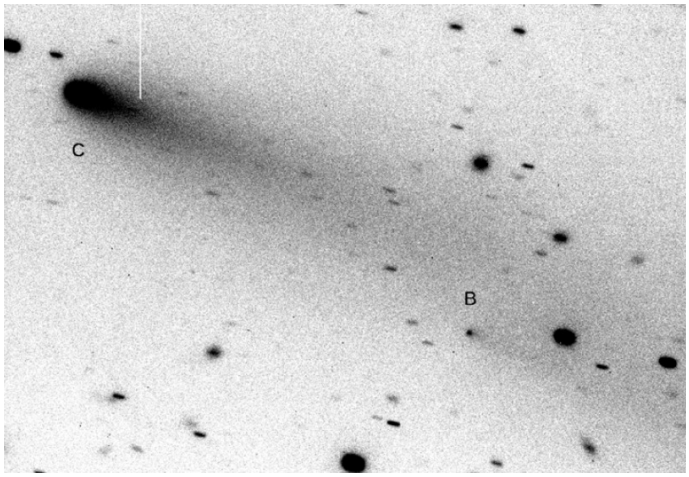

Figure 6.6: Fragments B and C of comet SW3 from observations with FORS2 at VLT through R_S filter (from Boehnhardt et al. 2002)

Villanueva et al. (2006) and Dello Russo et al. (2007) quantified the primary (parent) volatile compositions of fragments B and C using high-dispersion echelle spectroscopy at IR wavelengths. Kobayashi et al. (2007) studied primary volatiles in fragment B. The two components were similarly depleted in most forms of volatile carbon, consistent with the reported depletion in carbon-chain products ("daughter" species) (Schleicher 2006). These depletions could result from either thermal processing or cosmogony. The fact that SW3 is a fragmented comet suggests that material once stored deep in the original nucleus was likely activated after splitting. The two split components (B, C) showed remark-

ably similar compositions, supporting the latter (cosmogonic) hypothesis. A refinement of the cosmogonic hypothesis is that the depleted carbon chemistry may result from the sublimation of pre-cometary icy grains followed by gas-phase chemical changes in the protoplanetary disk before re-condensation (Mumma et al. 2001). This could explain the severe depletion of CH_3OH but smaller depletion of HCN and H_2S observed for comet C/1999 S4 (LINEAR) (Bockelée-Morvan et al. 2001, Mumma et al. 2001).

Fragment B was particularly active in 2006, providing an opportunity to investigate it in detail. Kobayashi et al. (2007) and Bonev et al. (2008) analyzed spectra acquired with IRCS/Subaru in May 2006 when the comet was at a geocentric distance of 0.074 AU. The spatial resolution was the highest ever achieved for a comet at infrared wavelengths. In three observing sequences, they detected H_2O emission lines in non-resonant fluorescence near 2.9 μm, and inferred water production rates ranging from 1.5 to 1.8 x 10^{28} s^{-1}.

Bonev et al. (2008) extracted the H_2O rotational temperatures and column densities from infrared spectra of SW3-B, averaged over different ranges of projected distances from the nucleus (Table 6.1). These measurements were based on analysis of optically-thin "hot-band" lines of H_2O detected with IRCS at Subaru telescope, atop Mauna Kea, HI (Figure 6.7 extracted from Bonev et al. 2008). In "hot-band" fluorescence, a molecule in its ground vibrational state is excited to a higher mode of vibration by absorbing a solar IR photon. This is followed by radiative decay back to an intermediate vibrational state that is not significantly populated in the Earth's atmosphere. These "hot-band" lines are the best means to directly detect H_2O from the ground. The methodology for their analysis is well established and has been tested against spectra from multiple comets (Dello Russo et al. 2004, 2005 Bonev et al. 2007, 2008, 2012 Villanueva et al. 2011 and references therein). The method is based on the fact that at the optimal rotational temperature (varied as a free parameter) the ratio of measured line flux and fluorescent g-factor is independent of rotational excitation energy. Then, as detailed in Bonev et al. (2008), the algorithm is an iterative process where for each iteration i:

- the rotational temperature $T_{rot}(i)$ is obtained for an assumed ortho-to-para ratio (OPR) value OPR(i)

- a series of fluorescence models is applied, with the rotational temperature set equal to $T_{rot}(i)$ and the OPR varied as a free parameter. The new OPR(i+1) value is obtained by minimizing the variance of the ratio of observed line flux and fluorescence g-factor for each individual line averaged over the set of observed lines <F/g($T_{rot}(i)$,OPR)>.

This process converges to an optimal and unique solution for T_{rot} and OPR.

Sample bounds (km, km)	FoV (km x km)	T_{rot} (K)	Column Density (10^{19} m^{-2})
$[-33.6, -19.0]$	14.6 x 14.5	100 ± 2	23.6 ± 0.99
$[-19.0, -7.3]$	11.7 x 14.5	113 ± 2	38.9 ± 1.53
$[-7.3, 7.3]$	14.6 x 14.5	110 ± 1	44.9 ± 1.85
$[7.3, 19.0]$	11.7 x 14.5	101 ± 2	31.8 ± 1.59
$[19.0, 33.6]$	14.6 x 14.5	92 ± 2	19.4 ± 0.95

Table 6.1: Physical parameters retrieved for water vapor in SW3-B

Bonev et al. (2008) quantified ortho-to-para ratios (OPR) and rotational temperatures at several distances from the nucleus, projected on the sky plane. The OPR measurements were consistent with the statistical equilibrium value of 3.0, implying a nuclear spin temperature higher than $\sim$ 45K. Bonev et al. (2008) found no compelling evidence of OPR change in the coma with increasing distance from the nucleus. The rotational temperature decreased from $\sim$ 110K to $\sim$ 90K as the field-of-view changed from being nucleus-centered to being centered $\sim$ 30 km from the nucleus, which is substantially slower than predicted if water vapor is released solely from the nucleus. The Subaru observations reveal the behavior of water molecules in the very innermost coma where collisions control the water rotational temperature (Bockelée-Morvan 1987). The summed signal of all detected water lines formed an intensity spatial profile with high signal-to-noise ratio. Since the intensity is proportional to the column density (Schultz et al. 1993), this profile reveals

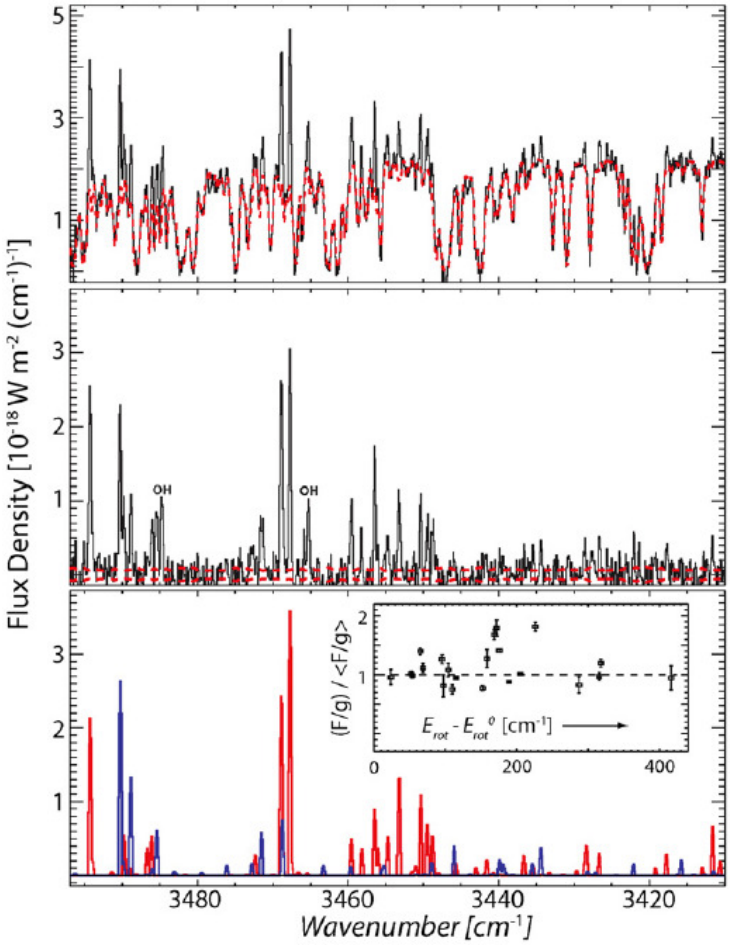

Figure 6.7: H_2O non-resonant fluorescent emission from the inner coma of SW3. The top panel shows the measured cometary spectrum and the best-fit terrestrial atmospheric transmittance model convolved to the instrumental resolution and normalized to the mean continuum intensity of the comet data. The middle panel shows the residual spectra after removing telluric absorption. The bottom panel shows modeled H_2O spectra with transitions of ortho-H_2O and para-H_2O in red and blue, respectively. Extracted from Bonev et al. (2008).

the variation of water column density with projected distance from the nucleus. Water column density decreased from $\sim$ 4.5 x 10^{20} m^{-2} to about $\sim$ 2 x 10^{20} m^{-2} as the field-of-view moved from nucleus-centered to about $\sim$ 30 km off the nucleus. These values are affected by atmospheric seeing, but the decrease in water column density remains slower than the $1/\rho$ decrease predicted by a model with water vapor released solely from the nucleus.

6.2.2 The DSMC Cometary Model of Fragment B of Comet 73P/Schwassmann-Wachmann 3

The DSMC approach was applied to model the rotational temperature and column density profiles of comet SW3-B, and the results are compared with those retrieved from IRCS/Subaru infrared spectra (Bonev et al. 2008). A first attempt using a 1D model with direct sublimation from the nucleus and a surface temperature of 180 K, which is of the same order of the sublimation temperature of water. SW3-B was assumed to have a spherical nucleus of 0.6 km of radius at a heliocentric distance of 1.027 AU releasing 1.6×10^{28} s^{-1} of H_2O with 5% of CO and 5% of CO_2. A first analysis will show (see next subsection) that, within a few tens of kilometers from the nucleus, the measurements indicate that the rotational temperatures of water molecules are much larger than those predicted by almost all coma models (Gombosi et al. 1986, Combi 1996, Crifo 1995, Tenishev et al. 2008). Moreoever, the column density profile suggests the presence of an extended source, whose existence is also suggested by the ongoing disintegration process of the nucleus. Indeed, it is most likely that particles of ice are released from the nucleus, and their sublimation then introduces an extended source of water molecules in SW3's coma. HST optical images of SW3-B show many sub-nuclei, each of which is a mini comet with an individual comae (Weaver et al., 2008).

It is then imperative to create a model of comet SW3-B including an extended source of sublimating icy grains. Due to the larger number of free parameters and the complexity of the problem, we decided to limit this study to a 1D problem. DSMC calculations with sublimating icy grains were performed for different cases with a total gas production rate of

1.6×10^{28} s^{-1} assuming a spherical nucleus with radius 0.6 km for SW3-B at a heliocentric distance of 1.027 AU. We used spherical grains with a power-law size distribution, which was approximated by 30 size bins. The minimum grain size was chosen to be 1 μm, which is consistent with the recent measurements of icy grains in comet 103P/Hartley 2 (A'Hearn et al. 2011), and the maximum size was taken to be the largest grain that can be lifted from the nucleus by the sublimating gas. This guarantees that all the mass that was injected into the system is lifted and eventually contributes to the water coma. Pure and dirty icy grains were considered using the modeled from Patashnick et al. (1975) and Lien et al. (1990), respectively, detailed in section 3.3. The different parameters used in the different DSMC models of comet SW3-B are summarized in Table 6.2.

Composition: 90% H_2O, 5% CO, and 5% CO_2
Photodecomposition of H_2O to OH, H_2, H, and O
Nucleus density: 300 $kg.m^{-3}$
Grain minimum size: a_m=10^{-6} m
Grain maximum size: a_M=6.62×10^{-2} m for 2:1, 3.95×10^{-2} m for 4:1, 2.45×10^{-2} m for 6:1, and 1.32×10^{-2} m for 8:1
Grain size distribution: $Z(a) \propto a^{-n}$, n varying from 2.7 to 4.5 (Jockers 1997)
Heliocentric distance: 1.027 AU
Total water production rate (nucleus + grains): 1.6×10^{28} s^{-1}
Global regime: $r = 0.6$km to $r = 10^6$km

Table 6.2: DSMC model parameters and assumptions for comet SW3-B

6.2.3 Retrieved Rotational Temperature and Column Density Affected by Atmospheric Seeing Effect

Bonev et al. (2008) extracted rotational temperatures at offset positions on both sides of the nucleus. However, in this first application of our one-dimensional spherically symmetric model to interpreting near IR observations, we arbitrarily decided to focus on three

projected distance ranges: [-7.3 km, 7.3 km], [7.3 km, 19.0 km], and [19.0 km, 33.6 km]. We refer to these as the close, medium, and far range, respectively. Within these regions, the rotational excitation of water is controlled by collisions (Bockelée-Morvan 1987) fully justifying the use of the Borgnakke-Larsen model included in the AMPS code to derive the water rotational temperature.

While the rotational temperature is expected to vary within each field of view, the value derived from "hot-band" spectra represents the mean of rotational temperatures at points along the line of sight, weighted by the relative molecular number density at each point:

$$\overline{T_{rot}} = \frac{\iint T_{rot}(r)n(r)dld\rho}{\iint n(r)dld\rho} \tag{6.1}$$

where $r^2 = \sqrt{l^2 + \rho^2}$, l is along the line of sight and ρ the projected distance, $T_{rot}(r)$ and $n(r)$ are the rotational temperature and number density in r, respectively. Each molecular species is treated independently in the data reductions, and their comparison then provides additional information on the coma physics.

However, ground-based measurements are affected by the Earth's atmosphere. Indeed, atmospheric 'seeing' mixes (distorts) the flux, i.e., part of the flux observed in each field of view originates in a coma region outside the aperture and, in addition, some of the flux originating within the field of view is lost. The Earth's atmospheric seeing effect can be simulated using a point spread function (PSF) which describes the response of the imaging system to a point source. We used the PSF measured from the flux of a standard star observed at a time close to the comet observation. The stellar profile was fitted with a linear combination of a Gaussian distribution and a quadratic term. This approximates the stellar PSF relatively well, especially since the exact functional form of the fit has only a weak influence on the estimated FWHM of the profile. Eight individual PSF measurements varied between 0.33" and 0.39" (FWHM), which agrees with the measurement reported by Kobayashi et al. (2007).

In addition to atmospheric seeing, inaccuracies in comet (non-sidereal) tracking are also a potential source of flux "mixing". We refer to the combined effect of atmospheric seeing and (potential) tracking issue as "effective seeing". Comet drift along the entrance slit has been corrected using a well-established registration procedure as described in Bonev (2005, pp. 263-267). In addition, we use the continuum emission profile from the comet as a firm upper limit of the "effective seeing". We emphasize this is strictly an upper bound because, while the shape of the continuum profile is affected by non-sidereal tracking and atmospheric seeing, the source of continuum radiation is not a point.

Figure 6.8 shows the measured profiles of both PSF and continuum. We first used the PSF profile to convolve with our predicted column densities and temperatures (see next paragraph). A similar convolution of our calculations with the continuum profile (instead of the PSF) in order to estimate an upper bound of the uncertainty caused by effective seeing showed a relatively small variation in the output results not affecting in any way the conclusions from this section. The PSF is one-dimensional and is measured along the spectrometer entrance aperture (the 'slit'). Since atmospheric seeing affects both directions, along and across the slit, we assumed the PSF across the slit width is equal to the one measured along the slit. This is a relatively good approximation when the standard star is well centered during its observation. The column densities affected by atmospheric seeing are computed by convolving the modeled column density and the PSF:

$$N_{conv}(\rho, x) = \iint N^{mod}(\rho - \rho', x - x')PSF(\rho', x')d\rho' dx' \tag{6.2}$$

where N_{conv} is the column density taking into account the atmospheric seeing, and N^{mod} is the modeled column density. Then, we average the values over each field of view to compare them to the measurements.

The rotational temperature is found as follows:

$$T_{rot} = \frac{\iint T_{rot}^{mod}(\rho, x)N_{conv}(\rho, x)dld\rho}{\iint N_{conv}(\rho, x)dld\rho} \tag{6.3}$$

where T_{rot} is the retrieved rotational temperature affected by the atmospheric seeing and

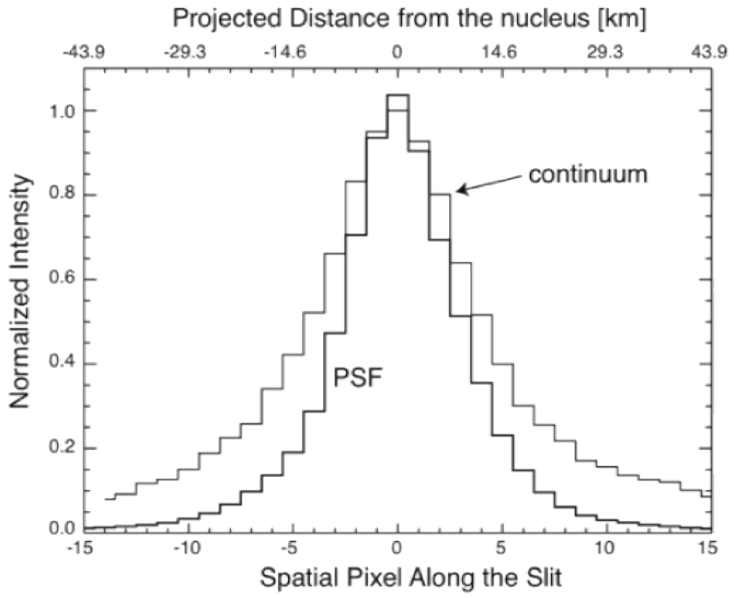

Figure 6.8: The measured point spread function (PSF) of the stellar profile (FWHM $\sim$ 0.35") and the continuum emission profile from the comet. The PSF includes the effects of atmospheric seeing only. The continuum profile provides a firm upper limit for the combined effects of atmospheric seeing and possible inaccuracies in the non-sidereal tracking. The resolution of the measurements was $\sim$ 0.055 arcsec/pixel ($\sim$ 2.9 km/pixel). These profiles were provided by our observer-collaborator Dr. Boncho Bonev.

T_{rot}^{mod} the modeled rotational temperature.

We computed a complete DSMC spherically symmetric coma model from the surface of the nucleus to 10^6 km with a water production rate of 1.6×10^{28} with 5% of CO and 5% of CO_2 as described in the previous section. Figure 6.9 shows the direct DSMC output for the SW3-B model for H_2O number density, temperature, and velocity. The water density starts at about 10^{19} m^{-3} close to the nucleus and decreases in a monotonic fashion while the velocity of the H_2O particles increases to reach a maximum value of about 750 m.s^{-1} at less than a hundred kilometers from the nucleus. The rotational temperature follows a similar trend as the kinetic temperature with a slow decrease to eventually be close to zero.

Then, we computed the different line-of-sight integrals (6.1), (6.2), and (6.3) with distance from the surface in the range of 0 to 50 km and averaged over the same projected slit areas as in the observations of Bonev et al. (2008). A model with release of water solely from the nucleus reveals water rotational temperatures which are much lower than those of the observations ($\sim$ 80-90 K) and a column density profile which decreases faster than the one measured (Figure 6.10). This behavior suggests that an additional effect is needed to match the observations. We next explored two such effects:

- sublimation from icy grains in the near-nucleus coma
- electron-molecule collisions.

The two free parameters regarding the icy grains in our model are the purity of the grains and their size distribution. Figures 6.11 and 6.12 show direct outputs for the water rotational temperature and velocity from the DSMC calculations with icy grains (before seeing correction). Rotational and kinetic temperature profiles are nearly identical in the region where rotational transitions are controlled by collisions (out to $\sim$ 500-1000 km from the nucleus). Then, when collisions become negligible, all water molecules do not have the exact same radial velocity, so the kinetic temperature remains constant at the temperature corresponding to this residual radial velocity range while the rotational temperature eventually decreases to zero due to radiative cooling (our model does not include

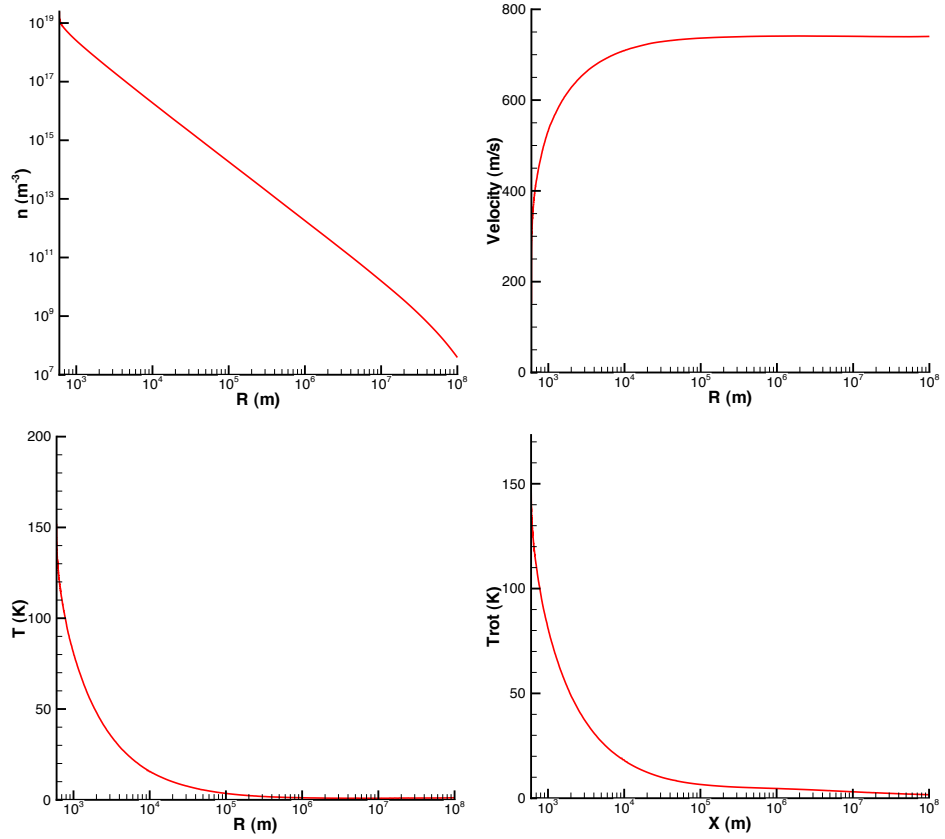

Figure 6.9: H_2O DSMC output for a model with the nucleus as solely source of water with a water production rate of 1.6×10^{28} with 5% of CO and 5% of CO_2 at 1.027 AU.

radiative pumping). Within $\sim$ 100 km from the nucleus for dirty icy grains and $\sim$ 300 km for pure icy grains, the thermodynamics of the coma strongly depends on the amount of icy grains injected. Water particles produced locally by sublimation of the icy grains are warmer than those that were released originally from the nucleus but would have cooled adiabatically through expansion as shown in the previous section dedicated to the thermodynamics of the coma with the presence of sublimating icy grains. Thus, the rotational

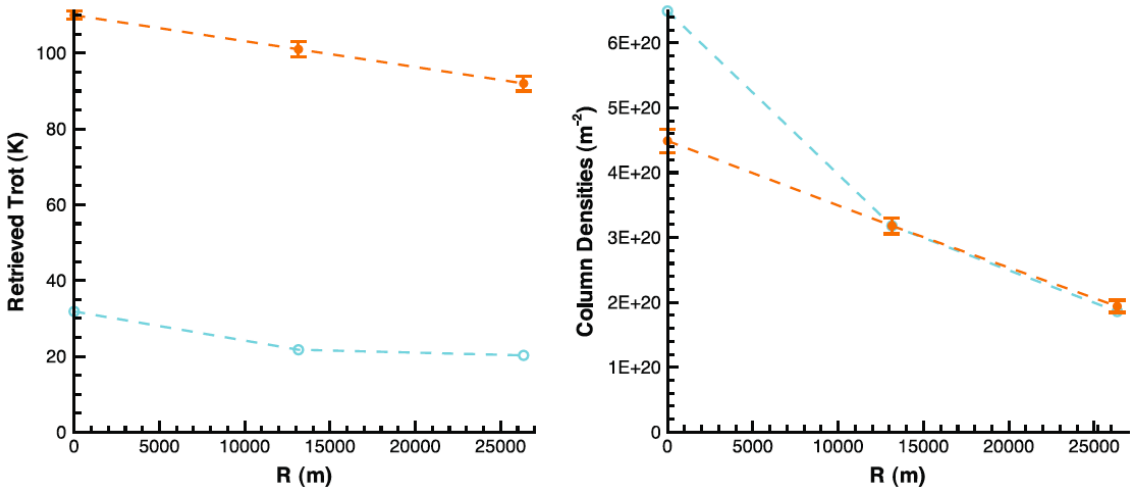

Figure 6.10: Rotational temperature and column density at the center of the field of view affected by seeing correction in function of distance from the nucleus for a model where the only source of sublimating water is the nucleus (blue circles). The orange circles represent the observations of Bonev et al (2008). The lines are visual aids for the reader and are not representative of the value of the rotational temperature at these distances between the data points.

temperature increases as the fraction of water production from grains increases (relative to nucleus release). This effect also results in somewhat lower velocities for cases with a higher fraction of icy grains.

We employed a range of size distribution exponents (-2.7 to -4.5) for both pure and dirty icy grains (Figures 6.13 and 6.14). This range spans the typical grain size distributions observed in comets (Jockers 1997). For a power law index (-a) with a>4 (e.g., -a=-6), the grain particles' mass resides in the small particles, while for indices a<4 (e.g., -a=-2), the large particles constitute most of the grains' mass. In the case of dirty icy grains, the modeled water column densities become "flatter" as the distribution exponent decreases in magnitude. At the same time the rotational temperature decays more slowly, and for very small values such as -2.7 an increase can result. Both effects arise from the long lifetimes of large grains in the coma, which allow them to contribute a source of water at large

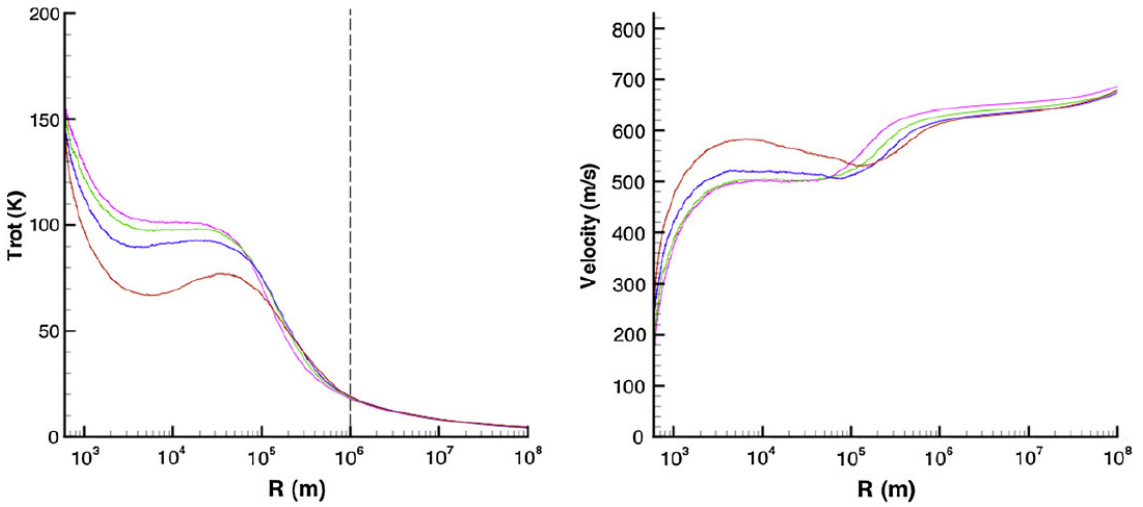

Figure 6.11: Outputs of the DSMC calculation water rotational temperature (left) and velocity (right) for a case with dirty icy grains with a size distribution exponent of -3.8 for different grain to water from the nucleus mass production rates: 2:1 (red), 4:1 (dark blue), 6:1 (green), and 8:1 (magenta). The dashed line is the approximate distance above which fluorescence effects become predominant in the coma.

distances from the nucleus. The opposite variation is observed for pure icy grains. Since they live longer and sublimate farther away from the nucleus, only small grains constitute an important source of water molecules in the very inner coma. Thus, the inner coma is more affected by grain distributions where the particles' mass mostly resides in the small particles (exponent indices with a>4). The results show that the column densities are best reproduced for distribution exponents of -3.8 and -3.9 for dirty icy grains (see details in Table 6.3), and between -4.3 and -4.5 for pure icy grains.

At the same time, the modeled rotational temperature shows a decrease similar to the measurements (Figure 6.15). However, even with dirty icy grains, the modeled rotational temperature is lower than the observed value by $\sim$ 10K for mass production rate ratios of 6:1 (grain: water from the nucleus) and 8:1, by $\sim$ 15K for a mass production rate ratio of

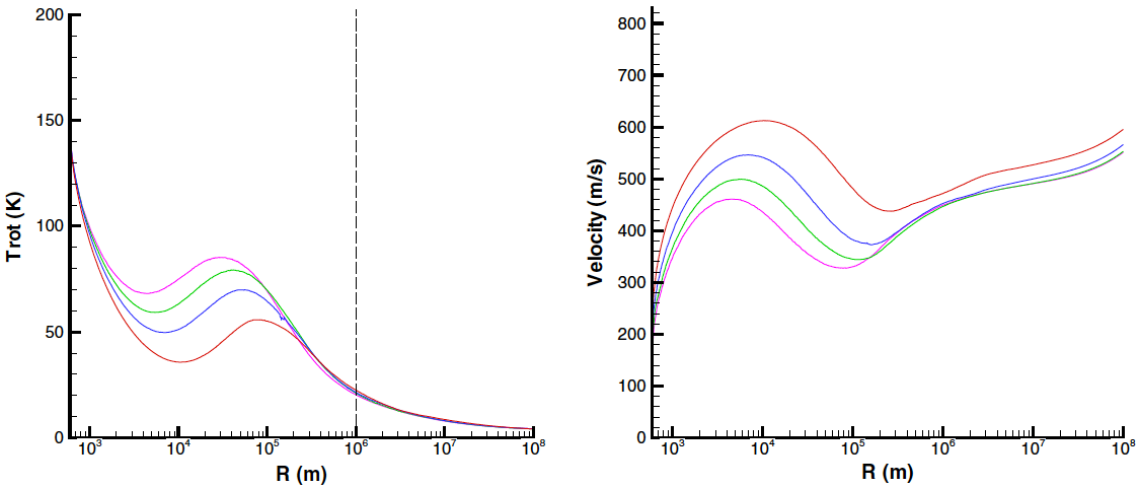

Figure 6.12: Outputs of the DSMC calculation water rotational temperature (left) and velocity (right) for a case with pure icy grains with a size distribution exponent of -3.8 for different grain to water from the nucleus mass production rates: 2:1 (red), 4:1 (dark blue), 6:1 (green), and 8:1 (magenta). The dashed line is the approximate distance above which fluorescence effects become predominant in the coma.

Range (km)	Average column densities (m^{-2})		
	Nucleus only	Case described	Observations
$[-7.3, 7.3]$	6.49×10^{20}	4.43×10^{20}	4.49×10^{20}
$[7.3, 19.0]$	3.18×10^{20}	3.18×10^{20}	3.18×10^{20}
$[19.0, 33.7]$	1.86×10^{20}	2.03×10^{20}	1.94×10^{20}

Table 6.3: Column densities for a case with a grain to water production ratio of 8 and a grain distribution exponent of -3.8 using dirty icy grains, compared to a model with nucleus source only and to the observations (Bonev et al. 2008).

4:1, and by $\sim$ 30K for a mass production rate ratio of 2:1. These modeled temperatures are in much better agreement with the measurements than are the best results that we could obtain using models where water is released solely from the nucleus. It also suggests that another possible phenomenon could play a significant role in controlling the rotational temperature of water in the very innermost coma.

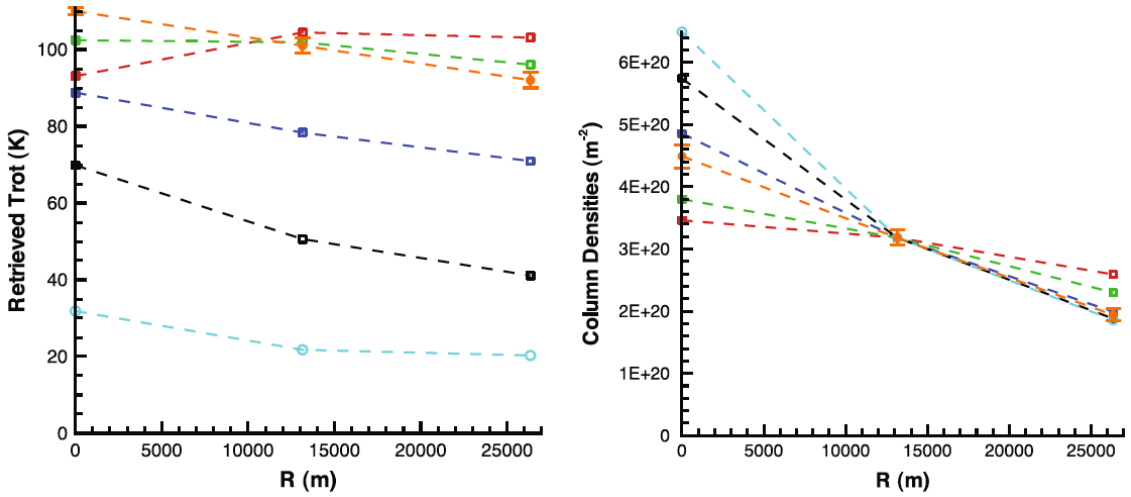

Figure 6.13: Rotational temperature and column density for water vs. distance from the nucleus, for cases with dirty icy grains and a grain to water from the nucleus mass production rate ratio of 6:1(grains:water from the nucleus). We show results for models with size distribution exponents of: -2.7 (red squares), -3.5 (green squares), -4.0 (dark blue squares), and -4.5 (black squares). The Bonev et al. (2008) observations are shown by the orange circles. The teal blue circles represent the model results where the only source of water is the nucleus. The production rate is set (arbitrarily) to exactly reproduce the middle of the three column density measurements, which is why all models go exactly through that point.

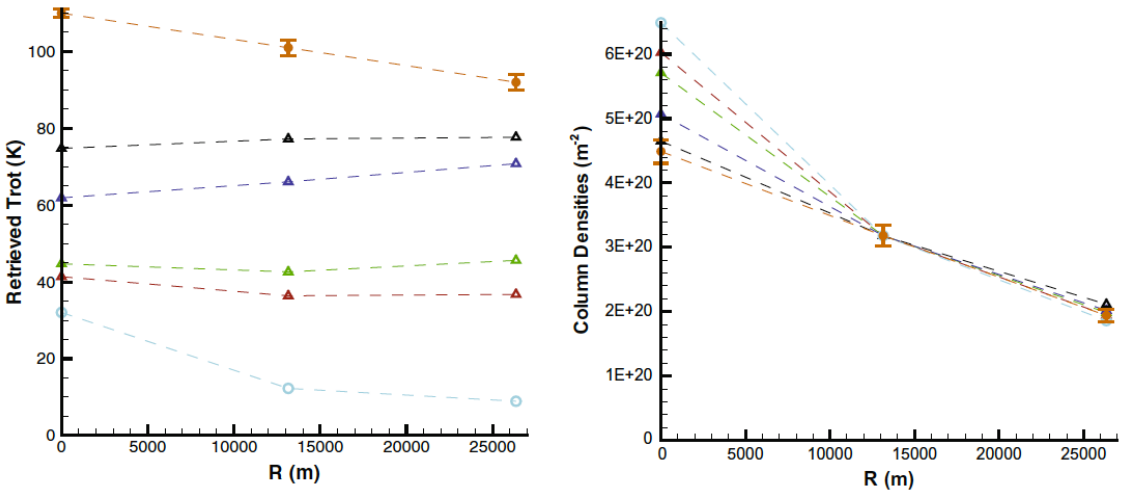

Figure 6.14: Rotational temperature and column density for water vs. distance from the nucleus, for cases with pure icy grains and a grain to water from the nucleus mass production rate ratio of 6:1(grains:water from the nucleus). We show results for models with size distribution exponents of: -2.7 (red squares), -3.5 (green squares), -4.0 (dark blue squares), and -4.5 (black squares). The Bonev et al. (2008) observations are shown by the orange circles. The teal blue circles represent the model results where the only source of water is the nucleus. The production rate is set (arbitrarily) to exactly reproduce the middle of the three column density measurements, which is why all models go exactly through that point.

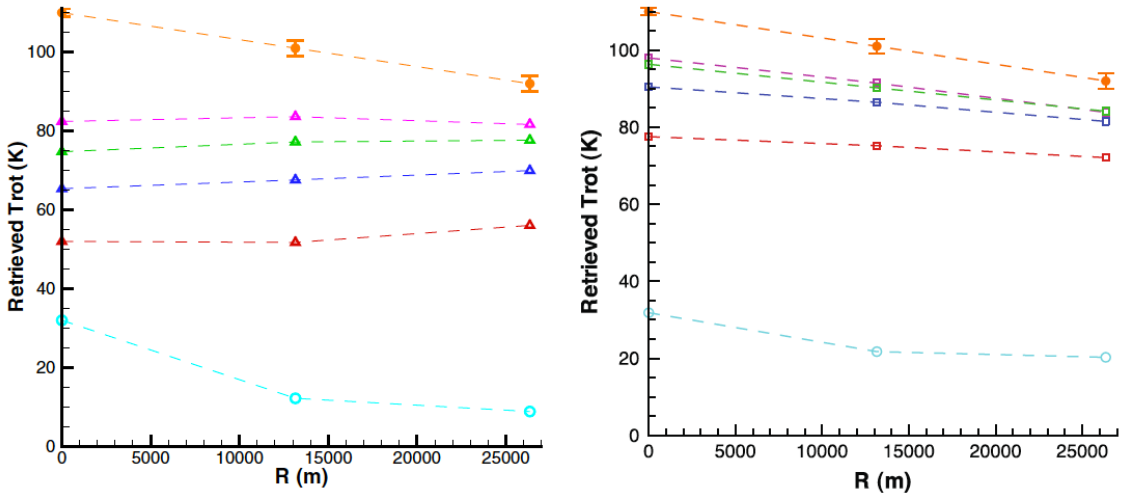

Figure 6.15: The modeled rotational temperature for cases with pure icy grains (left) and dirty icy grains (right). We show results for models with grain to water from the nucleus mass production rate ratios: 2:1 (red symbols), 4:1 (dark blue symbols), 6:1 (green symbols) and 8:1 (magenta symbols) for distribution exponents of -4.5 for pure grains and -3.8 for dirty ones. The Bonev et al. (2008) observations are shown by the orange circles. The teal blue circles represent the best fit when nuclear release is the sole source of water molecules in the coma.

In our model, the icy grains provide a second source of water in the coma. Thus, each water molecule in the coma can come either from the nucleus or the grains. The code enables us to distinguish between the two sources for each water molecule. Figure 6.16 shows the number density of H_2O as a function of distance from the nucleus, for each source, for the case with mass production rates in the ratio 6:1 (grain:water from the nucleus) within 100 km and 10^5 km. It appears that in the case presented here, the water that was released from sublimation of icy grains exceeds the one from the nucleus at a distance of about 2 nucleus radii. Then, the ratio from the contribution of the grains with respect to the nucleus increases up to a maximum of about 6 until a few 100 of kilometers, which is consistent with the input parameters. Finally, due to photochemistry, molecules from both sources are dissociated.

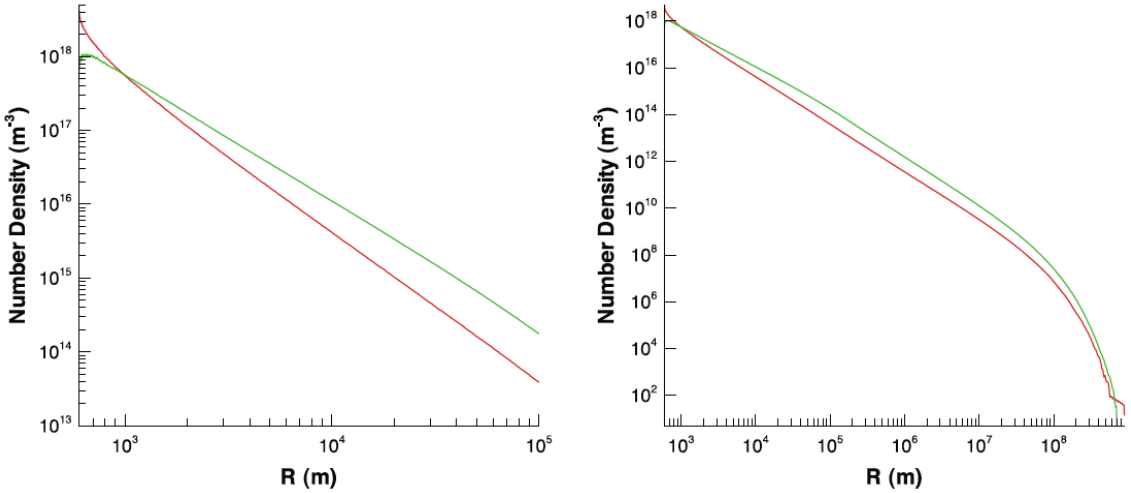

Figure 6.16: The contribution in number density for water released in two components. The model assumes a grain to water from the nucleus mass production ratio of 6:1 (grain: water from nucleus) and a grain distribution exponent of -3.9. The contributions shown are that of water released directly from the nucleus (red) and that released from dirty icy grains (green) within 100 km (left) and 10^6 km (right).

6.2.4 The Effect of Electron Collisions on the Rotational Temperature

Our study seems to give some satisfying results for the column density. However, the rotational temperature is still lower than that observed with IR measurements from Bonev et al. (2008). As mentioned by Xie and Mumma (1992), electron collisions with water molecules could have a non-negligible effect on the water rotational temperature as detailed in section 1.2.4. They studied the e-H_2O collisional rate for exciting rotational transitions in cometary water for conditions found at Comet Halley during the Giotto spacecraft encounter. Collisions with electrons were shown to be important in affecting rotational populations of the water molecule, such that the rotational temperature of water in the intermediate coma may be controlled by collisions with electrons rather than with neutral molecules. Cravens and Körösmezey (1986) studied the effect of collisions between electrons and water molecules on the vibrational and rotational temperature of water. They calculated theoretically the energy loss function for rotational excitation and de-excitation of water molecules by electron impact using cross sections for electron impact rotational transitions derived with the first Born approximation. Then, electron cooling rates were computed by integrating the loss function with the flux of thermal electrons as a function of energy given by Equation (1.21). These cooling rates are relatively large because the water molecule has a large permanent dipole moment.

We derived the electron density and temperature profiles from the model of Biver (1997) as described in section 3.4. Comet SW3-B is a considerably weaker comet than Halley was during this observation by the spacecraft. However, because information about comets other than Halley is sparse, we have undertaken electron modeling for SW3-B assuming that Biver's approach is valid. This assumption is justified by the observations of another weaker comet, 26P/Grigg-Skjellerup during the Giotto flyby.

26P/Grigg-Skjellerup, with a gas production rate of 7.5 x 10^{27} s^{-1}, provided the opportunity to study the solar wind interaction with a weakly active comet. Moreover, the encounter took place at a time when the solar wind velocity and density were undisturbed at values similar to those during the encounter with comet Halley, and it was performed

with the same in-situ instrumentation as for the comet Halley encounter. These conditions make relatively relevant the comparison of a productive comet like Halley with a weaker comet like 26P/Grigg-Skjellerup whose gas production rate is similar to, and actually somewhat below, that of 73P/Schwassmann-Wachmann 3. Weakly active comets seem to have much in common with the larger comets with a bow shock, an inner limit of fast ions, and a probable cavity (Johnstone et al., 1993). Reme et al. (1993) showed that the cometosheath of weaker comets is characterized by a higher modulation of the electron fluxes than for comet Halley. However, the inner region coincides with the magnetic pileup region and is relatively limited in the same way as in more active comets. The corresponding contact and recombination surfaces for SW3-B are respectively at distances of 284 km and 1280 km from the nucleus, which are lower than the values found for comet Halley due to the lower activity of comet SW3-B. Applying the electron density and temperature profiles from Biver's approach (such as in Figure 9) to the electron cooling rates computed by Cravens and Körösmezey, assuming that the energy lost by the electron is gained by the water molecules, we derived the additional rotational heating rates to which water molecules are subjected due to collisions with electrons.

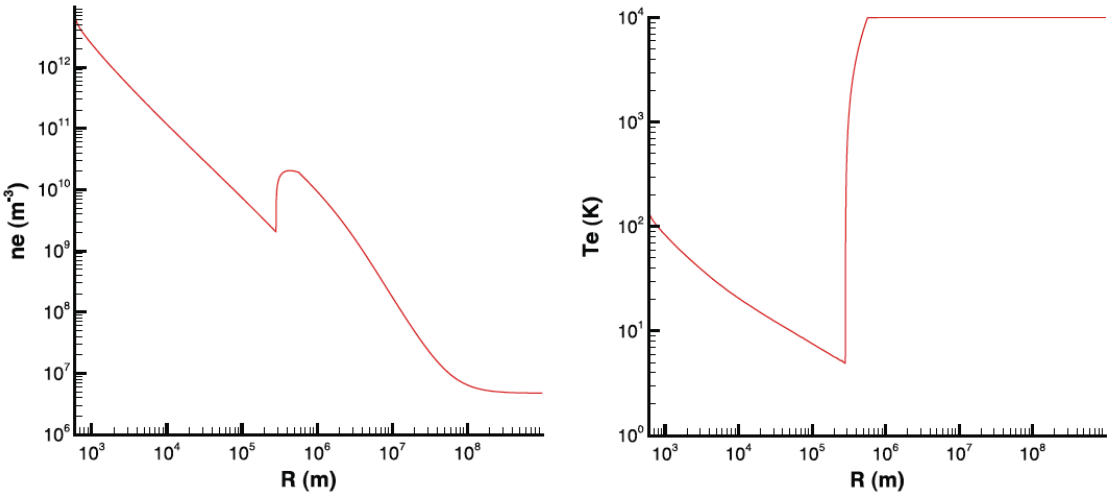

Figure 6.17: Electron densities (left) and temperature (right) in function of the distance from the nucleus using the model from Biver (1997) for comet SW3-B with a contact distance of 284 km and a recombination surface of 1280 km.

We reproduced the same approach as in the previous subsection using dirty icy grains using the heating due to collisions with electrons. Figure 6.18 shows the direct output from the corresponding DSMC calculations. Then, the influence of the grain distribution exponent was studied in a range from -2.7 to -4.5 (Figure 6.19). The rotational temperatures are $\sim$ 5-10 K higher than they were without the electrons' contribution. The column density appears not to be critically affected by the electrons, as expected. Therefore, the simulation results for the column density are similar to the observations for grain distribution exponents of -3.8 and -3.9.

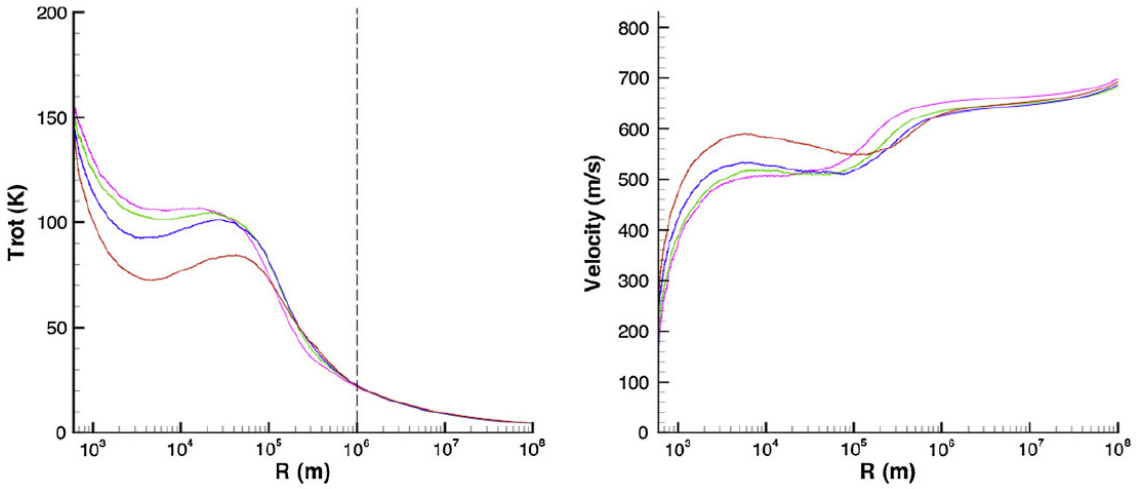

Figure 6.18: Outputs of the DSMC calculation water rotational temperature (left) and velocity (right) for a case with dirty icy grains with a size distribution exponent of -3.8 taking into account the contribution of electron-water collisions to the rotational temperature of H_2O for different grain to water from the nucleus mass production rates: 2:1 (red), 4:1 (dark blue), 6:1 (green), and 8:1 (magenta). The dashed line is the approximate distance above which fluorescence effects become predominant in the coma.

The rotational heating due to electrons allows the water molecules' rotational temperature to be very close to the measurements for the three ranges (Figure 6.20). The best fit is for a case with a grain production 8 times larger than the water coming from the nucleus and a grain distribution exponent of -3.8. Due to the uncertainty in the electron parame-

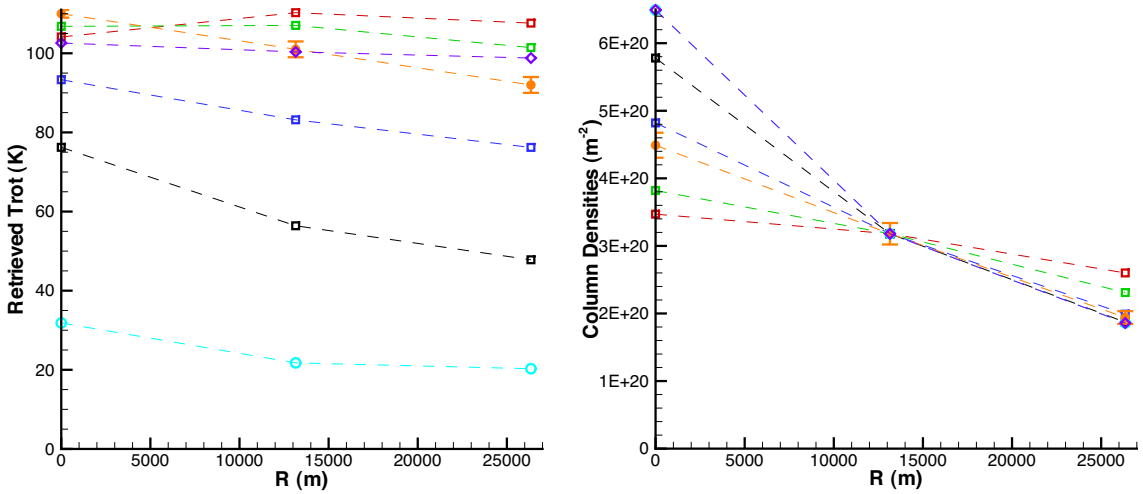

Figure 6.19: Rotational temperature and column density vs. distance from the nucleus for cases with dirty icy grains and a grain to water from the nucleus mass production rate ratio of 6:1 taking into account the contribution of electron-water collisions to the rotational temperature of H_2O. We show results for models with size distribution exponents of: -2.7 (red squares), -3.5 (green squares), -4.0 (dark blue squares), and -4.5 (black squares). The Bonev et al. (2008) observations are shown by the orange circles. The teal blue circles represent the model results where the only source of water is the nucleus. The production rate is set (arbitrarily) to exactly reproduce the middle of the three column density measurements, which is why all models go exactly through that point. The purple diamonds represent case of nuclear release as the sole source of water molecules in the coma, but taking into account the contribution of electron-water collisions with an electron density enhanced by a factor of 30.

ters, we added to Figure 6.20 the retrieved rotational temperatures and column densities for a case where nuclear release is the sole source of water molecules in the coma with an electron density 30 times higher than the one found using the model from Biver (1997). The corresponding rotational temperature profile is relatively close to the one from the measurements. However, this could not explain the column density profile. Hence, even if the electron density could be underestimated in our model, the presence of a secondary source of water in the coma from icy grains is the only way to reproduce both column density and rotational temperature profiles.

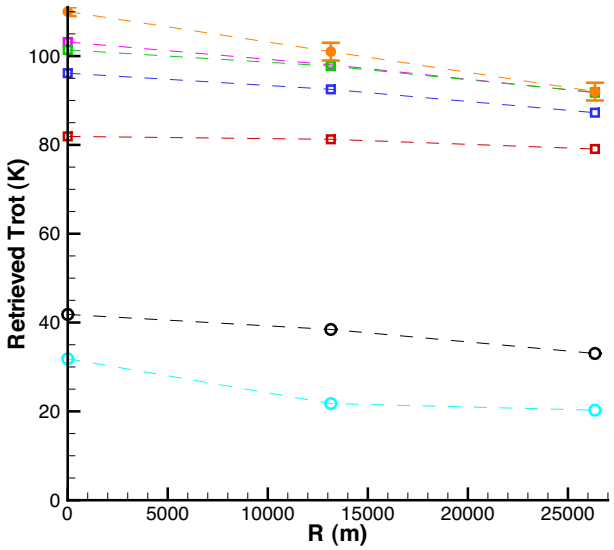

Figure 6.20: The modeled rotational temperature for cases with dirty icy grains taking into account the contribution of electron-water collisions to the rotational temperature of H_2O. We show results for models with grain to water from the nucleus production rate ratios: 2:1 (red squares), 4:1 (dark blue squares), 6:1 (green squares) and 8:1 (magenta squares) for a distribution exponent of -3.8. The Bonev et al. (2008) observations are shown by the orange circles. The black circles represent the case of nuclear release as the sole source of water molecules in the coma, but taking into account the contribution of electron-water collisions. The teal blue circles represent the best fit when nuclear release is the sole source of water molecules in the coma.

This model can be applied to a wide range of observations of comets with different geocentric distances, production rates, and spatial distributions of water. It is a very powerful tool that can give information about the amount of gas released by the nucleus and an eventual extended source of icy grains. The next section will show an application of this model to IR observations of comet ISON.

6.3 The coma of Comet ISON en route toward its full fragmentation

A similar model with icy grains can be applied to the coma of Comet ISON while on its way to perihelion to explain additional IR measurements from Bonev and collaborators. This provides a unique opportunity to better understand the gas release from comet ISON during its final weeks before it fully fragmented, when it was at very small heliocentric distances.

6.3.1 Introduction of the Observations

Prematurely called "the comet of the century", comet ISON did not live up to its expectations in term of spectacle for the public. Indeed, the comet did not brighten as much, or as rapidly, as people originally thought and exhibited a rather flat behavior. Although, about 15 days before perihelion, comet ISON very abruptly and dramatically began to flare up in brightness with water production rates up to 2×10^{30} s^{-1} (Combi et al. 2014) showing cometary wings on November 14, 16, and 18 (Boehnhardt et al. 2013) revealing the interactions of the gases flowing from the nucleus and fragments (Harris et al. 1997). Finally, comet ISON did not survive its close encounter with the Sun (0.012 AU) and eventually fully fragmented.

The large public and scientific interest for comet ISON led to a large global observational effort. HST measurements gave a rough upper limit on the nucleus size with a maximum of 2 km radius (Kelley et al. 2014). Then, HiRISE observations on board of MRO deduced a nucleus radius between 30 m and 650 m (Milkovich et al. 2013). These

measurements are consistent with the SWAN observations on board of the SOHO spacecraft, which suggested a nucleus radius between 250 and 1250 m (Combi et al. 2014).

Bonev et al. quantified rotational temperatures and column densities at several distances from the nucleus projected on the sky plane for observations on November 15 to 18, and November 22 by CSHELL at NASA IRTF (Bonev - private communication). The results for the first set of observations when the comet was at 0.53 AU with an observing geometry such that the Sun-Comet-Earth angle was 86°are presented in Figure 6.21 showing a very slow drop in rotational temperature for such a small heliocentric distance with a variation from about 118 K to $\sim$ 85 K as the field-of-view changed from being nucleus centered to being centered $\sim$ 1500 km from the nucleus. The column abundance presents a maximum of about 3.6×10^{31} s^{-1} slightly tilted sunward and then decreases by a factor 10 within 1500 km. All these results are given taking the average over the measurements from a FOV centered on the given distance and the two neighboring FOVs (one sunward and one anti-sunward).

It is important to notice that the observations show a strong asymmetry between sunward and anti-sunward hemispheres with a 2.9 micron continuum extended in the anti-solar direction. Moreover, the temperature profile is poorly correlated with the column abundance profile especially on the dayside of the coma (positive projected distances). This suggests that an extended source of water plays a critical part in the coma of comet ISON similar to SW3, which is consistent with the ongoing fragmentation process that was taking place at epoch of the observations. However, it is critical to point out that the observations of comet ISON and SW3 present some differences which will play a role in their interpretation with the use of the model in the following subsections. Indeed, comet ISON was observed much closer to the Sun than comet SW3 with a heliocentric distance varying by almost a factor 2 between the two observations. The solar UV flux was then about 4 times higher in the case of comet ISON implying that photochemical heating is much more important. Also, comets SW3 and ISON were observed at different heliocentric distances with very different instruments. Hence, the profiles related to comet SW3 extended in the closest $\sim$40 km from the nucleus, while the coma of comet ISON was sampled at about

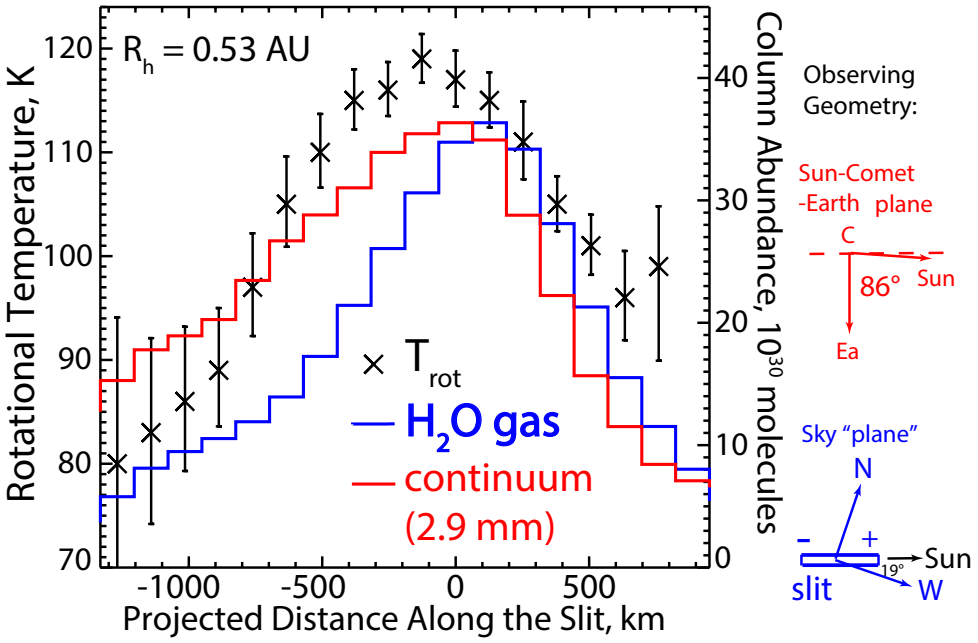

Figure 6.21: Rotational Temperature and Column Abundance Profiles of Comet ISON at 0.53 AU deduced from IR measurements obtained by Bonev and collaborators. The observing geometry is also detailed showing that the Sun is toward positive distances with a Sun-Comet-Earth angle of 86°. (Bonev - private communication)

1500 km from its nucleus. This difference of scale is important for testing of the model since it enables to explore the competition between cooling and heating processes in the coma with different spatial scales.

6.3.2 The DSMC Model of Comet ISON

The DSMC model was applied to comet ISON in order to compare the measured rotational temperature and column abundance profiles on November 17 observed with CSHELL at NASA IRTF when the comet was at 0.53 AU from the Sun (Bonev - private communication). Due to a large amount of free parameters, we decided to use a 1D model to

simulate the coma of comet ISON with a nucleus radius of 1.5 km for different sets of gas and dust production rates, and grain parameters (Table 6.4). These cases have been set up so that the total amount of mass released from the nucleus (gas + grains) always equals to 3887 kg.s^{-1}, so that when all the icy grains have been sublimated and have contributed to the coma, the total water production rate is 2.6 $\times$ 10^{29} s^{-1}. Moreover, all cases but case 1 (Nucleus only) take into account the electron-water molecules collision rotational heating effect described in section 3.4. The icy grains considered in this study are dirty icy grains with 10% of magnetite and 90% of ice similarly to what has been done with comet SW3-B due to its better reproduction of the observations in the work presented in the previous section. The grain minimal size is set to be 1 μm and the maximum grain size is the maximum liftable size a_M derived from Equation (3.4) with an assumed nucleus density of 300 kg.m^{-3}, so that for case 3 (0.5:1) a$_M$=2.51$\times$10^{-1}m, for case 4 (1:1) a$_M$=1.89$\times$10^{-1}m, and for case 5 (2:1) a$_M$=1.26$\times$10^{-1}m . The size distribution for all the presented cases follows a power-law distribution with an index of -2.7 split over 36 bins. Cases with steeper size distributions showed less good agreement with the measurements and will not be presented in this thesis to limit the number of cases and provide a clear description to the reader.

Case	$Q_N(H_2O)$ (s^{-1})	Q(grains) (kg.s^{-1})	a$_M$ (m)	size index
1) Nucleus only	2.6 $\times$ 10^{29}	0	NA	NA
2) Nucleus + Electrons	2.6 $\times$ 10^{29}	0	NA	NA
3) 0.5:1	1.73 $\times$ 10^{29}	2591	2.51 $\times$ 10^{-1}	-2.7
4) 1:1	1.3 $\times$ 10^{29}	1943	1.89 $\times$ 10^{-1}	-2.7
5) 2:1	8.67 $\times$ 10^{28}	1296	1.26 $\times$ 10^{-1}	-2.7

Table 6.4: Model parameters used for the DSMC model of comet ISON

Figure 6.22 shows the water number density, temperature, rotational temperature and velocity profiles for the different considered cases. At such small heliocentric distances, collisions with daughter species warm up the coma at large distances from the nucleus. Both water temperature and rotational temperature stay warmer within 1000 km from the

nucleus with the use of electron-neutral collision heating and sublimating icy grains. Comparing cases 5 (2:1) and 4 (1:1), we notice that both temperatures and rotational temperatures start dropping closer to the nucleus for case 5 due to the lower maximum liftable size and the lower gas flux directly released from the nucleus applying drag on the grains.

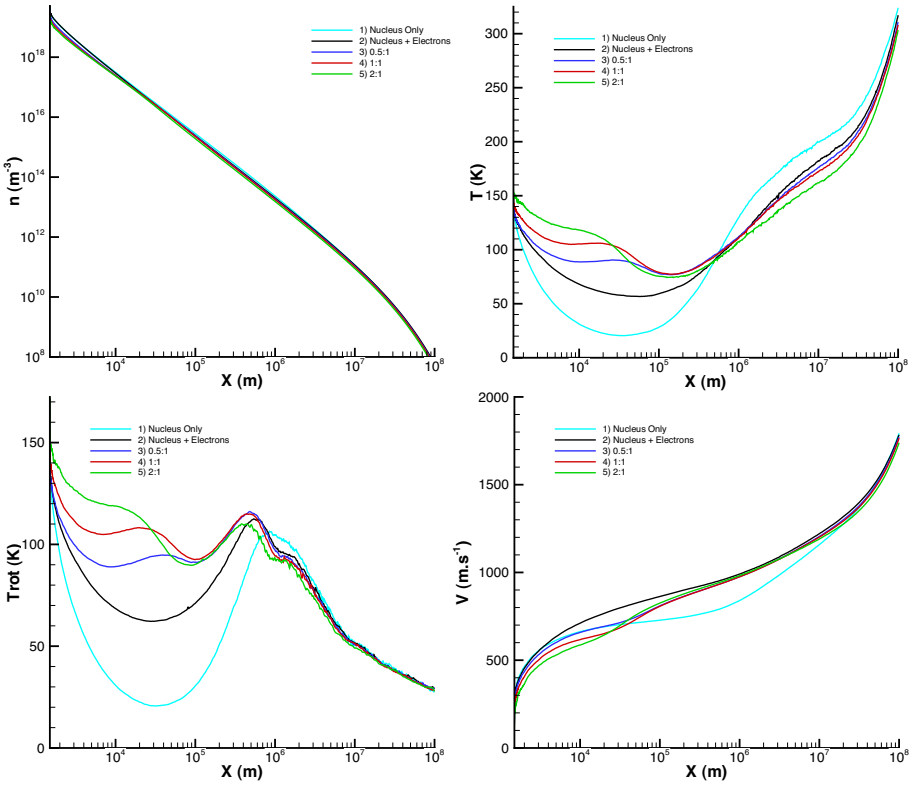

Figure 6.22: Direct water molecules output of the DSMC model for comet ISON: number density, temperature, rotational temperature and velocity.

6.3.3 Modeling the Rotational Temperature and Column Abundance of Comet ISON

In order to take into account the atmospheric seeing, we used the PSF corresponding to the observation approximated by a gaussian with an HWHM of 477 km (Bonev - private

communication). Then, a convolution process as detailed in the section related to comet SW3 was applied to the DSMC outputs for each pixel. Finally, the rotational temperature and column abundance from each pixel was averaged with the two neighboring pixels to enable direct comparison with the observations.

We arbitrarily decided to use the negative projected distance from the measurements presented above (Bonev - private communication) to fit our model, which correspond to the night side of the coma. This illustrates one of the drawbacks of using a 1D model, making it impossible to distinguish between day and night side. However, due to the large amount of free parameters, the use of a higher dimension model would be difficult in a physical way to analyze this dataset alone.

Figure 6.23 shows the comparison of the different model cases with the measurements. It clearly appears that a model with water only released by the nucleus cannot explain the high rotational temperature within the first 500 km, notably with a value centered on the nucleus of 48 K about 2.5 times lower than the observations. Electron-neutral collision heating warms up the inner coma but not enough to fully explain the observations. Also, the column abundance profile cannot be reproduced with these cases without sublimating icy grains. The addition of the extended source enables a better agreement for both the rotational temperature and the column density with the observations. However, the amount of grains released by the nucleus appears to not be clearly constrained with these observations. Indeed, the retrieved rotational temperature profiles are relatively similar for the range of grain to gas released by the nucleus ratios considered, all showing somehow still lower rotational temperatures close to the nucleus. While this rotational temperature small dependance with respect to the amount of grains introduced in the system may seem contradictory with the results presented for comet SW3-B where the retrieved rotational temperature increased with an increasing amount of grains, a careful look at the rotational temperature profile in Figure 6.22 explains this phenomenon. The rotational temperature varies strongly with the fraction of icy grains injected in the coma within about 100 km. Then, the rotational temperature of the three cases with icy grains converges toward a similar profile. The pixel size in the case of comet ISON represents 126.7 km while for the

observations of SW3-B the data was given with a spatial resolution an order of magnitude finer. Hence, the two measurements give information about different parts of the coma. The SW3-B measurements focused on the very inner coma where the amount of grains impacts strongly on the rotational temperature and then can easily be defined, while the observation of comet ISON does not have a sufficient spatial resolution to probe this region to give strong constraints about the fraction of grains in the coma. Also, the column abundance profile is better reproduced at large distances from the nucleus by case 5 with 2:1 ratio of grain to gas mass but it underestimates the column abundance close to the nucleus with a value of about 2.6×10^{31} molecules versus 3.6×10^{31} molecules for the data in the pixel centered on the nucleus.

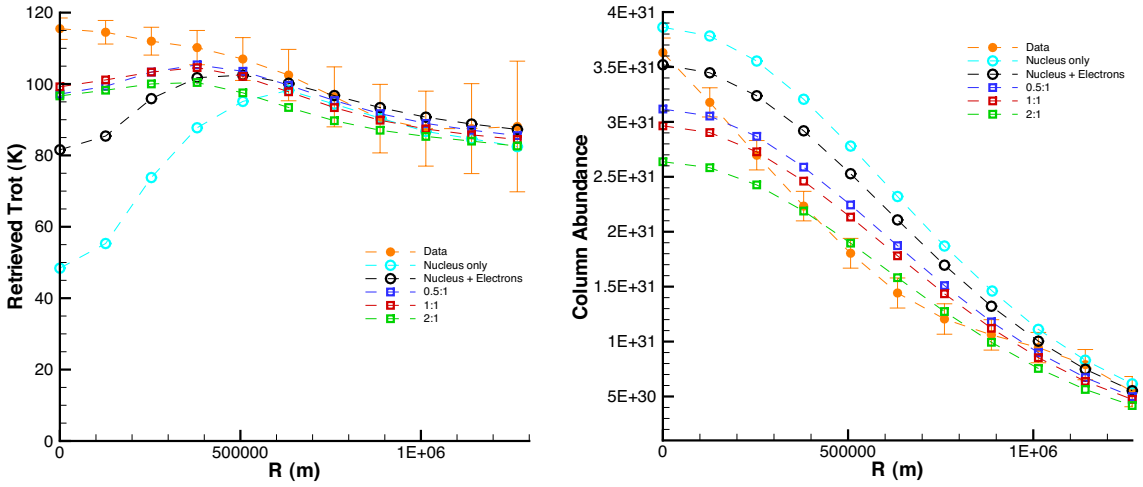

Figure 6.23: Retrieved rotational temperature and column abundance profiles of Comet ISON at 0.53 AU with dirty icy grains and comparison with the anti-sunward part (negative projected distance) of the measurements from Bonev and collaborators.

The model using electron-neutral collision heating with icy grains clearly improved the fitting of the model with the data confirming the hypothesis that the water observed with the IR measurements (Bonev - private communication) results from a non-negligible amount of sublimating icy grains acting as an extended source of gas in the coma. However, both column abundance and rotational temperature were underestimated at distances

lower than about 300 km. This difference can vanish with the addition of icy grains within this region that would fully be sublimated within 300 km of the nucleus. We propose two different processes that could account for this extra amount of icy grains in the inner coma. First, we chose to use the night side data from the measurements to be fitted with our model. The continuum clearly shows an asymmetric behavior with extension on the night side suggesting a larger amount of grains in the anti-sunward hemisphere. These grains could have been pushed by radiation pressure (Fougere et al. 2013) or rocket force for larger chunks (Hermalyn et al. 2013, Kelley et al. 2013) anti-sunward increasing their amount in the night side hemisphere where they will eventually sublimate (Fougere et al. 2013). Another explanation can result from the fragmentation of the nucleus where secondary nuclei could be trailing behind the primary nucleus, and constitute an additional source of gas in the night side of the coma confirming the observation from Boehnardt et al. (2013). Yet, the IR measurements from IRTF do not present any unambiguous clue for the presence of any secondary nucleus in the coma of comet ISON at epoch of the observation (Bonev - private communication).

The model has now been applied to two very different comets: SW3-B and ISON. Indeed, SW3-B is a periodic comet while comet ISON was undergoing its first inbound in the Solar System. Also, the gas production rates were different by more than an order of magnitude and the heliocentric distances at epoch of the observation were different by about a factor of 2. Despite all these differences, both comets showed a non-negligible amount of water molecules released by sublimation of icy grains. Also, the different spatial resolution in the observations enabled us to explore the competition between heating and cooling processes at different spatial scales. The SW3 measurements allows to test the model close to the nucleus where the effect of parameters such as the amount of grains released with respect to the nucleus gas production rate are important. While the ISON observations did not include this capability, they offered a complement by testing the underlying physical processes on a thousand kilometer scale where we can observe the region beyond all the grains sublimated and leave photochemical heating and near-adiabatic cooling predominate. In the future, this model will be extended to different comets and could be used with a higher dimension cometary model when more constraints are available.

This is ongoing work that will be completed over the next year and culminate with the publication of a paper. A continuous collaboration between observers and modelers is of critical importance to provide the best results and guarantee discoveries. Indeed, the initial work of interpretation of the IR observations of comet SW3-B has shown great insights and gave an incentive to the observers to push the measurements to their best capability in order to facilitate and constrain models. This synergy between observations and models results from continuous improvement so that each party can provide the best information.

The next chapter will present a model with a combination of both small active areas using the work presented in chapter 5 and sublimating icy grains following the results from this chapter.

Chapter 7

The Ice and Gas Coma Resulting from a Nucleus with Successive Areas Application to Comet Hartley 2

103P/Hartley 2 is a member of the Jupiter Family Comets (JFC) and most likely originated in the Kuiper Belt as shown by its short orbital period of 6.5 years and its low inclination of 13.6°. It was discovered by Malcolm Hartley in 1984 and has been observed over the past five apparitions. Its perihelion and aphelion distances were lowered to 1 AU and 6 AU due to a succession of encounters with Jupiter since 1875 (Carusi et al. 1985). However, Hartley 2 differs from a typical JFC due to its extremely high activity despite its small size (Lisse et al. 2009). Moreover, comet 103P/Hartley released relatively important amounts of CO_2 relative to water with a ratio of $\sim$10 to 20 % (Weaver et al. 1994; Colangeli et al. 1999).

103P/Hartley2 was the target of the Extrasolar Planet Observation and Deep Impact Extended Investigation (EPOXI) as an extension of the Deep Impact mission. The EPOXI mission was accompanied by a worldwide Earth- and space- campaign to complement the in situ mission. Nearly 200 astronomers helped to collect data over longer timescales, at different wavelengths, and with instruments not carried on the Deep Impact spacecraft

giving some critical clues to better interpret the EPOXI mission observations (Meech et al. 2011).

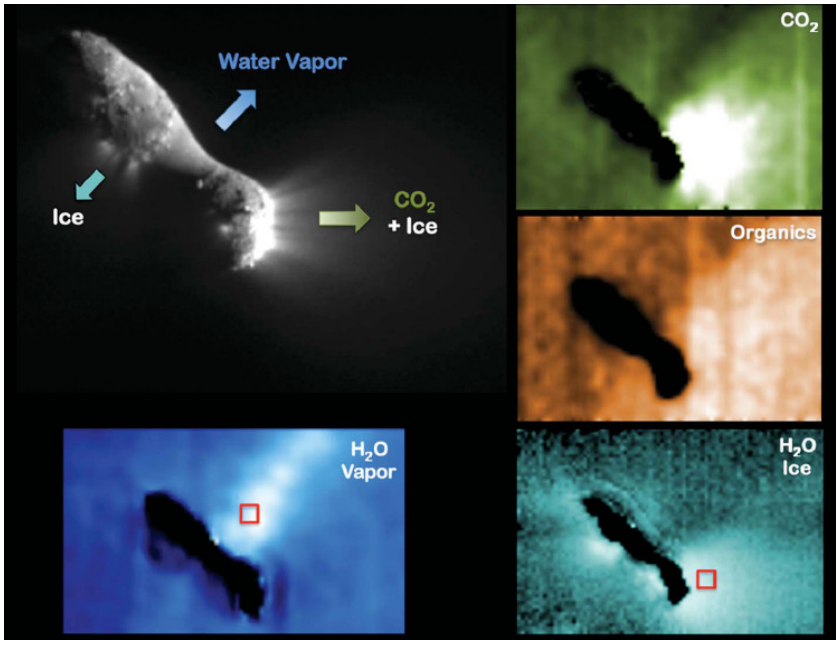

Figure 7.1: Relative spatial distribution in the coma of comet Hartley 2. Panels labeled CO_2, organics, and H_2O vapor are maps of the total flux in the relevant emission bands. The panel labeled H_2O ice is a map of the depth of the ice absorption feature at 3 μm. Extracted from A'Hearn et al. (2011).

At its closest approach on November 4th, 2010, the EPOXI mission's spacecraft was at a distance of 694 km from Hartley 2 and at 1.064 AU from the Sun (A'Hearn et al. 2011). The observations showed that Hartley 2's nucleus has a bi-lobed shape with a diameter varying from 0.69 to 2.33 km and a mean radius of 0.58 km (A'Hearn et al. 2011, Thomas et al. 2013) which is similar to the value of 0.57 km found with the Spitzer Space Telescope during the 2008 apparition of Comet Hartley 2 (Lisse et al. 2009). The Medium Resolution Instrument (MRI) and the High Resolution Instrument (HRI) on EPOXI revealed that Hartley 2 outgasses much CO_2 from portions of its nucleus, apparently driving a major component of its activity (Figure 7.1 extracted from A'Hearn et al. 2011); the

sub-solar lobe appears to be the origin of collimated jets releasing mostly CO_2 similar to the ones observed on Comet Tempel 1 (Belton et al. 2010, Farnham et al. 2007, Feaga et al. 2007) which, in the case of comet Hartley 2, carry out pure icy grains from the nucleus. The sublimation of these grains contributes to most of the total amount of water seen in the coma (A'Hearn et al. 2011). However, the waist with its smooth terrain released mostly water vapor sublimated directly from the surface of the nucleus without a significant amount of icy grains. It appears that the outgassing from comet Hartley 2 is complex with a combination of active areas, jets, and sublimating icy grains.

Ground based millimeter spectroscopy of CH_3OH and HCN at IRAM showed similar short-term variability of the spectral lines due to nucleus rotation (Drahus et al. 2012). Two oppositely directed jets were observed as the main sources of outgassing; a blueshifted jet releasing mostly HCN and icy grains while the redshifted one close to the region of the polar night was primarily a source of CH_3OH. The similarity in the variability in amplitudes of the mixing ratios of HCN and CH_3OH, and the values measured for CO_2 and H_2O by EPOXI led the authors to raise the hypothesis that a strong spatial correlation may exist between HCN and CO_2 on one hand, and for CH_3OH and H_2O on the other hand. Moreover, the rotational temperature of CH_3OH was measured at different times and showed strong variations that seem correlated with the varying production rate from the different areas of the nucleus.

First, the next subsection will describe the modeling of the observational data both by EPOXI and from ground-based measurements, which will enable us to derive the different gas source production rates and parameters. The model will require the use of the results from small active areas (chapter 5) and sublimating icy grains (chapter 6). Then, the overall structure of the coma of comet Hartley 2 for both gas and icy grains will be presented. Most of the results exposed in these chapter have already been published in an article by Fougere et al. (2013).

7.1 DSMC Simulation for a Non-Spherical Nucleus with Icy Grains

We have used a dusty-gas kinetic DSMC comet model code (Tenishev et al., 2008 and 2011) applied to examine the overall structure of the coma including the distribution and velocities of both gas and icy grains. 2D-cylindrically axisymmetric DSMC simulations were performed for a gas coma using a realistic bi-lobed shaped nucleus with dimensions corresponding to the ones observed by EPOXI with a diameter varying from 0.69 to 2.33 km (A'Hearn et al. 2011). The nucleus shape is approximated by an analytical formula where the distance from the principal axis d is a function of the abscise x and can be deduced by:

$$d(x) = \max\left(\sqrt{1-\left(\frac{x}{1165}\right)^2}\frac{1165}{1.3} - \frac{565}{2}\left(1+\cos\left(\frac{\frac{1980}{1165}x-200}{1800}\pi\right)\right), 0\right) \quad (7.1)$$

A visual representation of the approximation of the nucleus shape of comet Hartley 2 is given by Figure 7.2.

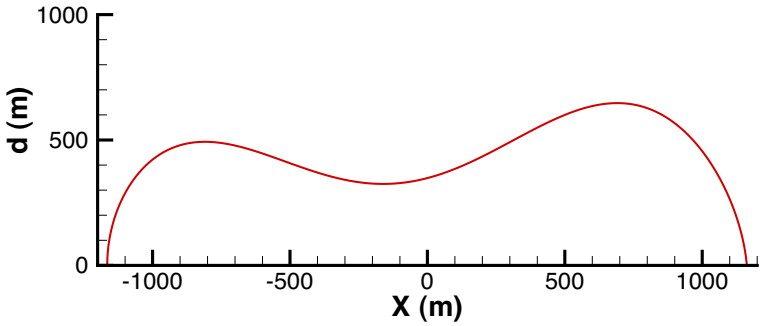

Figure 7.2: Analytical approximation of the shape of the nucleus of comet Hartley 2 used in the DSMC model.

To accurately simulate the coma of comet Hartley 2, different gas source areas of the nucleus need to be considered. The sub-solar lobe, with its jets releasing most of the

CO_2 present in the coma, extends from -40°to 40°solar zenith angle. Then, the waist region with an important water vapor outflow appears from 40°to 90°(and its symmetric component with respect to the x-axis due to the cylindrical symmetry from -40°to -90°). Finally, the region above 90°presents the night side of the nucleus. The determination of the different gas production rates for each area requires the computation of IR spectra, which are produced using the escape probability method as described in chapters 3 and 4. This technique enables us to reproduce optically thick IR emission spectra, which is critical in the very inner coma where the column densities are high enough so that the opacity is important.

The inner boundary condition for the gas temperature follows the distribution by Tenishev et al. (2008) (section 3.1) with a maximum value close to the sublimation temperature of water ($\sim$200 K) at the sub-solar point and then, decreasing with sub-solar angle. This assumption is questionable since the sublimation temperature of CO_2 is significantly lower than the one of H_2O with a value of $\sim$120 K. But, even at the sub-solar lobe in the CO_2 jet where we find the highest CO_2 production, the amount of water produced is the same order of magnitude as carbon dioxide. Hence, the actual value might be somewhere between these two extremes. A misestimated temperature would lead to somewhat different velocities for the gas and possibly different observed rotational temperatures, but does not affect the major results of this study.

Equation (3.2) shows that the gravity force plays a critical part in the dynamics of the grains. Then, since the icy grains may be the primary source of water, a proper gravity field needs to be computed to accurately model the gas distribution in the coma of comet Hartley 2. In the case of a spherical nucleus, the classical analytical formula for the gravity of a sphere is used. However, for more complicated nucleus shapes, the latter formula is not valid anymore and the computation of the gravity requires a special treatment. Most of the previous works including grains ejected from a non-spherical nucleus employ a gravity field obtained from origin-centered models with a "best-fit" spherical shape of the nucleus (Crifo and Rodionov 1999, Crifo et al. 2005 and references therein). The latter assumption raised some concerns mostly due to the fact that the assumed gravity field must actually

be centered at the center of mass of the nucleus, and the mass of the "best-fit" sphere is different from the one of the real nucleus (Zakharov et al. 2009). To avoid such concerns, we decided to use a more accurate gravity field in our DSMC computations. The nucleus was triangulated in 3 dimensions and meshed with a large number of tetrahedrons ($\sim$ 11000 for the bi-lobed shaped nucleus of comet Hartley 2). The gravity field of the nucleus is found by summation of the contributions of all tetrahedrons assuming a homogeneous density of 300 kg.m^{-3} (Thomas et al. 2013). The gravity acceleration reaches a maximum of a few times 10^{-5} m.s^{-2} close to the surface of the nucleus as illustrated in Figure 7.3.

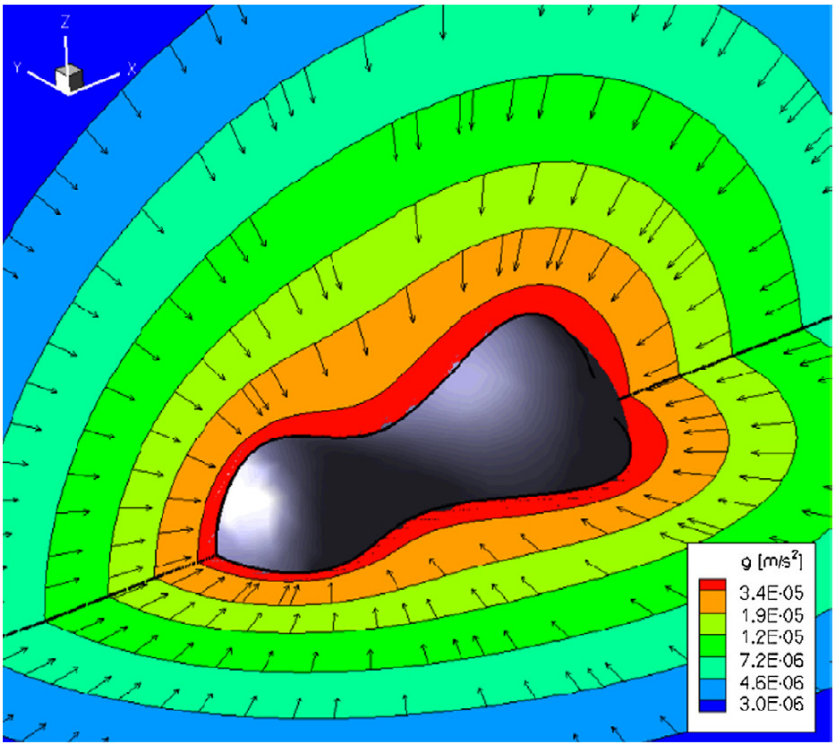

Figure 7.3: Two perpendicular cuts with contour levels of gravitational acceleration (in $m.s^{-2}$). The arrows show the direction of the gravity field. For illustrative purpose, the non-spherical nucleus used to compute the gravity field was also plotted. The axis orientation is shown on the top left of the figure.

A model of pure icy grains using the sublimation rate of Patashnick et al. (1975) (see section 3.3 for more details) was used for this study in agreement with the EPOXI observations from A'Hearn et al. (2011) who concluded that the ice must be pure for the grains to persist. This was confirmed by the work of Protopapa et al. (2014) who analyzed reflectance spectra from HRI on board EPOXI and concluded that the refractories are thermally and physically decoupled from the icy particles. The minimum grain radius was chosen to be 1 μm following the EPOXI observations (A'Hearn et al. 2011) and the maximum liftable size was taken to be the maximum liftable grain size of the sub-solar lobe following the formula from Equation (3.4) with the appropriate gravity and a grain density equal to that of water (1000 kg.m^{-3}). The flux that will be derived in the next section will lead to a corresponding maximum liftable size in the CO_2 dominated region of 8.0 cm. The grain density assumption is questionable if we consider the grains to be porous aggregates where the density may be as low as 100 kg.m^{-3} (Kelley et al. 2013), in which case larger particles would be lifted for a given gas flux. On the other hand, the grain density could be higher in the case of dirty icy grains with refractories. The size of the particles plays a critical part in their lifetimes and then in the amount of water released. Then, a different grain density may also affect other parameters used in this study. We assumed that the icy grains follow a power law size distribution with an index that is defined to best reproduce the observed day/night OH asymmetry as will be presented in section 7.2.2, which leads to a value of -3.5.

7.2 Modeling the Observational Data to Determine the Gas Source Parameters

Both ground-based and the EPOXI measurements constitute valuable information that give constraints for our model. By fitting the IR spectra measured by HRI on board of the Deep Impact spacecraft (A'Hearn et al. 2011), we can define the gas production of each area of the nucleus. Then, the contribution of each source to the coma of Hartley 2 is derived so that the total amount of water produced by both direct sublimation of the nucleus and the icy grains corresponds to the observed production rate on November 4,

2010, at EPOXI's closest approach. A numerical comparison of the OH day/night asymmetry (Knight and Schleicher 2013) gives an indication of the power-law size distribution of the icy grains. Finally, a qualitative comparison with the spectacular images made by MRI (A'Hearn et al. 2011) of the very inner coma is possible. This section describes in more details how we arrive at the best fit from our model for each set of measurements. To reach those results, many models were run varying different parameters such as the production rates for the gas and icy grains within the different areas, and the icy grain power-law exponent. Because this is an integrated physical model, the different source regions cannot be separated to allow a more direct inversion scheme to calculate the relative strengths of the different sources.

7.2.1 Fitting the Infrared Spectrum Measured by HRI

IR spectra have been measured in two different regions of the coma (one at the sub-solar lobe and the other one at the waist of the nucleus) between 2.5 and 4.5 microns by the EPOXI HRI instrument (A'Hearn et al. 2011). This range contains the strong emissions of H_2O at 2.7 μm and CO_2 at 4.3 μm. The EPOXI mission reports some molecular brightness ratios between two areas of the coma shown on Fig. 6 from A'Hearn et al. (2011) by two red squares; the sub-solar zone close to the lobe has a CO_2 emission 3 times brighter, 10 times higher for the ice, and 1.5 times fainter for H_2O than the area close to the waist of the nucleus (A'Hearn - private communication).

We used a line-by-line radiative transfer model using the escape probability method (described in chapter 4) to simulate the H_2O emission at 2.7 μm and the CO_2 emission at 4.3 μm along the line of sight projected into the points A=(-1000 m ; 800 m) and B=(-100 m ; 1000 m) from the geometric center of the nucleus, which approximate the regions probed by HRI (Figure 7.4). The degradation due to the instrument spectral resolution was done using boxes of the size of the HRI's resolution, which varies from 216 to about 350 in the wavelength range of interest (Hampton et al. 2005). Thus, we picked $\lambda/d\lambda$ of 216 and 300 for water and carbon dioxide, respectively. The modeled emission spectra are in relatively good agreement with the measured ones except the shape of the CO_2 spectrum

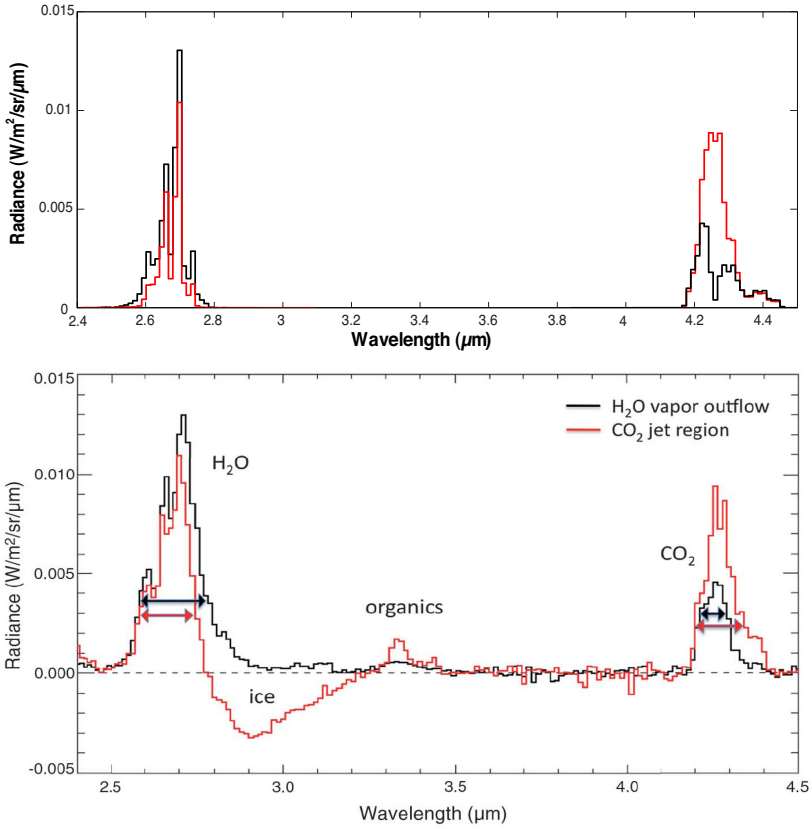

Figure 7.4: H_2O spectra at 2.7 μm and CO_2 emission at 4.3 μm. The top panel is the simulated plot in the CO_2 region selected as point A=(-1000 m; 800 m) (red) and the water vapor outflow pickes as point B=(-100 m; 1000 m) (black). The bottom panel shows the corresponding measured spectra by HRI on board of EPOXI from A'Hearn et al. (2011).

in B that less accurately reproduces the observations, although the integrated brightness matches the observations. Indeed, the different "spikes" due to water and CO_2 emissions are present at the same wavelengths as in the measurements. Moreover, the absolute radiance of each emission is close to the value measured by EPOXI with maxima of 0.013 and 0.011 W/m^2/sr/μm for H_2O respectively in the water vapor outflow (point B) and the CO_2 jet region (point A), and 0.004 and 0.009 W/m^2/sr/μm for CO_2 at the same locations. Then, we compared the brightness ratios of these two points to the values from EPOXI: $I_A/I_B(CO_2)= 3.1$ and $I_A/I_B(H_2O) = 0.65$ which are relatively close to the EPOXI values of 3 and 0.66, respectively. The best-fit spectra are obtained with DSMC calculations using two different types of gas production: a distribution such as in Tenishev et al. (2008) that results from a thermophysical model where the gas flux decreases with solar zenith angle, and an equally distributed flux to complete the amount of gas representing active areas (Figure 7.5) such that:

- 1.23×10^{27} s^{-1} of water coming from a distribution as in Tenishev et al. (2008) superimposed with 7.5×10^{26} s^{-1} of water equally distributed over a solar zenith angle range of 40°to 90°(symmetric with respect to the x-axis due to the 2D-cylindrical symmetry) to form the waist water vapor outflow.

- 2.4×10^{26} s^{-1} of CO_2 resulting from a distribution as in Tenishev et al. (2008) superimposed with 9.2×10^{26} s^{-1} of CO_2 equally distributed over a solar zenith angle range of -40°to 40°to constitute the sub-solar lobe CO_2 jet.

This process enabled us to precisely compute the gas production of each gas source. Notably, direct sublimation of the nucleus produces a total of 1.98×10^{27} s^{-1} of H_2O and 1.16×10^{27} s^{-1} of CO_2, which are distributed as follows:

- 1.37×10^{27} s^{-1} ($\sim9.2\times10^{20}$ m^{-2}.s^{-1}) of water from the waist region and 6.1×10^{26} s^{-1} from the rest of the nucleus (respectively 69% and 31% of the total amount of water released by the nucleus) with fluxes of $\sim3.1\times10^{20}$ m^{-2}.s^{-1} at the sub-solar lobe and $\sim8.1\times10^{19}$ m^{-2}.s^{-1} at the night side lobe.

- 1.02×10^{27} s^{-1} ($\sim4.6\times10^{20}$ m^{-2}.s^{-1}) of CO_2 from the sub-solar lobe and 1.4×10^{26} s^{-1} from the rest of the nucleus (respectively 88% and 12% of the total amount

of CO_2 released by the nucleus) with fluxes varying from $\sim 1.7 \times 10^{19}$ $m^{-2}.s^{-1}$ to $\sim 5.0 \times 10^{19}$ $m^{-2}.s^{-1}$ at the waist and $\sim 1.6 \times 10^{19}$ $m^{-2}.s^{-1}$ at the night side lobe.

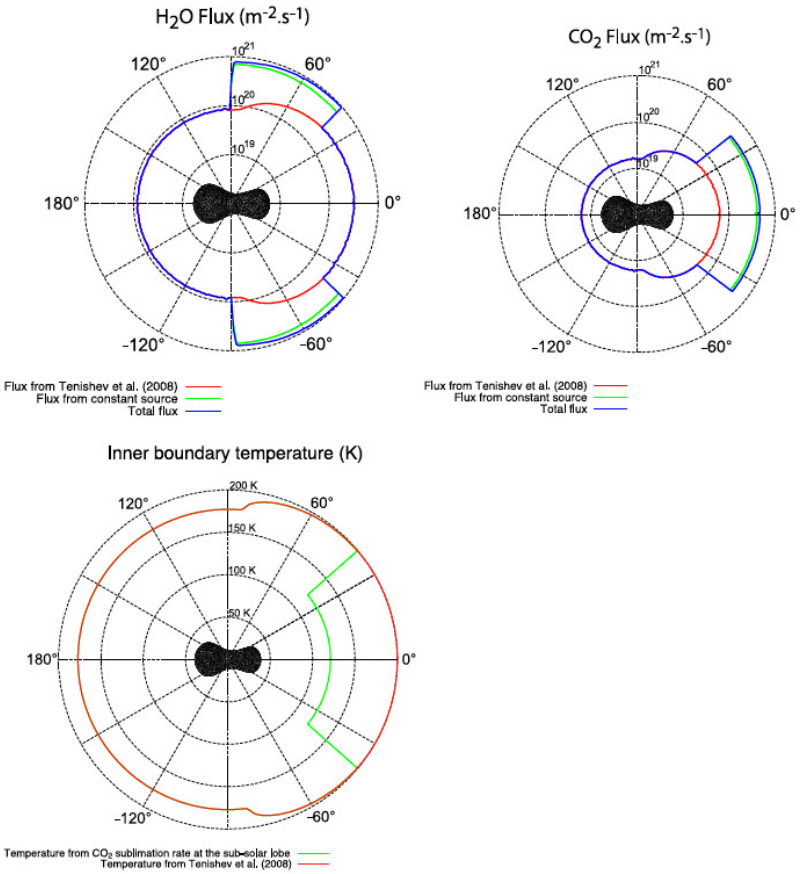

Figure 7.5: Gas fluxes (in $m^{-2}.s^{-1}$) and inner boundary temperature (K) of the different areas from the nucleus given in log scale with the direction to the Sun at 0°. On the flux plots (H_2O on the left and CO_2 on the right), the red line represents the sub-solar angle varying distribution such as in Tenishev et al. (2008), the green one is the constant distribution, and the blue one is the sum of those two giving the total flux. While on the surface temperature plot, the red line is the temperature from Tenishev et al. (2008) and the green one has a CO_2 sublimation temperature at the sub-solar lobe (-40°to 40°).

Then, the total amount of icy grains injected into the coma is chosen such that the total water production rate (nucleus + grains) corresponds to the observations on November 4th 2010 via different techniques, which give values between $\sim 7\times10^{27}$ s^{-1} and 1.4×10^{28} s^{-1} (A'Hearn et al. 2011, Combi et al. 2011, Dello Russo et al. 2011, Meech et al. 2011, Knight and Schleicher 2013). The corresponding production rate of icy grains contributing to the water coma required to provide this additional amount of water varies between $\sim$150 kg.s^{-1} and $\sim$360 kg.s^{-1} . Here, we used the value of $\sim$210 kg.s^{-1} which enabled us to reproduce the total production rate reported by observation of the Lyman-alpha emission with the SWAN instrument on board of the SOHO spacecraft (Combi et al. 2011).

The IR spectra presented in this thesis only present the gas ro-vibrational emissions. Indeed, the ice absorption at $\sim$2.9 μm, clearly appearing on the HRI water spectrum in the CO_2 jet region (A'Hearn et al. 2011), was not modeled in this study. This could lead to an underestimation of the water radiance in the CO_2 jet region of less than $\sim$8% as suggested by the decay of the water spectrum in the water vapor outflow where the ice emission appears to be negligible. Moreover, since we based our spectra fitting on the different main spikes of the emissions, the ice absorption should not affect in a significant way the retrieved water production rate at the sub-solar lobe.

As mentioned previously, the results are presented with a boundary condition for the temperature at the surface of the nucleus taken from Tenishev et al. (2008), obtained with the thermophysical model from Davidsson and Gutiérrez (2004, 2005, and 2006), with a distribution based on the sublimation temperature of water (temperature close to 200 K at the sub-solar point). Yet, we tried the CO_2 dominated region with both a water sublimation temperature from the Tenishev et al. (2008) model as well as a CO_2 sublimation temperature (120 K) (Figure 7.5). In the latter case, the velocity of the gas would have been lower in this region implying some higher optical depths resulting in lower brightnesses for a given gas density. Then, the production rates presented in this study may be slightly underestimated. Unfortunately, the shape of the different spectra does not vary in a significant way with this temperature variation, thus not enabling us to settle this issue based on the EPOXI spectra.

The modeled spectra computed with the resolution reported by the Deep Impact instrument overview (Hampton et al. 2005) have more "structure" than the HRI measurements. The use of a lower resolution would tend to make these structures disappear by smearing out the spectra, and the model would better reproduce the shape of the observations. This difference could be due to some missing line emissions resulting from hot-bands or rotational levels that were not included in the model, whereas the corresponding spectra using the recent database with levels and g-factors from Villanueva et al. (2012), assuming a constant temperature along the line of sight directly extracted from the DSMC output, shows to a lesser extent similar flaws. An additional source of error may be coming from the simplicity of the optical depth model (for example, we find that the modeled values of the optical depth $\tau_{\nu_3}(H_2O)$ in point A and B are 2.72 and 1.38, respectively) or even from the escape probability formalism to compute line fluxes itself. However, the study from Zakharov et al. (2007) clearly shows that the escape probability method is a reasonable approach for treating radiative transfer and line excitation of molecules in the coma, the errors resulting from uncertainties in model parameters being more important than those introduced by the escape probability method.

7.2.2 Earth-Based Measurements: the OH Day/Night Asymmetry

Previous studies presented the modeled distribution of the OH coma as would be observed from a ground-based telescope for the geometry of the 2009 apparition of comet 67P/Churyumov-Gerasimenko (Tenishev et al. 2008, Combi et al. 2012). It was shown that even for small active areas, the OH coma distribution appears relatively circular due to the combination of the initial tangential expansion of the gas, the rotation of the nucleus, the vectorial ejection of the daughter species by photodissociation, and the line-of-sight integration (Combi et al. 2012). Figure 7.6 shows the OH coma at 10^4 and 10^5 km from the nucleus for our Hartley 2 model with a Sun-comet-observer angle of 58.73°and a geocentric distance of 0.15 AU corresponding to the geometry during November 3rd 2010, assuming a nucleus orientation similar to during the closest approach of the EPOXI mission's spacecraft (i.e. with the small lobe sunward). These profiles confirm the results from Combi et al. (2012), which showed that the distribution of the column densities of

OH appear mostly circular even if the nucleus production is heterogeneous. Nevertheless, the presence of icy grains tends to expand those profiles towards the night side of the coma.

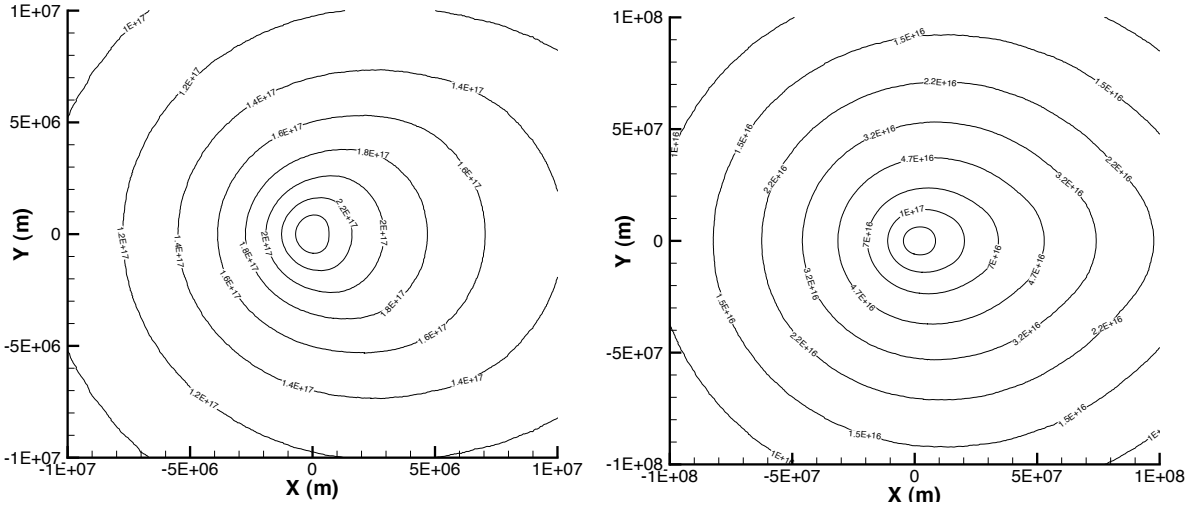

Figure 7.6: The OH distribution observed from Earth with a projected radius of 10^4 km (left) and 10^5 km (right) around the nucleus with a Sun-comet-observer angle of 58.73°and a geocentric distance of 0.15 AU corresponding to November 3^{rd}, 2010.

Knight and Schleicher (2013) observed Hartley 2 by means of photoelectric photometry during the different apparitions of the comet during the past two decades including November 3rd 2010, that is to say one day before EPOXI's closest approach. They observed that the OH and NH coma morphology was enhanced in the anti-sunward hemisphere, which could be explained if a substantial fraction of OH and NH were created by the sublimation of small icy grains which would survive long enough to be affected by radiation pressure and be pushed tailward. Indeed, in our model the lifetime of the icy grains is long enough to enable the radiation pressure to sweep the grains in the anti-sunward hemisphere. These grains constitute a secondary source of water molecules located on the night side of the coma, which then subsequently produce OH molecules by photodissociation. We applied a similar image treatment to the previously computed OH profiles with azimuthal average division such as was done by Knight and Schleicher (2013) for better comparison. The

nucleus is in the center of the image with a square range of 64000 km from side to side (Figure 7.7). When using a size distribution exponent of -3.5, the OH ratio compared to its azimuthal average varies between 0.8 on the dayside and 1.2 on the night side within the range of -32000 km to 32000 km from the nucleus, which is in agreement with the measurements. A similar image without the presence of icy grains would reveal the strong water vapor outflow coming from direct sublimation of the waist part of the nucleus, which is unable to explain the anti-sunward OH enhancement.

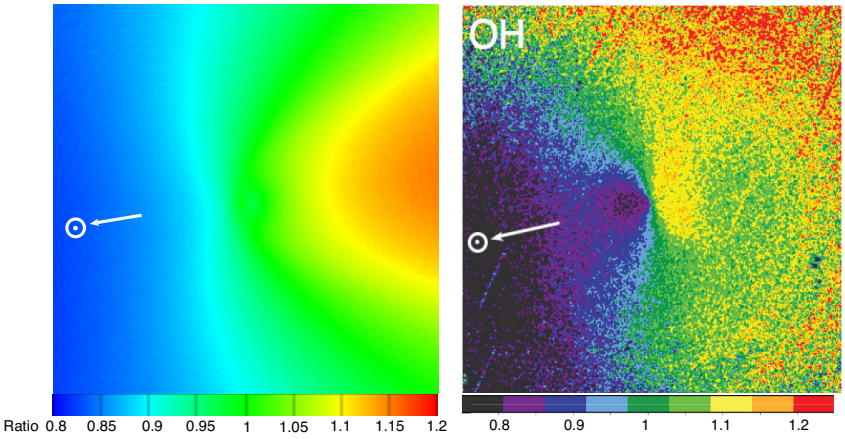

Figure 7.7: Modeled (left) and observed (right, originally published in Knight and Schleicher (2013)) OH coma morphology with ground-based observations using the geometry of November 3, 2010 (Sun-comet-observer angle of 58.13 °and a geocentric distance of 0.15 AU) assuming that the nucleus orientation was similar to the one during the closest approach of the Deep Impact spacecraft as part of the EPOXI mission. The nucleus is in the center of the image with a square range of 64,000 km from side to side. The image features were enhanced by division of an azimuthal median profile.

This comparison enabled us to set the size distribution index to a value of -3.5 that is within the range of values found by fitting ISOCAM 15 micron images with a dust dynamical model (Epifani et al. 2001). But, our model does not include the so-called rocket effect, which is the acceleration of the icy grains due to the higher sublimation

of water ice from the sunward side of the grain (Kelley et al. 2013). This rocket force is only effective if the icy grains and chunks do not rotate, which is probably true for large fragments similar to the ones observed in comet Hyakutake (Harris et al. 1997), but might not be true for the large number of small particles that dominate the extended source of water. Since the rocket effect pushes the grains anti-sunward, the OH asymmetry would be increased for a given size distribution exponent and then, a somewhat steeper size distribution would be required to fit the observations. This process may be reinforced by the value of the density of the grains which here was assumed to be 1000 kg.m^{-3} (pure water) but if the grains are extensively porous, the density may be lower than the one used in this study down to values of $\sim$ 100 kg.m^{-3} (Kelley et al. 2013). A lower grain density would result in a larger maximum liftable grain size and higher velocities. These larger grains would live longer and tend to populate even more the night side of the coma with H_2O and subsequently OH particles. Yet, being more porous, grains with lower density would contain proportionally less water to contribute to the extended source and a larger amount of grains would be required to reproduce the observations.

It is interesting to notice that a similar model, using dirty icy grains with 10% magnetite and 90% of ice with the sublimation rates and equilibrium temperature from Lien et al. (1990) cannot reproduce this asymmetry since the grains' lifetime is too short to enable the radiation pressure to push them to the night side of the comet. Thus, since the production of the grains is correlated to the CO_2 production, most of the grains are released at the sub-solar lobe and then, these dirty icy grains would tend to produce more water on the dayside of the coma and create a dayside enhanced OH distribution. This confirms the presence of pure icy grains as established by A'Hearn et al. (2011).

One last caveat that should be mentioned in comparing our modeled OH distribution with the observations of Knight and Schleicher is that the filling time for the OH coma out to 64000 km is a large fraction of a day and therefore between a half and one rotation period of the nucleus. Therefore, pushing the model parameters we have in order to improve the agreement with the data further is not warranted.

7.2.3 Column Density Computation to Qualitatively Compare the Shape of the Coma with the MRI Measurements

The MRI on board of the Deep Impact spacecraft determined the spatial distribution of water vapor, CO_2, water ice, and organics within a few kilometers from the nucleus showing the relative enhancement of CO_2 at the sub-solar lobe and H_2O at the waist (Fig. 5 of A'Hearn et al. 2011). Hence, for comparison, we computed the H_2O and CO_2 column densities obtained with our model within a square of 10 by 10 km with the nucleus at its center. The column densities were calculated starting at a distance of 694 km, which is the closest approach distance of the EPOXI satellite from the nucleus (A'Hearn et al. 2011) looking perpendicular to the Sun-nucleus direction in the ecliptic plane. Then, we applied a rotation of 135°anti-clockwise so that the nucleus has a similar orientation as in the corresponding figure from A'Hearn et al. (2011). Finally, we only kept the zone of interest within a few kilometers of the nucleus and applied some color filters for better comparison. Figure 7.8 shows intensity mapping of the described column densities for water, CO_2, and icy grains side by side to the MRI measurements from A'Hearn et al. (2011). The water column density is higher at the waist than in the rest of the nucleus showing the more prominent release of water molecules from the waist region than the other areas of the nucleus. In a similar way, the CO_2 column density is more important at the sub-solar lobe where the CO_2 jet carries away large amounts of icy grains. Then, those features appear prominent in our column density mapping as observed by the EPOXI mission. Although the small end of the nucleus was not pointed directly toward the Sun during the time of the EPOXI flyby (A'Hearn et al. 2011, Belton et al. 2013), we assumed an axisymmetric distribution of gas and ice particle about a cylindrical approximation to the shape of the nucleus. For comparison with the observations we rotated the nucleus to a realistic angle of the nucleus symmetry axis with respect to the actual line of sight. This assumption mostly impacts the model results with the apparition of a water vapor outflow at the waist invariant with rotation around the x-axis, which differs from the observations where the water vapor outflow strongly appears on the side of the nucleus directly reached by the sunlight (A'Hearn et al. 2011). The reader should understand that these column density plots are only for qualitative comparison since the brightness images measured

by MRI presented in A'Hearn et al. (2011) have been linearly enhanced for the reader to better see the features. Then, the fact that the opacity was not taken into account in those calculations does not affect their purpose of showing the different areas of the coma.

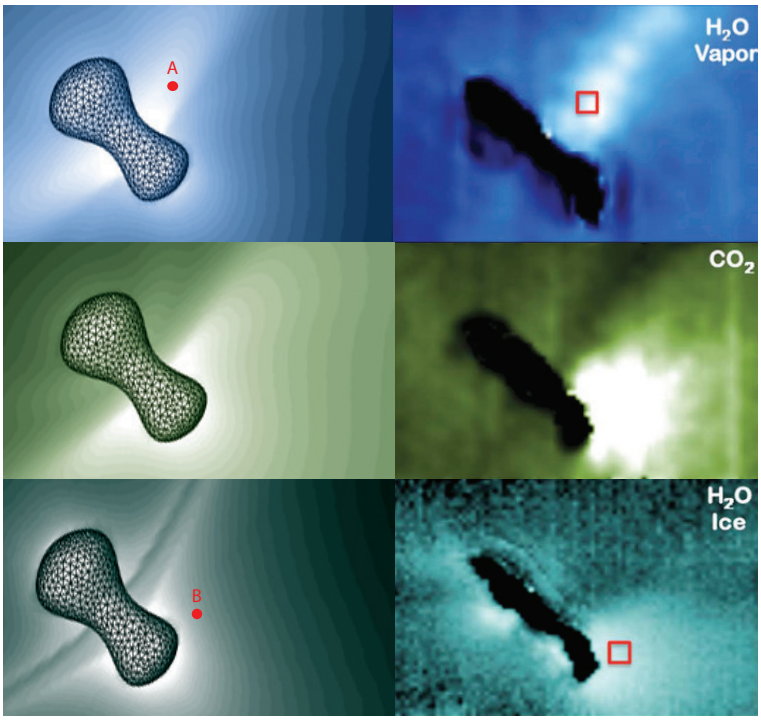

Figure 7.8: Modeled column density distribution (left) and observed relative spatial distribution (right, originally pubilshed by A'Hearn et al. (2011)) of water vapor (top), CO_2 (middle), and icy grains (bottom) in the inner 5 km of the coma revealing the water vapor outflow at the waist, the CO_2 sub-solar lobe jet, and a grain density decrease at the waist. The projection of the line of sights used to compute the IR spectra are illustrated as points A = (-100 m; 1000 m) and B = (-1000 m; 800 m).

7.3 Structure of the Coma of Comet Hartley 2

The previous section enabled us to derive the different gas production from the different sources and the icy grain parameters. A complete description of the modeled coma of

comet Hartley 2 is now possible for both the gas and the icy grains.

7.3.1 Gas Coma

The detailed physics of the modeled gas molecules in the coma of comet Hartley 2 involves direct sublimation of the nucleus and water molecules released from sublimation of icy grains. The gas distribution and thermodynamics are affected by the presence of these different gas sources. Figure 7.9 shows false color contour plots of the water and CO_2 density distribution within 10 and 10^4 km from the center of the nucleus obtained with the DSMC model. Since the comet is relatively close to the Sun, the gas densities are high enough to impose a hydrodynamic regime close to the nucleus. Then, the gas expands both tangentially and radially due to the lateral pressure gradient especially above the waist region since the bi-lobed geometry of the nucleus makes molecules from each side of the waist to be ejected toward the strong water outflow as illustrated by the kinetic temperature plots with superimposed streamlines within 2 km of the nucleus (Figure 7.10). The CO_2 distribution does not vary much with distance from the nucleus and conserves its higher densities on the dayside of the coma due to the dominant production rate from the sub-solar lobe. At a distance of 10 km, the H_2O profile is dominated by the molecules coming from the water vapor outflow at the waist of the nucleus. As the distance increases, the relative contribution of the sublimating icy grains to the H_2O abundance becomes more and more important which explains the broad water distribution at larger distances. This is illustrated by Figure 7.11, which shows a plot of the total water flux (from both direct sublimation of the nucleus and sublimation of icy grains) integrated over a sphere as a function of distance from the center of the nucleus.

The water molecular flux starts at a value of $\sim 2 \times 10^{27}\ s^{-1}$ close to the nucleus since the contribution from the icy grains is very small in that part of the coma, then increases up to a distance of $\sim 10^4$ km due to the progressive sublimation of grains to a maximum of $\sim 8.7 \times 10^{27}\ s^{-1}$, which is relatively close to the value of $8.51 \times 10^{27}\ s^{-1}$ found by measurements of the Lyman-alpha emission of hydrogen by the SWAN all-sky camera on the SOHO spacecraft on the day of closest approach (Combi et al. 2011). Then, the flux

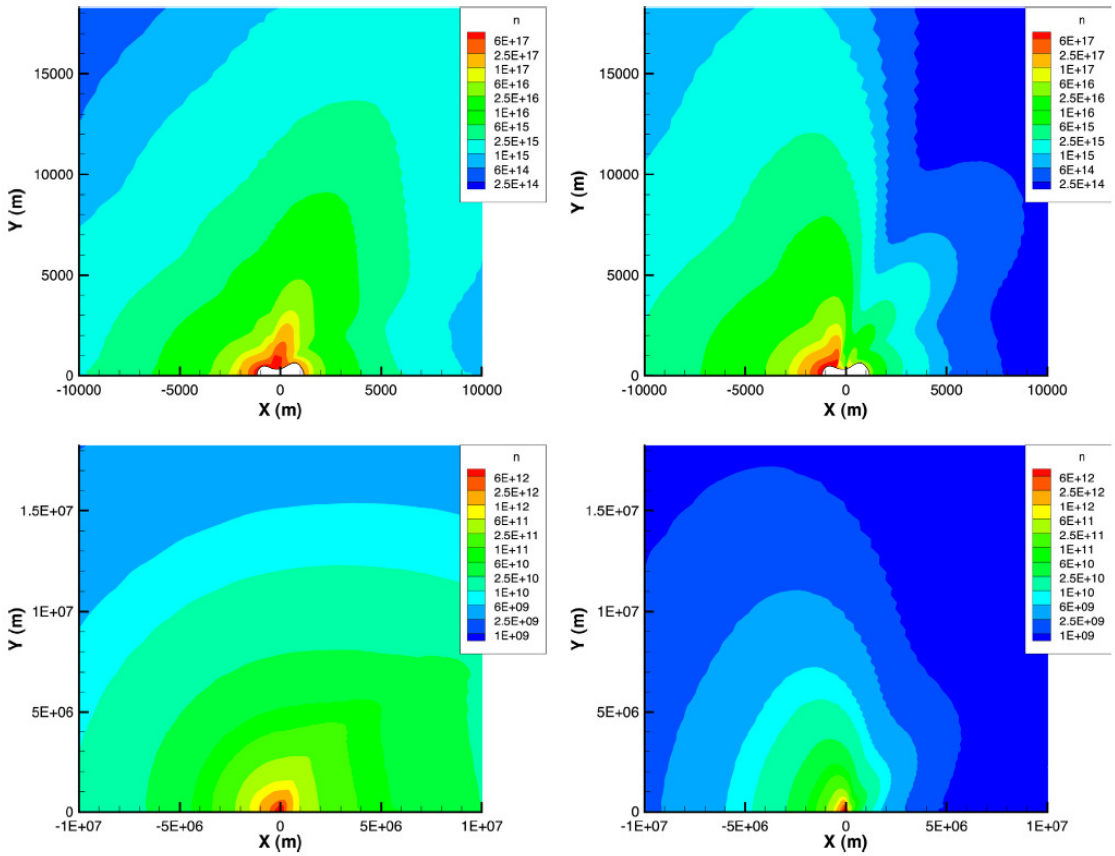

Figure 7.9: Distribution in m^{-3} of water vapor (left) and CO_2 (right) in the inner 10 km (top) and 10^4 km (bottom) of the coma of comet Hartley 2.

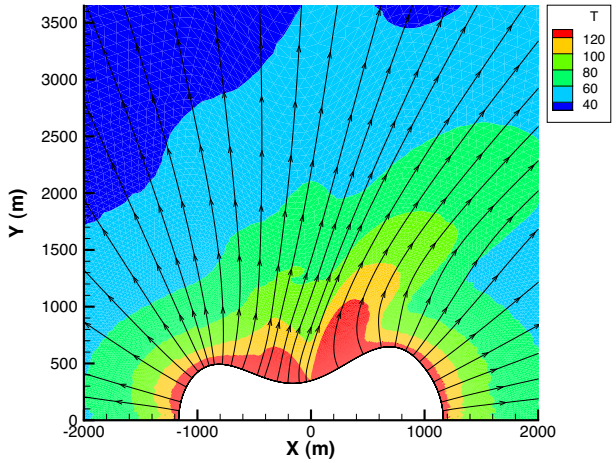

Figure 7.10: Gas temperature (in K) close to the nucleus with velocity streamlines showing the gas expansion.

starts decreasing because photodissociation of water molecules becomes important and the extended sublimation source is depleted. The distance of $\sim 10^4$ km, where the water flux reaches its maximum, implying that most of the sublimation happens by this distance, is very similar to the icy grain halo radius at 1 AU given by Delsemme and Miller (1971). However, water production rates determined from IR measurements with fields of view of a few hundred kilometers agree with those obtained from observations with much larger aperture sizes. This could be interpreted as indicating that most of the water from icy grains and chunks has sublimated by the first few hundred kilometers. Yet, the extended grain sublimation model does reproduce the measured offset of OH distribution which follows the results from Knight and Schleicher (2013) and does not depend on potential calibration differences among the different measurements to determine water production rates. This actually requires the existence of an extended source of icy grains fairly far down the antisunward direction. However, the use of a more complicated grain model with a distribution different than a simple power-law (for example: a "knee" distribution) could result in a better agreement with the IR measurements and still reproduce the OH anti-sunward enhancement. Moreover, the eventual presence of some dirty icy grains, in addition to the pure ones, that would sublimate at lower distances may reduce this apparent

inconsistency.

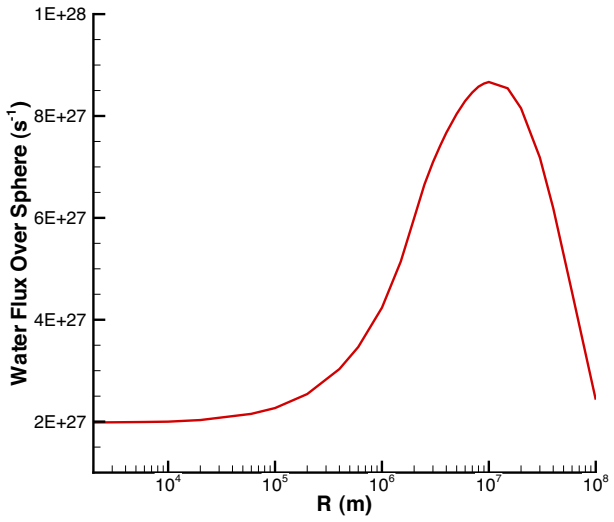

Figure 7.11: Water flux integrated over a sphere (coming from both direct sublimation of the nucleus and the icy grains) in function of the distance from the nucleus

The relative contributions from the different sources of water are as follows:

- $\sim$16% of the water flux results from direct sublimation at the waist region of the nucleus
- $\sim$7% of the flux comes from direct sublimation of the rest of the nucleus
- $\sim$77% of the water is produced by the sublimation of icy grains

These observations are quantitatively illustrated in Figure 7.12, which represents the water vapor and CO_2 density as a function of solar zenith angle at different distances from the center of the nucleus from 5 km to 5000 km. While the high CO_2 densities stay confined mostly in the low solar zenith angles corresponding to its sub-solar lobe jet, the water vapor jet feature becomes less and less important on the H_2O profiles as the distance increases because of the growing contribution of the icy grains. Indeed, overall the number

densities decrease slower than the classical $1/r^2$ approximation due to the slow release of water molecules by the grains.

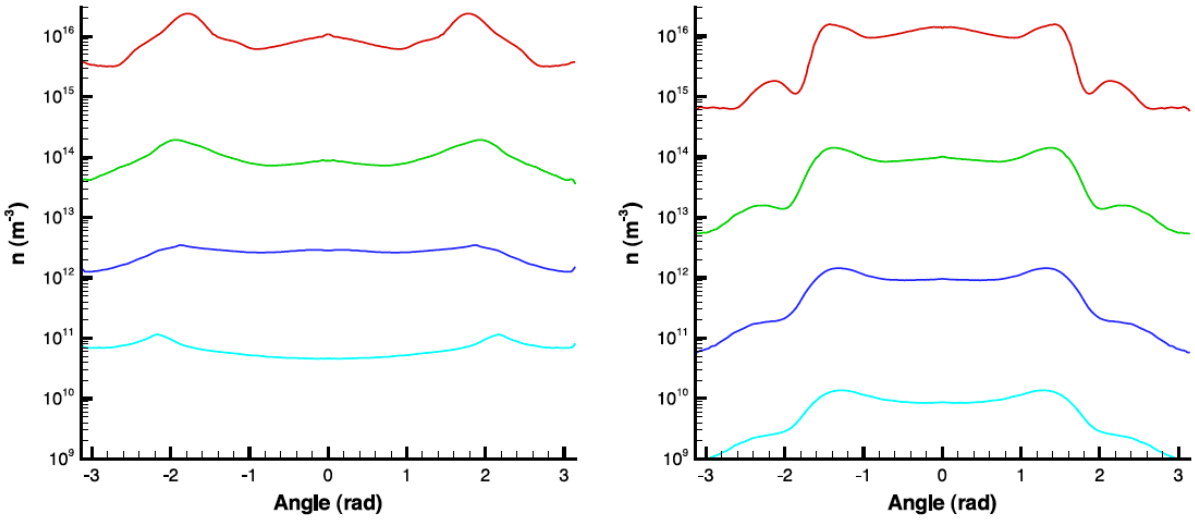

Figure 7.12: Number density of H_2O (left) and CO_2 (right) as a function of the solar zenith angle for different distances from the nucleus: 5 km (red), 50 km (green), 500 km (blue), and 5000 km (teal).

On October 22, 2012, Bonev et al. (2013), using infrared spectra from NIRSPEC/Keck 2, observed an asymmetry in the water rotational temperature profiles with a strong enhancement in the anti-sunward direction. As shown in the study of comets SW3-B and ISON detailed in chapter 6, increased water rotational temperatures can be caused by extended water sources (Fougere et al., 2012). However, the field of view of these water rotational temperature observations were two orders of magnitude smaller than the OH measurements from Knight and Schleicher (2013) discussed above. The radiation pressure is not strong enough to push the icy grains to the night side of the coma within such small distances from the nucleus. Then, these two asymmetries are most likely not related and our model does not reproduce this water rotational temperature increase that close to the comet. Moreover, the range of rotational temperatures from 55 K to 90 K is higher than the one from the model where the retrieved rotational temperatures dealing with the

atmospheric seeing effect using a PSF as discussed in section 6.2.3 with a FWHM of 49 km (Bonev et al., 2013), and including electron collisions heating, stays close to about 55 K. This difference may be due to the release of some large dirty (not made of pure ice) icy grains, with large lifetimes that would drift to the night side of the coma due to the rocket force from their sublimation (Kelley et al., 2013) and would introduce the excess of heat that maintains the rotational temperature above the adiabatic limit as discussed by Fougere et al. (2012). However, these observations were done about two weeks before EPOXI's closest approach. At that time, the outgassing of Comet Hartley 2 was different from that on November 4 and the orientation of the nucleus on that day with respect to both the Sun and the observation still needs to be ascertained even to begin to enable a rigorous modeling study to be performed.

7.3.2 Icy Grain Distribution

Most of the water released by comet Hartley 2 comes from the sublimation from icy grains as they are carried away from the nucleus by the gas drag. A strong correlation was found between the icy grain and the CO_2 densities, which raised the hypothesis that the icy grains were lifted by the hyper-volatiles in collimated jets mostly present at the sub-solar lobe of the nucleus (A'Hearn et al. 2011, Bruck Syal et al. 2013). The icy grain model used in our study presents the equilibrium temperatures and sublimation rates from Patashnick et al. (1975). Spherical pure icy grains were assumed with a radius size range of 1 micron in agreement with the EPOXI observations to 8 cm that is the maximum liftable size by the CO_2 dominated region assuming a grain density of 1000 kg.m^{-3} as was detailed in the section presenting the DSMC model.

The maximum distance reached by the grains before complete sublimation depends on their lifetimes and expansion velocities. Quantitative values for the lifetimes of such pure icy grains have been computed in previous studies. At $\sim$1 AU, pure icy grains completely sublimate within times ranging from $\sim$1 hour for micron sized particles to a few tens of years for the largest grains modeled in our study (8 cm) (Beer et al. 2006). The large lifetimes of the grains make them subject to radiation pressure that slowly pushes them

to the night side of the coma (Figure 7.13 and 7.14). Also the sublimation jet force (non-gravitational force) on the largest particles also might tend to push them to the night side. Although the largest particles actually contain most of the mass, their surface area to volume ratio is much smaller making them less effective at delivering important quantities of additional water vapor during the day or two of build-up time of the visible water coma.

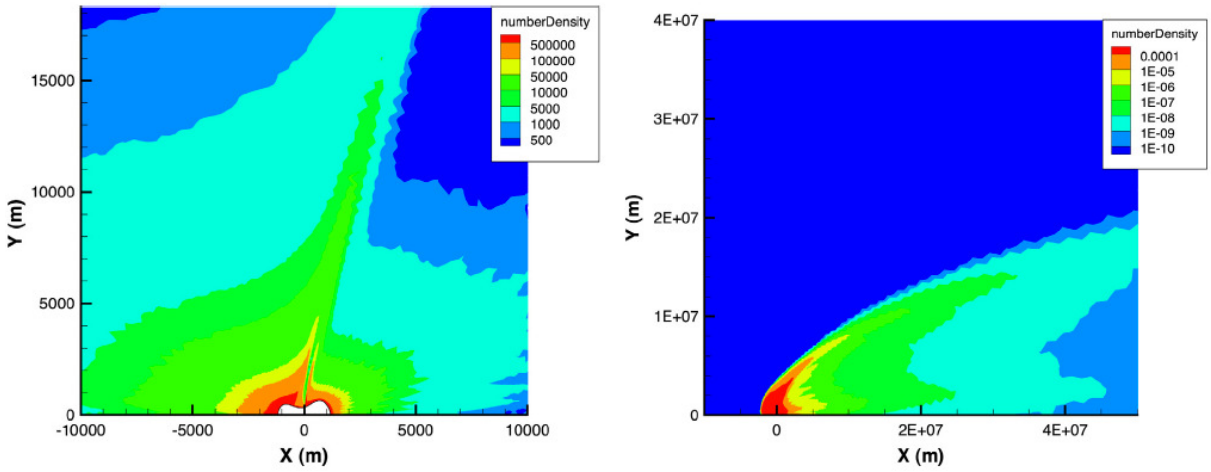

Figure 7.13: Total grain number density (in m^{-3}) within 10 km (left) and a few 10^4 km (right) with appearance of a tail due to radiation pressure.

The grain mass release is correlated with the CO_2 outflow at the nucleus surface boundary and then the grain density dominates at the small lobe close to the nucleus with values up to more than 5×10^5 m (Figure 7.13). Figure 7.14 shows the average speed of the grains within 2 km and 3000 km from the nucleus with streamlines. Since the grains decouple from the gas relatively fast (10 nucleus radii according to Finson and Probstein 1968) so that they tend to expand tangentially less than the underlying gas that drives them (Combi et al. 2012), their velocities close to the nucleus determine most of their dynamics until radiation pressure becomes important. Due to the power-law size distribution used here, the number of particles is driven by the small particles while most of the mass is present in the large grains. The grains are released normal to the local surface but their trajectories

when injected from the waist deviate toward more radial directions by the strong water vapor outflow. Moreover, the highest bulk speeds ($\sim$100 m.s^{-1}) are found above the waist where the grains come from regions of the nucleus with lower gravity and high gas flux. At large distances, radiation pressure becomes important and pushes the grains anti-sunward so that within $\sim$2000 km from the nucleus, all the grains expand toward the night side of the coma. This is an important process at large distances since the grains will constitute a source of water on the night side.

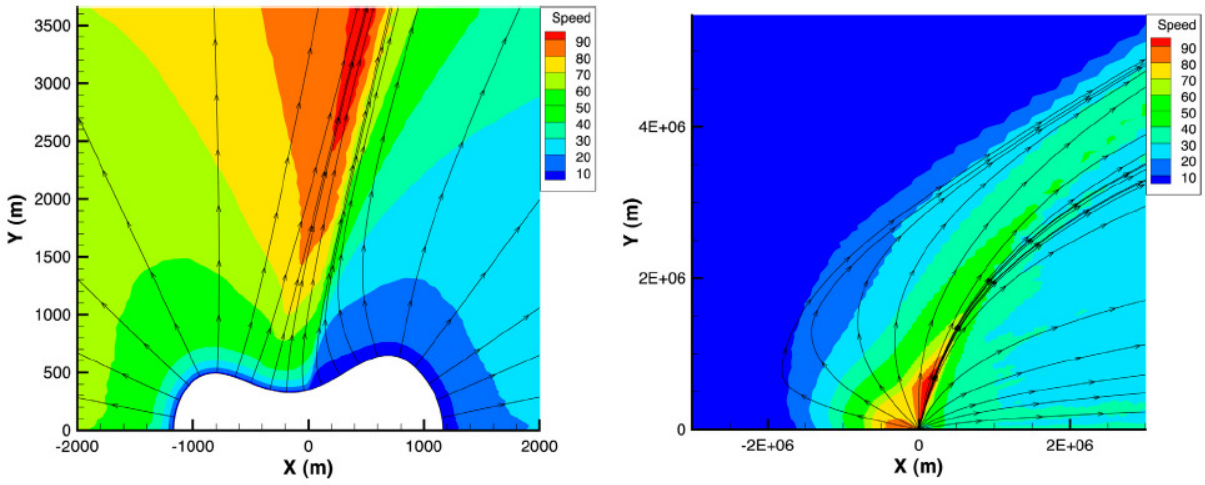

Figure 7.14: Average bulk speed of the grains (in m.s^{-1}) within 2 km (left) and 3000 km (right) from the nucleus with streamlines.

The distribution of the grain density at a given distance tends to stay relatively constant at low solar zenith angles where the CO_2 production rate is dominated by the constant jet source (Figure 7.15). Indeed, the CO_2 flux at the sub-solar lobe only varies due to the modest contribution from the distribution as in Tenishev et al. (2008), which is much lower than the jet contribution in this area of the nucleus (Figure 4.5). The main source of the residual density variation (a factor of $\sim$2) in this region of the coma is mostly due to the gravity field. Then, a density and bulk velocity spike arises at about 90°where the smallest grains, with radii of $\sim$1 micron, reach a speed of more than 100 m.s^{-1} while medium size

grains (radii of $\sim$5 mm) expand at 2 m.s^{-1} at a distance of 5 km from the nucleus (Figure 7.15). This grain flux increase is created by the sharp decrease of gas production rate with solar zenith angle forming a tangential gas flow and making the gas to expand into the regions of lower densities. The icy grains, coupled to the neutral gas, are thus also pushed toward the night side of the nucleus, which explains the variation of its location with distance from the nucleus (Tenishev et al. 2011). The shape and the different chemistry of the nucleus probably intensify this effect. Indeed, the grains produced on the faces of the "V" shape of the waist tend to be released in a converging fashion until the strong water outflow from the waist deviates them such that they expand parallel to its direction as seen in Figure 7.15, creating an apparent higher grain production from this region. Then, the grains keep expanding in that direction after decoupling from the gas. Similar features are reminiscent of the concave regions of the "bean-shaped" nucleus models of Crifo and Rodionov (1997).

7.4 Toward a 3D Representation of the Coma of Comet Hartley 2

While 2D kinetic models such as presented above can give some critical insights of the physics of the coma, the cylindrical symmetry around the Sun-Nucleus axis gives strong constraints that limit the geometry used in the model such as the solar orientation with respect to the nucleus or the position of a small active area limited to a range of latitudes. Then, the implementation of a 3D model of the coma of Hartley 2 would be a step forward into better understanding the physics of the coma resulting from such a complex outgassing system. The current restriction on doing so is the cell size limited by the mean free path that leads to some memory and run speed issues.

However, an attempt to prepare such a model has been made in order to show the improvement that would bring toward a better reproduction of the observations. In 3D, the Sun does not have to be aligned with the symmetry axis. Thus, the Sun position can be chosen similar to at epoch of the observations when the comet was at 1.064 AU from the

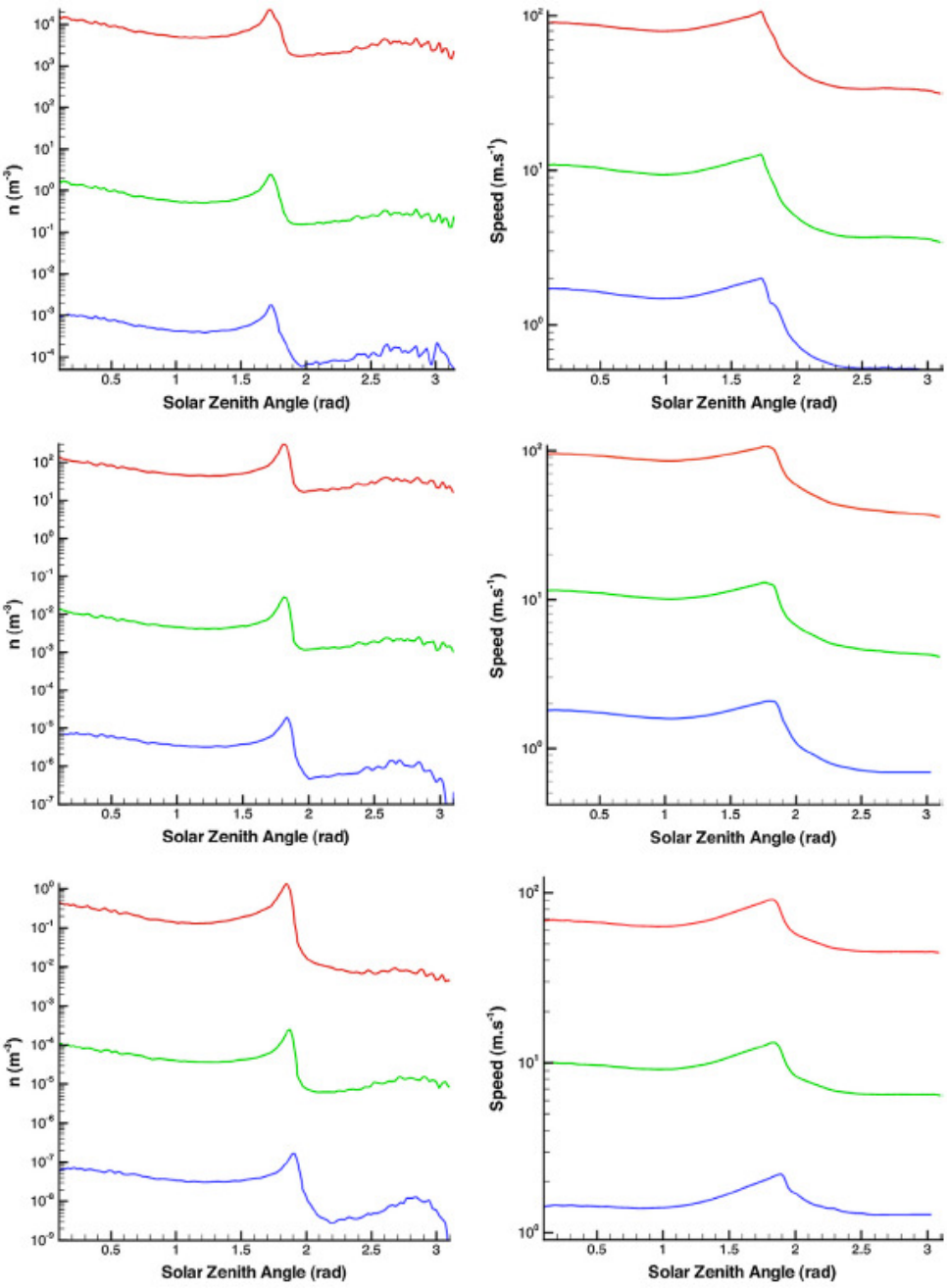

Figure 7.15: Number density (left) and speed (right) of the grains at different distances: 5 km (top), 50 km (middle), and 500 km (bottom) in function of the solar zenith angle for different grain sizes: $\sim 10^{-6}$m (red), $\sim 10^{-4}$m (green), and $\sim 5 \times 10^{-3}$m (blue).

Sun with an angle of about 53 degrees between the long axis of the nucleus and the solar direction (Belton et al. 2013). Then, arbitrarily choosing to have the XY plane with a positive y-coordinate, we can define the gas production rates and nucleus surface temperature distributions using the angle between the local normal at the surface of the nucleus and the solar direction (Figure 7.16). The temperature and local fluxes are then not anymore symmetrical with respect to the long axis of the nucleus but actually computed using the geometry at EPOXI's closest approach.

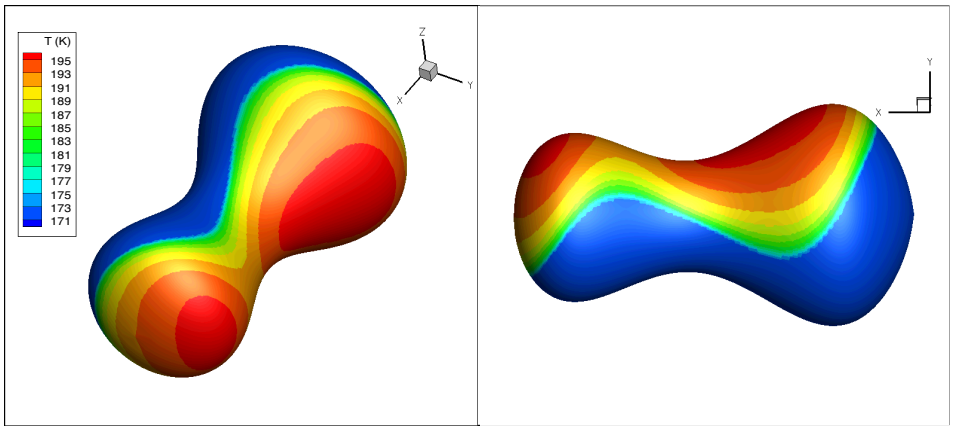

Figure 7.16: Surface temperature of comet Hartley 2 at epoch of EPOXI's closest approach assuming that the Sun is at an angle of 53° of the nucleus' long axis using the local normal and the model from Tenishev et al. (2008).

With such a geometry, the bigger lobe has part of its surface that has relatively low solar zenith angle implying higher temperature and higher gas fluxes, which seems to coincide with some secondary CO_2 jets observed by EPOXI (A'Hearn et al. 2011, Sunshine et al. 2013). Then, it is clear that the solar zenith angle dependent source of gas will have higher fluxes in that region than in our 2D model. A similar study modeling IR spectra would be necessary in order to derive the relative contribution from each source. For visual purposes, we ran a 3D simulation with gas production rates: for water 1.28×10^{27} s^{-1} distributed as in Tenishev et al. (2008) with respect to the local normal and an additional source of 9.0×10^{26} s^{-1} at the waist, while for CO_2 we kept the proportions from the 2D

model. It is necessary to understand that here the cell size used in the simulation does not respect the necessary conditions to be smaller than the local mean free path. Thus, the simulation is not rigorously exact and the results are only for showing the importance of such a 3D model. The next section will show that we have all the tools necessary to simulate such a rigorous 3D model. The density output of this simulation clearly shows an asymmetric profile (Figure 7.17). The H_2O vapor outflow at the waist is clearly enhanced on the side illuminated by sunlight. Moreover, the CO_2 density is tilted toward the direction of the Sun. Such a 3D model can prevent the inherent flows of our 2D axisymmetrical model and would enable a better reproduction of the data.

Another improvement can be done using a more realistic shape than the analytical form presented in our model. Indeed, Thomas et al. (2013) used mostly the data from MRI on board of the Deep Impact spacecraft during the EPOXI mission to derive a nucleus shape model illustrated in Figure (7.18) and surface feature maps. The model can then take into account the local topography of the nucleus.

The next section will describe a full 3D rigorous model of comet 67P/Churyumov-Gerasimenko with a realistic nucleus showing that we have all the tools necessary to build such a complex 3D model also for comet Hartley 2. However, a 3D model of the coma of comet Hartley 2 will require a careful treatment of the zone where the mean free path is relatively small, notably in the water vapor outflow, for example using a fluid solution or perhaps a collision limiting approach within the DSMC particle simulation, which is out of the scope of this thesis.

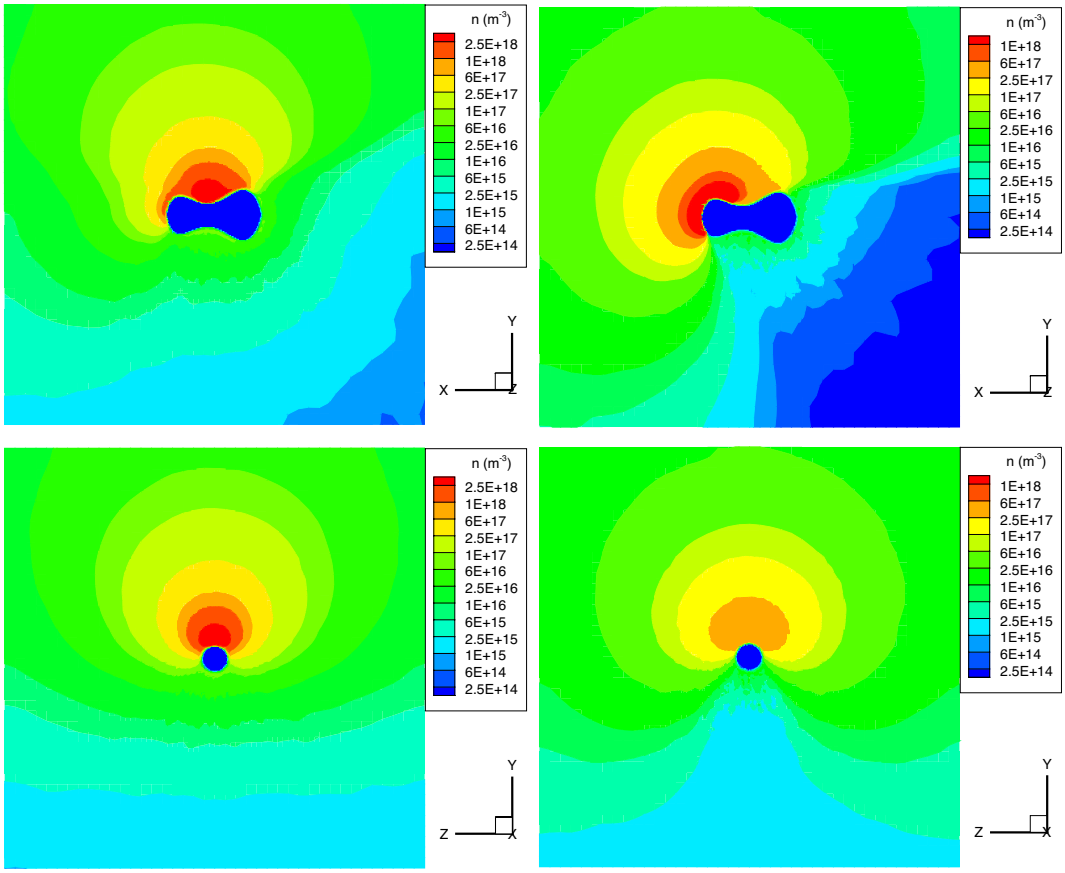

Figure 7.17: Number density for H_2O (left panels) and CO_2 (right panels) in the Z and X planes showing the influence of the geometry in the results output for comet Hartley 2. This is only for illustrative purposes since cells significantly larger than the mean free path were used for this simulation.

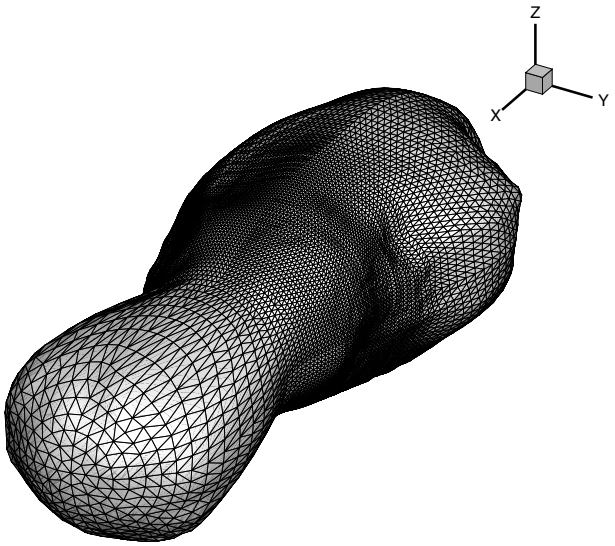

Figure 7.18: 3D representation of the nucleus of comet Hartley 2 from Thomas et al. (2013).

Chapter 8

A 3D Simulation of the Coma of Comet 67P/Churyumov-Gerasimenko

The Rosetta spacecraft is on its way to its target comet CG. Both for mission planning and data analysis, a detailed model CG's coma is necessary. While the existing 2D axisymmetrical models (Tenishev et al. 2008, 2011, Combi et al. 2012) can give invaluable information about the coma Rosetta's target, the cylindrical symmetry assumption has inherent issues such as the requirement to use a cylindrically symmetric nucleus, the necessity to have a sunward spin axis and active area. Our current knowledge of comet CG enables us to describe the nucleus and the sources with more details giving the chance to better constrain the model and have a more realistic cometary model. As this thesis is being completed more and more details are being released every few days about the shape of CG. So the 3D results described herein should be taken as a proof of concept of the methodology to be applied in the future. The present section details a 3D simulation of the coma of comet CG with Direct Simulation Monte Carlo using a realistic nucleus shape and outgassing.

8.1 Triangulated Surface Boundary Condition

In order to enable the use of a realistic nucleus shape, the AMPS code uses a triangulated mesh of the surface of the nucleus. This technique provides the ability to describe any irregular shape that the user would like to adopt for any application of the DSMC model, which is critical for cometary applications due to the dramatical differences in the nucleus shapes from one comet to another.

The 3D AMPS code uses adaptive cubical cells as described in section 2.2.4. It is then clear that the irregular triangulated shape of the nucleus will not coincide with the cubical meshing used for the simulation. Then, some of the cells have part of their volume inside the body of the nucleus while the rest remains outside. To take this effect into account and not make any further approximation with respect to the nucleus shape, the AMPS code uses cut cells. Each cube that intersects the surface body is split into a part that is within the body where the modeled particles cannot be located, and another region within the coma computational domain. It is then possible to figure out if a point is located inside or outside the irregular body shape by computing the number of intersections between a random ray and the nucleus' surface. If the number of intersections is an odd number, the corresponding point is located inside the body, if it is even, the point is outside. The use of cut cells permits the volume where particles can be located within each cube cell intersecting the nucleus to be computed accurately. This is critical for the calculation of the collision frequency close to the surface of the nucleus.

It is relatively straightforward to derive the local external normal of each triangular element giving a clear idea of the local solar zenith angle to define the boundary conditions at the surface of the nucleus correctly. The particles are then created at the surface of the realistic nucleus using the conditions defined by the user. To avoid strong jumps in the direction of the local normal, each node is assigned a normal direction being the average of all the normals of the neighboring triangles. Then, particles are emitted in a direction corresponding to a linear interpolation between the directions of the normals assigned to the three nodes included in the corresponding triangle.

AMPS can also refine and smooth the triangulation of the irregular body. This can be valuable when the triangulation of the nucleus is too coarse to enable the DSMC simulation to provide smooth results creating artificial features. Indeed, if the surface triangulation is not precise enough, unrealistic rough edges can appear on the body that could lead to some unphysical feature in the coma. Hence, AMPS has the ability to smooth the surface of the nucleus by increasing the resolution of the triangulation using the middle of the edges of the existing triangles, resulting in an increase of the number of triangles meshing the body. This process can be applied several times by the user until the body shape does not have any artificial rough edge.

With AMPS, coma simulations can be run with any nucleus as long as a triangulation of its surface is provided. The next section will show a direct application of this triangulated body within the DSMC simulation using a sphere, and will be followed by a section describing the coma with a realistic irregular nucleus.

8.2 Validation of the 3D Coma Model and Comparison with the 2D Model

Since the 3D model is a new tool using the AMPS computation with a new core for the sources of the code, it is necessary to make some comparisons with a previously validated model. Indeed, the current core of the code was tested for basic fluid dynamics applications such as normal shocks, and it has been used for numerous applications such as Mercury (Tenishev et al. 2012) , the Moon (Tenishev et al. 2013), or Mars (Lee et al. 2014). However, the current core had never been applied to comets, and the cometary coma requires some additional physical processes that were not present in the previous applications. Then, we decided to run a case similar to the 3.25 AU from Tenishev et al. (2008) with a total gas production rate of 1.0×10^{24} s^{-1} with a CO to H_2O production rate ratio of 5:100 and a dust to water mass production rate ratio of 0.8. The gas flux distribution and surface temperature follow the thermo-physical model from Davidsson and Guttierrez (2004, 2005, 2006) as mentioned in section 3.1.1 (Figure 3.1), which gives a

day/night asymmetry to the conditions. In both cases, the Sun is located along the negative x-axis. A spherical nucleus of 1.98 km radius is approximated by a mesh of about 7500 triangles (Figure 8.1).

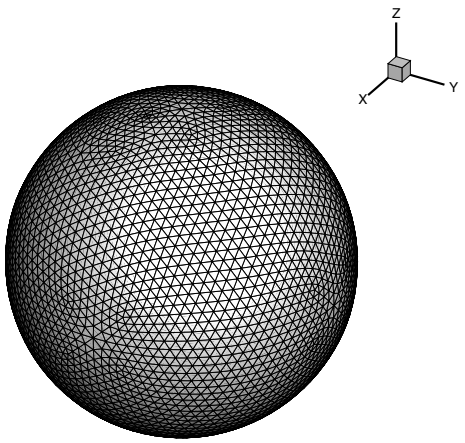

Figure 8.1: Sphere of 1.98 km of radius approximated by about 7500 triangles used for the comparison between the 3D and 2D coma models.

Figure 8.2 shows direct number density output of the DSMC model within a cube of 20 km centered on the nucleus. Panel A shows the number density profile for the 2D model of the 3.25 AU case from Tenishev et al. (2008). Panels B, C, and D illustrate the number density contours for the same case in the three principal planes. The case being by construction cylindrically symmetrical around the x-axis, the X plane density shows relatively circular contours, the surface conditions being the same for all latitudes. Also, the cylindrical symmetry imposes that the density profiles are similar in the Y and Z plans. Thus, while it was important to show that the 3D model is reproducing correctly all planes, we will perform a more quantitative analysis only within the Z plane. Table 8.1 gives examples of macroscopic numerical comparisons between the 2D and 3D DSMC models for a few points. We notice that the number density difference stays within about 15%, while the kinetic temperatures and velocities are within 10%. These small differences are mostly due to the coarser mesh used in the 3D case so that larger interpolation is required between the different nodes.

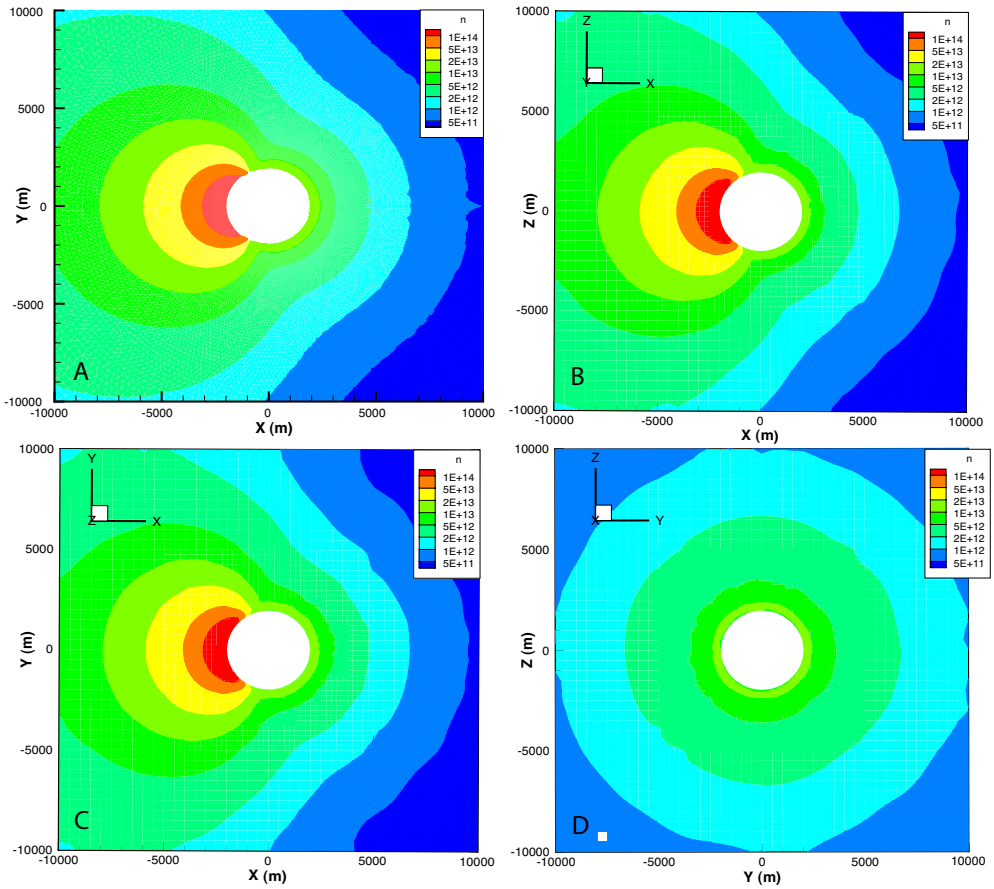

Figure 8.2: Direct H_2O number density output from the 2D coma model (panel A) and 3D coma model in the Y plane, Z plane, and X plane (panels B, C, and D respectively) for a case corresponding to the 3.25 AU case from (Tenishev et al. 2008).

This analysis shows that the 3D coma model reproduces correctly the 2D test case within an acceptable margin. Then, we now have the ability to use more complicated and realistic models without being restricted to the cylindrical symmetry. The next subsection will show the full capability of this tool by modeling the coma of comet CG in 3D using a realistic nucleus and a complex outgassing adapted to the topology of the nucleus.

Coordinates (km)	Dimension	n (m^{-3})	T (K)	V ($m.s^{-1}$)
(-5.0, 0, 0)	3D	2.91e13	36.96	447.67
(5.0, 0, 0)	3D	1.81e12	30.61	388.31
(0, 3.0, 0)	3D	6.40e12	52.88	357.81
(2.5, 2.5, 0)	3D	3.79e12	41.39	376.61
(-5.0, 0, 0)	2D	2.99e13	36.80	455.19
(5.0, 0, 0)	2D	1.52e12	30.78	403.78
(0, 3.0, 0)	2D	5.86e12	59.11	373.12
(2.5, 2.5, 0)	2D	3.79e12	40.21	370.02

Table 8.1: H_2O number density, kinetic temperature, and velocity comparison between the 2D and 3D DSMC models for a few locations.

8.3 3D modeling with a realistic nucleus shape and outgassing

While 2D axisymmetrical models require the use of a cylindrical nucleus, a full 3D simulation enables modeling of the coma of a comet with any particular nucleus shape. The first observations of CG's nucleus were based on ground-based CCD observations from 1991 suggesting an effective radius of 2.8 km assuming an albedo of 0.04 (Mueller 1992). Subsequent observations were only able to deduce upper limits for the radius that corroborate Mueller's observations: radio observations reported a maximum radius size of 3.0 km (Kamoun et al. 1999), while visible observations suggested 2.9 km (Lowry et al. 1999). In 2003, Hubble Space Telescope (HST) observations of comet CG enabled Lamy et al. (2006) to obtain a detailed portrait of its nucleus with an effective radius of 1.98 km for an assumed albedo of 0.04, and the inversion of the light curve led to a possible three-dimensional solution of the nucleus (Figure 8.3). A few years after, Lowry et al. (2012) presented a fully convex triangular-facet shape model based on optical imaging observations performed at ESO NTT as the comet was passing through aphelion, showing

that a convex nucleus can fit the observational data.

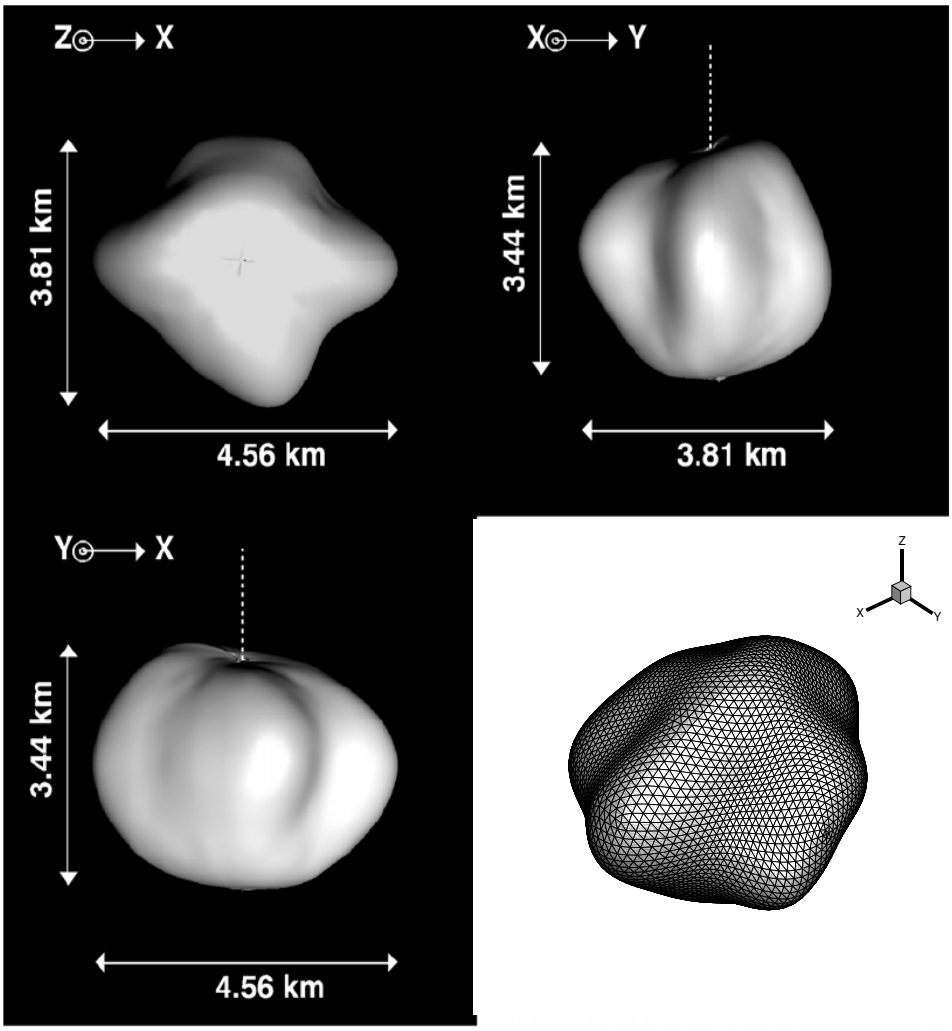

Figure 8.3: Three-dimensional shape of the nucleus of CG reconstructed from the inversion of the R light curve (Lamy et al. 2006) and the refined mesh around the nucleus used in the simulation (bottom right panel).

In our simulation, we used a triangulated representation of the nucleus shape from Lamy et al. (2006) enabling us to accurately represent the zones that will be in the sunlight at

a given instant. Then, we adapted the thermophysical model from Davidsson and Gutiérrez (2004, 2005, 2006) that was previously used in Tenishev et al. (2008, 2011) from a spherical shape to a more realistic shape using the angle between the local normal and the direction to the Sun. This approach enabled us to make an optimal use of the nucleus shape in the model deriving the areas in the shade and in direct sunlight, leading to the most realistic nucleus outgassing distribution possible. This is a similar approach for setting the surface conditions as used in previously published 3D coma models (Crifo and Rodionov 1997) based on hydrodynamics using non-spherical/non-axisymmetric nucleus shapes.

The DSMC approach requires that the cell size is smaller than the local mean free path. The dramatic variation of the involved characteristic temporal and spatial scales requires the use of adaptive grids that were presented in section 2.2.4 from this thesis. However, the lowest limit of spatial scales for a given simulation is given by the mean free path at the sub-solar point, which varies from 0.5 m at 1.3 AU to 400 m at 3.25 AU (Tenishev et al. 2008). Then, even with such an adaptive grid, the main difficulty in using a three-dimensional numerical kinetic simulation of cometary coma at small heliocentric distances will be the high number of cells that will build up close to the surface of the nucleus in order to resolve the Knudsen layer, that will overflow the processor memory, result in unmanageable data output files, and slow down considerably the simulation. When propositions of solution exist, we decided to limit this study to 2.7 AU and 3.25 AU cases where the mean free path is large enough to enable us to run a rigorous DSMC full 3D model.

Three-dimensional DSMC models were run for cases similar to the 2.7 AU and 3.25 AU cases from Tenishev et al. (2008, 2011) from the surface of the nucleus up to approximately 10 km assuming that the Sun is aligned with the x-axis enabling us to make a direct comparison of the results with the previously published 2D axi-symmetrical model with a spherical nucleus published in Tenishev et al. (2008, 2011) and presented in previous sections. However, we point out that the Sun can be placed at any position, enabling to reproduce all geometries at epoch of observations. The total gas production rates are assumed to be 8.0×10^{25} s^{-1} and 1.0×10^{24} s^{-1} respectively with a CO to H_2O production

rate ratio of 5:100 and a dust to water mass production rate ratio of 0.8. The dust power-law index was picked to be -4 with a radius size range of 10^{-7} m to 10^{-2} m such as in the original cases. Similarly as in the case of comet Hartley 2 in the previous section, the gravity acceleration around the non-spherical nucleus was computed adding the contribution of about 1300 tetrahedrons that fully describe the nucleus shape of comet CG reaching accelerations of the order of 10^{-4} m.s^{-2}.

8.4 Model Results and Comparison with Spherical Nucleus

8.4.1 The Water Coma

Direct outputs from the model are presented in Figures 8.4 and 8.5, with water number densities, velocities, and kinetic temperatures in each principal plane for the 3.25 AU case. A direct comparison of water number densities in the case of a spherical nucleus and a model with a realistic shape is enabled by Figure 8.4. While the X plane results seem relatively spherical since the Sun is located in a direction perpendicular to it, the results in the two other planes have a strong asymmetry with larger values in the sub-solar hemisphere. However, the geometry of the surface creates areas with low solar zenith angles in regions far from the x-axis. This implies that the gas distribution is somehow broader with strong fluxes less localized around the x-axis than in the case of a spherical nucleus.

Figure 8.6 illustrates the number density profile in contour plot for the 2.7 AU case, showing the influence of the heliocentric distance on the macroscopic parameters. The gas flux released from the nucleus is 80 times stronger at 2.7 AU than at 3.25 AU in the scenario chosen here, resulting in much larger gas densities in the 2.7 AU case than at perihelion. The day/night asymmetry is stronger at lower heliocentric distances where the relative contribution from the night side areas of the nucleus to the total gas production rate is smaller with 9.2% and 11.6% at 2.7 and 3.3 AU, respectively. The distribution being

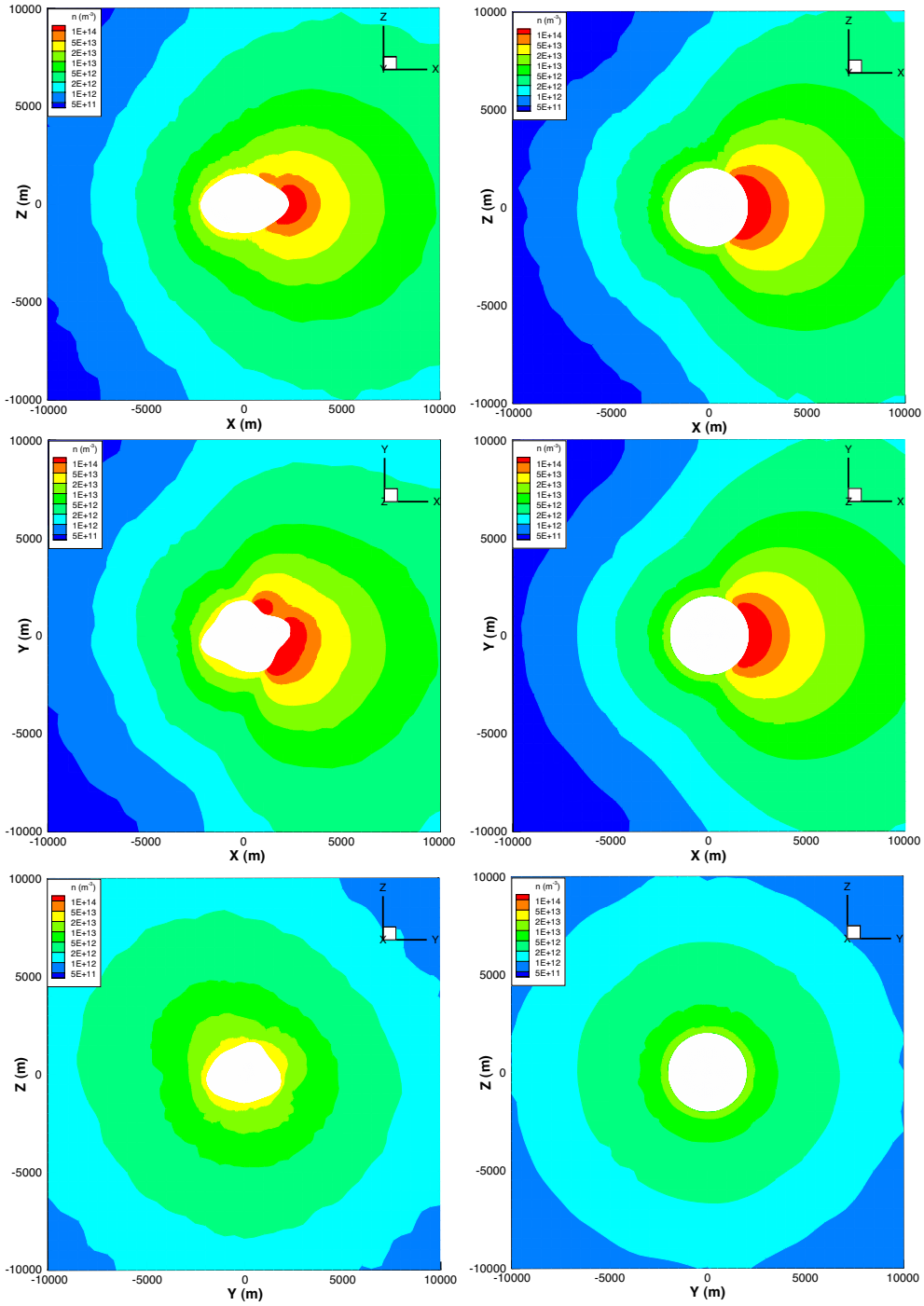

Figure 8.4: Number density (m^{-3}) of water molecules in the three different origin planes at 3.25 AU using a realistic nucleus shape (left panels) and a sphere (right panels).

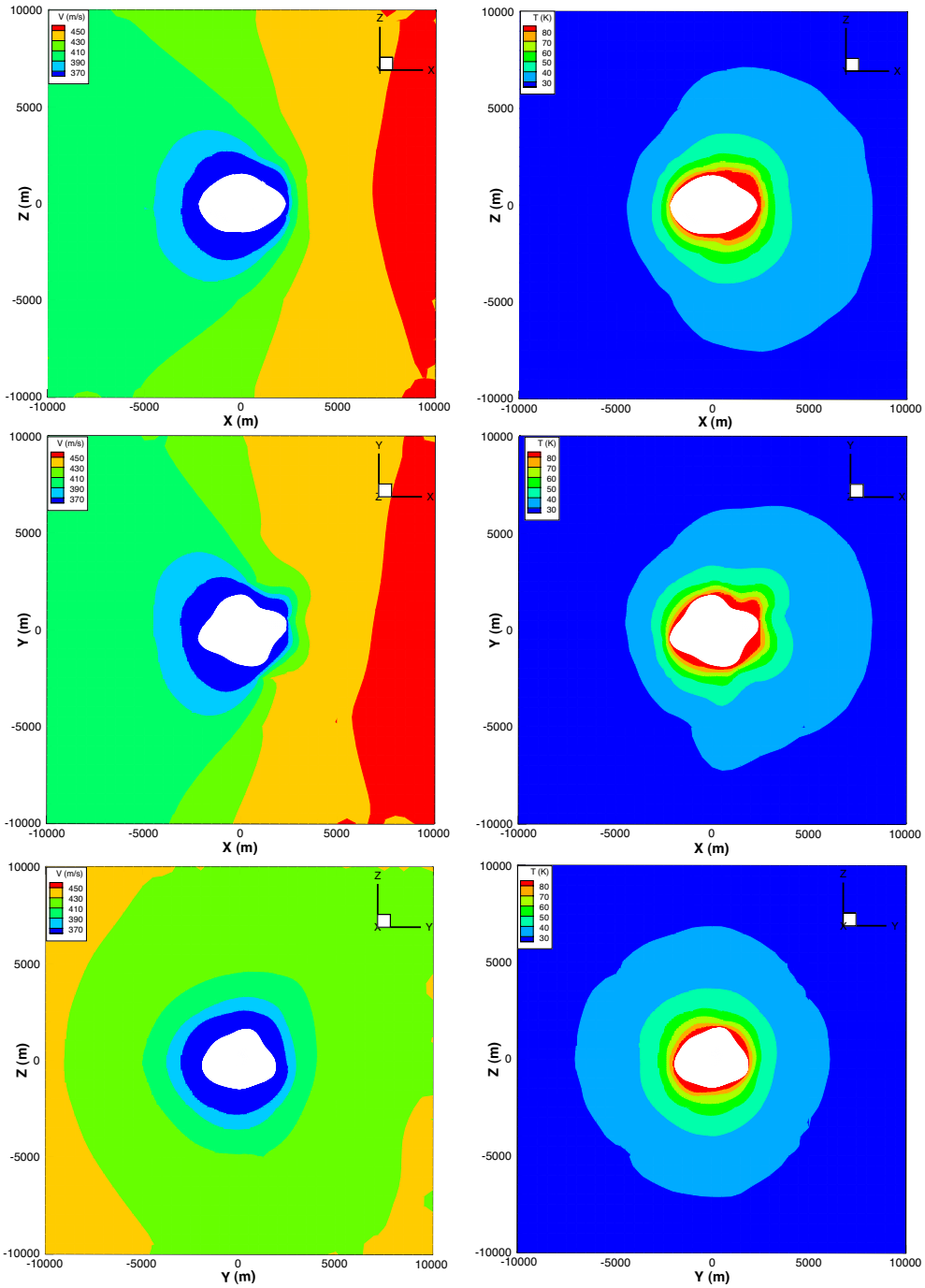

Figure 8.5: Velocity (m.s^{-1}) (left panels) and kinetic temperature (K) (right panels) of water molecules in the three different origin planes at 3.25 AU using a realistic nucleus shape.

more concentrated at lower heliocentric distances, the isolated areas that are with low solar zenith angles contribute even more to the total gas production rate and then appear more prominent.

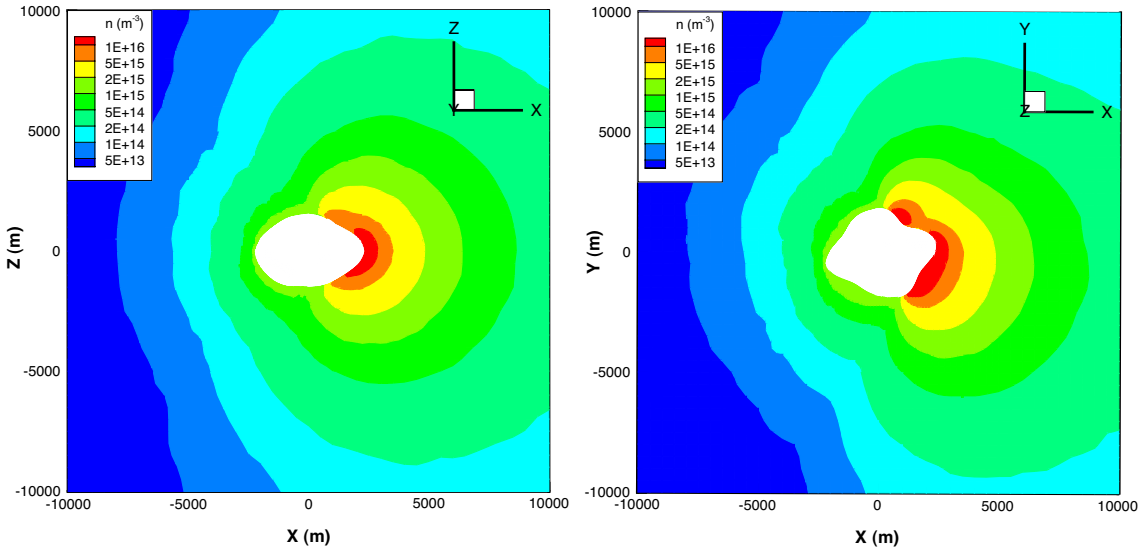

Figure 8.6: Number density (m^{-3}) of water molecules in the three different origin planes at 2.7 AU using a realistic nucleus shape in the Y (left panel) and Z (right panel) planes.

8.4.2 The Dust Coma

As discussed in section 5, the dust grains decouple from the gas within a few nucleus diameters and stay more collimated than the gas (Combi et al. 2012). Hence, the topography of the nucleus has a stronger impact on the dust than it has on the gas. Then, the use of a realistic nucleus shape is more critical to model the dust coma than the gas coma, and we expect to see more features such as narrow jets. Indeed, while the presence of a rough terrain is not necessary in order to create jets (Tenishev et al. 2011, Combi et al. 2012), the presence of concave areas creates converging flows that will result in jets (Zakharov et al. 2009). This justifies the importance of computing accurately the gravity field around the nucleus so that the grains are correctly accelerated.

Figure 8.7 shows the dust grain density and the mean grain speed for the 3.25 AU case in the Y and Z planes. While the section in the Y plane of the mean grain speed does not show much asymmetry between positive and negative z locations and is similar to the spherical nucleus case (Tenishev et al. 2011), the nucleus shape imposes a clear different behavior for positive and negative y locations in the Z plane. Indeed, the maximum mean grain speeds of about 4 m.s^{-1} are reached at closer distances from the nucleus for the negative y locations suggesting that the balance between the gas drag and gravity forces is more dominated by the gas drag in this region. This generates an apparent jet in the number density plot. From another part, a jet of a totally different nature appears in the Y plane in the upper side of the nucleus. Indeed, the velocity not showing any particular feature in this region suggests that this jet is created by a concavity at the surface of the nucleus implying that flows are converging in the same direction. Similarly, the total dust grain density and mean grain speed for the 2.7 AU case are represented in Figure 8.8. The mass flux of grains injected being proportional to the gas flux, the 2.7 AU case has a dust mass flux of 1.8 kg.s^{-1} compared to 0.023 kg.s^{-1} for the 3.25 AU case. It is then not surprising to see higher total dust number densities at lower heliocentric distance. Moreover, the gas drag is way more important in the 2.7 AU case so that the grains are accelerated to larger values reaching velocities of more than 30 m.s^{-1} within the first 10 km. .

Rubin et al. (2014) studied the mass back flux on a generic comet taking parameters relative to comet CG as an attempt to compute the amount of volatile material and icy grains that get trapped in regions in shadow for typical comets as an attempt to explain asymmetry in the seasonal gas production rate (Snodgrass et al. 2013). Using a simplified model with 2D axi-symmetrical DSMC simulations, this study showed that this effect can contribute to a fraction of such a seasonal difference in production rate (Rubin et al. 2014). Our model can go a step further in the case of comet CG by using a realistic nucleus shape where additional zones of shadow exist due to concavities. An interesting phenomenon with the grain back flux is the presence of some dust grains that are lifted and accelerated from the pre-terminator part of the coma but then do not reach the escape velocity and fall back with ballistic trajectories (Tenishev et al. 2011). For the 3.25 AU case, some grains with radius between 1.0×10^{-5} and 3.2×10^{-5} m fall back onto the nucleus'

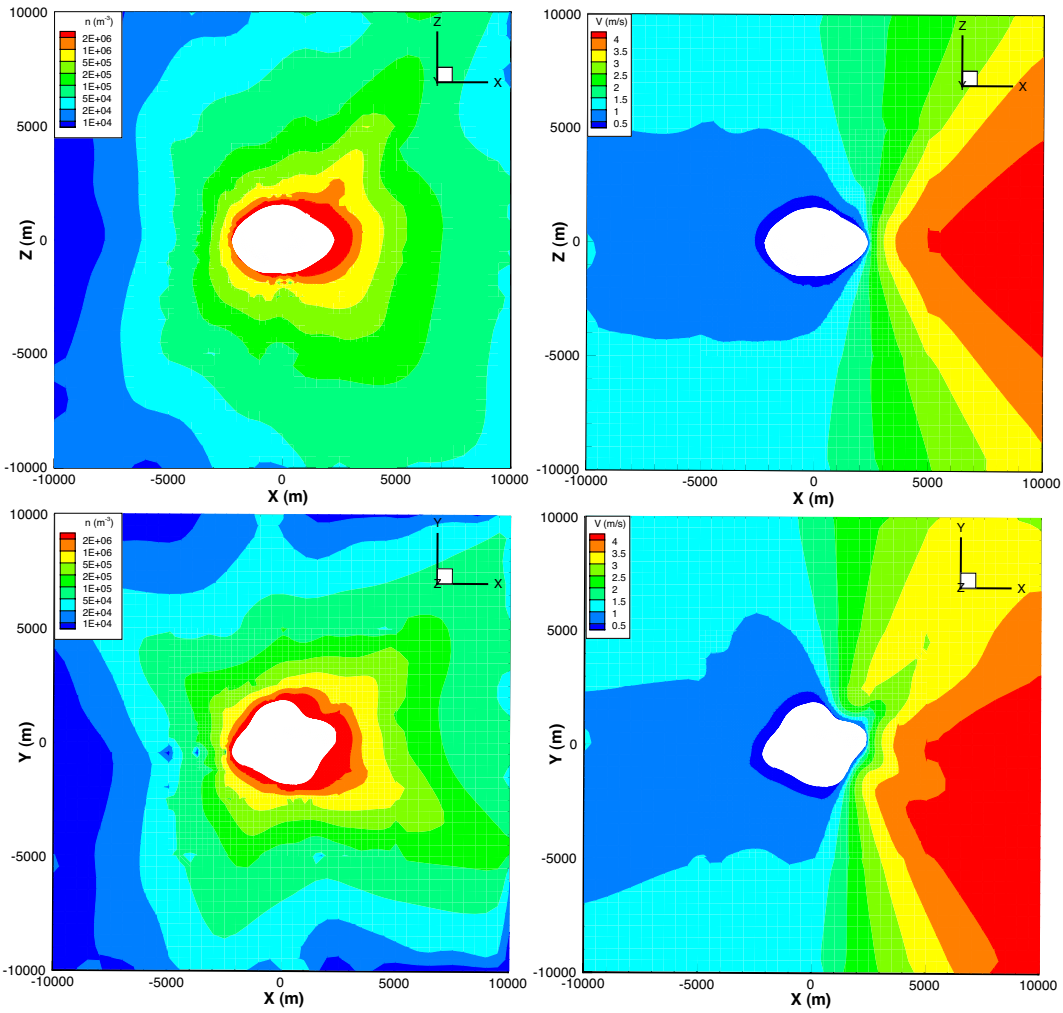

Figure 8.7: Number density of dust grains and mean grain speed in the Y plane (top panels) and Z plane (bottom panels) at 3.25 AU.

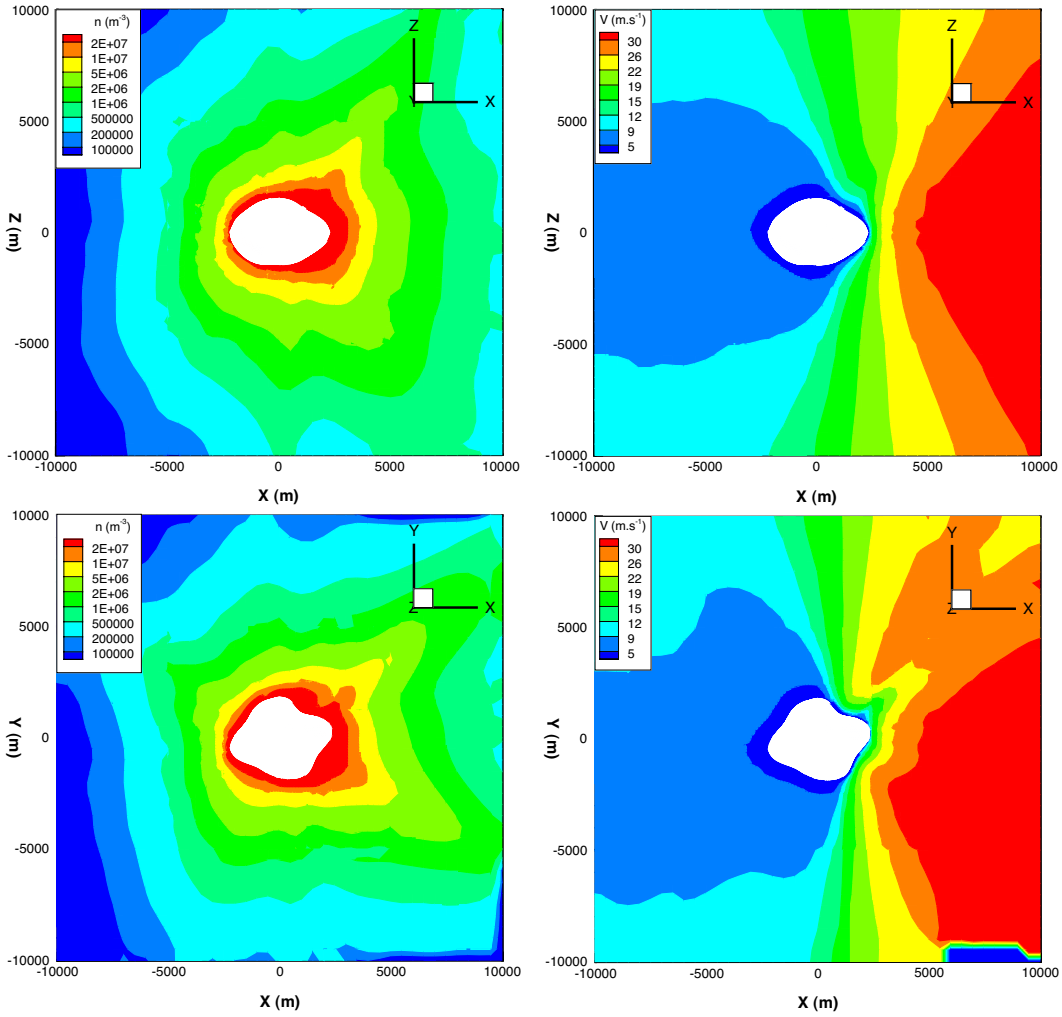

Figure 8.8: Number density of dust grains and mean grain speed in the Y plane (top panels) and Z plane (bottom panels) at 2.7 AU.

night side (Figure 8.9) and would contribute to the effect detailed in Rubin et al. (2014). Nevertheless, modeling such an environment at this stage, without knowing the active surface area location and the different dust parameters, such a detailed model of comet CG would have too rough assumptions to be accurate. However, Rosetta should provide this information and such a calculation will be enabled by our 3D DSMC model.

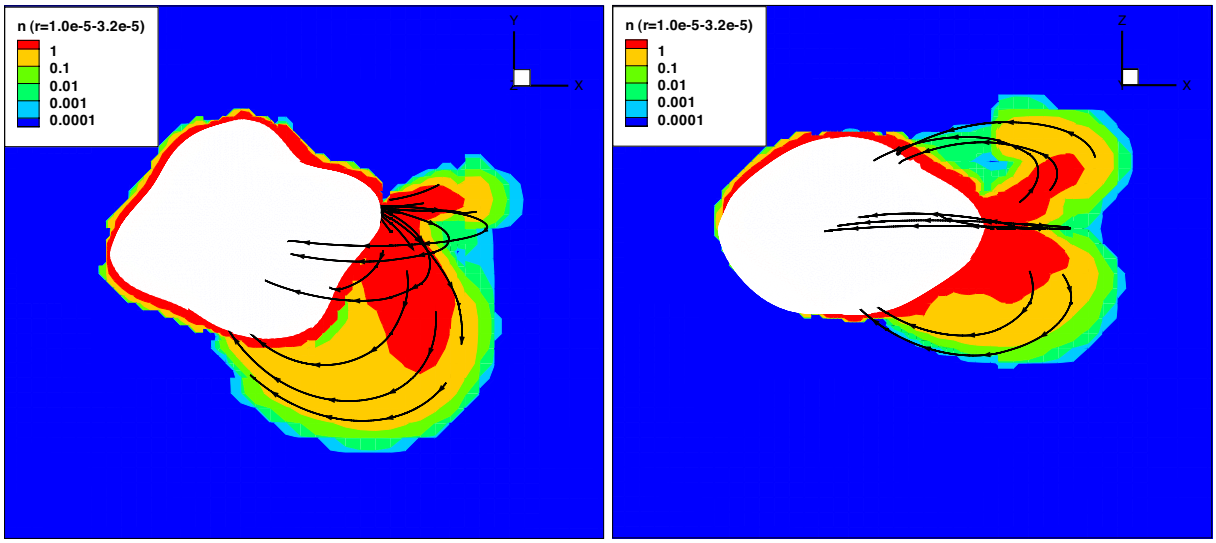

Figure 8.9: Number density in m^{-3} of dust particles with radii between 1.0×10^{-5} and 3.2×10^{-5} m with streamlines. The dust particles fall back onto the surface.

The use of a 3D DSMC model gives the best representation possible of the cometary coma of comet CG. In fact, the topography of the nucleus is important in order to determine the local gas flux and surface temperature, showing some asymmetries with the nucleus-Sun axis that would not be revealed by a simple 2D model. Even more so than for the gas, the dust flow is very sensitive to the nucleus shape due to the fast decoupling from the gas (Combi et al. 2012). However, at about 10 km, the gas density profiles become very similar as in the case of a spherical nucleus. Then, while a full 3D model with a realistic shape gives critical insight of the very inner coma, the assumption of a spherical nucleus can be used within a reasonable error margin for analysis of the gas distribution at

larger distances from the nucleus. The future major improvement on the model will be to take into account the rotation of the nucleus, which can be important when looking at the far coma. This can only be done within the 3D model framework and will eventually be included in our model.

Conclusion

In this work, the DSMC kinetic models provide the first study of the cometary coma resulting from complex outgassing such as extended sources of sublimating icy grains and small active areas such as jets. For the first time, with the use of modeled IR spectra resulting from a line-by-line calculation accounting for the detailed variation of species density and rotational temperature along the line of sight, we were able to derive the relative contribution of the different gas sources to the coma resulting in a complete description of the gas release from the studied comet, enabling a realistic analysis of the coma thermodynamics.

Previous studies of the cometary coma could not incorporate the full effects of extended sources in the coma together with small areas of activity. To model sublimating icy grains, the model needs to correctly simulate the dynamics of the grains and the sublimation process creating new gas particles, which this work has done for the first time.

Extended sources of gas provided by sublimation of icy grains constitute a non-negligible source of gas that can in certain cases prevail over direct sublimation of the nucleus such as in comets SW3, ISON and Hartley 2. The gas particles released by the grains in the coma are warmer and are deposited slower than the local gas produced by the nucleus, changing the general dynamics and thermodynamics of the coma. The coma is then warmer and the particle density decreases more slowly than the classical assumption of $1/r^2$. Also, the icy grains are subject to radiation pressure and rocket forces that tend to push them in the anti-sunward hemisphere of the coma creating an asymmetrical gas source. The inclusion of this extended source of gas is then critical in order to analyze data sets and observations

(Fougere et al. 2012 and 2013).

Jets and small active areas have been observed in many comets, notably comet CG, the Rosetta target, has only 4% of its area that is active (Schleicher et al. 2006). Then, while spherical and simple day/night asymmetry assumptions can be acceptable first order approximations far from the nucleus, they prevent any detailed analysis of the inner coma. The results from EPOXI showed that the outgassing from the nucleus was completely anisotropic with gas emitted from different areas having completely different compositions, the sub-solar lobe showing CO_2 jets which dragged icy grains while the waist released water vapor (A'Hearn et al. 2011). Moreover, the behavior of the gas and dust particles emanating from these small areas is completely different with the dust staying collimated around the active area, while the gas expands tangentially due to collisions for higher gas production rates and presents a nearly free expansion for lower gas production rates. The interpretation of observations of jets and small areas cannot be done with the current widely used simple spherical models. Some of these jet features can also be created by the complex shape of the nucleus notably by its concavities. Only a full 3D model can reproduce all these features enabling a complete interpretation of high spatial resolution data.

With all these capabilities, our DSMC model is the state of the art of the cometary coma models and it will have an invaluable contribution to interpret the data from the Rosetta spacecraft. AMPS has already been used within the Inner Coma Environment Simulator (ICES) tool (Hansen et al. 2009) providing working groups with model results for the cometary environment in-situ and for the different instruments on board of the Rosetta spacecraft, used both for mission and science planning as well as data interpretation.

Fully included in to the Space Weather Modeling Framework (SWMF) (Toth et al. 2005), AMPS can be coupled with the Block Adaptive Tree Solarwind Roe-type Upwind Scheme (BATS-R-US) (Powell et al. 1999) code that can solve various forms of the MHD equations and also has proven heritage in numerous space applications. This has successfully been applied to the atmosphere of Europa (Tenishev et al. 2013) and can be applied in

a similar way to the cometary coma to model both neutrals and ions, together with charged dust particles.

The methods and computer codes developed in this thesis will be extremely useful for the Rosetta mission and will enable interpretation of the data related to comet CG that the spacecraft will start sending within the next few weeks. Using the constraints from these data, we will be able to provide the best model of the cometary coma of CG using our 3D DSMC model. Similarly, a 3D model of the coma of comet Hartley 2 is now possible and will follow up the 2D representation that was detailed in this work and in Fougere et al. (2013) enabling a better reproduction of the observations. We will continue to add relevant species to our cometary model and IR spectra model, notably for the eventual inclusion of methanol which is critical to be able to fully reproduce measured spectra.

Appendices

Appendix A
Simulation results of modeled IR spectra

In this appendix, IR spectra resulting from our model are presented before spectral resolution degradation due to the instrument in the case of comet CG at 2.0 AU presented in section 4 for a limb observation where the spacecraft is at 50.1 km from the center of the nucleus and the closest distance of observation is at 2 km above the nucleus surface.

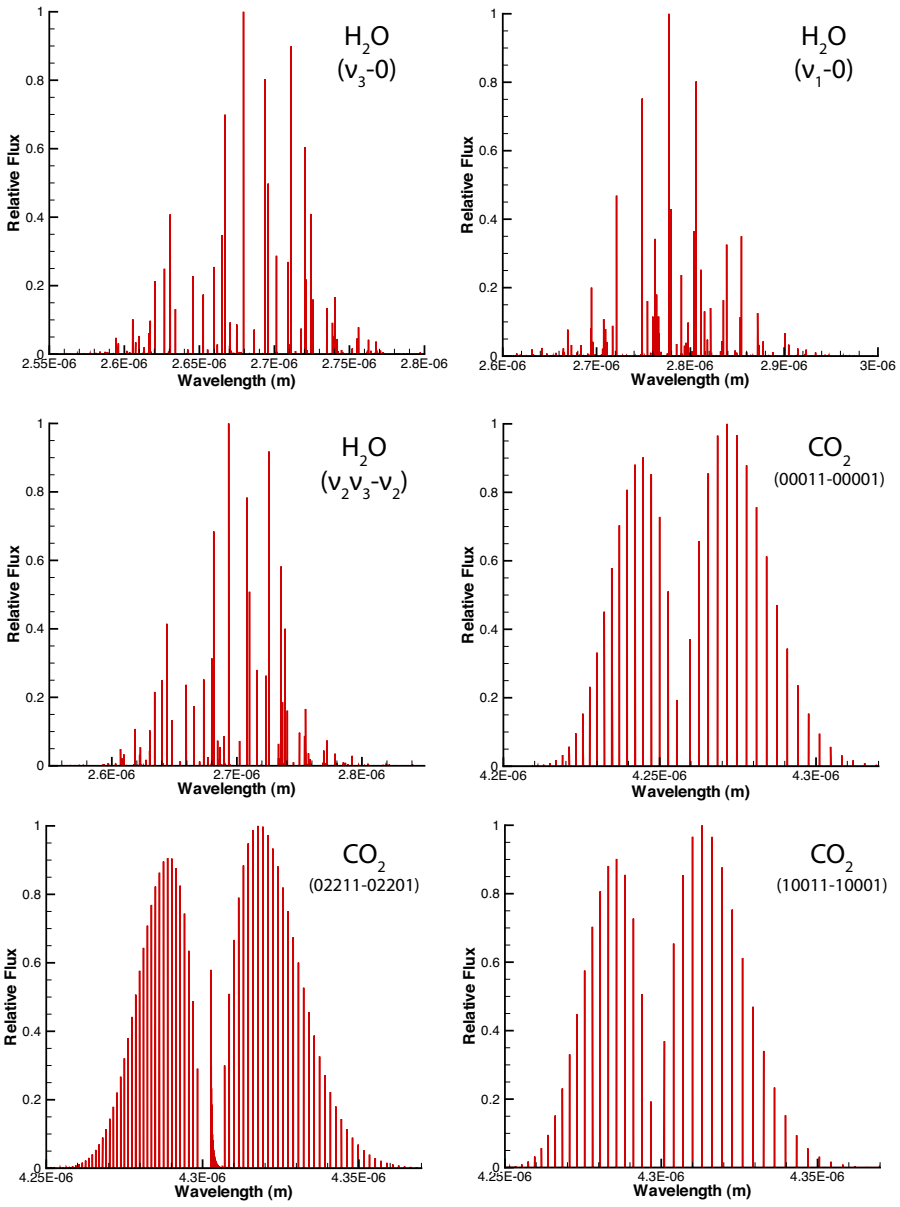

Figure 10: Relative flux spectra for the different modeled bands of each species (part 1).

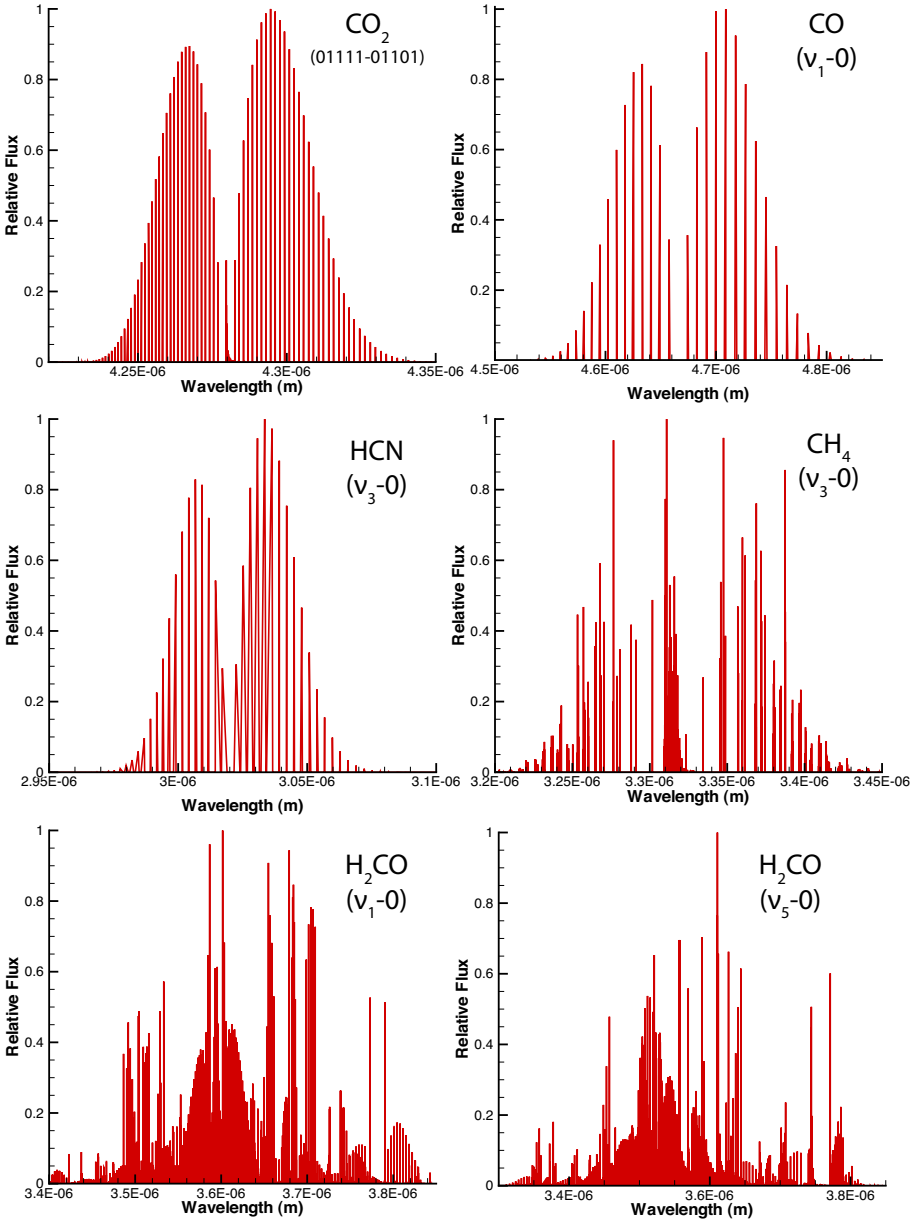

Figure 11: Relative flux spectra for the different modeled bands of each species (part 2).

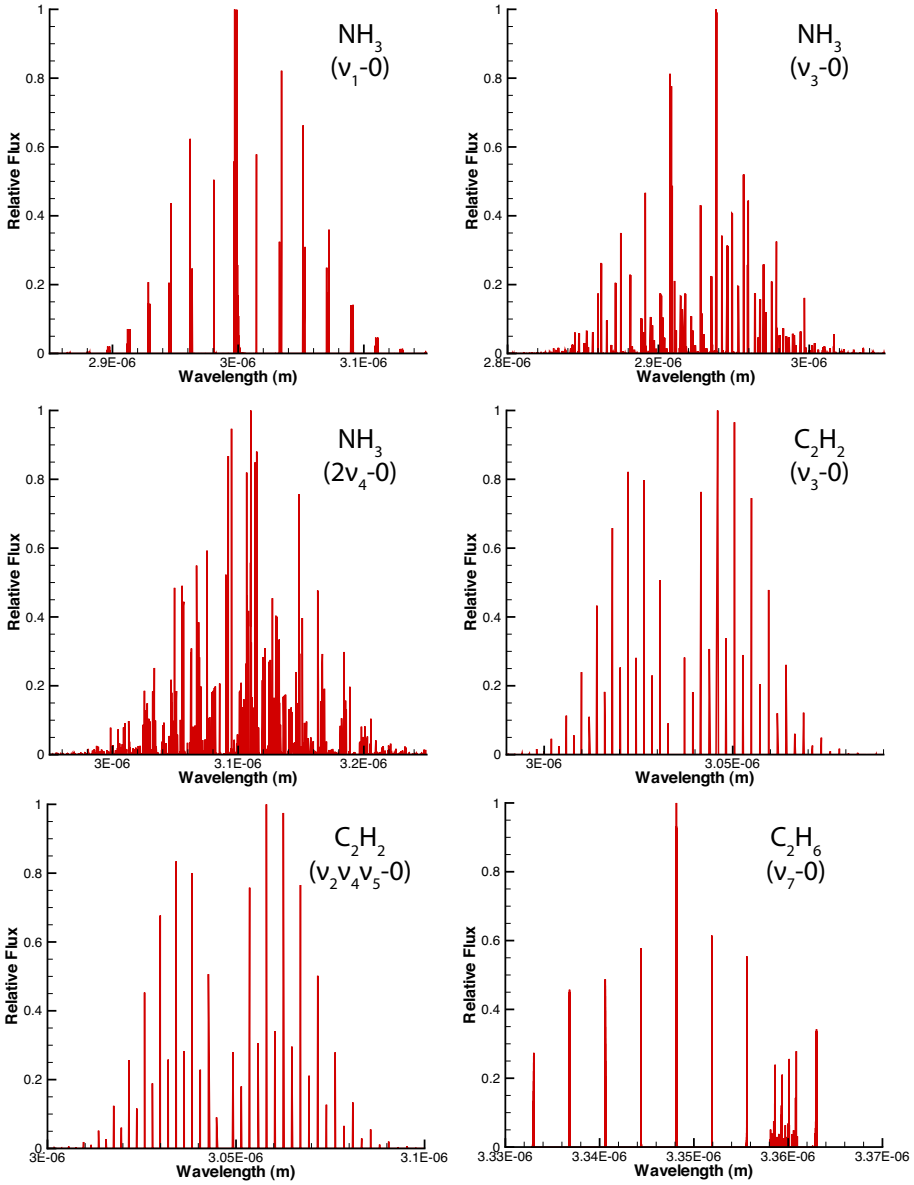

Figure 12: Relative flux spectra for the different modeled bands of each species (part 3).

Appendix B
Coma resulting from a 4% active area

This section of the appendix presents additional plots of the different 2D models that were run with a 4% active area of the nucleus releasing 95% of the total gas production. While the 1.29 AU results are presented in the text for water and OH, the coma of such a comet with a small active area has been modeled at different heliocentric distances corresponding to critical phases of the Rosetta mission (2.0 AU, 2.7 AU, and 3.25 AU). This enables a comparison of the physical conditions of the coma resulting from a patch of the nucleus at different distances from the Sun giving a clear insight of its macroscopic properties. Indeed, gas production rates and lifetimes with respect to photochemistry decrease as the heliocentric distance increases changing the conditions of the flow with different regimes with Knudsen numbers varying by several orders of magnitude.

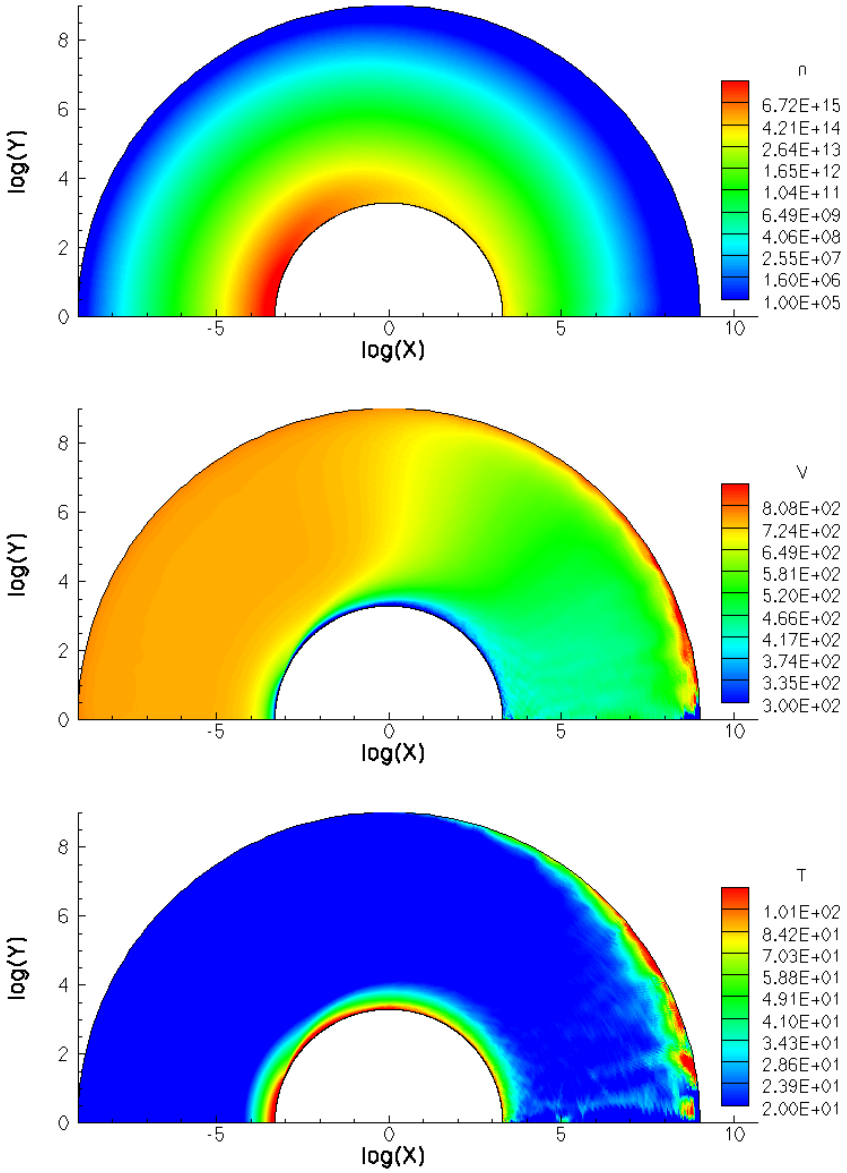

Figure 13: Number density (m^{-3}), velocity ($m.s^{-1}$), and temperature (K) of water at a heliocentric distance of 2.0 AU for a 4% active area case (left) and a broad day/night asymmetrical source from Tenishev et al. (2008) (right) using a logarithmic scale such as in Figure 5.2.

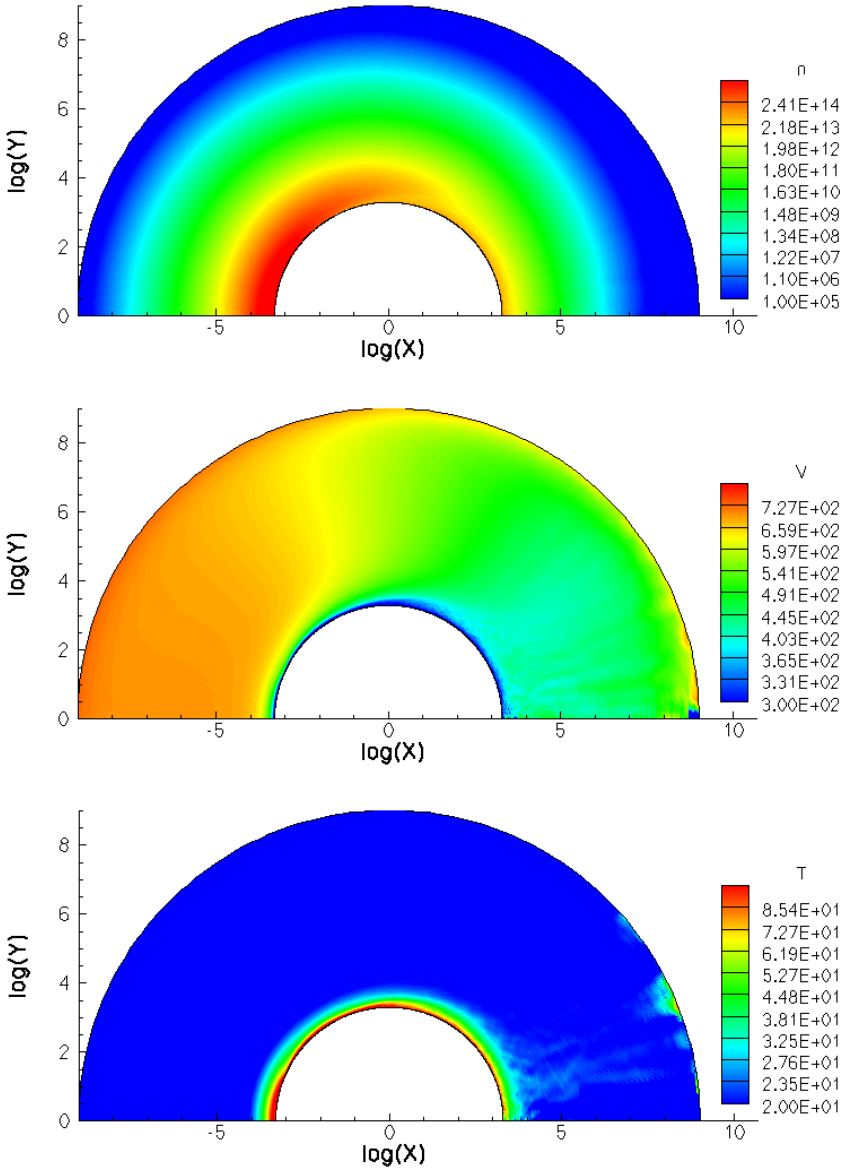

Figure 14: Number density (m^{-3}), velocity ($m.s^{-1}$), and temperature (K) of water at a heliocentric distance of 2.7 AU for a 4% active area case (left) and a broad day/night asymmetrical source from Tenishev et al. (2008) (right) using a logarithmic scale such as in Figure 5.2.

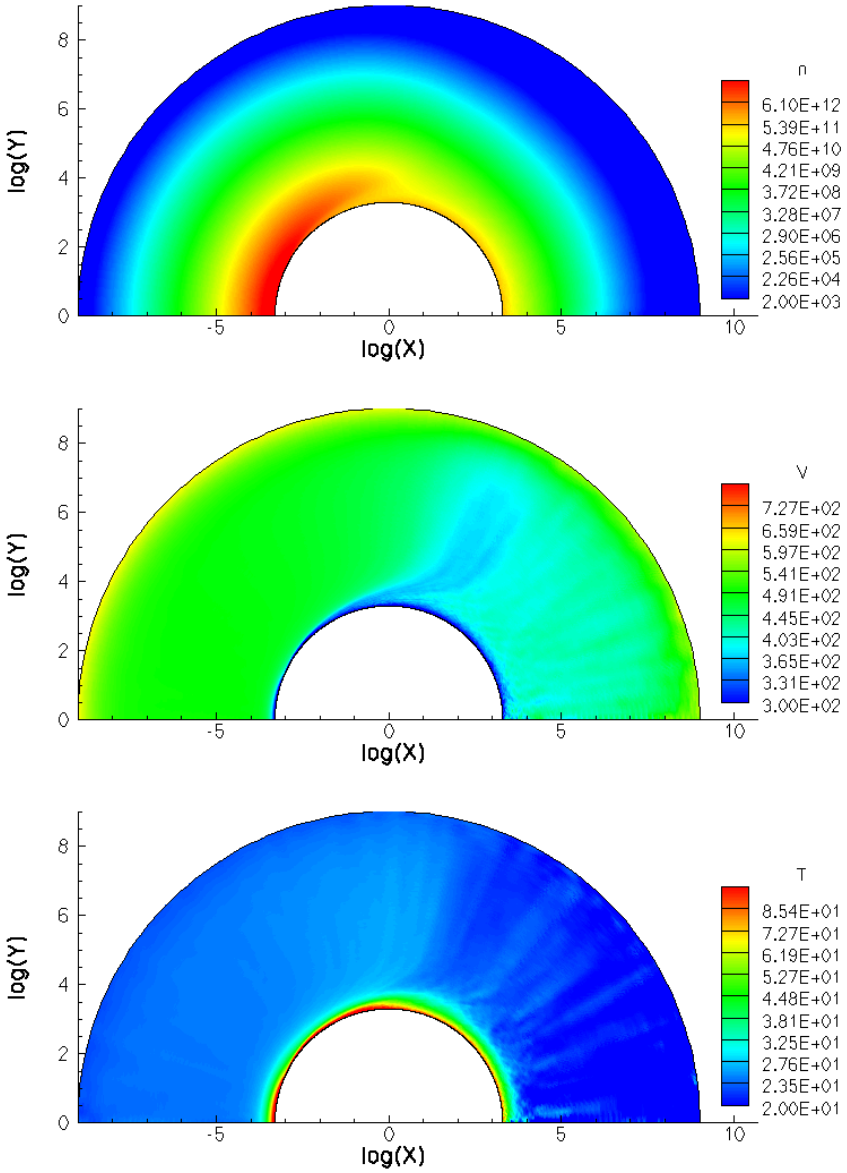

Figure 15: Number density (m^{-3}), velocity ($m.s^{-1}$), and temperature (K) of water at a heliocentric distance of 3.25 AU for a 4% active area case (left) and a broad day/night asymmetrical source from Tenishev et al. (2008) (right) using a logarithmic scale such as in Figure 5.2.

References

A'Hearn, M. F. et al. (2011), EPOXI at Comet Hartley 2, *Science, 332*, 1396.

A'Hearn, M. F. (2012), Cometary Volatiles and the Origin of Comets, *The Astrophysical Journal, 758*, 29.

Abe, T. (1993), Generalized scheme of the no-time-counter scheme for the DSMC in rarefied gas flow analysis, *Computers and fluids, 22(2)*, 253-257.

Agarwal, J., Muller, M., and Grun, E. (2007), Dust environment modelling of comet 67P/Churyumov-Gerasimenko, *Space science reviews, 128(1-4)*, 79-131.

Allen, M., Delitsky, M., Huntress, W., Yung, Y., Ip, W. H., Schwenn, R., Rosenbauer, E. Shelley, H. Balsiger, and Geiss, J. (1988), Evidence for methane and ammonia in the coma of comet P/Halley, *In Exploration of Halley's Comet (pp. 502-512). Springer Berlin Heidelberg*.

Babovsky, H., and Illner, R. (1989), A convergence proof for Nanbu's simulation method for the full Boltzmann equation, *SIAM journal on numerical analysis, 26(1)*, 45-65.

Balsiger, H., et al. (1986), Ion composition and dynamics at comet Halley, *Nature*, 330-334.

Beer, E. H., Podolak, M. A., and Prialnik, D. (2006), The contribution of icy grains to the activity of comets: I. Grain lifetime and distribution,*Icarus, 180(2)*, 473-486.

Bergemann, F., and Boyd, I. D. (1994), New discrete vibrational energy model for the direct simulation Monte Carlo method, *Progress in Astronautics and Aeronautics, 158*.

Belton, M. J. S. (2010), Cometary activity, active areas, and a mechanism for collimated outflows on 1P, 9P, 19P, and 81P, *Icarus, 210*, 881-897.

Belton, M. J. et al. (2013), The complex spin state of 103P/Hartley 2: Kinematics and orientation in space, *Icarus, 222(2)*, 595-609.

Benkhoff, J., and Boice, D. C. (1996), Modeling the thermal properties and the gas flux from a porous, ice-dust body in the orbit of P/Wirtanen, *Planetary and Space Science, 44*, 665-673.

Bensch, F., and Bergin, E. A. (2004), The pure rotational line emission of ortho-water vapor in comets. I. Radiative transfer model, *The Astrophysical Journal, 615(1)*, 531.

Bertie, J. E., Labbe, H. J., and Whalley, E. (1969). Absorptivity of ice I in the range 4000-30 cm^{-1}. *The Journal of Chemical Physics, 50(10)*, 4501-4520.

Bird, G. A. (1976), Molecular gas dynamics, *NASA STI/Recon Technical Report A, 76, 40225*.

Bird, G. A. (1978), Monte Carlo simulation of gas flows, *Annual Review of Fluid Mechanics, 10(1)*, 11-31.

Bird, G. A. (1989), Comment on "False collisions in the direct simulation Monte Carlo method"[Phys. Fluids 3 1, 2047 (1988)], *Physics of Fluids A: Fluid Dynamics (1989-1993), 1(5)*, 897-897.

Bird, G. A. (1994), Molecular Gas Dynamics and the Direct Simulation of Gas Flows, *Oxford University Press*.

Biver, N. (1997), Molécules mères cométaires: observations and modélisations. PhD thesis, University of Paris 7.

Biver, N. et al. (1997), Evolution of the outgassing of Comet Hale-Bopp (C/1995 O1) from radio observations, *Science, 275* 1915-1918.

Biver, N. et al. (1999), Spectroscopic Monitoring of Comet C/1996 B2 (Hyakutake) with the JCMT and IRAM Radio Telescopes, *The Astronomical Journal, 118*, 1850-1872.

Bockelée-Morvan, D. (1987), A model for the excitation of water in comets, *Astronomy and Astrophysics, 181*, 169-181.

Bockelée-Morvan, D., Crovisier, J. (1989), The nature of the 2.8-micron emission feature in cometary spectra, *Astronomy and Astrophysics, 216*, 278-283.

Bockelée-Morvan, D., Brooke, T. Y., and Crovisier, J. (1995), On the origin of the 3.2- to 3.6-μm emission features in comets, *Icarus, 116(1)*, 18-39.

Bockelée-Morvan, D. et al. (2001), Outgassing behavior and composition of comet C/1999

S4 (LINEAR) during its disruption, *Science, 292(5520)*, 1339-1343.

Boehnhardt, H., Holdstock, S., Hainaut, O., Tozzi, G. P., Benetti, S., and Licandro, J. (2002), 73p/Schwassmann-Wachmann 3-One Orbit after break-up: Search for fragments, *Earth, Moon, and Planets, 90(1-4)*, 131-139.

Boehnhardt, H. et al. (2013), Comet C/2012 S1 (Ison), *Central Bureau Electronic Telegrams, 3715*, 1.

Boltzmann L. (1872), Weitere studien ueber das warmegleichgewicht unter gas-molekulen, *Sitzungber. Kais. Akad. Wiss. Wien Math. Naturwiss. Classe 66*, 275-370.

Bonev, B. P. (2005), Towards a Chemical Taxonomy of Comets: Infrared Spectroscopy Methods for Quantitative Measurements of Cometary Water, PhD Thesis, University of Toledo, Ohio.

Bonev, B. P., Mumma, M. J., Villanueva, G. L., Disanti, M. A., Ellis, R. S., Magee-Sauer, K., and Dello Russo, N. (2007), A search for variation in the H_2O ortho-para ratio and rotational temperature in the inner coma of Comet C/2004 Q2 (Machholz), *The Astrophysical Journal Letters, 661(1)*, L97.

Bonev, B. P., Mumma, M. J., Kawakita, H., Kobayashi, H., and Villanueva, G. L. (2008), IRCS/Subaru observations of water in the inner coma of Comet 73P-B/Schwassmann Wachmann 3: Spatially resolved rotational temperatures and ortho para ratios, *Icarus, 196*, 241-248.

Bonev, B. P. et al. (2013), Evidence for two modes of water release in Comet 103P/Hartley 2: Distributions of column density, rotational temperature, and ortho-para ratio, *Icarus, 222(2)*, 740-751.

Borgnakke, C., and Larsen, P. S. (1975), Statistical collision model for Monte Carlo simulation of polyatomic gas mixture, *Journal of computational Physics, 18(4)*, 405-420.

Boyd, I. D. (1991), Analysis of vibrational?translational energy transfer using the direct simulation Monte Carlo method, *Physics of Fluids A: Fluid Dynamics (1989-1993), 3(7)*, 1785-1791.

Bruck Syal, M., Schultz, P. H., Sunshine, J. M., A'Hearn, M. F., Farnham, T. L., and Dear-

born, D. S. (2013), Geologic control of jet formation on Comet 103P/Hartley 2, *Icarus, 222(2)*, 610-624.

Bruggeman, V. D. (1935), Berechnung verschiedener physikalischer Konstanten von heterogenen Substanzen. I. Dielektrizitätskonstanten und Leitfähigkeiten der Mischkörper aus isotropen Substanzen, *Annalen der physik, 416(7)*, 636-664.

Budzien, S. A., Festou, M. C., and Feldman, P. D. (1994), Solar Flux Variability and the Lifetimes of Cometary H_2O and OH, *Icarus, 107(1)*, 164-188.

Buffa, G., Tarrini, O., Scappini, F., and Cecchi-Pestellini, C. (2000), H_2O-H_2O collision rate coefficients, *The Astrophysical Journal Supplement Series, 128(2)*, 597.

Burger, M. M. (1969), A difference in the architecture of the surface membrane of normal and virally transformed cells, *Proceedings of the National Academy of Sciences, 62(3)*, 994-1001.

Burns, J. A., Lamy, P. L., and Soter, S. (1979), Radiation forces on small particles in the solar system, *Icarus, 40(1)*, 1-48.

Cameron, A. G. W. (1973), Accumulation processes in the primitive solar nebula, *Icarus, 18*, 407-450.

Carusi, A., Kresak, L., Perozzi, E., and Valsecchi, G. B. (1985), Long-term evolution of short-period comets, *Bristol, England and Accord, MA, Adam Hilger, Ltd., 1985, 272 p., 1*.

Chen, P. H., Boyd, I. D., and Camberos, J. A. (2003): Assessment of Entropy Generation Rate as a Predictor of Continuum Breakdown, *AIAA Paper 2003-3783*.

Cheng, C. Z. (1992), Kinetic extensions of magnetohydrodynamics for axisymmetric toroidal plasmas, *Physics reports, 211(1)*, 1-51.

Cheng, H. K., and Emanuel, G. (1995), Perspective on hypersonic nonequilibrium flow, *AIAA journal, 33(3)*, 385-400.

Chin, G., and Weaver, H. A. (1984), Vibrational and rotational excitation of CO in comets Nonequilibrium calculations, *The Astrophysical Journal, 285*, 858-869.

Clube, V., and Napier, B. (1982), The role of episodic bombardment in geophysics,*Earth and Planetary Science Letters, 57*, 251-262.

Colangeli, L. et al. (1999), Infrared spectral observations of Comet 103P/Hartley 2 by ISOPHOT, *Astronomy and Astrophysics, 343*, L87-L90.

Combi, M. R. (1987), Sources of cometary radicals and their jets: Gases or grains, *Icarus, 71(1)*, 178-191.

Combi, M. R. (1996), Time-Dependant Gas Kinetics in Tenuous Planetary Atmospheres: The Cometary Coma, *Icarus, 123*, 207-226.

Combi, M. R., DiSanti, M. A., and Fink, U. (1997), The spatial distribution of gaseous atomic sodium in the comae of comets: Evidence for direct nucleus and extended plasma sources, *Icarus, 130(2)*, 336-354.

Combi, M. R., Harris, W. M., and Smyth, W. H. (2004), Gas dynamics and kinetics in the cometary coma: theory and observations, *Comets II, M. C. Festou, H. U. Keller, and H. A. Weaver (eds.), University of Arizona Press, Tucson*, 523-552.

Combi, M. R., Mäkinen, J. T. T., Bertaux, J. L., and Quemerais, E. (2005). Temporal deconvolution of the hydrogen coma: II. Pre-and post-perihelion activity of Comet Hyakutake (1996 B2). Icarus, 177(1), 228-245.

Combi, M. R., Bertaux, J. L., Quemerais, E., Ferron, S., and Mäkinen, J. T. T. (2011), Water production by Comet 103P/Hartley 2 observed with the SWAN instrument on the SOHO spacecraft, *The Astrophysical Journal Letters, 734(1)*, L6.

Combi, M. R., Tenishev, V., Rubin, M., Fougere, N., Gombosi, T. I. (2012), Narrow Dust Jets in a Diffuse Gas Coma: A Natural Product of Small ACtive Regions on Comets, *The Astrophysical Journal, 749*, 13.

Combi, M. R., Fougere, N., Mäkinen, J. T. T., Bertaux, J. L., Quemerais, E., and Ferron, S. (2014), Unusual Water Production Activity of Comet C/2012 S1 (ISON): Outbursts and Continuous Fragmentation, *The Astrophysical Journal Letters, 788(1)*, L7.

Committee on the Planetary Science Decadal Survey (2011), Vision and Voyages: For Planetary Science in the Decade 2013-2022, *National Academies Press*.

Coradini, A. et al. (2007), VIRTIS: an imaging spectrometer for the Rosetta mission, *Space Science Reviews, 128(1-4)*, 529-559.

Cravens, T. E., and Körösmezey, A. (1986), Vibrational and rotational cooling of electrons by water vapor, *Planetary and space science, 34(10)*, 961-970.

Crifo, J. F. (1987), Improved gas-kinetic treatment of cometary water sublimation and recondensation - Application to comet P/Halley, *Astronomy and Astrophysics, 187*, 438-450

Crifo, J. F. (1995), A general physicochemical model of the inner coma of active comets. 1: Implications of spatially distributed gas and dust production, *The Astrophysical Journal, 445*, 470-488.

Crifo, J. F., and Rodionov, A. V. (1997), The dependence of the circumnuclear coma structure on the properties of the nucleus I. Comparison between a Homogeneous and an Inhomogeneous Spherical Nucleus, with Application to P/Wirtanen, *Icarus, 127(2)*, 319-353.

Crifo, J. F., and Rodionov, A. V. (1997), The dependence of the circumnuclear coma structure on the properties of the nucleus II. First investigation of the Coma Surrounding a Homogeneous, Aspherical Nucleus, *Icarus, 129(1)*, 72-93.

Crifo, J. F., and Rodionov, A. V. (1999), Modelling the circumnuclear coma of comets: objectives, methods and recent results, *Planetary and space science, 47(6)*, 797-826.

Crifo, J. F., Lukianov, G. A., Rodionov, A. V., Khanlarov, G. O., and Zakharov, V. V. (2002), Comparison between Navier-Stokes and direct Monte-Carlo simulations of the circumnuclear coma: I. Homogeneous, spherical source, *Icarus, 156(1)*, 249-268.

Crifo, J. F., Loukianov, G. A., Rodionov, A. V., and Zakharov, V. V. (2003), Navier-Stokes and direct Monte Carlo simulations of the circumnuclear coma II. Homogeneous, aspherical sources, *Icarus, 163*, 479-503.

Crovisier, J., and Encrenaz, T. (1983), Infrared fluorescence of molecules in comets-The general synthetic spectrum, *Astronomy and Astrophysics, 126*, 170-182.

Crovisier, J. T. (1984), The water molecule in comets-Fluorescence mechanisms and ther-

modynamics of the inner coma, *Astronomy and Astrophysics, 130*, 361-372.

Davidsson, B. J., and Gutiérrez, P. J. (2004), Estimating the nucleus density of Comet 19P/Borrelly, *Icarus, 168(2)*, 392-408.

Davidsson, B. J., and Gutiérrez, P. J. (2005), Nucleus properties of Comet 67P/Churyumov-Gerasimenko estimated from non-gravitational force modeling, *Icarus, 176(2)*, 453-477.

Davidsson, B. J., and Gutiérrez, P. J. (2006), Non-gravitational force modeling of Comet 81P/Wild 2: I. A nucleus bulk density estimate, *Icarus, 180(1)*, 224-242.

Debout, V. , Bockelée-Morvan, D., and Zhakarov, V., A radiative transfer model for simulating VIRTIS/Rosetta molecular spectra, *AAS/Division for Planetary Sciences Meeting Abstracts (Vol. 45)*.

Delsemme, A. H., and Swings, P. (1952), Hydrates de gaz dans les noyaux cométaires et les grains interstellaires, *Annales d'Astrophysique, 15*, 1.

Delsemme, A. H., and Miller, D. C. (1971), The continuum of Comet Burnham (1960 II): The differentiation of a short period comet, Planetary and Space Science, 19, 1229-1257.

Dello Russo, N., DiSanti, M. A., Magee-Sauer, K., Gibb, E. L., Mumma, M. J., Barber, R. J., and Tennyson, J. (2004), Water production and release in Comet 153P/Ikeya-Zhang (C/2002 C1): Accurate rotational temperature retrievals from hot-band lines near 2.9-?m, *Icarus, 168(1)*, 186-200.

Dello Russo, N. et al. (2005), Water production rates, rotational temperatures, and spin temperatures in Comets C/1999 H1 (Lee), C/1999 S4, and C/2001 A2, *The Astrophysical Journal, 621(1)*, 537.

Dello Russo, N. , Vervack, R. J., Weaver, H. A., Biver, N., Bockelée-Morvan, D., Crovisier, J., and Lisse, C. M. (2007), Compositional homogeneity in the fragmented Comet 73P/Schwassmann-Wachmann 3, *Nature, 448(7150)*, 172-175.

Dello Russo, N. et al. (2011), The volatile composition and activity of Comet 103P/Hartley 2 during the EPOXI closest approach, *The Astrophysical Journal Letters, 734(1)*, L8.

DiSanti, M. A., Mumma, M. J., Dello Russo, N., and Magee-Sauer, H. (2001), Carbon Monoxide Production and Excitation in Comet C/1995 O1 (Hale-Bopp): Isolation of Native and Distributed CO Sources, Icarus, 153, 361-390.

DiSanti, M. A., Bonev, B. P., Magee-Sauer, K., Russo, N. D., Mumma, M. J., Reuter, D. C., and Villanueva, G. L. (2006), Detection of formaldehyde emission in Comet C/2002 T7 (LINEAR) at infrared wavelengths: Line-by-line validation of modeled fluorescent intensities, *The Astrophysical Journal, 650(1)*, 470.

Divine, N. et al. (1986), The Comet Halley dust and gas environment, *Space science reviews, 43(1-2)*, 1-104.

Donn, B., and Rahe, J. (1982), Structure and origin of cometary nuclei, *Comets. (A83-13376 03-90) Tucson, AZ, University of Arizona Press*, 206-226.

Drahus, M. et al. (2011), Rotation state of comet 103P/Hartley 2 from radio spectroscopy at 1 mm, *The Astrophysical Journal Letters, 734(1)*, L4.

Eberhardt, P., and Krankowsky, D. (1995), The electron temperature in the inner coma of comet P/Halley, *Astronomy and Astrophysics, 295*, 795.

Eberhardt, P., Krankowsky, D., Schulte, W., Dolder, U., Lammerzahl, P., Berthelier, J. J., Woweries, J., Stubbermann, U., Hodges, R. R., Hoffman, J. H., and Illiano, J. M. (1987), The CO and N_2 abundance in comet P/Halley, *Exploration of Halley's Comet. Springer Berlin Heidelberg*, 481-484.

Eddington, A. S. (1910), The Envelopes of Comet Morehouse (1908 c), *Monthly Notices of the Royal Astronomical Society 70*, 442-458.

Epifani, E. et al. (2001), ISOCAM imaging of Comets 103P/Hartley 2 and 2P/Encke, *Icarus, 149(2)*, 339-350.

Farnham, T. L. et al. (2007), Dust coma morphology in the Deep Impact images of Comet 9P/Tempel 1, *Icarus 187*, 26-40

Feaga, L. M., A'Hearn, M. F., Sunshine, J. M., Groussin, O., and Farnham, T. L. (2007), Asymmetries in the distribution of H_2O and CO_2 in the inner coma of Comet 9P/Tempel 1 as observed by Deep Impact, *Icarus, 190*, 345-356.

Fegley, B, Prinn, R. G. (1989), Solar nebula chemistry - Implications for volatiles in the solar system, *The formation and evolution of planetary systems; Proceedings of the Meeting, Baltimore, MD, May 9-11, 1988 (A90-31251 12-90), Cambridge University Press*, 171-205.

Festou, M. C., Rickman, H., and West, R. M. (1993), Comets, *The Astronomy and Astrophysics Review, 5(1-2)*, 37-163.

Festou, M. C. (1999), On the Existence of Distributed Sources in Comet Comae, *Space Science Reviews, 90*, 53-67.

Finson, M. J., and Probstein, R. F. (1968), A theory of dust comets. I. Model and equations, *The Astrophysical Journal, 154*, 327-352.

Fougere, N., Combi, M. R., Tenishev, V., Rubin, M., Bonev, B. P., and Mumma, M. J., Understanding measured water rotational temperatures and column densities in the very innermost coma of Comet 73P/Schwassmann-Wachmann 3 B,*Icarus, 221*, 174-185.

Fougere, N., Combi, M. R., Rubin, M., and Tenishev, V. (2013), Modeling the heterogeneous ice and gas coma of Comet 103P/Hartley 2, *Icarus, 225*, 688-702.

Fougere, N., Combi, M. R., and Tenishev, V. (2013b), Global 3D kinetic model of cometary rarefied atmosphere toward a description of the coma of Comet 103P/Hartley 2, *AAS/Division for Planetary Sciences Meeting Abstracts (Vol. 45)*.

Fujita, K., and Abe, T. (2002), State-to-state nonequilibrium rotational kinetics of nitrogen behind a strong shock wave, *AIAA paper*, 3218.

Gallis, M.A., Torczynski, J. R., Rader, D. J., Tij, M., and Santos, A. (2006), Normal solutions of the Boltzmann equation for highly nonequilibrium Fourier flow and Couette flow, *Physics of Fluids, 18*, 104.

Gan, L., and Cravens, T. E. (1990), Electron energetics in the inner coma of comet Halley, *Journal of Geophysical Research: Space Physics (1978-2012), 95(A5)*, 6285-6303.

Gibb, E. L., Mumma, M. J., Dello Russo, N., DiSanti, M. A., and Magee-Sauer, K. (2003), Methane in Oort cloud comets, *Icarus, 165(2)*, 391-406.

Gombosi, T. I., Cravens, T. E., and Nagy, A. F. (1985), A time dependent theoretical model of the polar wind: Preliminary results, *Geophysical research letters, 12(4)*, 167-170.

Gombosi, T. I., Nagy, A. F., and Cravens, T. E. (1986), Dust and neutral gas modeling of the inner atmospheres of comets, *Reviews of Geophysics, 24(3)*, 667-700.

Gombosi, T. I. (1998), Physics of the space environment, *Cambridge University Press*.

Grad, H. (1958), Principles of the kinetic theory of gases, *Thermodynamik der Gase/Thermodynamics of Gases (pp. 205-294). Springer Berlin Heidelberg*.

Groussin, O. et al. (2007), Surface temperature of the nucleus of Comet 9P/Tempel 1, *Icarus, 191(2)*, 63-72.

Grun, E. et al. (1989), Mechanisms of dust emission from the surface of a cometary nucleus, *Advances in Space Research, 9(3)*, 133-137.

Haas, B. L., and Boyd, I. D. (1993), Models for direct Monte Carlo simulation of coupled vibration-dissociation, *Physics of Fluids A: Fluid Dynamics (1989-1993), 5(2)*, 478-489.

Häberli, R. M., Altwegg, K., Balsiger, H., and Geiss, J. (1995), Physics and chemistry of ions in the pile-up region of comet P/Halley, *Astronomy and Astrophysics, 297*, 881.

Häberli, R. M., Altwegg, K., Balsiger, H., and Geiss, J. (1996), Heating of the thermal electrons in the coma of comet P/Halley, *Journal of Geophysical Research, 101*, 15579-15590.

Hampton, D. L. et al. (2005), An overview of the instrument suite for the Deep Impact mission, *Space Science Reviews, 117(1-2)*, 43-93.

Hanner, M. S., Tedesco, E., Tokunaga, A. T., Veeder, G. J., Lester, D. F., Witteborn, F. C., Bregman, J. D., Gradie, J., and Lebofsky, L. (1985), The dust coma of periodic Comet Churyumov-Gerasimenko (1982 VIII), *Icarus, 64(1)*, 11-19.

Hansen, K. C., Gombosi, T. I., and Team, I. C. M. (2009), A Comprehensive Set of Comet Environment Models: The Inner Coma Environment Simulator (ICES), *AAS/Division for Planetary Sciences Meeting Abstracts# 41 (Vol. 41)*.

Harris, W. M., Combi, M. R., Honeycutt, R. K., and Mueller, B. E. A. (1997), Evidence for interacting gas flows and an extended volatile source distribution in the coma of Comet C/1996 B2 (Hyakutake), *Science, 277*, 676-681.

Hartogh, P. et al. (2010), HIFI observations of water in the atmosphere of comet C/2008 Q3 (Garradd), *Astronomy and Astrophysics, 518*, 150-155.

Haser, L. (1957), Distribution d'intensité dans la tête d'une comète, *Bulletin de la Class des Sciences, 43*, 740-750.

Herzberg, G. (1957), *Molecular spectra and molecular structure*.

Hinshelwood, C. N. (1940), The Kinetics of Chemical Change, *Oxford University Press. New York*.

Hodges, R. R. (1990), Monte Carlo simulation of nonadiabatic expansion in cometary atmospheres - Halley, *Icarus, 83*, 410-433.

Horanyi, M., Gombosi, T. I., Cravens, T. E., Körösmezey, A., Kecskemety, K., Nagy, A. F., and Szego, K. (1984),The friable sponge model of a cometary nucleus, *The Astrophysical Journal, 278*, 449-455.

Houpis, H. L. F., and Mendis, D. A. (1981), On the development and global oscillations of cometary ionosphere, *The Astrophysical Journal, 243*, 1088-1102.

Houpis, H. L. F.,Ip, W. H., and Mendis, D. A. (1985), The chemical differentiation of comet nuclei: The process and its consequences, *The Astrophysical Journal, 295*, 654-667.

Huebner, W. F., and Carpenter, C. W. (1979), Solar Photo Rate Coefficients, *Los Alamos Scientific Laboratory report LA-8085-MS*.

Huebner, W. F., and Keady, J. J. (1983), Energy balance and photochemical processes in the inner coma, *Inst. für Astrophysik*.

Huebner, W. F. (1985), The photochemistry of comets, *The photochemistry of atmospheres: Earth, the other planets, and comets (A86-21076 08-88). Orlando, FL, Academic Press, Inc., p. 437-481., 1*, 437-481.

Huebner, W. F., Boice, D. C., and Sharp, C. M. (1987), Polyoxymethylene in comet Halley, *The Astrophysical Journal, 320*, L149-L152.

Huebner, W. F. (1990), Physics and chemistry of comets, *In Physics and chemistry of comets (Vol. 1)*.

Huebner, W. F., Keady, J. J., and Lyon, S. P. (1992), Solar photo rates for planetary atmospheres and atmospheric pollutants, *Astrophysics and Space Science, 195(1)*, 1-294.

Huebner, W. F., and Benkhoff, J. (1999), From Coma Abundances to Nucleus Composition, *Space Science Reviews, 90*, 117-130.

Hull, C. (1929), International critical tables of numerical data, physics, chemistry and technology (Vol. 5), *National Academies*.

Ip, W. H. (1983), On photochemical heating of cometary comae: The cases of H_2O and CO_2-rich comets, *The Astrophysical Journal, 264*, 726-732.

Irvine, W. M., and Pollack, J. B. (1968), Infrared optical properties of water and ice spheres, *Icarus, 8(1)*, 324-360.

Irvine, W. M., Schloerb, F. P., Crovisier, J., Fegley, B., and Mumma, M. J. (2000), Comets: a Link Between Interstellar and Nebular Chemistry, *Protostars and Planets IV (Book - Tucson: University of Arizona Press; eds Mannings, V., Boss, A. P., Russell, S. S.)*, 1159.

Ishiguro, M. (2008), Cometary dust trail associated with Rosetta mission target: 67P/Churyumov-Gerasimenko, *Icarus, 193(1)*, 96-104.

Itikawa, Y. (1972), Rotational Transition in an Asymmetric-Top Molecule by Electron Collision: Applications to H_2O and H_2CO, *Journal of the Physical Society of Japan, 32(1)*, 217-226.

Ivanov, M. S., and Rogasinsky, S. V. (1988), Analysis of numerical techniques of the direct simulation Monte Carlo method in the rarefied gas dynamics, *Russian Journal of numerical analysis and mathematical modelling, 3(6)*, 453-466.

Ivanov, M. S., and Gimelshein, S. F. (1998), Computational hypersonic rarefied flows, *Annual Review of Fluid Mechanics, 30(1)*, 469-505.

Jackson, W. M. (1980), The lifetime of the OH radical in comets at 1 AU, *Icarus, 41(1)*, 147-152.

James, T. C., and Kumer, J. B. (1973), Fluorescence of CO_2 near 4.3 microns: Application to daytime limb radiance calculations, *Journal of Geophysical Research, 78(34)*, 8320-8329.

Jockers, K. (1997), Observations of scattered light from cometary dust and their interpretation, *Earth, Moon, and Planets, 79(1-3)*, 221-245.

Johnstone, A. D. et al. (1993), Observations of the solar wind and cometary ions during the encounter between Giotto and comet Grigg-Skjellerup, *Astronomy and Astrophysics, 273*, L1-L4.

Josyula, E., and Bailey, W. F. (2001), Vibration-dissociation coupling using master equations in nonequilibrium hypersonic blunt-body flow, *Journal of thermophysics and heat transfer, 15(2)*, 157-167.

Jung, K., Antoni, T., Muller, R., Kochem, K. H., amd Ehrhardt, H. (1982), Rotational excitation of N2, CO and H_2O by low-energy electron collisions, *Journal of Physics B: Atomic and Molecular Physics, 15(19)*, 3535.

Kamoun, P., Campbell, D., Pettengill, G., and Shapiro, I. (1998), Radar observations of three comets and detection of echoes from one: P/Grigg-Skjellerup, *Planetary and space science, 47(1)*, 23-28.

Kannenberg, K. C., and Boyd, I. D. (2000), Strategies for efficient particle resolution in the direct simulation Monte Carlo method, *Journal of Computational Physics, 157(2)*, 727-745.

Keller, H. U., et al. (1986), First Halley multicolour camera imaging results from Giotto, *Nature, 321*, 320-326.

Kelley, K. K. (1935), US Department of the Interior Bureau of Mines, *Bulletin, 584*.

Kelley, M. S. et al. (2013), A distribution of large particles in the coma of Comet 103P/Hartley 2, *Icarus, 222(2)*, 634-652.

Kelley, M. S., Li, J., Mutchler, M. J., Weaver, H. A., and Knight, M. M. (2014), The Pre-Perihelion Size of the Nucleus of Comet C/2012 S1 (ISON), *American Astronomical Society Meeting Abstracts (Vol. 223)*.

Klinger, J. (1981), Some consequences of a phase transition of water ice on the heat balance of comet nuclei, *International Astronomical Union and American Astronomical Society, Colloquium on Comets: Gases, Ices, Grains, and Plasma, 61st, Tucson, AZ, Mar. 11-14,1981. Icarus, 47*, 320-324.

Knight, M. M., and Schleicher, D. G. (2013), The highly unusual outgassing of Comet 103P/Hartley 2 from narrowband photometry and imaging of the coma, *Icarus, 222(2)*, 691-706.

Kobayashi, H., Kawakita, H., Mumma, M. J., Bonev, B. P., Watanabe, J. I., and Fuse, T. (2007), Organic volatiles in comet 73P-B/Schwassmann-Wachmann 3 observed during its outburst: A clue to the formation region of the Jupiter-family comets, *The Astrophysical Journal Letters, 668(1)*, L75.

Koura, K. (1986), Null?collision technique in the direct?simulation Monte Carlo method, *Physics of Fluids (1958-1988), 29(11)*, 3509-3511.

Koura, K. (1990), A sensitive test for accuracy in evaluation of molecular collision number in the direct?simulation Monte Carlo method, *Physics of Fluids A: Fluid Dynamics (1989-1993), 2(7)*, 1287-1289.

Knudsen, M. (1950), The kinetic theory of gases.

Lammerzahl, P. et al. (1986), Expansion velocity and temperatures of gas and ions measured in the coma of comet P/Halley, *Astronomy and Astrophysics, 187*, 169-173.

Lamy, P. L., Toth, I., Davidsson, B. J., Groussin, O., Gutiérrez, P., Jorda, L., Kaasalainen, M., and Lowry, S. C. (2007), A portrait of the nucleus of comet 67P/Churyumov-Gerasimenko, *Space science reviews, 128(1-4)*, 23-66.

Landau, L., and Teller, E. (1936), Theory of sound dispersion, *Physik. Z. Sowjetunion, 10*, 34.

Lee, S., Von Allmen, P., Kamp, L., Gulkis, S., and Davidsson, B. (2011), Non-LTE ra-

diative transfer for sub-millimeter water lines in Comet 67P/Churyumov-Gerasimenko, *Icarus, 215(2)*, 721-731.

Lee, Y., Combi, M. R., Tenishev, V., and Bougher, S. W. (2014), Hot carbon corona in Mars' upper thermosphere and exosphere: 1. Mechanisms and structure of the hot corona for low solar activity at equinox, *Journal of Geophysical Research: Planets*.

Leech et al. (1997), The Infrared Spectrum of Comet Hale-Bopp as Seen by the Intrared Space Observatory, *Earth, moon, and planets, 78*, 81-83.

Leger, A., Gauthier, S., Defourneau, D., and Rouan, D. (1983), Properties of amorphous H_2O ice and origin of the 3.1-micron absorption, *Astronomy and Astrophysics, 117*, 164-169.

Lien, D. J. (1990), Dust in comets. I-Thermal properties of homogeneous and heterogeneous grains, *The Astrophysical Journal, 355*, 680-692.

Lilley, C. R., and Sader, J. E. (2008), Velocity profile in the Knudsen layer according to the Boltzmann equation, *Proceedings of the Royal Society, 464*, 2015-2035.

Lisse, C. M. et al. (2009), Spitzer Space Telescope observations of the nucleus of Comet 103P/Hartley 2, *Publications of the Astronomical Society of the Pacific, 121(883), 968-975*.

Litvak, M. M., and Kuiper, E. R. (1982), Cometary NH-Ultraviolet and submillimeter emission, *The Astrophysical Journal, 253*, 622-633.

Llorca, J. (1999), Hydrocarbon synthesis in cometary grains, *Physics and Chemistry of the Earth, Part C: Solar, Terrestrial and Planetary Science, 24(5)*, 591-595.

Lopez-Valverde, M. A. et al. (2005), Analysis of CO_2 non-LTE emissions at in the Martian atmosphere as observed by PFS/Mars Express and SWS/ISO, *Planetary and Space Science, 53(10)*, 1079-1087.

Lopez-Valverde, M. A., Drossart, P., Carlson, R., Mehlman, R., and Roos-Serote, M. (2007), Non-LTE infrared observations at Venus: from NIMS/Galileo to VIRTIS/Venus Express, *Planetary and Space Science, 55(12)*, 1757-1771.

Lowry, S. C., Fitzsimmons, A., Cartwright, I. M., and Williams, I. P. (1999), CCD photometry of distant comets, *Astronomy and Astrophysics, 349*, 649-659.

Lowry et al. (2012), The nucleus of Comet 67P/Churyumov-Gerasimenko: a new shape model and thermophysical analysis, *Astronomy and Astrophysics, 548*.

Lunine, J. I. (1989), Primitive bodies-Molecular abundances in Comet Halley as probes of cometary formation environment, *The Formation and Evolution of Planetary Systems, 1*, 213-238.

Lutisan, J. (1995), The Treatment of Molecular Collisions in DSMC Methods, *Molecular Simulation, 14(3)*, 189-206.

Marconi, M. L., and Mendis, D. A. (1982), The photochemical heating of the cometary atmosphere, *The Astrophysical Journal, 260*, 386-394.

Marconi, M. L., and Mendis, D. (1983), The atmosphere of a dirty-clathrate cometary nucleus-A two-phase, multifluid model, *The Astrophysical Journal, 273*, 381-396.

Maxwell, G. J. C. (1904), Colours in metal glasses and metal films, *Philos. Trans. R. Soc. London, Sect. A, 3*, 385-420.

McClatchey, R. A., Benedict, W. S., Clough, S. A., Burch, D. E., and Calfee, R. F. (1973), AFCRL atmospheric absorption line parameters compilation, *AIR FORCE CAMBRIDGE RESEARCH LABS HANSCOM AFB MA*.

Meech, K. J. et al. (2011), EPOXI: Comet 103P/Hartley 2 observations from a worldwide campaign, *The Astrophysical Journal Letters, 734(1)*, L1.

Meier, R., Eberhardt, P., Krankowsky, D., and Hodges, R. R. (1993), The extended formaldehyde source in comet P/Halley, Astronomy and Astrophysics, 277, 677.

Mendis, D. A., and Brin, G. D. (1977), Monochromatic brightness variations of comets, *the Moon, 229*, 359-372.

Milkovich, S. M., Delamere, W. A., and McEwen, A. S. (2013), Observation of Comet ISON by the High Resolution Imaging Science Experiment (HiRISE) on Mars Reconnaisance Orbiter (MRO), *AGU Fall Meeting Abstracts (Vol. 1, p. 09)*.

Miller, R. H., and Combi, M. R. (1994), A Coulomb collision algorithm for weighted particle simulations, *Geophysical research letters, 21(16)*, 1735-1738.

Millican, R. C., and While, D. R., Systematics of vibrational relaxation, *The Journal of Chemical Physics, 39*, 3209-3213

Mocknatsche, D. O. (1938), *Leningrad State Univ. Annals, Astron. Series Issue, 4*.

Mukai, T. (1986), Analysis of a dirty water-ice model for cometary dust, *Astronomy and Astrophysics, 164*, 397-407.

Mukai, T., Fechtig, H., Gr§n, E., and Giese, R. H. (1989), Icy particles from comets, *Icarus, 80(2)*, 254-266.

Mumma, M. J., Weissman, P. R., and Stern, S. A. (1993), Comets and the origin of the solar system - Reading the Rosetta Stone, *Protostars and planets III (A93-42937 17-90)*, 1177-1252.

Mumma, M. J. et al. (2001), Organic composition of C/1999 S4 (LINEAR): A comet formed near Jupiter?, *Science, 292(5520)*, 1334-1339.

Mumma, M. J. et al. (2005), Parent volatiles in comet 9P/Tempel 1: Before and after impact, *Science, 310(5746)*, 270-274.

Mumma, M. J., and Charnley, S. B.(2011), The Chemical Composition of Comets - Emerging Taxonomies and Natal Heritage, *Annual Review of Astronomy and Astrophysics, 49*, 471-524.

Muntz, E. P., Weaver, D. P., and Campbell, D. H. (1989), Rarefied gas dynamics: theoretical and computational techniques, *American Institute of Aeronautics*.

Nanbu, K. (1980), Direct simulation scheme derived from the Boltzmann equation. I. Monocomponent gases, *Journal of the Physical Society of Japan, 49(5)*, 2042-2049.

Nanbu, K. (1983), Derivation from Kac's master equation of the stochastic laws for simulating molecular collisions, *Journal of the Physical Society of Japan, 52(12)*, 4160-4165.

Nebel, H., Wintersteiner, P. P., Picard, R. H., Winick, J. R., and Sharma, R. D. (1994),

CO_2 non-local thermodynamic equilibrium radiative excitation and infrared dayglow at 4.3 μm: Application to Spectral Infrared Rocket Experiment data, *Journal of Geophysical Research: Atmospheres (1984-2012), 99(D5)*, 10409-10419.

Ootsubo, T. et al. (2012), KARI near-infrared spectroscopic survey for CO_2 in 18 comets, *The Astrophysical Journal, 752(1)*, 15.

Oppenheimer, M., and Downey, C. J. (1980), The effect of solar-cycle ultraviolet flux variations on cometary gas, *The Astrophysical Journal, 241*, L123-L127.

Oran, E. S., Oh, C. K., and Cybyk, B. Z. (1998), DIRECT SIMULATION MONTE CARLO: Recent Advances and Applications, *Annual Review of Fluid Mechanics, 30*, 403-441.

Paganini, L., Villanueva, G. L., Lara, L. M., Lin, Z. Y., Kuppers, M., Hartogh, P., and Faure, A. (2010), HCN spectroscopy of Comet 73P/Schwassmann-Wachmann 3. A study of gas evolution and its link to CN, *The Astrophysical Journal, 715(2)*, 1258.

Panale, F. P., and Salvail, J. R. (1984), An idealized short-period comet model: Surface insolation, H_2O flux, dust flux, and mantle evolution, *Icarus, 60*, 476-511.

Patashnick, H., Rupprecht, G., and Schuerman, D. W. (1974), Energy source for comet outbursts, *Nature, 250*, 313-314.

Patashnick, H., and Rupprecht, G. (1975), The size dependence of sublimation rates for interplanetary ice particles, *The Astrophysical Journal, 197*, L79-L82.

Podolak, M., and G. Herman, Numerical simulations of comet nuclei: II. The effect of the dust mantle, *Icarus, 61*, 267-277.

Powell, K. G., Roe, P. L., Linde, T. J., Gombosi, T. I., and De Zeeuw, D. L. (1999), A solution-adaptive upwind scheme for ideal magnetohydrodynamics, *Journal of Computational Physics, 154(2)*, 284-309.

Protopapa, S. et al. (2014), Water ice and dust in the innermost coma of Comet 103P/Hartley 2, *Icarus, 238*, 191-204.

Reme, H. et al. (1993). Electron plasma environment at comet Grigg-Skjellerup: General

observations and comparison with the environment at comet Halley, *Journal of Geophysical Research: Space Physics (1978-2012), 98(A12)*, 20965-20976.

Reuter, D. C., Mumma, M. J., and Nadler, S (1989), Infrared fluorescence efficiencies for the nu1 and nu5 bands of formaldehyde in the solar radiation field, *Astrophysical Journal, 341*, 1045-1058.

Rubin, M., Fougere, N., Altwegg, K., Combi, M. R., Le Roy, L., Tenishev, V. M., and Thomas, N. (2014): Mass Transport around comets and its impact on the seasonal differences in water production rates, *The Astrophysical Journal, 788*, 168-175.

Rybicki, G. B. (1984), Escape probability methods, *Methods in Radiative Transfer, 1*, 21-64.

Schleicher, D. G., and A'Hearn, M. F. (1988), The fluorescence of cometary OH, *The Astrophysical Journal, 331*, 1058-1077.

Schleicher, D. G. (2006), Compositional and physical results for Rosetta's new target Comet 67P/Churyumov Gerasimenko from narrowband photometry and imaging, *Icarus, 181*, 442-457.

Schultz, D., Li, G. S. H., Scherb, F., and Roesler, F. L. (1993), The O (^{1}D) Distribution of Comet Austin 1989c1= 1990 V, *Icarus, 101(1)*, 95-107.

Schunk, R. W. (1975), Transport equations for aeronomy, *Planetary and Space Science, 23(3)*, 437-485.

Schunk, R., Nagy A. (2009), Ionospheres: physics, plasma physics, and chemistry, *Cambridge university press*.

Sekanina, Z., and Farrell, J. A. (1982), Two dust populations of particle fragments in the striated tail of Comet MRKOS 1957 V, *The Astronomical Journal, 87*, 1836-1853.

Sekanina, Z. (1990), Gas and dust emission from comets and life spans of active areas on their rotating nuclei, *Astronomical Journal, 100*, 1293-1314.

Sekanina, Z., Brownlee, D. E., Economou, T. E., Tuzzolino, A. J., and Green, S. F. (2004), Modeling the nucleus and jets of comet 81P/Wild 2 based on the Stardust encounter data,

Science, 304(5678), 1769-1774.

Sekanina, Z. (2005), Comet 73P/Schwassmann-Wachmann: Nucleus fragmentation, its light-curve signature, and close approach to Earth in 2006,*International Comet Quarterly, 27*, 225-240.

Serikov, V. V. (1991), Weighting schemes for Monte Carlo simulation and their applications to the calculation of shock waves in multicomponent and reactive gases, *Rarefied Gas Dynamics (Vol. 1, pp. 808-815)*.

Shimizu, M. (1976), The structure of cometary atmospheres, *Astrophysics and Space Science, 40(2)*, 243-251.

Skorov, Y., and Rickman, H. (1998), Simulation of gas flow in a cometary Knudsen layer, *Planetary and Space Science, 46*, 975-996.

Smoluchowski, R. (1981), Amorphous ice and the behavior of cometary nuclei, *Astrophysical Journal, Part 2 - Letters to the Editor, 244*, 31-34.

Snodgrass, C., Tubiana, C., Bramich, D. M., Meech, K., Boehnhardt, H., and Barrera, L. (2013), Beginning of activity in 67P/Churyumov-Gerasimenko and predictions for 2014-2015, *Astronomy and Astrophysics, 557*, A33.

Soderblom, L. A., Britt, D. T., Brown, R. H., Buratti, B. J., Kirk, R. L., Owen, T. C., and Yelle, R. V. (2004), Short-wavelength infrared (1.3-2.6 ?m) observations of the nucleus of Comet 19P/Borrelly, *Icarus, 167(1)*, 100-112.

Sokolov, V. F., and Sokolova, Y. A. (1982), *Soviet Technical Physical Letter, 7*, 268.

Squires, R. E., and Beard, D. B., Physical and Orbital Behavior of Comets, *Astrophysical Journal, 133*, 657.

Takayanagi, K., and Itikawa, Y. (1970), Elementary processes involving electrons in the ionosphere, *Space Science Reviews, 11(2-3)*, 380-450.

Tenishev, V., Combi, M. R., and Davidsson, B. (2008), A Global Kinetic Model for Cometary Comae: The Evolution of the Coma of the Rosetta Target Comet Churyumov-Gerasimenko throughout the Mission, *The Astrophysical Journal, 685*, 659-677.

Tenishev, V., Combi, M. R., and Rubin, M. (2011), Numerical Simulation of Dust in a Cometary Coma: Application to Comet 67P/Churyumov-Gerasimenko, *The Astrophysical Journal, 732*, 104.

Tenishev, V., Rubin, M., Combi, M. R., Slavin, J. A., and Raines, J. M. (2012), Kinetic modeling of sodium in the exosphere of Mercury, *AGU Fall Meeting Abstracts (Vol. 1, p. 1932)*.

Tenishev, V., Rubin, M., Tucker, O. J., Combi, M. R., and Sarantos, M. (2013), Kinetic modeling of sodium in the lunar exosphere, *Icarus, 226(2)*, 1538-1549.

Tenishev, V., Rubin, M., Borovikov, D., Jia, X., Combi, M. R., and Gombosi, T. I. (2013), Kinetic modeling of Europa's neutral atmosphere and pick-up ions, *AGU Fall Meeting Abstracts (Vol. 1, p. 1829)*.

Thomas, P. C. et al. (2013), Shape, density, and geology of the nucleus of Comet 103P/Hartley 2, *Icarus, 222(2)*, 550-558.

Toth, I., Lamy, P. L., and Weaver, H. A. (2003), Hubble Space Telescope observations of the nucleus fragment 73P/Schwassmann-Wachmann 3-B, *In Bulletin of the American Astronomical Society (Vol. 35, p. 985)*.

Toth, G. et al. (2005), Space Weather Modeling Framework: A new tool for the space science community, *Journal of Geophysical Research: Space Physics (1978-2012)*, 110(A12).

Valeille, A., Combi, M. R., Tenishev, V., Bougher, S. W., and Nagy, A. F. (2010), A study of suprathermal oxygen atoms in Mars upper thermosphere and exosphere over the range of limiting conditions, *Icarus, 206(1)*, 18-27.

Van De Hulst, H. C. (1957), Light scattering by small particles, *Courier Dover Publications*.

Van Dishoeck, E. F., and Dalgarno, A. (1984), The dissociation of OH and OD in comets by solar radiation, *Icarus, 59(3)*, 305-313.

Villanueva, G. L., Bonev, B. P., Mumma, M. J., Magee-Sauer, K., DiSanti, M. A., Salyk, C., and Blake, G. A. (2006), The volatile composition of the split ecliptic comet 73P/Schwassmann-Wachmann 3: A comparison of fragments C and B, *The Astrophysical Journal Letters,*

650(1), L87.

Villanueva, G. L. et al. (2011), The molecular composition of Comet C/2007 W1 (Boattini): Evidence of a peculiar outgassing and a rich chemistry, *Icarus, 216(1)*, 227-240.

Villanueva, G. L., DiSanti, M. A., Mumma, M. J., and Xu, L. H. (2012), A quantum band model of the $\nu 3$ fundamental of methanol (CH3OH) and its application to fluorescence spectra of comets, *The Astrophysical Journal, 747(1)*, 37.

Villanueva, G. L., Mumma, M. J., Bonev, B. P., Novak, R. E., Barber, R. J., and DiSanti, M. A. (2012), Water in planetary and cometary atmospheres: H_2O/HDO transmittance and fluorescence models, *Journal of Quantitative Spectroscopy and Radiative Transfer, 113*, 202-220.

Wagner, W. (1992), A Convergence Proof for Bird's Direct SImulation Monte Carlo Method for the Boltzmann Equation, *Journal of Statistical Physics, 66*, 1011-1044

Wallace, L. V., Miller, I., and Freeman, D. (1958), Isophote configurations for model comets, *The Astronomical Journal, 63*, 213.

Wallis, M. K. (1980), Radiogenic melting of primordial comet interiors, *Nature, 284*, 431-433.

Weaver, H. A., Feldman, P. D., McPhate, J. B., A'Hearn, M. F., Arpigny, C., and Smith, T. E. (1994), Detection of CO Cameron band emission in comet P/Hartley 2 (1991 XV) with the Hubble Space Telescope, *The Astrophysical Journal, 422*, 374-380.

Weaver, H. A. (2006), The Amazing Apparition of 73P/Schwassmann-Wachmann 3 in 2006, *In Bulletin of the American Astronomical Society (Vol. 38, p. 484)*.

Weaver, H. A., Lisse, C. M., Mutchler, M., Lamy, P. L., Toth, I., Reach, W. T., and Vaubaillon, J. (2008), Hubble investigation of the B and G fragments of comet 73P/Schwassmann-Wachmann 3, *LPI Contributions, 1405*, 8248.

Weissman, P. R., and Kieffer, H. H. (1984), An improved thermal model for cometary nuclei, *Journal of Geophysical Research: Solid Earth (1978-2012), 89*, 358-364.

Whipple, F. L. (1950), A comet model. I. The acceleration of Comet Encke, *Astrophysical*

Journal, 111, 375-394

Whipple, F. L. (1964), Evodence for a Comet Belt beyond Neptune, *Proceedings of the National Academy of Sciences of the United States of America, 51*, 711-718.

Whipple, F. L., Stefanik, R. P. (1966), On the physics and splitting of cometary nuclei, *Mem. R. Soc. Liege, 12*, 33-52.

Whipple, F. L., and Huebner, W. F. (1976), Physical processes in comets, *Annual review of astronomy and astrophysics, Volume 14, (A76-46826 24-90) Palo Alto, California, Annual Reviews, Inc.*, 143-172.

Xie, X., and Mumma, M. J. (1992), The effect of electron collisions on rotational populations of cometary water, *The Astrophysical Journal, 386*, 720-728.

Xie, X., and Mumma, M. J. (1996), Monte Carlo Simulation of Cometary Atmospheres: Application to Comet P/Halley at the Time of the Giotto Spacecraft Encounter.II.Axisymmetric Model, *Astrophysical Journal, 464*, 457.

Zakharov, V. V., Bockelée-Morvan, D., Biver, N., Crovisier, J., and Lecacheux, A., Radiative transfer simulation of water rotational excitation in comets. Comparison of the Monte Carlo and escape probability methods, *Astronomy and Astrophysics, 473(1)*, 303-310.

Zakharov, V. V., Rodionov, A. V., Lukianov, G. A., and Crifo, J. F. (2009), Monte-Carlo and multifluid modelling of the circumnuclear dust coma II. Aspherical-homogeneous, and spherical-inhomogeneous nuclei, *Icarus, 201*, 358-380.

Zelejnik, F. J. (1969), A comparison of rotational collision numbers obtained from different definitions, *National Aeronautics and Space Administration, TN D-5321*.